Etude électromécanique de nanofils piézoélectriques semi conducteurs. Application aux capteurs et recuperateurs d'énergie mecaniques

Ronan Hinchet

▶ **To cite this version:**

Ronan Hinchet. Etude électromécanique de nanofils piézoélectriques semi conducteurs. Application aux capteurs et recuperateurs d'énergie mecaniques. Micro and nanotechnologies/Microelectronics. Université de Grenoble, 2014. English. NNT : 2014GRENT013 . tel-01280914

HAL Id: tel-01280914
https://theses.hal.science/tel-01280914

Submitted on 1 Mar 2016

HAL is a multi-disciplinary open access archive for the deposit and dissemination of scientific research documents, whether they are published or not. The documents may come from teaching and research institutions in France or abroad, or from public or private research centers.

L'archive ouverte pluridisciplinaire **HAL**, est destinée au dépôt et à la diffusion de documents scientifiques de niveau recherche, publiés ou non, émanant des établissements d'enseignement et de recherche français ou étrangers, des laboratoires publics ou privés.

UNIVERSITÉ DE GRENOBLE

THÈSE

Pour obtenir le grade de

DOCTEUR DE L'UNIVERSITÉ DE GRENOBLE

Spécialité : **Nano Electronique et Nano Technologies**

Arrêté ministériel : 7 août 2006

Présentée par

Ronan HINCHET

Thèse dirigée par **Mireille MOUIS**
codirigée par **Gustavo ARDILA** et **Laurent MONTES**

préparée au sein de **l'Institut de Microélectronique Electromagnétisme et Photonique et le LAboratoire d'Hyperfréquences et de Caractérisation (IMEP-LAHC)**
dans **l'école doctorale d'Electronique Electrotechnique Automatique Traitement du Signal (EEATS)**

Electromechanical study of semiconductor piezoelectric nanowires.

Application to mechanical sensors and energy harvesters.

Thèse soutenue publiquement le **Vendredi 4 avril 2014**,
devant le jury composé de :

Mr Marc LETHIECQ
Pr au GREMAN à Tours, Rapporteur
Mr Laurent PICHON
Pr à l'IETR à Rennes, Rapporteur
Mr Olivier THOMAS
Pr à l'IM2NP à Marseille, Président
Mrs Mireille MOUIS
Dr à l'IMEP-LAHC à Grenoble, Membre
Mr Laurent MONTES
MCF à l'IMEP-LAHC à Grenoble, Membre
Mr Gustavo ARDILA
MCF à l'IMEP-LAHC à Grenoble, Membre
Université Joseph Fourier / Université Pierre Mendès France / Université Stendhal / Université de Savoie / Grenoble INP

It is the broadcast version of this thesis.

This version does not include all reproductions for copyright reasons.

Il s’agit de la version de diffusion de cette thèse.

Cette version ne comprend pas toutes les reproductions pour des raisons de droits d'auteur.

Acknowledgements

First, I would like to thank my director Mireille Mouis for her contribution and advices, and my advisors at IMEP-LAHC, Gustavo Ardila and Laurent Montes, for all the time they spent advising me on my research. They helped me immensely by sharing their knowledge and skills. They followed my advances step by step and carefully reviewed my dissertation. In addition to being well qualified in the field of MEMS, they have been a great support during the last three years. They gave me the opportunity to present my work in numerous conferences and set up numerous collaborations, giving a strong impulse to my thesis. It has been a unique experience to work with them and I could never thank them enough for their tremendous help. I also wish to express my gratitude to Dr. Xin Xu and Dr. Alexis Potie, who were the first to investigate this field of research in IMEP-LAHC and offered their guidance and advice at the beginning of my thesis.

My next acknowledge goes to my thesis collaborators, especially Pr. Zhong Lin Wang, Pr. Yiming Li and Dr. Emmanuelle Pauliac-Vaujour. Their collaboration and help were determinant for my thesis. I will never forget my exchange in Pr. Zhong Lin Wang's laboratory in Georgia Tech which gives me a new perspective on my thesis and the research. I would also like to thank all my Georgia Tech colleagues for their warm welcome and helping hand for scientific and personal matters, especially Yusheng Zhu, Ken Pradel and Dr. Sangmin Lee. I would like to thank our partners who made my thesis and collaborations possible: the Rhône-Alpes region, the NanoFunction program and the UJF Grenoble (Smingue). Their invaluable support allowed me to conduct the experiments and to develop the collaborations necessary for my thesis.

The development of my thesis would not have been possible without the decisive support and help of my colleagues who shown interest and engagement. Also, I sincerely praise all the PhD students who were of great help for scientific and personal matters, and especially Rémy Lefevre, Arnaud Salette, Imed Ben akkez and Minju Shin. Thanks also to all my students and interns who made my PhD an enjoyable experience. I am grateful to all the staff of IMEP-LAHC who allowed me to work and to conduct research in good situation. Special thanks to Xavier Mescot, Martine Gri and Antoine Gachon who supported my experimental research and gave me all the attention necessary to develop new tools and measurements.

Last, but not the least, I would like to express my gratitude to all my friends for always being there for me and to my family for their unconditional support.

Abstract

Smart systems are the combined result of different advances in microelectronics leading to an increase in computing power, lower energy consumption, the addition of new features, means of communication and especially its integration and application into our daily lives. The evolution of the field of smart systems is promising, and the expectations are high in many fields: Industry, transport, infrastructure and environment monitoring as well as housing, consumer electronics, health care services but also defense and space applications. Nowadays, the integration of more and more functions in smart systems is leading to a looming energy issue where the autonomy of such smart systems is beginning to be the main issue. Therefore there is a growing need for autonomous sensors and power sources. Developing energy harvesters and self-powered sensors is one way to address this energy issue. Among the technologies studied, piezoelectricity has the advantage to be compatible with the MEMS industry, it generates high voltages and it has a high direct coupling between the mechanic and electric physics. Among the piezoelectric materials, semiconductor piezoelectric nanowires (NWs) could be a promising option as they exhibit improved piezoelectric properties and higher maximum flexion.

Among the different piezoelectric NWs, ZnO and GaN NWs are the most studied, their piezoelectric properties are more than doubled at the nanoscale. They have the advantage of being IC compatible and reasonably synthesizable by top-down and bottom-up approaches. Especially we studied the hydrothermal growth of ZnO NWs. In order to use them we studied the behavior of ZnO NWs. We performed analytical study and FEM simulations of a ZnO NW under bending. This study explains the piezoelectric potential distribution as a function of the force and is used to extract the scaling rules. We have also developed mechanical AFM characterization of the young modulus of ZnO and GaN NWs. Following we perform piezoelectric AFM characterization of these NWs, verifying the behavior under bending stresses. Once physics understood, we discuss limitation of our piezoelectric NWs models and a more realistic model is developed, closer to the experimental configurations. Using this model we evaluated the use of ZnO NW for force and displacement sensors by measuring the potential generated, and from experiments, the use of GaN NW for force sensor by measuring the current through the NW. But energy harvesting is also necessary to address the energy issue and we deeper investigate this solution. To fully understand the problematic we study the state of the art of nanogenerator (NG) and their potential architectures. We analyze their advantages and disadvantages in order to define a reference NG structure. After analytical study of this structure giving the basis for a deeper understanding of its operation and challenges, FEM simulations are used to define optimization routes for a NG working in compression or in bending. The fabrication of prototypes and theirs preliminary characterization is finally presented.

Keywords: NEMS, Energy harvesting, Nanostructures, AFM, Piezoelectric Nanowires.

Résumé

Les systèmes intelligents sont le résultat combiné de différentes avancées en microélectronique et en particulier de l'augmentation des puissances de calcul, la diminution des consommations d'énergie, l'ajout de nouvelles fonctionnalités et de moyens de communication et en particulier à son intégration et application dans notre vie quotidienne. L'évolution du domaine des systèmes intelligents est prometteuse, et les attentes sont élevées dans de nombreux domaines : pour la surveillance dans l'industrie, les transports, les infrastructures et l'environnement, ainsi que dans le logement, l'électronique grand public et les services de soins de santé, mais aussi dans les applications pour la défense et l'aérospatial. Aujourd'hui, l'intégration de plus en plus de fonctions dans les systèmes intelligents les conduisent vers un problème énergétique où l'autonomie devient le principal problème. Par conséquent, il existe un besoin croissant en capteurs autonomes et sources d'alimentation. Le développement de dispositifs de récupération d'énergie et de capteurs autoalimentés est une façon de répondre à ce problème énergétique. Parmi les technologies étudiées, la piézoélectricité a l'avantage d'être compatible avec l'industrie des MEMS. De plus elle génère des tensions élevées et elle possède un fort couplage direct entre les physiques mécaniques et électriques. Parmi les matériaux piézoélectriques, les nanofils (NFs) semi-conducteurs piézoélectriques pourraient être une option prometteuse car ils présentent des propriétés piézoélectriques plus importantes et une plus grande gamme de flexion.

Parmi les différents NFs piézoélectriques, les NFs de ZnO et de GaN sont les plus étudiés. A l'échelle nanométrique leurs propriétés piézoélectriques sont plus que doublées. Ils ont l'avantage d'être compatible avec l'industrie microélectronique et raisonnablement synthétisable par des approches top-down et bottom-up. En particulier, nous avons étudié la croissance par voie chimique de NFs de ZnO. Pour les utiliser correctement, nous avons étudié le comportement des NFs de ZnO. Nous avons effectué une étude analytique et des simulations par éléments finis (FEM) d'un NF de ZnO en flexion. Ces études décrivent la distribution du potentiel piézoélectrique en fonction de la force et permettent d'établir les règles d'échelle et de dimensionnement. Ensuite, nous avons développé la caractérisation mécanique par AFM du module de Young de NFs de ZnO et de GaN, puis nous avons effectué des caractérisations piézoélectriques par AFM de ces NFs pour vérifier leur comportement sous des contraintes mécaniques de type flexion. Une fois leur comportement physique compris, nous discutons des limites de notre modèle de NFs piézoélectriques en flexion et nous développons un modèle plus réaliste et plus proche des configurations expérimentales. En utilisant ce nouveau modèle, nous avons évalué le potentiel des NFs de ZnO pour les capteurs de force et de déplacement en mesurant le potentiel généré sous une contrainte, puis, sur la base d'expériences, nous avons évalué l'utilisation de NFs de GaN pour les capteurs de force en mesurant le courant au travers des NFs contraints. De même, nous avons évalué le potentiel de ces NFs pour les applications de récupération d'énergie liées aux capteurs autonomes. Pour bien comprendre la problématique, nous avons étudié l'état de l'art des nano générateurs (NG) et leurs architectures potentielles. Nous analysons leurs avantages et inconvénients, afin de définir une structure de NG de référence. Après une brève étude analytique de cette structure pour comprendre son fonctionnement et les défis, nous avons effectué plusieurs simulations FEM pour définir des voies d'optimisation pour les NG utilisé en mode de compression ou de flexion. Enfin la fabrication de prototypes et leurs caractérisations préliminaires sont présentées.

Mots clés : NEMS, Récupération d'énergie, Nanostructures, AFM, Nanofil piézoélectrique.

Table of contents

Notations

Symbol	Description	Value	Unit
a	Cristal mesh parameter		m
A	Surface		m^2
C	Capacitance		F
c	Elasticity matrix		Pa
d	Diameter		m
D	Electric displacement		$C.m^{-2}$
d_{pq}	Constant of proportionality between the charge and the stress at zero or constant electric field. The index refers to the indices of the matrix coefficients.		$C.N^{-1}$ or $m.V^{-1}$
E	Electric field		$V.m^{-1}$
e_{pq}	Constant of proportionality between the charge and the deformation at zero or constant electric field. The index refers to the indices of the matrix coefficients.		$C.m^{-2}$
F	Force		N
f	Frequency		Hz
G	Free enthalpy		J
g_{pq}	Constant of proportionality between the stress and the electric field at zero or constant induction. The index refers to the indices of the matrix coefficients.		$m^2.C^{-1}$
h	Planck constant	$6.626\ 069\ 57\times10^{-34}$	J·s
h_{pq}	Constant of proportionality between the deformation and the electric field at zero or constant induction. The index refers to the indices of the matrix coefficients.		$N.C^{-1}$ or $V.m^{-1}$
I	Current		A
i	Imaginary number		-
I_i	Area moments of inertia to the i axis		m^4
J	Current density		$A.m^{-2}$
k	Boltzmann constant	$1.380\ 648\ 8\times10^{-23}$	$J\cdot K^{-1}$
l	Length		m
L	Inductance		H
M	Mass		Kg
m*	Effective mass		Kg

M_W	Molar weight		g
n	Electron concentration		m^{-3}
$\vec{n}$	Normal vector		-
N_a	Acceptor doping concentration		cm^{-3}
N_d	Donor doping concentration		cm^{-3}
P	Pressure		Pa
$\vec{P}$	Electric polarization		V
p	Hole concentration		m^{-3}
$\mathscr{P}$	Electrical power		W
Q	Charge		C
q	Elementary charge	$1.602\ 176\ 565\times10^{-19}$	C
r	Radius		m
R	Resistance		Ω
R_c	Radius of curvature		m
S	Strain		-
s	Stiffness		$m^2.N^{-1}$
T	Stress		Pa
t	Time		s
U	Potential		V
v	Volume		m^3
ν	Speed		$m.s^{-1}$
V	Voltage		V
w	Width		m
W	Work		J
Y	Young's modulus		Pa
Z	Electric impedance		-
α	Form factor or ratio		-
β	Impermeability constant		$m.F^{-1}$
δ	Displacement		m
ε	Dielectric constant		$F.m^{-1}$
η	Efficiency		-
θ	Temperature		ºC or K
λ	Wavelength		m

μ	Permeability	$H.m^{-1}$
μ_i	Electrical mobility of i	$m^2.V^{-1}.s^{-1}$
ξ	Energy	J
ρ_v	Density	$Kg.m^{-3}$
ρ	Resistivity	$\Omega.m$
ρ_i	Density of charge i	$C.m^{-3}$
σ	Conductivity	$S.m^{-1}$
τ	Time constant	s
τ_i	Mechanical load tensor	-
υ	Poisson coefficient	-
φ	Phase	rad
ϕ	Electrostatic potential	eV
χ	Electric susceptibility	-
ω	Pulsation	$rad.s^{-1}$

Acronyms

Acronym	Designation
AAO	Anodized Aluminum Oxide
AFM	Atomic Force Microscope
ALD	Atomic Layer Deposition
BAW	Bulk Acoustic Wave
CAD	Computer Aided Design
CB	Conduction Band
CMOS	Complementary metal–oxide–semiconductor
CPU	Central processing unit
CVD	Chemical Vapor Deposition
DART	Dual AC Resonance Tracking
DI	DeIonized
DIL	Dual InLine package
DRIE	Deep Reactive Ion Etching
EDX	Energy Dispersion X ray
FEM	Finite Element Method
FET	Field Effect Transistor
HEMT	High Electron Mobility Transistor
HMTA	HexaMethyleneTetrAmine
HVPE	Hydride vapour phase epitaxy
ID	Identification
ITO	Indium tin oxide
KFM	Kelvin Force Microscopy
LED	Light-emitting diode
LING	Lateral Integrated Nano Generator
MBE	Molecular Beam Epitaxy
MEMS	Micro Electro Mechanical System
MOCVD	Metalorganic chemical vapour deposition
MOVPE	Metalorganic vapour phase epitaxy
NEMS	Nano Electro Mechanical System

NG	Nano Generator
NSOM	Near-field Scanning Optical Microscopy
NW	Nano Wire
P_3HT	Poly-3-hexylthiophène
PDMS	PolyDiMethylSiloxane
PFM	Piezoelectric Force Microscopy
PIE	PolyEthylenImine
Piezo	Piezoelectric
PL	Photo Luminescence
PLD	Pulse Laser Deposition
PMMA	PolyMethyfilmethAcrylate
PVDF	PolyVinylidene DiFluoride
PZT	Lead Zirconium Titanate
RF	Radio Frequency
RHEED	Reflection High Energy Electron Diffraction
SBH	Schottky Barrier Height
SC	Semi-Conductor
SEM	Scanning Electron Microscopy
SFM	Scanning Force Microscopy
SP	Spectro Photometry
STM	Scanning Transition Microscopy
TCO	Transparent Conductive Oxide
TED	Thermionic Emission Diffusion
TEM	Tunneling Effect Microscope
TFE	Thermionic Field Emission
UHV	Ultra High Vacuum
USD	United State Dollars
UV	Ultra Violet
VING	Vertical Integrated Nano Generator
VLS	Vapor Liquid Solid
Vo	Oxygen Vacancy
XRD	X Ray Diffraction

Introduction: Development of autonomous sensors

Over the last few years miniaturization progress resulted in microelectronics to an increase of the computing power together with a decrease of the energy consumption of each transistor, thus opening a new era of portable devices (laptops, cell phones, tablets). Simultaneously the development of MEMS created new functions bringing additional features while the evolution of communication technologies allowed them being organized into networks, leading to the concept of smart systems. It is the integration of multi-functional micro or nano devices with the capability to sense, control, communicate and actuate (or respond) which could be organized into an internet of things. Recently this concept met a large success in many fields such as in industry for the predictive maintenance of machinery, in automotive with tire pressure sensors for example and in infrastructure and environment for monitoring failures, cracks and temperature variations. But also in housing for presence wireless sensors, in consumer electronics with smart phone and health care services with blood pressure sensors. And, in defense and space applications, with for monitoring equipment and people (border surveillance).

Currently smart systems are everywhere in our daily life, resulting in the integration of more and more functions and capabilities. Despite all the progress in decreasing the power consumption, smart systems are consuming more and more energy. Thus an energy issue of autonomous systems is looming. Therefore there is a growing need for autonomous sensors and power sources. But batteries are taking a lot of space. For example, smart phone battery currently holds toughly only one day. Batteries do not evolve a lot and have poor perspectives. In addition it can be difficult to replace them when considering huge autonomous sensors networks in harsh environments. Thus the development of energy harvester and self-powered sensors is an effective way to complement batteries by extending the operating time of smart systems and solving this energy issue.

Among the energy available in our daily life environment, mechanical energy is widespread and one of the most abundant in power. Then within mechanical energy harvesting technologies, piezoelectricity has the advantages to be possibly compatible with the IC industry, it generates high voltages and it has a high direct coupling between the mechanic and electric physics compared to electromagnetic or electrostatic. Currently the study and application of nanowires (NWs) is drawing a lot attention due to their integration capabilities and enhanced properties at nanoscale. For the same reasons, among the piezoelectric materials, semiconductor piezoelectric NWs could have a competitive advantage as they exhibit enhanced piezoelectric properties and withstand multiple integrations routes with the IC industry.

This problematic is new and in the IMEP-LAHC laboratory in Grenoble, the work on piezoelectric NWs started in 2011 with the electromechanical AFM characterization of GaN NWs [1]. The main goal of this thesis is to study the electromechanical behavior of GaN and ZnO semiconductor piezoelectric NWs for mechanical force and displacement sensors and energy harvesting applications. This work has been developed through the collaboration with several laboratories that provided samples of bottom up GaN NWs (Neel Institute, Grenoble, France), top down GaN NWs (CHREA, Nice, France) and bottom up ZnO NWs (Chimie Paris, France). In addition, CBD growth of ZnO NWs and nanogenerator (NG) prototyping have been studied thanks to a close collaboration with Georgia Tech, Atlanta, USA. In this thesis, GaN and ZnO NWs have been studied and evaluated as sensors or integrated in energy harvesters using theoretical models to proof of concept devices.

To address these objectives the research conducted are presented in this manuscript and distinguished into 4 steps:

1. First we describe the context of the looming energy issue of autonomous sensors which is related to the current IC industry market integrating still more features into micro devices which decrease their autonomy. Thus batteries are not sufficient anymore to power autonomous sensors for a long term use. To address this problem we decided to develop energy harvesting and low self-powered sensors based on piezoelectric NWs. Among the possible energy sources we chose to harvest the mechanical energy thanks to the piezoelectric phenomenon. More specifically we focused on piezoelectric semiconducting ZnO and GaN NWs for their good properties and compatibility with the IC industry. We present the theoretical bases of the piezoelectric physics, materials properties, applications and we also discuss piezoelectric NWs properties.

2. Then we study various fabrication processes of ZnO and GaN NWs. We have chosen to develop the hydrothermal growth of ZnO NWs in IMEP-LAHC. But before to use NWs array it is important to theoretically study the behavior of individual ZnO NWs. Thus we performed an analytical study and FEM simulation of a ZnO NW under bending. This study explains the piezoelectric potential distribution as a function of the force and extracts scaling rules of ZnO NWs. Then we investigate the mechanical AFM characterization of individual ZnO and GaN NWs. While the Young modulus of ZnO and GaN individual NW could be a clue of any mechanical scale effect, we perform AFM characterization of these NWs to have a deeper insight into the behavior of individual NW under bending stress. Preliminary PFM and electrical characterization are then discussed.

3. Once their individual physics better understood, we discuss the limits of the piezoelectric NWs models and a more realistic model is developed, closer to the experimental NWs array configurations and taking into account NWs size distribution. We study the behavior of ZnO NW under high forces (nonlinear mechanic) and as a function of shape, substrate material, surrounding environment and doping. Following, simulation show that it was possible to use ZnO NWs for force and displacement sensors by monitoring the potential generated and that their sensitivity and space resolution could be tune by selecting the NWs. Experimentally GaN NWs for force sensor is demonstrated by measuring the current through the NW.

4. But energy harvesting is also necessary to address future energy issue in autonomous devices and we deeper investigate mechanical energy harvesters. First we give a state of the art of the mechanical energy resources and the systems of mechanical energy harvesting. For that ZnO and GaN NWs could be good candidates. To fully understand the problematic we study the state of the art of NGs and their potential architectures. We analyze pros and cons in order to define a reference NG structure for our study. After an overall analytical study of this structure to have a deeper understanding of its operation, we perform multiple FEM simulations to define optimization routes and to design an optimized NG working in compression or in bending. Finally we fabricate and characterized NG prototypes.

Chapter I. Context and theoretical bases

I.1. Energy supply issue for autonomous systems

I.1.1. Driving trend: reduction of energy consumption and integration of new functions

Since the beginning of the microelectronics industry, the miniaturization of electronic components has allowed a continuous reduction in their power consumption to the point that, while the processors become more powerful (Moore's Law), power consumption remained substantially the same. The index of consumption of a transistor within Intel processors, standardized by its operating frequency has been decreasing in recent years [2]. Improving the energy efficiency of electronics components made possible to operate increasingly complex systems (microprocessors, memories ...).

This outstanding improvement of microelectronic technologies (typically CMOS) has been complemented by the emergence and the development of new technological processes allowing the surface and volume machining of silicon. These new techniques have allowed the development of electro mechanical systems. Thus was born the concept of MEMS (Micro-Electro-Mechanical Systems). The first MEMS appeared in the 1960s, but it was only in the 1980s that this technology took off with pressure sensors on silicon, print nozzles (printers) or accelerometers (airbags) and replaced the older technologies. Since then, MEMS experienced significant growth and are still booming.

By definition, MEMS are composed of mechanical and electronic components with µm size, allowing the realization of sensing functions (pressure, acceleration, mass ...) or actuators (motors ...). These structures are obtained by techniques used in microelectronics such as lithography, etching, deposition ... and are characterized by the presence of a "free" element capable of moving under the action of external forces (acceleration, pressure, voltage ...). Today, MEMS market covers diverse fields in defense (micro-caps), medicine (micro-pumps, micro-valves, blood pressure), electronics (micro-relays, printers nozzle jet ink), telecommunications (accelerometers, magnetometers, gyroscopes in phones and game consoles, optical data transfer), automotive (sensor for paths correction, management of the airbag, tire pressure sensors) aeronautics or biology.

I.1.2. From MEMS to Smart systems

Thanks to the combination of microsystems improvement and scale reduction of new elementary functions due to MEMS technologies, it is now possible to imagine a full system, “intelligent”, able to measure, treat and to transmit information (acceleration, pressure, temperature ...), all integrated into less than 1cm². With tens, a hundred or a thousand of these smart systems, it becomes possible to design a network capable of mappings (pressures, temperatures ...) and transmit this information to a management system. Furthermore, in order to limit costs, weight and to simplify installation, the general will is to integrate the wireless technology to these systems and to make them autonomous. The elementary block of these systems is the autonomous system or more often the autonomous sensor. An autonomous sensor is an integration of multi-functional micro or nano devices with the capability to sense, control, communicate and actuate (or respond) which could be organized into a network (Figure 1).

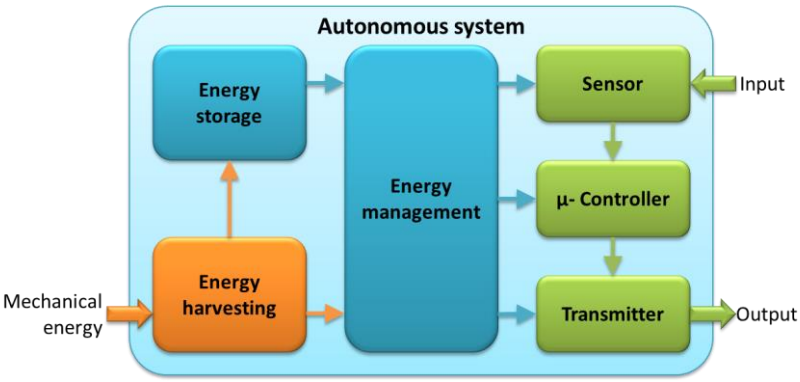

Figure 1 Schematic of an autonomous system using an energy harvesting unit.

These smart systems made of autonomous sensors lie at the crossroads of four areas of progress:

- The evolution of silicon technology with a reduction in size and power consumption of electronic components at equivalent performance, allowing a reduction of microsystems power consumption to less than a microwatt.
- The contribution of MEMS features that, with higher photolithography resolution, can design and manufacture extremely compact functional objects (sensors and actuators) and thus minimally invasive. Today the integration level of MEMS is very advanced and microsystems are increasingly complex and heterogeneous [3].
- the evolution of computers and networks since the birth of the concept of the computer in 1960 [4] have made spectacular progress: it is possible to design reconfigurable ad hoc networks where nodes are mobile, with fault-tolerant connections.
- The evolution of energy storage has been widely miniaturized with energy densities rising sharply since the advent in the 1990s of Li-ion batteries [5].

One of the most widespread applications of autonomous sensors is the network of wireless sensors: many autonomous sensors are distributed over the area to be monitored, where they collect relevant data from their environment (temperature, gas, vibrations ...) and then transmit it to the user or to a dedicated system of automatic diagnosis [6]. The first proof of concept of such a wireless sensors network is the Smart Dust [7] with the aim to design microscopic sensors for monitoring a military operation field. The idea was to integrate into $1mm^3$ sensors, power supply, electronics, optical communication system and microprocessor.

Societal and economic issues of wireless sensor networks are important as they relate to the integration of intelligence around the human being and his environment in many application fields: health (monitoring of sickness ...), the environment (fire prevention ...), security (military or civilian), food, transportation (tire pressure control ...), aeronautics, space and housing. According to the Technology Review from MIT, wireless sensor networks are one of the ten technologies that will change the world and our way of life. In the short term, three main application areas are interesting for autonomous sensor networks:

- The environmental monitoring and study
- Monitoring to interact with the environment
- Monitoring of human activity (health, mechanical structures, industrial equipment …)

For the operation of such autonomous sensors which are capturing, processing and transmitting data, it is necessary to supply electricity. In the case of a network of autonomous sensors, each building block must have its own source of energy. Thus, energy supply and management of electrical energy is a central issue in the design of autonomous sensors. The integrated microelectronic modules are

becoming smaller and they are consuming less and less power. Strategies of network organization to minimize the RF transmissions [8], optimize the components, limit the frequency and precision of measurement are implemented, but they all provide only a limited economy of the energy resources embedded. Therefore new approaches considering energy harvesting are now deeply investigated to increase the life time of autonomous sensors.

I.2. Towards self-powered smart sensors

I.2.1. Batteries limits: a need for new energy sources

With the arrival each year of new technologies, it is thus clear that the power supply of microsystems and especially autonomous sensors will become a challenge. Our project takes place in the current need for these systems to find autonomous and continuous sources of energy where power on the scale of microwatts is usually needed. There are various possibilities to address the problem of powering the autonomous systems:

- Improve the energy density of storage systems.
- Develop novel methods to distribute power to nodes.
- Develop technologies that enable a node to generate or harvest its own power.

One possibility is to use batteries. Research to increase the storage density of both rechargeable and primary batteries has been conducted for many years and continues to receive substantial focus [9], [10]. But it appears that the electrochemical tanks even if they are little used or not, lose the stored energy because of the phenomenon of self-discharge. The self-discharge is 30% of the total load per month for NiMH storage against 2-3% per month for Lithium storage [11]. In addition, we are already seeing the environmental problems that the arrival of any new technology poses today. This is particularly the case with regard to batteries of a growing number of autonomous devices such as mobile phones which presents difficulties to be properly recycled. Extend the autonomy of these devices would be a valuable help for this example of environmental problem. The past few years have also seen many efforts to miniaturize fuel cells which promise several times the energy density of batteries [12], [13]. While these technologies promise to extend the lifetime of wireless sensor nodes, they cannot extend their lifetime indefinitely. The too low energy density of electrochemical storage limits the lifetime of deployed sensors networks. In addition, such a sensor network will be almost impractical if each sensor has to be powered by a battery because of the huge number of sensors. They would imposes a difficult maintenance because of their possible difficult access (e.g. in hostile territory, delicate body, fragile structures or hard environment) and environmental and health concerns.

Many passive electronic devices, such as electronic ID tags and smart cards, are powered by a nearby energy rich source that transmits RF energy to the passive device, which then uses that energy to run its electronics [14]. However, this method is not practical when considering dense networks of wireless nodes because an entire space, such as a room, would need to be flooded with RF radiation to power the nodes. The amount of radiation needed to do this would probably present a health risk and today exceeds regulations.

Nevertheless, the current low power consumption of smart sensors makes possible to use the energy harvested from the environment to power such a system [15]. Therefore, new technologies that can harvest energy from the environment as sustainable self-sufficient micro / nano-power sources offer a possible solution. In addition a wireless sensor can have an active mode but most importantly, a

standby mode, during which the device is “sleeping” with minimum energy consumption. The power generated by an energy harvester may not be sufficient to continuously drive the operation of a device, but an accumulation of charges generated over a period of time is sufficient to drive the device for few seconds. This could be of practical use for devices that have standby and active modes, such as glucose and blood pressure sensors for example, which are only required to be in active mode periodically. The energy generated when the device is in standby mode is likely to be sufficient to refill a battery and drive the device when it is in active mode.

I.2.2. The emergence of energy harvesters and self-powered sensors

By reducing the scale of sensors, the power consumption has also decreased and it becomes possible to power microsystems using only the energy present in the environment: light, vibrations or temperature gradients for instance. The major advantage of energy harvesting is the realization of completely autonomous microsystems requiring no human intervention throughout the life of the system. Energy harvesting aims to power portable or fixed electronic devices in order to make them energy independent. The target markets are devices where it is difficult to change or recharge batteries when the systems are placed in concrete (building security) or in hard to reach places (monitoring the environment, on animals, in humans). Moreover, in the case of a wireless sensor network consisting of 1,000 building blocks, it quickly becomes expensive to change the batteries of each element one by one every 5 years. In each case, the energy harvesting can solve the problem of energy supply.

However, it is also potentially the most difficult method to exploit because each environment has different forms of ambient energy, and therefore, there is no one general solution that will fit all, or even a majority, of applications. The first limitation in the use of energy harvesting systems comes from physics: the recoverable power depends on the size of the system. To stay in the dimensions of the order of 1 cm^3, the power output of the energy harvesting system sould be in the order of 10-100µW in the ideal case. The microstructures of energy harvesting are therefore not intended to continuously feed a laptop or a mobile phone, instead, they are ideally suited to provide the energy required to operate simple sensors (measuring pressure, acceleration, temperature ...). The main advantage of energy harvesting is the duration of the power supply: in theory, it lasts as long as there is the energy source required by the harvester in the environment. However, the second limitation comes from non-predictable variations of the energy present in the environment of the sensor. For example for solar energy it is possible to predict the night but not the clouds that can drastically reduce the energy harvested. Thus, there still remains a need to combine a system of energy storage to energy harvesting devices to supplement the intermittent and inadequacies of production and consumption of energy. Progresses on the storage devices are needed. The comparison between the finite energy reservoir (electrochemical storage) and the energy available in the surrounding environment is made by S.J. Roundy in 2003 [16]. These phenomena are specific to each storage system and in all cases they are not feasible or convenient for systems where the maintenance at long-term want to be avoided. Finally the objective of the ambient energy harvesting is to provide flexibility to the energy storage device and thus to be less restrictive and cheaper for investment and operating.

I.2.3. From an economical point of view

Yole [17] analyzed that the 2009 economic crisis has hit hard the semiconductor industry with a fall in turnover of 23%. Over the same period the market for MEMS related to consumer applications behaved pretty well, since it generated 1.2 billion USD, with an increasing trend. In 2010, the MEMS market represented 8.6 billion USD [17]. The majority of turnover was achieved through print heads,

pressure sensors, accelerometers, inertial sensors and gyroscopes. However, they found that the turnover distribution is changing due to the emergence of new markets related to the integration of MEMS in consumer electronics. The iSuppli study [18] forecast that this market will be drived by the development of consumer electronic (smartphones) which should represent 30% of the MEMS's turnover and telecommunications (BAW filters, RF Switch ...).

They forecast that MEMS industry has a strong future and claim that despite the global economic downturn, innovation is still there. Innovation in MEMS no longer comes solely from new devices, but also from the integration of mature MEMS technologies into new applications. Along with mature devices used for new applications, innovation in new MEMS devices is active and will continue to strongly participate to the MEMS market growth in the next years [19]. 15 emerging MEMS technologies have been identified by Yole and are supposed to enter into the market within the next 5 years. Most of those developments have been motivated by the same 3 forces: The smartphone industry, the home-care industry and the Internet of things.

In 2012, the IC industry saw a 2% decline, but Yole reveals that the MEMS sector managed another 10% growth to become an $11B business. Analysts expect a 12-13% annual growth rate through 2018 to create a $22.5B MEMS market, growing to 23.5 billion units. Consumer will be the leading MEMS application with increasing needs for sensory interface. Meanwhile, the traditional major MEMS markets of micro mirrors and inkjet heads have matured and slowed. Thus analysts note that the expanding demand for MEMS in both smartphones and automotive applications is creating a rising group of players that can expect to see solid sales in their future. It is interesting to note the market for standalone accelerometers is decreasing as mobile devices increasingly use combo and compact sensors. Considering the evolution and the prediction made on the MEMS market, this trend will probably continue.

It is difficult to predict the revenue that will generate energy harvesting in the next years since energy harvesting is still emerging. Energy harvesting to supply power to MEMS autonomous sensors is a rapidly growing field and now widely explored. Energy harvesting may be developed in small devices, but it could be a big market in just 10 years from now. That according to recent research from IDTechEx [20], which is forecasting revenue for these technologies at around 4.4 billion USD by 2021. Today, the biggest outlet is in consumer electronics gadgets. But emerging applications for smart grid and energy storage should reshape the market over the next decade, according to IDTechEx.

Nowadays, most of the harvesters used in the above market segments are solar cells followed by electrodynamos, two relatively mature energy harvesting technologies. However, many new technologies are now taking some market share supplying power in fields not possible before. This includes thermoelectrics, but piezoelectric energy harvesters have even greater interest due to their small form factor and high efficiency. Thus in 2021, these four energy harvester types should have near similar market share for industrial sensing applications. IDTechEx figures that there could be 250 million wireless sensors deployed by that time, powered by energy harvesters. In 2014 there will be 1.6 million in place. There will be a big leap in 10 years' time.

I.3. Potential of piezoelectric NWs for energy harvesting

I.3.1. Availability of mechanical energy

The main advantage of energy harvesting is the duration of the power supply which remains as long as there is the adapted energy source in the environment. Nevertheless ambient resources, including those present in the human environment, are not necessarily renewable but are "almost free" resources. These resources could be limited in power but may be sufficient for various applications. Ambient energy resources, particularly in the human environment are diverse. Many energy sources (Table 1) are likely to provide sufficient levels of power to supply communicating autonomous systems: the mechanical energy resulting from vibration, strains or stresses, the photovoltaic solar energy coming from the sun or the artificial light, the electromagnetic energy, the thermal energy or the chemical energy from biological processes are examples of natural energy or inherent in human activity, which are being considered to power supply autonomous systems. The comparison of these different sources is difficult because it dependents on many factors and the targeted application. However conventional comparative studies [16], [21] were able to compare the power densities of most of conventional sources. It appears that the exploitation of the energy from mechanical vibrations can potentially provide high energy density similar to solar energy. Mechanical energy source also has the advantage of being simple to implement and to be available in many applications where solar energy is not always available, especially in domestic, industrial and transport environments where the use of autonomous sensor networks may be considered. The characteristic of mechanical energy resources and their harvesting will be discuss in the energy harvesting section (Chapter IV.).

Table 1 Power density of various technologies for energy harvesting [16], [21]

Technology	Power density
Outside photovoltaic (cell performance 15%, incident irradiance of 100 mW/cm^2)	15000 $\mu W/cm^2$ Direct sun 150 $\mu W/cm^2$ Cloudy day
Inside photovoltaic (performance 6%, incident irradiance of 0.5 mW/cm^2)	6-30 $\mu W/cm^2$
Piezoelectric (shoe inserts)	330 $\mu W/cm^3$
Vibrations (small microwave oven)	116-200 $\mu W/cm^3$
Thermoelectric (for a 10°C gradient)	10-40 $\mu W/cm^3$

I.3.2. The interest of NW for piezoelectric energy conversion

The transformation of the ambient energy into electricity is currently driving one of the largest scientific efforts. In addition the development of piezoelectric materials is a key technology in a wide range of industrial and consumer products: actuators (resonators, speakers, motors, inkjet printer, cell phones cameras, etc.), sensors (shock sensors, acoustic devices, sonar, arrays for Structural Health Monitoring, etc.) and energy related applications (transformers and energy harvesters). But very few experimental and theoretical studies on the piezoelectric effect at nanoscale can be found in the literature. At nanoscale, NWs are foreseen as fundamental building blocks of future electronic, electromechanical and optoelectronic nanosystems [22]. Given the remarkable progress in their synthesis in the last two decades [22], [23], researchers demonstrated unique and new nanosystems with innovative functionality such as high-mobility single- NW transistors [24], strain-controlled logic gates [25], single- NW lasers [26] and strain sensors [27] for example. Most of these applications are the result of the enhancement of the material properties at the nanoscale including mechanical [28] and electromechanical [29], [30] properties. Among NWs, those that exhibit piezoelectricity have received

increased attention. The most studied are NWs made up of single material such as ZnO [31], GaN [32], BaTiO3 [33] and CdS [34]. ZnO is the most studied material, not only in the form of NW but also nanoribbons [35] and nanobelts [36]. Unfortunately, and contrary to NWs, the growth of these nanostructures occurs randomly on top of the substrate and, therefore, their implementation into a working device is even more complex than the integration of ordered NWs. The success of these NWs is due to their high potential for nanosystems with great functionality. For example, strain sensors with increased sensitivity, provided by the piezoelectric effect, are possible [37]. Another example that received most attention are NGs [38] where the piezoelectric phenomenon is used to convert mechanical energy to electrical energy to power supply autonomous sensors and smart systems [39]. Although all these applications are very promising, reliability, robustness, and performance optimization remain to be addressed. Nevertheless studies on properties of piezoelectric semiconducting NWs [40], such as ZnO and GaN NWs, show a large improvement of the piezoelectric properties at nanoscale compared to bulk material. Thus the understanding of the piezoelectric phenomena at the nanoscale should allow optimizing and fabricating better structures generating more voltage at a lower strain (improved piezoelectric coefficients). Indeed, for performance optimization it is desirable to know which set of NW morphological (diameter, length), structural (crystal structure, defect type and density), and electrical properties (conductivity) gives the best performance for a particular application. Thus this could be translated directly into a better sensibility for applications as sensors, transducers or into a higher power density and voltage for mechanical energy harvesting applications, which is one of the markets addressed.

Several groups are presently involved at various extents in the domain of energy harvesting using nanostructures. However, only few of them have integrated their nanostructures into a working device able to harvest energy [31], [41], [42]. Moreover, several theoretical and experimental aspects are still under hot debate within the scientific community [43]. Presently, the most studied piezoelectric nanostructures are ZnO NWs, in particular those carried out by Z. L. Wang and collaborators at Georgia Tech, who have been the initiators of the current interest in NW based energy harvesting devices. Princeton University has developed PZT nanoribbons on polymers and PZT nanofibers [41], as well as at Berkeley, in which nanofibers (based on PVDF) have been integrated into a working mechanical energy harvesting device [42]. Some of these realizations have led to patents [44]–[46] in USA and Asia. In Europe, contributions can be found from Germany [47] and France [1], [48]. European projects addressed mechanical energy harvesting based on nanostructures: NANOFUNCTION, devoted to explore new concepts, processes and nanodevices for adding functionalities to CMOS.

A recent experimental study at IMEP-LAHC on the piezoelectric effect on GaN NWs with an embedded heterojunction (GaN/AlN/GaN) shows that this kind of structure enables to generate almost 10 times more voltage than simple homogeneous GaN NWs [1]. This result suggests that the piezoelectric coefficient could be multiplied by 10 using an AlN embedded heterojunction in a GaN NW. Based on experimental results on heterostructured NWs, we can expect an improvement on the piezoelectric coefficient (d_{33}) of 4 times compared to ZnO. However these results were preliminary and need to be supported by a thorough understanding of the mechanisms of this improvement in order to open the way to further optimization. Therefore we need to investigate in details the piezoelectric physical mechanisms and the various optimization routes offered by material, doping and contact engineering. For the present study, GaN and ZnO have been chosen due to their maturity in terms of electronic and optoelectronic applications and their integration capabilities. In addition, besides their rather good piezoelectric coefficients, GaN and ZnO have the advantage to be able of reliable and

reproducible doping and the compatibility with Si technology, in particular the possibility to be grown on Si substrates. Furthermore, GaN can be chemically and dry-etched, enabling top-down processing, and allows for a large variety of quantum heterostructures to be built when alloyed with In and Al.

All this makes the semiconductor piezoelectric NWs perfect candidate for the study and the realization of mechanical energy harvesters. Our study will be first performed at the level of the individual NW, and then extended to the understanding of collective effects in an array of NWs, which is the structure of use for practical applications. The goal is to study and exploit the piezoelectric effect in ZnO and GaN NWs for fundamental and applied purpose with realistic applications. Among these applications, mechanical energy harvesting has been chosen as a core application of interest and mechanical displacement and force sensors as a promising prospect.

I.4. Semiconducting piezoelectric materials

I.4.1. Introduction to the piezoelectric phenomenon

I.4.1.1. History of the piezoelectricity

The word "piezoelectricity" comes from Greek ("piézein" = leverage) and means "pressure electricity". This name was proposed by Hankel in 1881 to name the phenomenon discovered a year before by brothers Pierre and Jacques Curie working on the relationship between pyroelectricity and crystal structure. While pyro electricity reflects the coupling between thermal effects and electrical effects, piezoelectricity characterizes the coupling between the mechanical and electrical quantities. This is a feature available to some materials that have the propensity to become electrically polarized as a result of mechanical stress (direct effect) and, conversely, can be deformed mechanically by the action of an electric field (reverse effect). In 1880 the Curies brothers began to experimentally demonstrate this phenomenon by applying mechanical stress on certain phases of a quartz crystal [49]–[51]. Then they observed that positive and negative charges appear on different parts of the surface of a quartz crystal. This phenomenon was approached in the middle of the nineteenth century by René Just Haüy. This discovery immediately attracted the attention of scientists. The Curie brothers confirmed one year after their discovery, the existence of the reverse process, predicted in 1881 by Gabriel Lippmann [52]. The theory associated with this phenomenon has been almost entirely developed in the late nineteenth century. During the First World War, piezoelectricity entered in the field of practical applications. In 1917 Paul Langevin used quartz crystals to generate compression waves which gave birth to sonar. In the 1940s, the discovery of piezoelectric salts such as $BaTiO_3$ increased the electromechanical coupling. In 1950-60, the emergence of new ceramics created a renewal of the interest for piezoelectricity, through the use of lead oxides (PZT). The main advantages of these materials reside in their excellent piezoelectric properties and a high electromechanical coupling coefficient, leading to high operating efficiency and high linearity properties. The bulk ceramics, used to perform micro displacements or micro positioning, are now integrated as films increasingly thin. Recently other derivatives of PZT materials (PZNT, PMN-PT, PLZT ...) are developed because of their superior properties than PZT. But piezoelectric nanostructures open new possibilities for piezoelectricity.

I.4.1.2. Definition of the piezoelectricity

Piezoelectricity is the property possessed by few materials to be electrically polarized under the action of mechanical stress and vice versa to be deformed when an electric field is applied to them (Figure 2).

Figure 2 Schematic of the (a) direct piezoelectric effect and (b) inverse piezoelectric effect.

The piezoelectric effect is not present in all materials. In crystals for example, only crystals composed of at least two compounds and having no center of symmetry have this characteristic. On the 32 classes of crystalline solids known [53], 21 classes have no center of symmetry and of these, 20 have the piezoelectric property. In such a piezoelectric crystal at rest (no external mechanical stress), the centers of gravity of positive and negative charges of each elementary cell coincide (Figure 3a). Therefore, the effects of positive and negative charges are mutually canceled. The electrical neutrality is reached. When strain is applied on the material, the crystal lattice is distorted, thereby causing separation of the centers of gravity of the positive and negative charges which generates small dipoles [54] et al. 2001 (Figure 3b). The poles facing inside the material distribution cancel each other and a charge appears on surfaces of the material (Figure 3c). The material is polarized in a preferred axis. In fact, interactions exist between the electrical, thermal and mechanical phenomenon, but some considerations allow to only take into account the electro-elastic coupling relative to piezoelectricity [55].

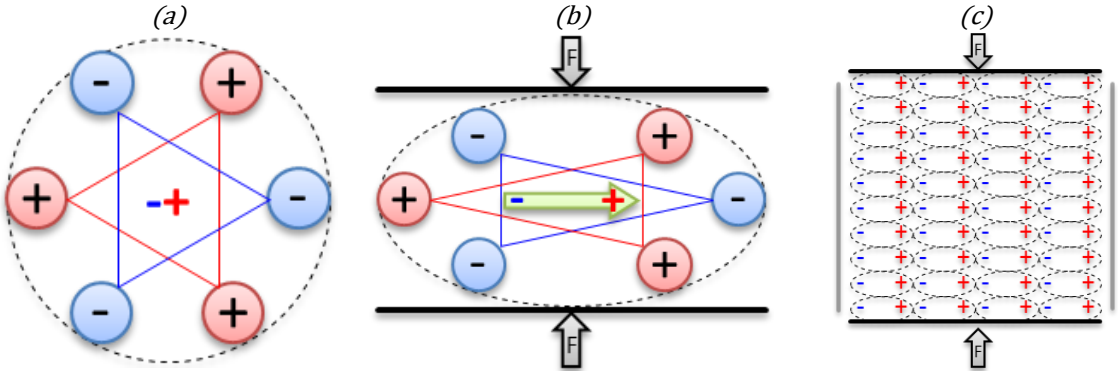

Figure 3 Simple molecular model explaining the piezoelectric effect, (a) undisturbed molecule, (b) a molecule subjected to external force, (c) effect of polarization on the surfaces of a material.

Figure 4 represents a piezoelectric material on which a pressure is applied. Two metal plates used as electrodes are deposited on the surfaces where charges of opposite sign appear. Assume that these electrodes are in short circuit via a galvanometer. When we exert a certain pressure on the piezoelectric material, a charge density appears on crystal areas in contact with electrodes. This polarization generates an electric field that causes the flow of existing free charges in the connected conductors. According to their sign, the free charge carriers move towards the contacts, where the charge density generated by the polarization of the crystal is of opposite sign. This flow of free charges will continue until the free charges neutralize the effect of the piezoelectric polarization (Figure 4). When the pressure on the crystal is released, the piezoelectric polarization of the material will disappear, and the flow of free charges will thus be reversed, so to return to the initial state [56]–[58]. If an electrical load is connected instead of a short circuit, and if a variable pressure is applied, a current will flow through the resistor and mechanical energy will be transformed into electrical energy.

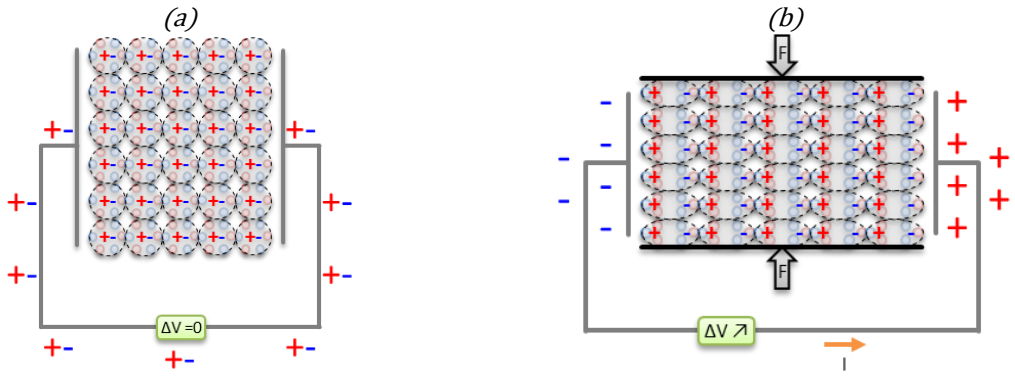

Figure 4 Schematic of the direct piezoelectric phenomenon on a short circuited piezoelectric material (a) undisturbed state, no current through the circuit, (b) piezoelectric material subjected to an external force, a current flows through the circuit to neutralize the piezoelectric potential.

I.4.2. Piezoelectric equations

The core idea of piezoelectricity is in the notion of coupling between the mechanical and electrical properties. Both are linked through a tensor representation. Thus, before discussing the equations of piezoelectricity, it is important to define the different electrical and mechanical parameters in play as well as their coupling tensor [56]. Then we will introduce the piezoelectric physics and equations but only considering linear effects [59]. The nonlinear phenomenon or dynamic effects will not be taken into account [60].

Piezoelectric materials are anisotropic; it is conventional to choose the axis 3 as the collinear axis to the direction of the remnant polarization of the material (Figure 5). The other two directions form a direct triad (orthonormal) with axis 3. Thus 3 translations and 3 rotations are allowed. To describe these movements the single subscript notation use the numbers 1, 2, 3, 4, 5, 6 and the pair notation use i, j = 1, 2, 3 (Figure 5). In this work, only piezoelectric materials with wurtzite structures will be considered, thus all the tensors will be simplified by considering the geometry of the structure.

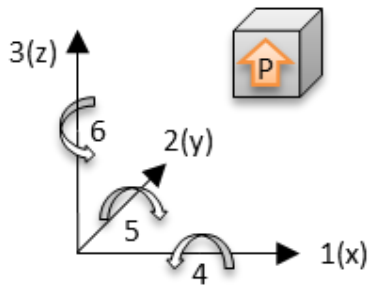

Single subscript	*Pair subscript*
1	*11*
2	*22*
3	*33*
4	*23 or 32*
5	*13 or 31*
6	*12 or 21*

Figure 5 Schematic of the movements considered in a piezoelectric material and table of their notation in single subscript and pair subscript

I.4.2.1. Definition of electrical parameters

The electric field E is a vector quantity that expresses the force created by distant electrically charged particles. This field is expressed in $N.C^{-1}$ equivalent to $V.m^{-1}$ and is represented by:

$$\nabla . E = \frac{\rho_r}{\varepsilon} \qquad \textit{Equation 1}$$

where ρ_r is the residual electrical charge density ($C.m^{-3}$) and ε the permittivity ($F.m^{-1}$).

The electric displacement D ($C.m^{-2}$) represents how an electric field E influences the organization of electrical charges in a given environment. It is represented by:

$$\nabla . D = \rho_r \qquad \textit{Equation 2}$$

The permittivity ε ($F.m^{-1}$) is a measure of the "resistance" encountered during the formation of an electric field in a medium. It represents how an electric field affects, and is affected by a dielectric medium.

$$\varepsilon = \varepsilon_0 . \varepsilon_r = \varepsilon_0 . (1 + \chi) \quad \varepsilon^{-1} = \beta^{-1} \qquad \textit{Equation 3}$$

where ε_0 = 8.85 10^{-12} $F.m^{-1}$ is the vacuum permittivity ε_r the relative permittivity of the material, χ the electric susceptibility of the material and β the inverse of the permittivity.

In the very simple case of linear, homogeneous, isotropic materials with instantaneous response to changes in electric field, the relation between E and D is:

$$D = \varepsilon . E + P \qquad \textit{Equation 4}$$

where P is the intrinsic polarization of the material.

Table 2 Summary of the electrical parameters

Name	Expression	Unite	Matrix size
Electric displacement field	D	$C.m^{-2}$	(3,1)
Electric field	E	$V.m^{-1}$	(3,1)
Permitivitty	$\varepsilon = \frac{\partial D}{\partial E}$	$F.m^{-1}$	(3,3)
Inverse permitivitty	$\beta = \frac{\partial E}{\partial D}$	$m.F^{-1}$	(3,3)

I.4.2.2. Definition of the mechanical quantities

The mechanical parameters are summarized in Table 3. The mechanical stress T ($N.m^{-2}$) is a physical quantity that expresses the internal forces that neighboring particles of a continuous material exert on each other. Inside a body, this is a measure of the average force per unit area on which internal forces act. These internal forces are generated in response to external forces applied to the body. For example, for an homogenous cylinder compressed by a small force F, the stress is

$$T = \frac{F}{A} \qquad \textit{Equation 5}$$

Where F is the applied force and A the top surface of the cylinder.

The strain S (%) or deformation, quantifies the transformation of a solid volume under the effect of applied forces. This volume change is quantified by the strain tensor which is the ratio of the displacement over the initial volume. The strain is in general a tensor quantity. Physical insight into strains can be gained by observing that a given strain can be decomposed into normal and shear components. The amount of stretch or compression along material line elements is the normal strain, and the amount of distortion associated with the sliding of plane layers over each other is the shear strain. This could be seen by an elongation, shortening, or volume changes, or angular distortion. For example, a cylinder under axial compression has a strain given by:

$$S = \frac{l' - l}{l} \qquad \textit{Equation 6}$$

Where l is the length of the cylinder before compression and l' its length after compression

The elasticity matrix c (c_{ij} in $N.m^{-2}$); in the case of an anisotropic material, relates the deformation and the mechanical stress instead of using the Young's modulus (Y) (isotropic case). This tensor initially contains 81 elastic coefficients, however, Due to the inherent symmetries only 21 elastic coefficients

of the latter are independent and it can be greatly simplified by the symmetry of the structures that we study.

For continuous media, the Hooke's law describes the relation between the stress and the strain:

$$T = -c.S \qquad where \qquad c^{-1} = s \qquad \textit{Equation 7}$$

Where s is the stiffness matrix ($m^2.N^{-1}$)

Table 3 Summary of the mechanical parameters

Name	Expression	Unite	Matrix size
Stress	T	$N.m^{-2}$	(6,1)
Strain	S	%	(6,1)
Elasticity	$c = \frac{\partial T}{\partial S}$	$N.m^{-2}$	(6,6)
Stiffness	$s = \frac{\partial S}{\partial T}$	$m^2 .N^{-1}$	(6,6)

I.4.2.3. Piezoelectric coefficients and relations

To relate the electrical and mechanical parameters of a piezoelectric material, the piezoelectric coefficients are defined Table 4.

- d is the proportional constant linking the electric displacement to the stress for a given electric field
- e is the proportional constant linking the electric displacement and the strain for a given electric field
- g is the proportional constant linking the electric field and the stress for a given electric displacement field
- h is the proportional constant linking the electric field and the strain for a given electric displacement field

- *Table 4 Summary of the piezoelectric coefficients*

Name	Expression	Unite	Matrix size
d	$d = \left(\frac{\partial D}{\partial T}\right)_E = \left(\frac{\partial S}{\partial E}\right)_T$	$C.N^{-1}$ or $m.V^{-1}$	(3,6)
e	$e = \left(-\frac{\partial T}{\partial E}\right)_S = \left(\frac{\partial D}{\partial S}\right)_E$	$C.m^{-2}$	(3,6)
g	$g = \left(\frac{\partial S}{\partial D}\right)_T = \left(-\frac{\partial E}{\partial T}\right)_D$	$m^2.C^{-1}$	(6,3)
h	$h = \left(-\frac{\partial T}{\partial D}\right)_S = \left(-\frac{\partial E}{\partial S}\right)_D$	$V.m^{-1}$ or $N.C^{-1}$	(6,3)

The relations between these coefficients are the following:

$$d = \varepsilon^T.g = e.s^E \qquad \textit{Equation 8}$$

$$e = \varepsilon^S.h = d.c^E \qquad \textit{Equation 9}$$

$$g = \beta^T.d = h.s^D \qquad \textit{Equation 10}$$

$$h = \beta^S.e = g.c^D \qquad \textit{Equation 11}$$

Exponents (D, E, T, S) means that these quantities are assumed to be zero or constant.

In the direct piezoelectric effect case, the equation giving the electric displacement field D generated by the stress T at constant electric field is:

$$D_i = \sum_p d_{ip} \, . \, T_p \qquad \textit{Equation 12}$$

In the same way the equation giving the electric displacement field D generated by the strain S at constant electric field is:

$$D_i = \sum_q e_{iq} \, . \, S_q \qquad \textit{Equation 13}$$

The laws of electrostatics explain how an electric displacement D is equal to the appearance of a surface charge Q at the interface of a dielectric, this means the surface of the piezoelectric crystal considered. Therefore the above equation can also be written in function of the applied force F on these surfaces in the form:

$$Q_i = \sum_j d_{ij} . F_j \qquad \textit{Equation 14}$$

Concerning the reverse piezoelectric effect, the equation giving the stress T generated by an electric field at constant strain is:

$$T_p = -\sum_k e^t_{kp} \, . \, E_k \qquad \textit{Equation 15}$$

Where the exponent t reflects the transpose of the considered matrix.

And the equation giving the strain S generated by an electric field at constant stress is:

$$S_q = \sum_k d^t_{kq} \, . \, E_k \qquad \textit{Equation 16}$$

I.4.2.4. Main piezoelectric equations

Now we can write the piezoelectric equations connecting the electrical and mechanical equations, taking into account the direct and reverse piezoelectric effect (the notation is not given as a tensor for clarity). Electromechanical coupling can be observed in the Gibbs energy function of the material G, in function of the stress T and the electric field E [61], [62]:

$$G = -\frac{1}{2} s^E_{ij} T_i T_j - d_{ki} T_i E_k - \frac{1}{2} \varepsilon^T_{kl} E_k E_l \qquad \textit{Equation 17}$$

From the above equation we can deduce the following relations:

For the strain:

$$S_i = \left|\frac{\partial G}{\partial T}\right| = S^E_{ij} T_j + E_k d_k \; avec \; i,j \in \{1 \dots 6\} \; et \; k \in \{1 \dots 3\} \qquad \textit{Equation 18}$$

For the electric displacement:

$$D_k = \left|\frac{\partial G}{\partial E_k}\right| = d_{ki} T_i + \varepsilon_{kl} E_l \; avec \; i,j \in \{1 \dots 6\} \; et \; k \in \{1 \dots 3\} \qquad \textit{Equation 19}$$

From these equations we can deduce all the piezoelectric relations between the mechanical and electrical quantities taking into account the piezoelectric coupling effect:

	T	S
E	$S = s^E.T + d^t.E$	$T = c^E.S - e^t.E$
	$D = d.T + \varepsilon^T.E$	$D = e.S + \varepsilon^S.E$
D	$S = s^D.T + g^t.D$	$T = c^D.S - h^t.D$
	$E = -g.T + \beta^T.D$	$E = -h.S + \beta^S.D$

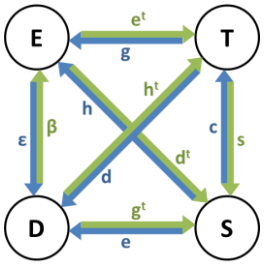

Figure 6 Relation between the piezoelectric quantities.

The combination most commonly used is:

$$\begin{cases} \boldsymbol{T_p} = \boldsymbol{c_{pq}} \,.\, \boldsymbol{S_q} - \boldsymbol{e^t_{kp}} \,.\, \boldsymbol{E_k} \\ \boldsymbol{D_i} = \boldsymbol{e_{iq}} \,.\, \boldsymbol{S_q} + \boldsymbol{\varepsilon^S_{ik}} \,.\, \boldsymbol{E_k} \end{cases}$$

Equation 20

I.4.3. Piezoelectric materials

Piezoelectric materials can be of different nature. Some natural crystals as quartz, berlinite, sucrose and topaz are inherently piezoelectric. Synthetic materials can also be piezoelectric. We can classify the artificial piezoelectric material into 3 classes: the single crystals, the ceramics and the polymers.

I.4.3.1. Single crystals

Natural or synthetic piezoelectric materials crystal can be classified in large families according to their chemical composition, crystal structure, or their scientific and industrial interest. The piezoelectric effect is not present in all crystals. Indeed, only materials having no center of symmetry have piezoelectric characteristics.

A crystal is a regular and periodic arrangement of atoms. The most popular and used piezoelectric single crystals existing in the natural and artificial state is quartz (SiO_2). It has a very good temperature stability and high mechanical linearity. There are other single crystals synthesized like lithium niobate ($LiNbO_3$) or the lithium tantalate ($LiTaO_3$) which have high Curie temperatures (it is the temperature where a material's permanent magnetism changes to induced magnetism), low dielectric permittivity and low piezoelectric coefficients. We then distinguish the single-domain and multi-domain if one or more directions of polarization coexist in the single crystal. In crystallographic description, multi-domain crystals are not strictly single crystals but twinned crystals, which is why they are often confused with piezoceramic. Today, multi-domain single crystals like PZN-PT and PMN-PT are by far the piezoelectric materials with the largest piezoelectric coefficients and the best electromechanical coupling

I.4.3.2. Ceramics

A ceramic material is solid at room temperature and is neither metallic nor organic. The ceramics are made by high-temperature solidification of a plastic paste (mineral glass) or sintering (heating agglutination) of a dry powder previously compressed, without going through a liquid phase (polycrystalline ceramics). By assimilation we call "ceramic" these manufactured materials.

Belonging to the ferroelectric family, the piezoelectric ceramics are mainly binary or ternary mixtures with a distorted perovskite structure. They are usually mixtures of oxides (generally based on titanates) formed of crystalline element (particles) each having a spontaneous polarization. By applying a high electric field, the polarizations of the grains are aligned and a macroscopic polarization is generated. In principle, there is no limitation to the forms and directions of polarization

of the ceramic elements, which is their great advantage compared to single crystals. They are the most common piezoelectric materials because of their high piezoelectric coefficients. This properties is far superior compared to those of all the other families of compounds [63]–[66]. The first piezoelectric synthetic material based on barium titanate (BaTiO3) was synthetized after 1945 [67]. Among the piezoelectric synthetic material, the ferroelectric oxides from perovskite structure are the most common. PZT: lead zirconate titanate (1954) is the most common piezoelectric ceramic used in industry. The great advantage of these piezoelectric materials is their fabrication. These ceramics are obtained by sintering which allows to perfectly control the grain size and therefore adjust their dielectric, mechanical and piezoelectric properties on request [68]. But this manufacturing method has some limitations at smaller dimensions.

I.4.3.3. Polymers

A polymer is a macromolecule, organic or not. Historically, products arising from the linkage of repeating units or monomer by covalent chemical bonds have been the primary focus of polymer science; emerging important areas of the science now focus on non-covalent links. Since their discovery in 1969, the piezoelectric semi-crystalline polymer films of PVDF have been extensively used in the manufacture of sensors and piezoelectric applications. Unlike piezoelectric ceramics, where the crystal structure of the material creates the piezoelectric effect, in polymers, the long chains intertwined are attracted or repelled when an electric field is applied. These polymers are ferroelectric [68] and have the advantage of being resilient to chemicals, naturally flexible and light. PVDF for example is also biocompatible, making it a very good candidate for use in the biomedical field [42], [69], [70]. However their piezoelectric properties are modest compared to ferroelectric oxides and strong polarization is necessary [71].

I.4.3.4. The case of semiconducting crystals

A semiconductor is a material that has the electrical characteristics of an insulator, but with a high probability that a charge can contribute to an electric current, although small, is large enough. In other words, the electrical conductivity of a semiconductor is intermediate between that of metals and that of insulators. Piezoelectric semiconductors mostly belong to the group II-VI such as ZnO and group III-V nitride such as GaN (Figure 7). These two families of semiconductors have a large direct band gap (ZnO= 3.37eV and GaN=3.43eV) ideal for micro and nanoelectronics. They are used in a wide range of applications: optics [26], [72], optoelectronics [73], [74] and sensors [75] for example.

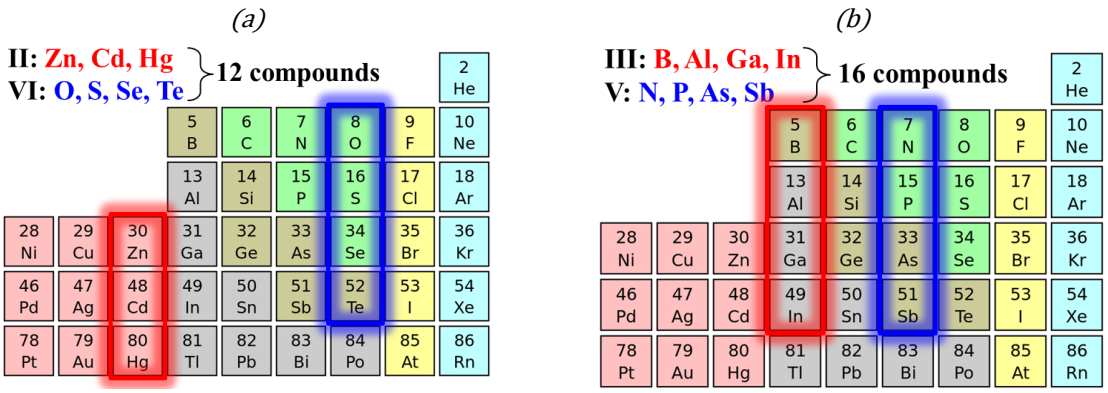

Figure 7 Mendeleyev's periodic table (a) II-VI semiconductor materials (b) III-V semiconductor materials

Oxides from II-VI elements and III-V nitrides elements crystallize in two main phases: wurtzite (hexagonal) and zinc blende (cubic). Wurtzite structure belongs to the space group $P6_3mc$ and zinc blend to the space group $\bar{F}43m$ in Hermann Mauguin notation [53]. Only the wurtzite structure is

piezoelectric [76]. The oxygen atoms (for ZnO) or nitrogen atoms (for GaN) form an hexagonal lattice. The Zn and Ga atoms occupy half of the tetrahedral sites available. We obtain two sub-compact hexagonal networks. The parameters used to describe the structure are the side of the hexagon in the plane (0001) and c corresponding to the height of the mesh along the axis [0001].

I.4.3.5. The case of ZnO and GaN

Among semiconducting piezoelectric wurtzite compounds, ZnO and GaN are the most extensively characterized under various geometries and especially as NWs and many applications have been reported on piezotronics and optoelectronics. In this work we mainly focused on the mechanical, electrical and piezoelectric properties of these materials.

Zinc oxide has been used for centuries for many purposes such as painting, roofs and cosmetics. The first work on ZnO crystal appeared in 1930 [77]. Difficulties both for obtaining bulk crystals and p-type doping have slowed its development for several years. The rebirth of ZnO took place in 1995 with the UV laser emission from ZnO thin films at room temperature [78] because of its thin layers and nanostructures rather easy to produce compared to other similar materials at this time. Nowadays, even if III-V semiconductors have been studied for UV emission, ZnO still attracts researchers. ZnO is inexpensive, relatively abundant, chemically stable, easy to prepare and non-toxic. Most of the doping materials that are used with ZnO are also readily available. Thus today, the most widely publicized application for ZnO is an ITO replacement for displays [79] and photovoltaic panels, where ZnO could simplify the manufacturing process and lower the costs of transparent conductors. But new applications for ZnO are much broader than that. In addition to cost savings, ZnO offers the following properties: high carrier mobility, transparency, wide band gap and low temperature process. However, technical difficulties exist, one important challenge is that there is yet no “stable” p-type doping.

The first synthesis of III-N was in the early 20th century. In 1907, Fichter et al. [80] synthesize polycrystalline AlN, GaN followed in 1932 by Johnson et al. [81]. However, it is only in 1971 that it was obtained in large areas GaN single crystals on sapphire substrate using HVPE (Hydride Vapor Phase Epitaxy) [82]–[84], metal organic precursors MOVPE (metal organic vapor phase epitaxy) [85] and by MBE (molecular Beam Epitaxy) [86]. These first layers of mono crystalline materials, although very defective, allowed the first experimental measurements of the gap of GaN [87], [88] and the synthesis of the first device based on nitrides, the LED (Light Emitting Diode) [83]. Since the 1970s, III nitride materials such as: GaN, AlN, InN and their alloys have been presented as interesting semiconductors for the development of optoelectronic devices. Then, for several years, advances in the field of III nitrides have been relatively limited compared to other semiconductors. Several technological problems prevent their development: the lack of substrate lattice matching with GaN, the difficulties to dope p-type and the high residual n-type doping. A radical change occurred in 1983 when Yoshida [89] successfully synthetized GaN by MBE with good quality by using an intermediate layer of AlN, used at low temperature on a sapphire substrate. This method, applied to MOVPE, was refined and perfected by Alasaki Amano between 1986 and 1989 [90], [91]. They presented the first layers of GaN p-type doped using magnesium atoms [92] and the first GaN diodes emitting in the UV (3.35eV), and blue (2.9eV) [93], [94]. Nowadays, the characteristics of III-V semiconductors such as their large direct band gap, their high thermal conductivity, high breakdown field, high mechanical stability and electron mobility, attract the research in many areas especially microelectronics.

a.Crystal properties

ZnO crystal as found in nature is known as Zincite. It usually crystallizes in the hexagonal close-packed wurtzite phase. However it can be synthesized in the cubic zinc blende phase when deposited

on some substrates of cubic symmetry. Throughout this work, we focus only on the ZnO wurtzite structure. The ZnO wurtzite hexagonal close-packed structure can be described as a succession of alternating planes, positively or negatively charged and consisting of the tetrahedron formed by the ions Zn^{2+} and O^{2-} respectively. This tetrahedral coordination results in a piezoelectric non-Centro symmetric structure [95].

The III nitrides are semiconductors III-V with direct gap, composed of nitrogen atoms and elements of column 13 (p-block) of Mendeleyev's periodic classification: these compounds GaN, AlN, InN and their alloys. III-N materials exhibit a stable wurtzite phase. This is an exception in semiconductor III-V whose most easily synthesized phase is the zinc-blende phase [96].

The wurtzite structure consists of two hexagonal subnets, comprising a group II or III atoms (cations) the other being oxygen or nitrogen (anions). The two subnets are shifted along the c-axis by a value of 3/8×c for non-deformed ideal wurtzite structure. Although it put into play anions and cations, the bond between II-III atoms and oxygen or nitrogen atoms is covalent. However, it is obviously also highly ionic because involving II^{2+} or III^{3+} cations and anions O^{-} or N^{3-}. Each atom is at the center of a tetrahedron and therefore forms four bonds metal-nitrogen. By convention, the +c (or [0001]) is defined by the direction of the Zn-O or Ga-N bond. Table 5 summarizes the parameters of the crystal lattice of ZnO and GaN. The c/a ratio corresponds to the length of the cation-anion binding. This structure has no center of symmetry. Therefore directions [0001] and $[000\bar{1}]$ are not equivalent.

Table 5 Crystal lattice parameters for ZnO and GaN as function of the crystal structure at 300K [75], [97]–[100].

Parameters	Wurzite			Zinc Blende
	a (Å)	c (Å)	c/a	a (Å)
ZnO	3.249	5.2069	1.602	4.47
GaN	3.189	5.185	1.626	4.5

In practice, this means that we can expect that the properties, as well as growing conditions differ depending on whether the material is oriented +c or -c. These two orientations (or polarities) are respectively called polarity metal (Zn or Ga) and polarity O or N. If the metal-oxygen or nitrogen bond points to the surface, the surface polarity is metal or it is O or N polarity. Figure 8 shows these two situations. It should be noted that the growth in one direction or the other will not presage the preferential termination of the surface metal atoms O or N. In particular, about the growth of metal polarity materials, the surface will tend (in vacuum) to be completed by metal atoms [101] Under sub atomic nitrogen flow (the case of PA-MBE), the surface will be covered with a layer of nitrogen atoms [102], [103]. The nature of the polarity influences the surface morphology and stability of the structure. It has been shown that thin layers of GaN with a N polarity are more reactive and can be etched unlike GaN layers with a Ga polarity [104]–[107]. The polarity obtained for the growth of thin film structures depends on the substrate used, the composition and growth conditions of the buffer layer [108], [109]. The Ga orientation or [0001] is the most common for 2D structures. For the growth of GaN NWs, the polarity of the structures is controversial. Indeed, it has been shown that GaN NWs grow along the N polarity or Ga polarity depending on growing conditions and choice of substrate has also been observed [110]–[112]. It was also observed that the two polarities can coexist in the same sample [113], [114].

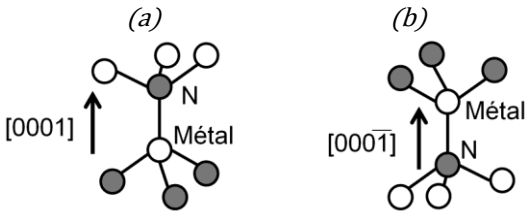

Figure 8 Schematic of the III-N element bond as function of the polarity (a) metal +c (b) nitride –c.

As indicated, a piezoelectric semiconductor is formed by the regular assembly of positive charge carriers (cations) and negative (anions). If the barycenter of the positive and negative charges do not superpose, it appear in the material an electric field which polarize the semiconductor. If the polarization occurs under stress, it is called piezoelectric polarizations. If the polarization is intrinsic of the material, it is called spontaneous polarization. Due to the strong ionicity of III-nitrogen bonds and due to the absence of an inversion center, III-nitride are characterized by the existence of a spontaneous polarization in their steady state. Indeed, there is a difference in electronegativity between the metal and nitrogen, nitrogen having a higher electronegativity. This means that the electron cloud of the III-N or II-O bond is shifted to the nitrogen and oxygen respectively. The centroids of positive and negative charges do not overlap in the individual cell, thereby creating a dipole therein, giving rise to a macroscopic polarization along the c axis. In addition, the structure of wurtzite III-nitrides is not an ideal structure and the tetrahedron is slightly distorted. This makes the III-N bond shorter in the [0001] direction, thus shifting the centroids of positive and negative charges [98], [115]. Table 6 shows the estimated spontaneous polarization on ZnO and GaN.

Table 6 Spontaneous polarization in ZnO and GaN wurtzite crystal

	GaN	ZnO
$\overrightarrow{P_{spont}}$ (V)	-0.029 [98]	-0.057 [100], [115]

The total polarization in the material is then:

$$\vec{P} = \overrightarrow{P_{piezo}} + \overrightarrow{P_{spont}} \qquad \textit{Equation 21}$$

Where $\vec{P}$ is the total polarization, $\overrightarrow{P_{piezo}}$ the piezoelectric polarization and $\overrightarrow{P_{spont}}$ the intrinsic polarization.

b.Semiconducting properties

Zinc oxide is a II-VI semiconductor with wide direct band gap of 3.37eV at room temperature [116], [117]. Concerning GaN, it is a III-V wide direct band gap semiconductor of 3.4eV at 300K [118], thus very similar. For optoelectronic applications, the control of doping p and n is essential. But the simultaneous control of both doping type in large band gap materials is difficult: doping is said asymmetric [119]. For ZnO, the unintentional doping is n-type, while the p-type doping is very difficult to obtain. The intrinsic defects such as oxygen vacancies (VO) and interstitial zinc (Zn_i) are not the cause of unintentional n-doping. Indeed, VO is a deep donor and Zn_i is a superficial donor, but its formation energy is very high [120], [121]. Nevertheless these intrinsic defects may compensate possible acceptors during the p-type doping, thus the Fermi level get close to the valence band and the formation energy of donor levels decreases. The valence band of ZnO is very small, therefore the p-type doping is very difficult. Similarly the valence band of GaN is quite small which explains the average quality of its p-type doping of GaN.

The dopants usually used for ZnO generally belong to groups III and IV. The n-type intentional doping is usually done with elements of the column III in substitution of zinc such as Al, Ga, and In reaching electron concentrations of $10^{21}cm^{-3}$ and resistivity of $10^{-4}\Omega.cm$ [122]. The minimal residual electron concentration observed is $10^{14}cm^{-3}$ for the unintentionally doped ZnO [123]. Residual

concentrations observed in the literature are generally much higher, on the order of $10^{17}cm^{-3}$. The unintentional n-type doping is due to residual impurities that may be present in the source material (such as Al, Ga and In), or hydrogen [124]–[126] which can be found in most growing methods. Indeed, various studies have shown that hydrogen can easily diffuse into the crystal lattice and interact with point defects to form more stable complexes [127]–[130]. Although hydrogen is present in traces in most semiconductors, it usually has an amphoteric role regarding doping, that is to say it is as much as a donor as an acceptor. However, it mainly behaves as a donor in ZnO and can no longer be self-compensated. This feature damages the control of doping. Indeed, in the case of a residual n-type doping, the presence of donors must be compensated by acceptors before starting to really boost the p-type doping considered. To summarize for ZnO films having a thickness between 0.1µm and 10µm deposited on sapphire substrates, the n-type doping reached very high values between $10^{17}cm^{-3}$ and $5.10^{18}cm^{-3}$ [131], [132]. The n-type doping can be reduced to values close to $10^{16}cm^{-3}$ using a ZnO buffer between the substrate and the film [132]. The lowest value ($10^{14}cm^{-3}$) have been found for films of ZnO with thicknesses between 0.1mm and 1mm [133], [134]. On NWs, the n-type doping typically varies between $10^{16}cm^{-3}$ and $5.10^{18}cm^{-3}$ [135], [136].

The early unintentionally doped GaN was n-type, which at the time was believed due to nitrogen vacancies. The high n-type background carrier concentration on the order of $10^{18}cm^{-3}$ was difficult to minimize and the absence of a shallow acceptor did not help. Nevertheless, early work using zinc compensation led to the demonstrations of metal-insulating-n-type GaN LEDs [137]. p-type GaN research progressed in 1989 [92] with the use of a low temperature AlN buffer layer and Mg doping. Nowadays conductivity modulation can be achieved by doping with donors such as Si, O and Ge or with acceptors such as Mg, Zn and Be. Si and Mg are primarily the n-type and p-type dopants of choice. Si doping is used to produce films with free electron concentrations from the low 10^{17} to the mid $10^{19}cm^{-3}$ with almost complete room temperature donor activation. Furthermore, Si doped GaN can be grown with bulk electron mobility above 300 $cm^2/V.s$. The maximum reproducible hole concentration achieved in p-GaN with conventional doping techniques rarely exceeds $10^{18}cm^{-3}$ without compromising the surface morphology. Furthermore, the deep nature of the Mg acceptor leads to a poor room temperature hole activation of several percent. This leads to high Mg concentrations for heavy p-doping which can degrade hole mobility.

c.Electrical properties

ZnO and GaN materials can be highly conductive or resistive depending of their synthesis process. In function of whether they act as a metal, a semiconductor or an insulator, several electrical quantities are useful to describe their behavior. For example, the resistivity ρ is a physical quantity of interest depending of the areas covered by applications. For microelectronic devices such as transistors, low resistivity is preferable to facilitate the current transport. For applications of electromechanical transduction, a high value of ρ is preferable to avoid screening the electric field created by the piezoelectric effect.

The resistivity of ZnO extends over several orders of magnitude, with values from $10^{-3}\Omega.cm$ to $10^{12}\Omega.cm$ [138]. Generally, thick films are highly resistive ($\rho\approx10^5\Omega.cm$) [139] while the resistivity for thin films extends on several orders of magnitude. Depending on the elaboration methods, there will be thin films very conductive ($\rho\approx10^{-2}\Omega.cm$) [140], [141] or poorly conductive ($\rho\approx10^4\Omega.cm$) [142] which are similar to bulk properties [143]. Concerning NWs, their resistivity extends over a wide range of values from $10^{-1}\Omega.cm$ to $150\Omega.cm$ [144]. For an n-type semiconductor, the resistivity ρ and conductivity $\sigma=1/\rho$ are related to the mobility of electrons and holes through the relationships:

$$Conductivity\ in\ n-type\ semiconductor: \sigma = q.\mu_e.n \qquad \textit{Equation 22}$$

$$Conductivity\ in\ p-type\ semiconductor: \sigma = q.\mu_h.p \qquad \textit{Equation 23}$$

where μ_e and μ_h the electron and hole mobility, n and p the electron and hole concentration.

The mobility μ_e is a characteristic of conducting and semiconducting materials. It is expressed in $cm^2.V^{-1}.s^{-1}$. At low electric fields, the drift velocity ν is proportional to the electric field and mobility:

$$\overrightarrow{v_e} = \mu_e.\vec{E} \qquad \textit{Equation 24}$$

Where $\vec{v}$ is the current density and $\vec{E}$ the electric field [145].

It defines the ease that charges have to move in the influence of the electric field. The higher the mobility, the larger the current density will be for a given electric field:

$$\vec{J} = q.\mu_e.n.\vec{E} \qquad \textit{Equation 25}$$

Where $\vec{J}$ is the current density and $\vec{E}$ the electric field [145].

Usually thick films exhibit high mobility (μ_e>100 $cm^2.V^{-1}s^{-1}$). For thin films, μ_e varies depending of the process, the growing conditions and the post-processing. It is generally in the order of 30-150 $cm^2.V^{-1}s^{-1}$ [132]. Concerning ZnO NWs, the values of μ_e are comparable to thin films [135] or even smaller [146].

The electrical properties of ZnO can vary depending of the environment. First of all the electronic properties of ZnO are very sensitive to temperature θ. When θ increases, thermal agitation causes an increase in energy levels of the electron donor levels that are in the conduction band. For the average doped ZnO ($n \leq 10^{17} cm^{-3}$), n is proportional to $\theta^{1/2}$. μ_e is also related to the temperature by a law θ^{α} with α ranging from α=3/2 for low temperatures to α=-3/2 for high temperatures [147]. Secondly the pressure P also has an impact on the electronic properties of ZnO. When P increases, the crystal lattice is compressed and the space between the impurities is reduced, resulting in an increase in the concentration of defects. However, this effect is compensated by the piezoresistive effect: an increase in P tends to increase the gap between donors levels and the conduction band, making it more difficult to ionize. For high pressure (P>15GPa), wurtzite ZnO undergoes a stable phase transition to a cubic crystal lattice. ZnO in its cubic structure is still a semiconductor, but it is not anymore piezoelectric. Finally, surface defects can also affect the electronic transport properties of ZnO. Several studies have indeed demonstrated the dependence of conductivity with the environment of the sample. This dependence is mainly due to the adsorption of the surrounding molecules, which will modify the electronic properties at the surface of the single crystal [148] and trap charges on the surface of ZnO, which induces a decrease in conductivity. This physicochemical property of ZnO is at the origin of its use as a sensor for various gases like O_2 [149] , H_2O [150], N_2O [151] and CO [152].

As we have seen, thick films of ZnO are generally very resistive. In its bulk form ZnO is often regarded as a dielectric. A dielectric material does not contain electrical charges that could move macroscopically. In other words, this is a medium that cannot conduct electricity. As such, it is sometimes called electrical insulator. The dielectric materials are characterized in particular by their dielectric permittivity and dielectric strength. Permittivity describes the response to a given applied electric field. Due to their anisotropy, the relative permittivity of ZnO and GaN had the form of a 3x3 tensor reflecting the symmetry of the crystal and has the following form:

$$\varepsilon = \begin{vmatrix} \varepsilon_{11} & 0 & 0 \\ 0 & \varepsilon_{11} & 0 \\ 0 & 0 & \varepsilon_{33} \end{vmatrix} \qquad \textit{Equation 26}$$

Where ε is the permittivity, ε_{11} is the in-plane permittivity and ε_{33} the normal permittivity.

However, in the case of III-N, the difference between ε_{11} and ε_{33} is low. It is even negligible in the case of AlN. The dielectric strength of an insulating medium is the maximum value of the electric field that can sustain the medium before the start of an electric arc (and therefore a short circuit).

As for III-nitride materials, they have very interesting transport properties. The combination of a high voltage breakdown, high electron mobility (up to 2650 $cm^2.V^{-1}s^{-1}$ for bi-dimensional electron gas) and the possibility of obtaining high surface electron density using heterostructures such as (Al, Ga)N/GaN, make these materials a good choice for the realization of future microelectronic devices. The electrical properties of ZnO and GaN are compared in Table 7.

d.Mechanical properties

III-N materials are highly anisotropic materials. Their mechanical properties are defined by a stiffness matrix c. The shape of the stiffness matrices of a material depend on its crystal structure. In the case of III-N materials, the stiffness matrix has the following form [153]:

$$c = \begin{vmatrix} c_{11} & c_{12} & c_{13} & & & \\ c_{12} & c_{11} & c_{13} & & & \\ c_{13} & c_{13} & c_{33} & & & \\ & & & c_{44} & & \\ & & & & c_{44} & \\ & & & & & c_{66} \end{vmatrix} \qquad \textit{Equation 27}$$

Coefficients c_{11} and c_{33} represent the stiffness of the crystal under normal stress, in the plane and along the axis of the crystal respectively. Coefficients c_{13} and c_{12} represent the stiffness of the crystal faces due to shear stresses. The coefficients c_{44} and c_{66} describe the torsional behavior of the crystal. The mechanical properties of ZnO and GaN are compared in Table 7.

The limit of plastic deformation of ZnO is low (10 MPa), especially compared to GaN (100 MPa). This means that during the application of stress, dislocations are more readily induced in ZnO than in GaN. The dislocation mobility is also relatively high in ZnO. Yonenaga et al showed that during the production of heterostructures, the dislocations are formed relatively easier in ZnO than in GaN [154]. Thus, the homo-epitaxial growth on substrates without dislocations is to avoid the propagation of the highly mobile dislocations in the heterostructures.

e.Piezoelectric properties

Piezoelectricity is related to the non-symmetry of the crystal lattice. However, depending on the materials, the lack of symmetry is not marked in the same way. For example, the less symmetrical structure (triclinic) has 27 independent piezoelectric coefficients (Its strain tensor is not a symmetric matrix). However, piezoelectric ceramics with a wurtzite or perovskite structure are more symmetrical and the number of coefficients decreases. The piezoelectric coefficient matrices are then 3×6 matrices whose shape depends on the class of crystalline piezoelectric material considered. In the case of II-VI and III-N semiconductor piezoelectric materials, the e and d matrices have the following form:

$$e = \begin{vmatrix} 0 & 0 & 0 & 0 & e_{15} & 0 \\ 0 & 0 & 0 & e_{15} & 0 & 0 \\ e_{31} & e_{31} & e_{33} & 0 & 0 & 0 \end{vmatrix} \qquad \textit{Equation 28}$$

It may be noted that the matrices e and d are reduced to three non-zero elements: e_{31}, e_{33}, e_{15} and d_{31}, d_{33}, d_{15}, which correspond to the three main operation modes: the longitudinal, transverse and shear mode respectively [56] as shown in Figure 9.

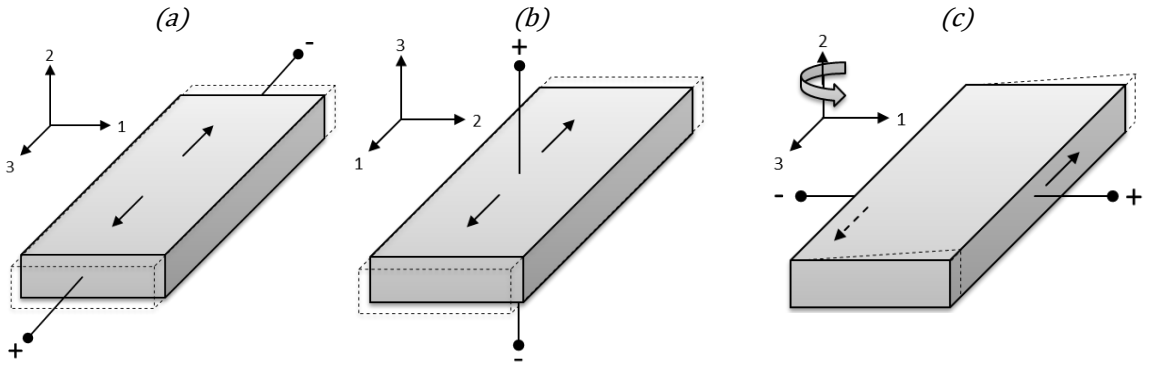

Figure 9 Three main operation modes: (a) the longitudinal mode 33, (b) the transverse mode 31 and (c) the shear mode 15.

It is noted that the components of the piezoelectric polarization present in the crystal plane (ie. P_x and P_y) depend only of shear stresses. In contrast, the vertical component of the polarization (P_z) reflects the influence of all the normal stresses. In most scenarios, the value of the P_z component of the polarization vector is several orders of magnitude higher than its planar components. Thus, if $\vec{P}$ is the electric polarization, any distribution of electric dipoles will have the same effect as a charge distribution of volume density ρ

$$\rho = -div(\vec{P}) \qquad \textit{Equation 29}$$

P expressed in $C.m^{-3}$ has a surface density σ equal to:

$$\sigma = \vec{P}.\vec{n} \qquad \textit{Equation 30}$$

where n is the normal vector to the surface in question (directed outwards) expressed in $C.m^{-2}$.

As mentioned before, ZnO and GaN possess three piezoelectric coefficients: e_{15}, e_{31} and e_{33}. In the case of a single crystal of ZnO, e_{33} and e_{31} relate the polarization $\vec{P}$ along the c axis to the deformation of the mesh along the c-axis and in the plane orthogonal to c. e_{15} describes the polarization induced by shear deformations. The values of the piezoelectric coefficients of ZnO and GaN bulk crystals are listed in Table 7. For thin films, the piezoelectric coefficients are of the same order of magnitude. These are highly correlated to the temperature of the substrate during the deposition phase. e_{33} reaches a maximum for temperatures of around 200°C. The use of doping (using copper for instance) also increases e_{33} [155]. In both cases, this is also certainly due to the fact that the films have a better orientation along the c-axis [156]. The values of the piezoelectric coefficients are generally reported for the matrices d or e as these are more convenient to use. Table 7 gives the common values of piezoelectric coefficients of ZnO and GaN. Although the differences between the various reported results are much larger than those observed in the case of stiffness coefficients, they are much less discussed within the scientific community. It should be emphasized that this is an important source of potential error for modeling.

The piezoelectric coefficients of ZnO are higher than those of other II-VI piezoelectric semiconductors. In its 1D form, ZnO has high elasticity and good resistance to fatigue. Although little has been done at the nanoscale, it seems that the piezoelectric properties of ZnO nanostructures are superior to those of bulk ZnO. In addition, its manufacturing processes are controlled at large scale (processes compatible with industry) and ZnO contains no lead unlike PZT for example which is important against toxic pollution. Moreover, it offers interesting possibilities in terms of heterogeneous integration in microelectronic industries. The piezoelectric properties of GaN are lower than those of ZnO and AlN. However GaN and AlN are well above any other III-N and III-V materials. Nevertheless, the piezoelectric performance of GaN, ZnO and AlN are very different from those of piezoelectric ceramics such as PZT or alloy of barium titanate $BaTiO_3$. The piezoelectric

coefficients of these ceramic materials are usually 50 to 200 times higher than those of III nitrides [157] in their bulk state.

Table 7 Physical properties of ZnO and GaN.

	ZnO	GaN
Phase	Wurtzite	Wurtzite
Density ρ_v (g.cm^{-3})	5.606	6.150
Young modulus Y (GPa)	Y=111.2 [100], [158]	Y=210 [159]
Poisson ratio υ	υ=0.33 [160] to 0.356 [161]	υ=0.183 [162] to 0.198 [163]
Elasticity c_{ij} (GPa)	c_{11}=209 c_{12}=121 c_{13}=105 c_{33}=211 c_{44}=42.5 $c_{66}=\frac{c_{11}-c_{12}}{2}$ [164]	c_{11}=390 c_{12}=145 [165] c_{13}=106 c_{33}=398 [166] c_{44}=105 $c_{66}=\frac{c_{11}-c_{12}}{2}$ [167]
Intrinsic polarization P_i (C.m^{-2})	P_i=-0.047 to -0.057 [100], [115]	-0.029 [98]
Piezoelectric coeficient e_{ij} (C.m^{-2})	e_{15}=-0.45 to -0.59 e_{31}=-0.51 to -0.61 e_{33}=1.22 [168] to 1.14 [153]	e_{15}=-0.30 to -0.30 e_{31}=-0.33 to -0.49 e_{33}=0.65 [168] to 0.73 [169]
Dielectric Constant ε	ε=8.656 [170]	ε=8.9[171]
Relative permitivitty ε_r	ε_{11}=8.22 [168] to 8.49 [172] ε_{33}=7.40 [172] to 7.83 [164]	ε_{11}=9.5 [168] ε_{33}=10.4 [173]
Band gap E_g (eV)	E_g=3.40 (direct) [167]	E_g=3.42 (direct) [167]

I.5. State of the art of piezoelectric applications

I.5.1. Applications of bulk piezoelectric materials

Piezoelectric devices have applications in many areas. The direct effect is used in sensor applications, such as force or displacement sensors. The reverse effect is used in actuation applications, such as motors and accurate positioning devices. Specifically, 3D nanoscale movements required in a number of instrumental characterization techniques with atomic resolution (scanning probe microscopes type STM, AFM, NSOM fields ...) are generally provided by piezoelectric elements. Other applications include acoustic technology (production and detection of sound), power electronics (high voltage generation), electric transformers, resonators and oscillating systems (electronic frequency generation), mass spectroscopy (microbalance) and optics (optical assemblies). Piezoelectricity also finds its place in everyday applications, for example as a source of ignition for lighters.

I.5.2. Piezoelectric nanostructures using semiconductor materials

I.5.2.1. From ZnO single crystal to nanostructures

In addition to the 2D thin film, 1D nanopillars and 0D nanoparticles, there are many exotic ZnO nanostructures such as nanoribbons, nanotetrapods, nano desert roses, nanopropellers, etc. These structures can be obtained by physical means using different synthesis methods such as MOCVD, MBE and CVD between others, but also chemically, for example, using the reaction at a controlled pH

of zinc acetate and hydroxide. The latter methods are of significant interest due to the quantity of material produced and the relatively low cost of the materials necessary to the synthesis [174], [175]. NWs have been grown on a variety of substrates (more or less conductive and expensive). It is interesting to note that most of the grown nanostructures are highly anisotropic. This anisotropy is due to the presence of charged planes according to the directions +c (0001) being negatively charged and -c ($000\bar{1}$) being positively charged [176]. The existence of such planes is considered disruptive to the structure because of the strong dipole moment they induce. To minimize their energy, nanostructures will try to avoid having such plans, which has the effect of anisotropic growth along the c-axis, leading for example to propeller or pillar structures [177], [178].

The transition from single-crystal to nanostructures may induce nano-specific effects, such as quantum confinement or the exaltation of surface effects. But quantum confinement effects are only accessible at very small sizes. The exaltation of surface effects varies as the surface / volume ratio and can therefore play a role in the structures of a size about 50 nm [28], [29]. In this case, the only difference with the bulk phase is rather related to the form and synthesis of the structures considered [179].

I.5.2.2. Nanostructure effect and characteristics

At the nanoscale, materials react differently. For example a piezoelectric NW will bend at lower forces compared to a microwire. Its electromechanical properties may vary. This may be due to several phenomena that are increasingly studied even if few experiment, simulations and theoretical calculations have been realized on ZnO and GaN semiconductor piezoelectric NWs. However a review of mechanical and electromechanical properties of piezoelectric NWs has been done by Espinosa [40] where is discussed most of the aspects and difficulties of this domain.

a.The role of defects

Stacking faults [180], [181], inversion of domain boundaries [182], [183], dislocations or nanopipes [184], and surface defects [185] have all been reported on nanostructures [169]. Their presence depends mainly on the nanostructure synthesis method used. For example, MBE used for some of our GaN NW samples generate high crystalline quality and few stacking faults [186], while the more intensively used VLS method used for the growth of our ZnO NWs is known for higher density of such defects [181]. Defects can affect mechanical [185], optical [187] and electrical [188] properties of the material at nanoscale. Today the role of defect in mechanical behavior is widely accepted although their precise influence in NWs is still under investigation. It has been shown that dislocations increase the number of collisions of the free carriers and therefore limit the carrier mobility [189]. Dislocations can also contribute to a leakage current through GaN/AlN heterostructures [190]. Stacking faults change the local band structure [191]. But the possible influence of defects on the piezoelectric properties of nanostructures is largely unknown. Dislocations and inversion domain boundaries have an effect on bulk piezoelectricity. Dislocations modify the local strain fields and create a local piezoelectric polarization [191]. This affects the electric fields near surfaces or interfaces [192]. As a result, the overall piezoelectric response may change. However, the occurrence of dislocations in nanostructures are not as extended as in bulk or thin-films [181], [183] because they can migrate to the surface and disappear. But the role of stacking faults and surface defects is not fully elucidated. Concerning the inversion of domain boundaries, it creates an inversion of the direction of the piezoelectric response. There exists evidence that this type of defect appears in NWs [182], [183], although it is not clear to what extent.

b.Dopants

Intentional or unintentional doping is possible during the NW synthesis. Dopants in NWs play a role in the conductivity of the carrier and therefore influence the electromechanical response. Concerning piezoelectric materials it can have a strong impact on the amplitude and time constant of the piezoelectric phenomenon [144], [193]–[195]. If the conductivity is high, the direct piezoelectric response will decrease as free charges introduced by dopants can screen the piezoelectric potential [196].

c.Mechanical properties

The mechanical properties of nanomaterial such as the Young modulus and the fracture strength are key values to estimate the deformation or strain undergo by nanostructures under a load. It is especially important for piezoelectric material where electro mechanical coupling plays a major role for applications. Failure and fracture mechanism are also important because they influence the mechanical reliability and robustness of the systems and determine the mechanical operational limits of the devices. Many experimental and modeling approaches have been used to characterize the mechanical properties of piezoelectric NWs. The state of the art concerning piezoelectric NWs has been reported in by Espinosa et al. [40].

As summarized by Espinosa, most of the techniques developed for mechanical characterization of one-dimensional nanostructures have been applied to ZnO NW. Currently, there is a general consensus on the existence of a size-effect on the modulus of elasticity for ZnO NWs oriented in the [0001] direction, [28], [197]. But the failure values and mechanisms, although known to be higher than in bulk, are still under investigation. It has been shown that the Young modulus increases as the diameters decrease below 100 nm whereas in larger NWs the modulus of elasticity agreed well with the bulk value. In addition the size-dependence measured in bending modes is stronger than the one measured under uniaxial loading [198]. ZnO NWs have fracture strengths several times higher than that of bulk. In principle, the fracture behavior of ZnO NWs may be the result of a combination of surface defects [185] and point defects [199]. However, the quantification of each defect role in the fracture mechanism remains under study.

Similar to ZnO, several methods have been applied to the elastic characterization of GaN NWs but very little has been reported on failure properties. Bernal et al. [200] summarized the elasticity results reported in the literature, which, similarly to ZnO, show significant scatter due to defects role and experimental artifacts. Nevertheless studies show that GaN NWs display bulk elastic properties for diameters larger than 20 nm. As commented by Espinosa it is in contrast to the stronger size effect observed in ZnO NWs (at 80nm). Nevertheless, for our simulations we will keep the bulk mechanical properties of ZnO and GaN from the literature. But we should keep in mind that the defect density and the mechanical properties of nanomaterial depend a lot on the fabrication process used. At least concerning the NWs we studied, if the maximum stress in the NW is higher than its bulk fracture strength then the simulations are not realistic.

d.Electrical properties

The small section of the NWs makes them very sensitive to surface effects. Conduction in NWs is strongly influenced by surface states [201]. Indeed, in an n-doped GaN NWs, surface states are known to pin the Fermi level. To meet the electronic neutrality of the NW, a depletion region is created on its surface. Electrical conduction is confined to the core of the NW in the non-depleted zone. There is a dependence of the radial profile strip according to the diameter of the NW. It exist a critical diameter below which the NW is fully depleted. This critical size depends on the doping of the NW and also of the Fermi level at the surface which depends on the surface states. By varying the density of surface

states by different mechanisms (photoconductivity [202], environmental parameters [203], molecules addition [204]), the electrical conduction in the NW will change . The large variation in the critical diameter depending of surface conduction makes NWs very sensitive to their environment. When the diameter of the NW is less than the critical diameter, the NW is completely depleted and sideband curvature decreases as the radius decreases, thereby reducing the effect of the space charge zone.

The influence of the nanostructure on electron transport is highly dependent on the experimental methods used to probe the transport properties and the size of the nanostructures studied. Indeed, an individual nanostructure, larger than ten nanometers, shows no quantum effects. In this case, the conductivity comes from the extended states, but its activation energy strongly depends on the atmosphere in which the experience takes place. These measurements confirm the importance of surface quality on transport mechanisms, which has already been seen in the case of single crystal and exalted in the case of nanostructures. In addition, these results are related to the transport measurements (I-V) on single NWs. Hall Effect measurements, which could give us information about the doping of such NWs, cannot be done on single NWs because of their shape. If the surface has an important role in the case of individual nanostructures, one important question would concern the effect of nanostructuring on an assembly of such objects.

Thus the electrical transport properties of NWs differ significantly from those of bulk material. A review shows that the resistivity of ZnO NWs varies between 10^{-3} and $10^{5}\Omega$.cm [150]. This variation of the resistivity of eight orders of magnitude is attributed in particular to the crystallinity, the density of local defects and surface morphology. But a crucial parameter is the ambient atmosphere: resistivity varies over several orders of magnitude depending on whether the measurement is done under vacuum, air, nitrogen or oxygen. This is due to the adsorption of molecules on the surface that trap more or less carriers. Under UV illumination, the resistivity decreases because the molecules are desorbed by the photo-induced carriers. For example, concerning NWs grown at CEA-LETI, two studies on electrical properties were performed. They have shown that the electrical conduction under vacuum was realized by a two-dimensional electron gas on the surface of the NWs [205]. On the contrary, the presence of holes was measured at the surface of the NWs when they are encapsulated by a polymer [206]. This was attributed to a curvature of the conduction band at the interface with the polymer. These studies show that surface effects are predominant for the electrical conduction on ZnO NWs.

e.Piezoelectric properties

In contrast to the characterization of mechanical properties, where atomic structural characterization, experimental measurements and simulations have been performed, much remains to be done in establishing synthesis-structure-properties relations in the field of nanopiezoelectricity. Due to coupling between mechanical and electrical effects, these experiments are more challenging than nanomechanical ones, and as a result the number of studies focusing on characterization of piezoelectricity in NWs is much smaller when compared to those on mechanical characterization.

In the particular case of piezoelectric semiconducting materials, piezoelectric force microscopy (PFM II.5.4.) has been applied to ZnO nanobelts on the (0001) surface and the piezoelectric constant d_{33} was measured from 14.3 to 26.7pm/V [36] which is higher than the bulk constant (9.9pm/V). But they observed that the effective piezoelectric constant decreased by increasing the frequency of the applied electric field. Another study reported a piezoelectric constant d_{33} of 7.5pm/V on ZnO nanopillars of diameters around 300nm [207]. A similar study reported a variation of piezoelectric constant from 0.4 to 9.5pm/V [144] for ZnO nanorods with diameters from 150 to 500nm and length from 400 to 600nm. These results are lower but they found a direct correlation between the piezoelectric

coefficient and the resistivity of the nanorods studied. Indeed nanorods with low piezoelectric constant had low resistivity from 0.1 to 155Ω.cm. This confirms that electrical properties have an effect on the piezoelectric response [196]. PFM have also been applied to individual GaN NWs with 65nm diameter [208]. Wurtzite GaN NWs grown by catalyst-free MBE process revealed a piezoelectric constant (d_{15}≈10pm/V) three times higher than that of bulk. For NWs with diameters from 64 to 190nm, piezoelectric coefficients d_{33}=12.8pm/V, d_{13}=8.2pm/V, and d_{15}=10.2pm/V were measured, which show that piezoelectric constants of GaN NWs can be up to six times that of bulk values [30]. Despite all the challenges, experimental results point to an enhancement of piezoelectricity for NWs below 100nm.

Computational investigation of piezoelectricity by ab-initio methods is mainly limited due to the computational cost of simulation of large size NWs. As a result, studies are rare, with most calculations dealing with homogeneous nanostructures smaller than 5nm. Ab initio methods have been utilized several years ago to calculate the bulk piezoelectric properties of ZnO nanostructures [98]. Recently, Dai et al [209] introduced size-effects in piezoelectric NWs models and extracted surface piezoelectric constants, FEM methods on ZnO NWs [47], [210], [211], Atomistic Field Theory and FEM methods on $BaTiO_3$ nanocubes [212], and recent DFT approaches on ZnO nanostructures [213], showing apparent piezoelectric constants that can be larger or smaller than the expected bulk values [29], [214]. Especially Espinosa and co-workers studied the size-dependence of piezoelectricity in GaN and ZnO NWs for diameters from 0.6 to 2.4nm, using first principle-based DFT calculations. A giant piezoelectric size effect was observed [29] for both NWs with almost two orders of magnitude enhancement in piezoelectric coefficient that could be achieved if the diameter of the NW is reduced to less than 1nm.

In order to understand the size-dependence, the authors performed an analysis of distribution of charges and dipole moments. One of the observations from the computational modeling was that the absolute value of polarization in NWs was smaller than the bulk value. However, when normalized by the volume, the NWs exhibited larger values. For the same number of atoms, the NW had smaller volume respect to the bulk material due to the radial contraction caused by surface relaxation. This observation asserted that the reduction of volume due to surface reconstruction in NWs plays an important role in the enhancement of the piezoelectric constants [29]. Similar trend were found in ZnO NWs up to 2.8nm in diameter [215]. In that work, it was found that ZnO NWs have larger effective piezoelectric constant with respect to their bulk counterparts due to their free boundary. Another study focusing on the surface piezoelectricity shows that at nanoscale this contribution becomes important because of the increase of the surface to volume ratio [209].

Table 8 Piezoelectric coefficients in nanostructured materials compared to the bulk.

d_{33} (pm/V)	Theoretical (nano)	Experimental (nano)	Experimental (Bulk)
PVDF	-	-38 [42]	-25 [216]
PZT	-	101 [64]	650
ZnO	168.2 [29]	14-26.7 [36]	9.93 [36]
GaN	65.8 [29]	12.8 [30]	1.86 [29]
PMN-PT	-	381 [217]	2500 [217]

An inspection of these data (Table 8) reinforces the idea that further characterization efforts are needed to reduce the existing scatter and identify size effects trends in the piezoelectricity of NWs. In addition computational studies still need to simulate larger sizes. Another fact is that there is a gap in the characterization of piezoelectricity between 10 and 100nm. This size range is very relevant as the advantages of scaling usually appear below 100 nm. In addition, NW diameters, achievable with current synthesis methods, are typically above 10nm. The coupling of improved experimental

techniques, which allow in situ structural characterization, and enhanced computational methods are needed before reaching a unified set of values and better understanding the physics behind the observed effects. One thing seems sure, according to the publications, the decrease in the size of piezoelectric structures leads to the improvement of the conversion of mechanical energy into electrical energy. This explains the interest of research teams and companies which want to synthesize and integrate these objects in energy conversion devices and sensors.

I.6. Conclusion

In this first chapter we have introduced the scientific and international context of the thesis, mostly in terms of energy issues of smart systems and autonomous sensors. Indeed, these systems are consuming more and more energy while the improvement of battery capacity is very moderate and not sufficient enough to support this trend. One solution to address this problematic is to develop self-powered sensors and energy harvesters. We have presented a state of the art of energy sources that are available in our daily life environment altogether with the main technologies to harvest them. Among the different principles, mechanical energy harvesting presents the significant advantage to be highly related to human activities with high energy densities that makes it very promising for future industrial implementation into different objects. Piezoelectric technology and more precisely piezoelectric NWs devices seem to be relevant to efficiently harvest mechanical energy. The success of these NW-based devices relay mostly in their high potential for nanosystem integration with great functionality. For example, strain sensors with increased sensitivity, provided by the piezoelectric effect [37], or NGs [38] to power supply autonomous sensors [39] have already been demonstrated. Most NW-based applications utilize semiconducting NWs [40] such as ZnO and GaN NWs, which show a large improvement on their piezoelectric performance at nanoscale when compared to bulk material efficiencies. However a deeper understanding of the piezoelectric performance of such NWs is needed as only few works have been done on the study of the electromechanical properties of such individual NWs. We will thus study in detail in Chapter II the piezoelectricity and we deeper investigate the properties of ZnO and GaN NWs at the nano scale.

Chapter II. Piezoelectric study of ZnO and GaN NWs

The understanding of the piezoelectric phenomenon and the knowledge of piezoelectric material physics allow a wide range of applications. In addition the evolution in semiconductor physics and micro fabrication process led to the synthesis of micro and nano structures such as NWs and their application in microelectronic. Thus we can imagine new devices such as nano mechanical sensors or energy harvesters. But for research and development, controlling an easy fabrication process of ZnO NWs is a key point. Therefore we reviewed the various method to synthetize ZnO and GaN NWs. Then we chose and learned the hydrothermal synthesis of ZnO NWs and we studied its control for future integration. Indeed, control the size and the density of NWs is important because that influence their piezoelectric responses to stimulus. In addition we worked on the quality and the integration of NWs carpet with few defects to properly use them. Then we need to understand the behavior of piezoelectric semiconducting NWs such as ZnO and GaN NWs. In this context the analytical modeling and the FEM simulation are two important tools to describe ZnO and GaN NWs and thus scale and functionalize them in view of future applications. These approaches are complementary to explain piezoelectric issues such as the inversion of the potential at the base of a bend ZnO NW. Therefore we studied and developed these two aspects. At last, ZnO and GaN NWs have to be characterized to study their real parameters and behavior in order to correct the models if needed and develop functional applications. To proceed we chose near field methods and especially AFM characterization to study the mechanical properties of ZnO and GaN NWs such as their Young modulus. Then piezoelectric studies were developed to measure the piezoelectric potential generated by strained NWs and deeper investigate their piezoelectric effect.

II.1. Fabrication techniques of piezoelectric semiconductor NWs

Recently, the characterization of nanostructures, and in particular ZnO and GaN piezoelectric semiconducting NWs in order to integrate them into devices, has been the subject of numerous studies. Indeed, these materials are compatible with the synthesis methods of nanostructures and with the CMOS technology which makes them ideal candidates for multiple applications. Other studies are trying to make nanostructures using piezoelectric ceramics or polymers, although the tendency is the reduction of the piezoelectric effect due to their low crystallinity [42], [218]. Many techniques are used to achieve growth of piezoelectric semiconductors NWs. Some growths can be performed on various homogeneous substrates or with predefined patterns. A homogeneous substrate is a flat surface corresponding to a crystal plane of the material used. A patterned substrate is a substrate having undergone operations (lithography) to delimitate areas of preferential nucleation of NWs. The growth techniques of NWs have very different characteristics and very different results can be obtained. We can classify these manufacturing processes into two categories (Table 9): bottom-up processes and top-down processes. The first is to achieve nanoscale objects from a molecular precursor by chemical synthesis and self-assembly of atoms or molecules. These techniques are based on the natural way in which minerals crystallize. The second approach is to remove material from a large object to obtain an object having smaller dimensions and desired shape. Finally, it is possible to combine top-down and

bottom-up approach to achieve an orderly growth of NWs. A step of lithography or nano imprint is typically used to pattern a thin layer of growth catalyst. Thus the localized growth of NWs will follow along the defined patterns. In the following I will detail the Top-down etching process and the MBE and MOCVD process whose we obtained ZnO or GaN NWs form different laboratory. Then the next section will focus on the hydrothermal growth of ZnO NWs that we learned in Georgia Tech and developed in IMEP-LAHC for extensive study of ZnO NWs.

Table 9 Manufacturing processes of piezoelectric semiconductor NWs.

Bottom-up	Top-down
Chemical Synthesis	Micro machining
Electro Chemical Synthesis	Nano imprint
Pulse laser deposition (PLD)	Deep reactive-ion etching (DRIE)
Chemical vapor deposition (CVD)	
Metal organic chemical vapor deposition (MOCVD)	
Molecular beam epitaxy (MBE)	

II.1.1. Top-down approaches

The top-down approach can be used to fabricate NWs, by various means such as lithography or electrophoresis. Recently gallium nitride nanostructures fabrication has focused on the bottom-up approach since defect-free and high aspect ratios nanostructures can be grown. Nevertheless, some of the perceived benefits, such as strain relaxation and the opportunity for three dimensional devices can also be realized with top-down approach. In addition, top-down processing is more suited for wafer-scale ordered arrays that can be reliably integrated into large-area devices than a bottom-up approach. Such top down nanorods can be used to create photonic crystal structures [219], [220], scaffolds for devices with 3D active areas [221]. Here we focused on lithographic top down process which consists of:

- The deposition of the material layer wanted for nanostructures. The quality of the deposit is important for the nanostructure quality and properties.
- The lithography of which depends the size and the pattern of the nanostructures.
- The etching of which depend the shape, aspect ratio and conformity of the nanostructure compared to the mask.

This method can create very good GaN NW array [222] as shown on Figure 10.

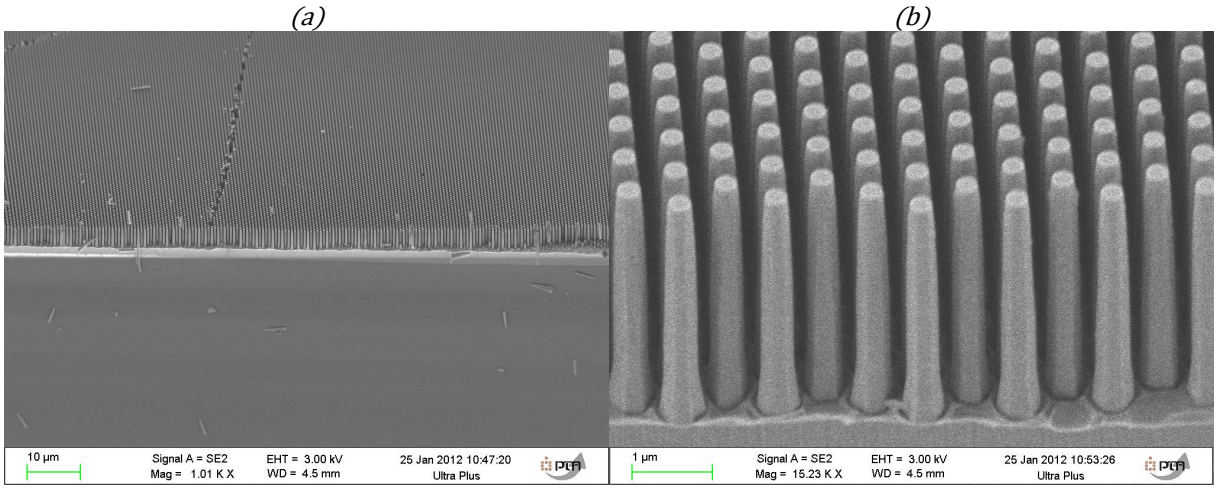

Figure 10 Top down GaN NWs array on sapphire substrate (CHREA).

II.1.2. Bottom-up approaches

II.1.2.1. The substrate issue

The delay in the development of III-nitrides compared to other III-V semiconductor is largely related to the lack of suitable substrate for epitaxial growth. The production of bulk GaN single crystals [223] and AlN [224], which are substrates suited to the growth of nitrides with low dislocation densities of 10^2 cm^{-2} [224], is at present very difficult and costly. The most commonly used substrates for heteroepitaxial growth of nitrides are c-sapphire (0001) (the lattice mismatch with GaN is 14%), silicon carbide (lattice mismatch: 3.4%) and silicon (111) (lattice mismatch: -17%). The large mesh mismatch between these substrates and GaN in addition with the difference in the coefficient of thermal expansion induces a high dislocation density in the epitaxial layers (10^8 to 10^{10} cm^{-2}). On layers under tension, this can cause the formation of cracks during cooling of the sample from the growth temperature to room temperature. This explains the difficulties and delays encountered in the development of the growth techniques for of GaN NWs and their application in recent decades compared to ZnO whose growth is much simpler and less expensive. These issues are much less critical for NWs due to lateral strain relaxation.

II.1.2.2. NWs growth principle

Many NW growth mechanisms are based on the vapor–liquid–solid (VLS) growth process. The VLS mechanism was proposed in 1964 as an explanation for silicon whisker growth [225] from the gas phase in the presence of a liquid gold droplet placed upon a silicon substrate.

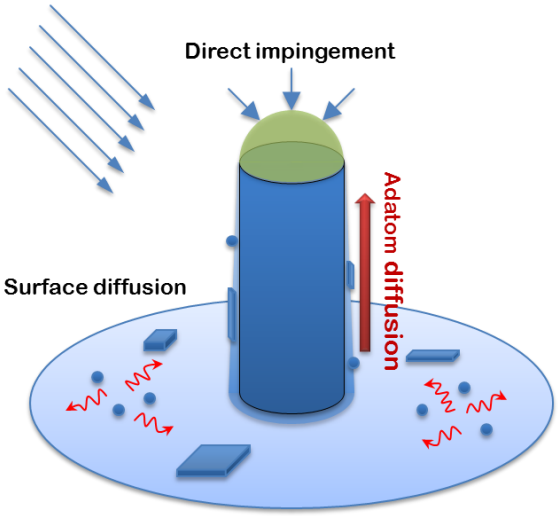

Growth governed by nucleation rates and adatom surface diffusion

Deposited materials contribute to:

- Axial growth
- Lateral growth
- 2D growth

Figure 11 VLS growth mechanism. Diffusion process occurring during the nucleation and growth step of the VLS mechanism. Impingement (act of encroaching) and adatom (atom that lies on a crystal surface) diffusion control the NW growth (adapted from [226]*).*

The VLS method is a mechanism for the growth of one-dimensional structures, such as NWs, from chemical vapor deposition. The growth of a crystal through direct adsorption of a gas phase on to a

solid surface is generally very slow. The VLS mechanism circumvents this by introducing a catalytic liquid alloy phase which can rapidly adsorb a vapor to super saturation levels, and from which crystal growth can subsequently occur from nucleated seeds at the liquid–solid interface (Figure 11). The VLS mechanism is typically described in three stages: first the preparation of a liquid alloy droplet upon the substrate from which a wire is to be grown. Secondly the introduction of the substance to be grown as a vapor, which is adsorbed on the liquid surface, and diffuses into the droplet. Thirdly the super saturation and nucleation at the liquid/solid interface leading to axial crystal growth. The physical characteristics of NWs grown in this manner depend, in a controllable way, upon the size and physical properties of the liquid alloy. The advantages of the VLS process are its much smaller reaction energy compared to normal vapor-solid growth, the fact that wires grow only in the areas activated by the metal catalysts and the fact that the size and position of the wires are determined by that of the metal catalysts.

II.1.2.3. Molecular Beam Epitaxy (MBE)

Molecular Beam Epitaxy (MBE) is a technique of depositing single crystals. It sends one or more molecular beams to a substrate previously chosen for epitaxial growth. It allows growing nanostructured samples of several cm^2. MBE is widely used in the manufacture of semiconductor devices, including transistors for cellular phones and WiFi.

a.MBE working mechanism

MBE is carried out under ultra-high vacuum (UHV) (10^{-8}Pa) conditions where the mean-free-path (distance between collisions) of source atoms or molecules is on the order of meters. Therefore, evaporated source atoms (i.e. an effusion cell) act as a beam of particles directed towards the substrate. The term "beam" means that evaporated atoms do not interact with each other or vacuum chamber gases until they reach the wafer, due to the long mean free paths of the atoms. The growth rate of the process is very slow, about one atomic layer per second, which allows the films to grow epitaxially. MBE also offers the possibility of cutting the atomic flow almost instantaneously. This is the technique of choice to obtain abrupt interfaces and to control the thickness at the monolayer scale. An advantage of MBE is the ability to control the growth in situ using diffraction of high-energy electrons at grazing incidence Reflection High Energy Electron Diffraction (RHEED). Thus it is possible to know in real time the number of monolayers deposited, the variation of the lattice parameter and, the 2D-3D transitions (Jain et al. 2000). The absence of carrier gases as well as the ultra-high vacuum environment results in the highest achievable purity of the grown films. MBE is a technique that has several advantages compared to other epitaxy techniques:

- The growth rate is low, between 0.1 and 1µm/h, allowing precise control of the thicknesses. Slow growth allows also control a homogeneous doping of the material.
- The fast and easy opening and closing of cell's covers containing species allow to easily changing the materials or its compositions. The advantage of this slow growth is to be able to get sharp heterojunction in multilayer materials.
- The possibility to put dopant cells in the epitaxy chamber makes easy the doping of the grown layers with a rather high accuracy.
- The very low pressure in the epitaxy chamber allows removing species that have not participated in the growth cycle without the need to drain.
- The UHV environment of the MBE reactor allows the use of in-situ characterization techniques using electrons or photons as a probe. Thus, a permanent and highly accurate control of the surface and the quality of epitaxial layers can be assured.

- MBE technology do not requires large quantities of toxic gases, as used in other synthesis techniques of semiconductors, which results in improved safety.

However, the slow growth and the very pure atmosphere (otherwise the impurities come contaminate the sample) make it a difficult technique to use in the world of industry.

b.Growth of NWs

To grow GaN and AlN structures in solid-source MBE, the Ga and Al elements are provided by an effusion Knudsen cells. Nitrogen is supplied either by cracking ammonia NH_3 or by a radio-frequency plasma cell which dissociates N_2 molecules in gas phase. The main parameters controlling the growth are: (1) the temperature of the cell which determines the flow and (2) the temperature of the substrate which determines the mechanisms of surface diffusion and incorporation of species. Elements such as gallium and arsenic, in ultra-pure form, are heated in separate quasi-Knudsen effusion cells until they begin to slowly sublime. The gaseous elements then condense on the wafer, where they may react with each other. In the example of gallium and arsenic, single-crystal gallium arsenide is formed. NW growth by MBE can be performed with or without a catalyst [227]. For the growth of III-nitrides NWs, it is necessary to have a high substrate temperature and high ratio of V/III flow. The growth rate is relatively low (0.1 to 1µm/h) which allows incorporating heterostructures defined close to the atomic monolayer. It is thus possible to fabricate heterostructures within NWs, preferentially in the axial direction as the axial growth is faster than the radial growth allowing a better control of the size of the heterostructures.

Thank to collaboration with Neel Institute (CNRS) we characterized GaN NW samples grown by MBE process. The GaN NWs have been grown on (111) Si wafer with and without a very thin AlN seed layer (few nm). These GaN NW have n-type intrinsic doping and can be doped artificially using Si as donor. The amplitude of this doping can be tune using different growing temperature from 1100 to 1250°C. Figure 12 shows an example of SEM images of GaN NWs provided by Neel Institute. Depending of the growth conditions and doping level, the diameter can vary from 25 to 60nm and the length from 300 to 600nm. In addition the density of NW can by very high.

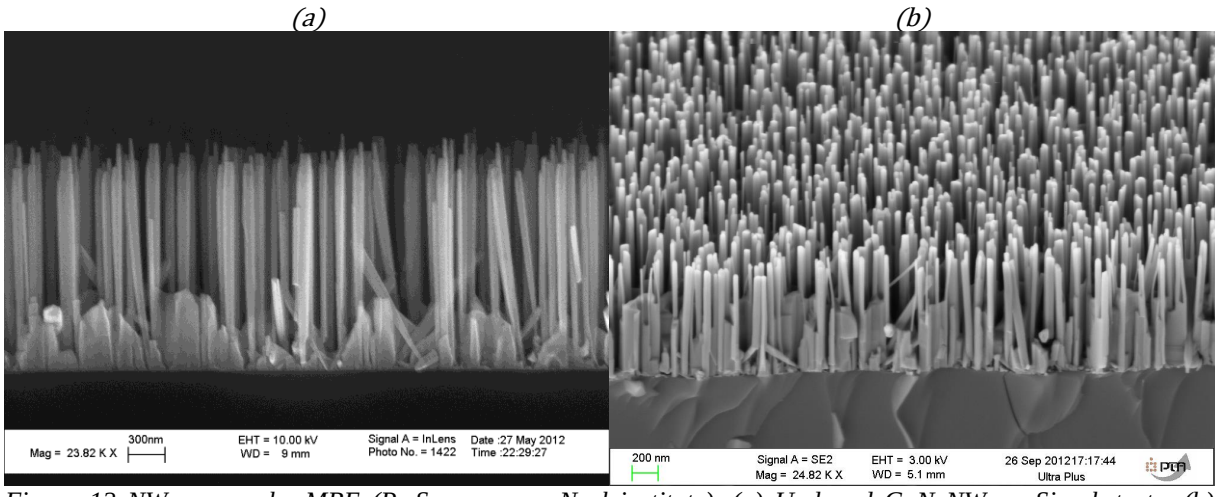

Figure 12 NWs grown by MBE (R. Songmuang, Neel institute). (a) Undoped GaN NW on Si substrate, (b) undoped GaN NW on Si p-type doped substrate.

Despite a better control of the synthesis of nanostructure, the ability to choose the polarity of material depending on the substrate or the buffer layer, and the easier p-type doping of III-V compared to MOCVD (because of the passivation of acceptor by hydrogen) ; MOCVD is today the main method used to synthetize commercial nitride compound. This because of technical issues such as the instability and uniformity problems of nitrogen cell and the high temperature required for example.

II.1.2.4. Metal organic chemical vapor deposition (MOCVD)

MOCVD is the main technique for growing III-nitrides. Its flexible implementation, its relatively low cost, the rapid growth over large areas compared to the MBE and the good reproducibility make it interesting for the manufacture of industrial components. This epitaxy method is based on the use of organometallic precursors consisting of metal atoms bonded to organic radicals.

a.MOCVD working mechanism

This method consists on the pyrolysis of organometallic compounds and hydrides (NH_3, SiH_4) transported by a carrier gas (N or H) in the vicinity of the substrate at high temperature. The flow of the sources used are stabilized and then mixed immediately before their introduction into the reactor. Epitaxy is made by the adsorption of precursors on the surface which diffuse and decompose. It follows desorption of the by-products and their removal by the flow of an inert gas. For gallium, trimethylgallium or triethylgallium are the main compounds used. The growth of GaN is made at a temperature between 800˚C and 1150˚C. Growth rates depend on the deposition conditions but are in the order of a few microns per hour.

b.Growing process and morphology

To make NWs by MOCVD growth, a catalytic growth using metal nanoparticles is generally used (Au, Ni or Fe). NW growth of III-nitrides using this method was demonstrated in 2003 [228] (see also section II.1.2.2. concerning the VLS method). Another approach to grow NWs by MOCVD is to use substrates with predefined patterns ex situ (defined patterns on a SiNx layer) [229]. For example, the NWs grown by MOCVD at CEA Grenoble were made from an original technique allowing growing NWs without catalyst and without ex situ predefined pattern. The method is based on an in situ SiN_x deposition of about 2nm. The inhomogeneity of the density and the roughness of the SiN_x layer permits the formation of islands of GaN [230] facilitating the NWs growth. Unlike the case of MBE, radial growth is faster than the axial growth. The radial coverage is uniform over the six facets of the NW. The NW heterostructures grown by MOCVD are thus core-shell heterostructures.

II.1.2.5. Hydrothermal growth process

In this thesis I have developed the hydrothermal growth in the IMEP-LAHC laboratory with the collaboration of Professor Z. L. Wang's group from Georgia Institute of Technology. We will see in more detail this growth technic at low temperature in the next part.

II.2. Hydrothermal grown of ZnO NWs layer

The learning of hydrothermal growth of ZnO has been done in Georgia Tech with the help of Dr. S. Lee, K. Pradel and the interns F. Saunier and A. Lauri who I co-advised. The goal was to understand and control the ZnO NW hydrothermal growth for experimental studies and developments.

II.2.1. Growth mechanism

The creation of the 1D structure of zinc oxide is obtained by hydrolysis of zinc salt into a supersaturated basic solution, since divalent metal compound do not hydrolyze in an acid environment. Into the basic solution we have the zinc ions, which can be present in the form of different intermediates accordingly to the pH of the solution and their hydrolysis, which gives the formation of the NWs. The wet chemical method used for the growth is driven by the minimization of the Gibbs free energy for the whole system and is considered reversible. The growth process can be divided in two parts: Firstly, the preparation of the growth solution. In water solution, the fabrication

products will reacts to create aqueous solution where all the reactants are available for the growth with good concentration. For the growth of ZnO NWs, the sub layers such as GaN template or ZnO seed layer are generally used. Secondly the growth of ZnO NWs, it starts by thermally activating the growth solution, putting the solution in a thermal drying oven, and the solution is brought to the temperatures generally around 90˚C [231], [232]. The next sections explain the growing steps and show what is happening.

II.2.1.1. Preparation and dissolution reactions

To prepare the ZnO NW growth solution, mix Zinc Nitrate and Hexamethylenetetramine in water. When diluted, Polyethylenimine and Ammonium hydroxide is added in the solution which is ready to the growth after a short agitation. The chemical reactions happening during the preparation of the solution and their equations are the following:

Equation 31 presents the reaction of dissolution of a salt in water giving the different reactants useful for the growth reaction. It will provide the zinc ions that will concur in the NWs growth together with O^- ions provided by water.

$$Zn(NO_3)_{2\,(s)} + 6H_2O_{\,(aq)} \leftrightarrow Zn^{2+}{}_{(aq)} + 2NO_3{}^- + 6H_2O_{\,(aq)} \qquad \textit{Equation 31}$$

where $Zn(NO_3)_2\,6H_2O_{\,(s)}$ is Zinc Nitrate. It is a solid compound, inorganic salt with acute toxicity. $Zn^{2+}{}_{(aq)}$ is zinc ion and NO_3^- Nitrate ion in solution from the dissolution of Zinc Nitrate.

Equation 32 and Equation 33 involve the HMTA compound whose role is still not clear now. It is believed that it acts as a weak base which coordinates and bridges the zinc ions creating highly charged compound which will be absorbed faster by the polar surfaces. This first mechanism should speed up the growth along the c-axis of the NWs The HMTA is a non-polar chelating agent absorbed on the non-polar facets and thanks to its rigidity it hindrances the growth on the lateral sides of the NWs favoring an anisotropic growth. Moreover, as can be seen from Equation 32 and Equation 33 the HMTA plays the role of pH buffer. Basically due to its rigidity the HMTA molecules start to hydrolyze in water and gradually release the HCHO and the ammonia. This is critical in the growth process because if the HMTA would have released all the OH- ions immediately the pH of the solution would have been changed into the one of an acid solution bringing the precipitation of the Zn ions. Thus, a fast consumption of the nutrient inside the solution would have occurred disadvantaging the aligned growth of the zinc oxide NWs. This is the reason why the HMTA is often referred as a pH buffer since the rate of its hydrolysis increase with the decrease of the pH and vice versa, maintaining in this way an equilibrium in the value of the pH during the growth process.

$$(CH_2)_6N_{4\,(s)} + 6H_2O_{\,(aq)} \leftrightarrow 6HCHO_{\,(g)} + 4NH_{3\,(g)} \qquad \textit{Equation 32}$$

where $(CH_2)_6N_{4\,(s)}$ is hexamethylenetetramine (HMTA or Hexamine). It's a solid organic compound, flammable, toxic and highly water-soluble. $HCHO_{\,(g)}$ is formaldehyde. It's a colorless organic gaseous compound. It's highly volatile and toxic and has irritating odor. It's also a highly water-soluble gas. $NH_{3\,(g)}$ is Ammonia, a colorless, volatile and pungent smell gas. At the end of the growth, it is better to manipulate the solution under an exhaust hood to avoid its inhalation.

$$NH_{3\,(g)} + H_2O_{\,(aq)} \leftrightarrow NH_4{}^+{}_{(aq)} + OH^-{}_{(aq)} \qquad \textit{Equation 33}$$

where $NH_4{}^+{}_{(aq)}$ is Ammonium ion in solution, coming from the protonation of NH_3. $OH^-{}_{(aq)}$ is hydroxide ion in solution, coming from the deprotonation of H_2O.

II.2.1.2. Optimized and fast growing process

The hydrothermal growth (Equation 34, Equation 35 and Equation 36) is performed at 95°C (or less: 85°C). In order to initiate the growth, a thin seed layer of Zinc Oxide (50 to 150nm) has been deposited on the top of the substrate by a PVD process. Indeed, this seed layer reduces the crystal structure mismatch between the substrate and the NWs and thus helps the growth to start providing already the nucleation sites on the substrate. From this starting point the following growing reactions occur.

Equation 34 shows the first and most important role of the ammonium, the main component of this reaction, which is to provide a basic environment for the growth (which is the one required by a divalent metal). But it also helps to mediate the heterogeneous nucleation of zinc oxide in the bulk solution which otherwise could consume important reactant useful for the growth of the NWs. Basically the ammonium coordinates with the zinc ions in the solution through Equation 34 stabilizing the amount of compound inside the bulk solution. In fact the reversible reaction will move in one or the other way accordingly to the concentration of zinc inside the bulk solution in order to maintain a low level of super saturation and thus preventing the depletion of the reactant and then use it only for the growth of the NWs.

$$Zn^{2+}{}_{(aq)} + nNH_{3\,(aq)} \leftrightarrow Zn(NH_3)_n{}^{2+}{}_{(aq)} \qquad \textit{Equation 34}$$

where $NH_{3\,(aq)}$ is Ammonium hydroxide. It is hazardous to the aquatic environment, acute toxicity and corrosive liquid. Better to manipulate it under an exhaust hood to avoid its inhalation. $Zn(NH_3)_n{}^{2+}{}_{(aq)}$ is a Zinc complex.

Equation 35 illustrates why the presence of PolyEthylenImine (PEI) in the reaction is really important and accordingly to its concentration really different results can be achieved. The first and most important role of the PEI is to prevent the homogeneous nucleation in the bulk solution; this is achieved thanks to its strongly chelating ability with zinc ions. And it is the presence of the HCHO which will allow the PEI to release the zinc ions and maintain the minimum super saturation level of the solution (the reaction of Equation 35) during the growth of the wires. Moreover the PEI agent is absorbed preferentially on some crystal facets, changing their Gibbs free energy and thus strongly affecting the morphology of the wires. The main result of this effect is that longer and thinner NWs can be obtained.

$$H(NHCH_2CH_2)NH_2 + HCHO \rightarrow H(NHCH_2CH_2)NCH_2 + H_2O \qquad \textit{Equation 35}$$

where $H(NHCH_2CH_2)NH_2$ is Polyethylenimine (PEI), a water-soluble polymer, acute toxicity and hazardous to the aquatic environment.

Equation 36 is a reaction of precipitation. It is responsible of the formation of the NWs on the substrate. A solid precipitate of Zinc Oxide is formed thanks to the insolubility of this compound in aqueous solution and its super saturation in the same solution. The growth process can be described as follow; the Zinc ions and the OH^- ions coordinate and undergo dehydration due to a proton transfer forming the zinc-oxygen ions bond. The agglomerate formed is a Zinc-OH compound with an octahedral geometry whiles the molecules of water generated by the reaction flow back into the solution. When these kinds of ions agglomerate reaching dimension, usually around 100-200 ions, at the center of the agglomerate there is the nucleation of ZnO Wurtzite structure domain. The center of the nucleation site contains zinc and oxygen atoms only whereas the external regions are still mainly formed by agglomerate of zinc and OH^- ions. With agglomerates of 200-300 ions we get nanometers sized nuclei of zinc oxide. When a nucleation site is formed the molecule of the nutriment is favorably absorbed on the highly energetic and polar surfaces along the c-axis such as the (+0001) in order to minimize their surface over the whole volume of the structure. The polar surfaces of the wurtzite

structure are an alternation of Zn^{+} ions plane and O^{-} planes, thus the polarity is always maintained during the growth, the absorption on this faces is continuous and the 1D dimensional structure with the maximum area of non-polar surfaces exposed (energy minimization) to the solution is created.

$$2OH^{-}{}_{(aq)} + Zn^{2+}{}_{(aq)} \rightarrow ZnO_{(s)} + H_2O_{(aq)} \qquad \textit{Equation 36}$$

where $ZnO_{(s)}$ is Zinc Oxide, the piezoelectric material, compound of the NWs.

Following this recipe, a ZnO NW carpet can be created on various substrates using a ZnO seed layer. By tuning the concentration of the reactant, the temperature and the growth time it is possible to vary the size, the shape and the density of hexagonal ZnO NWs. Experimentally the NWs we grown using this method had a length between 4 and 7µm (Figure 13). The diameters vary from 50 to 250nm and the densities have been estimated between 10^{10} to $10^{8}cm^{-2}$.

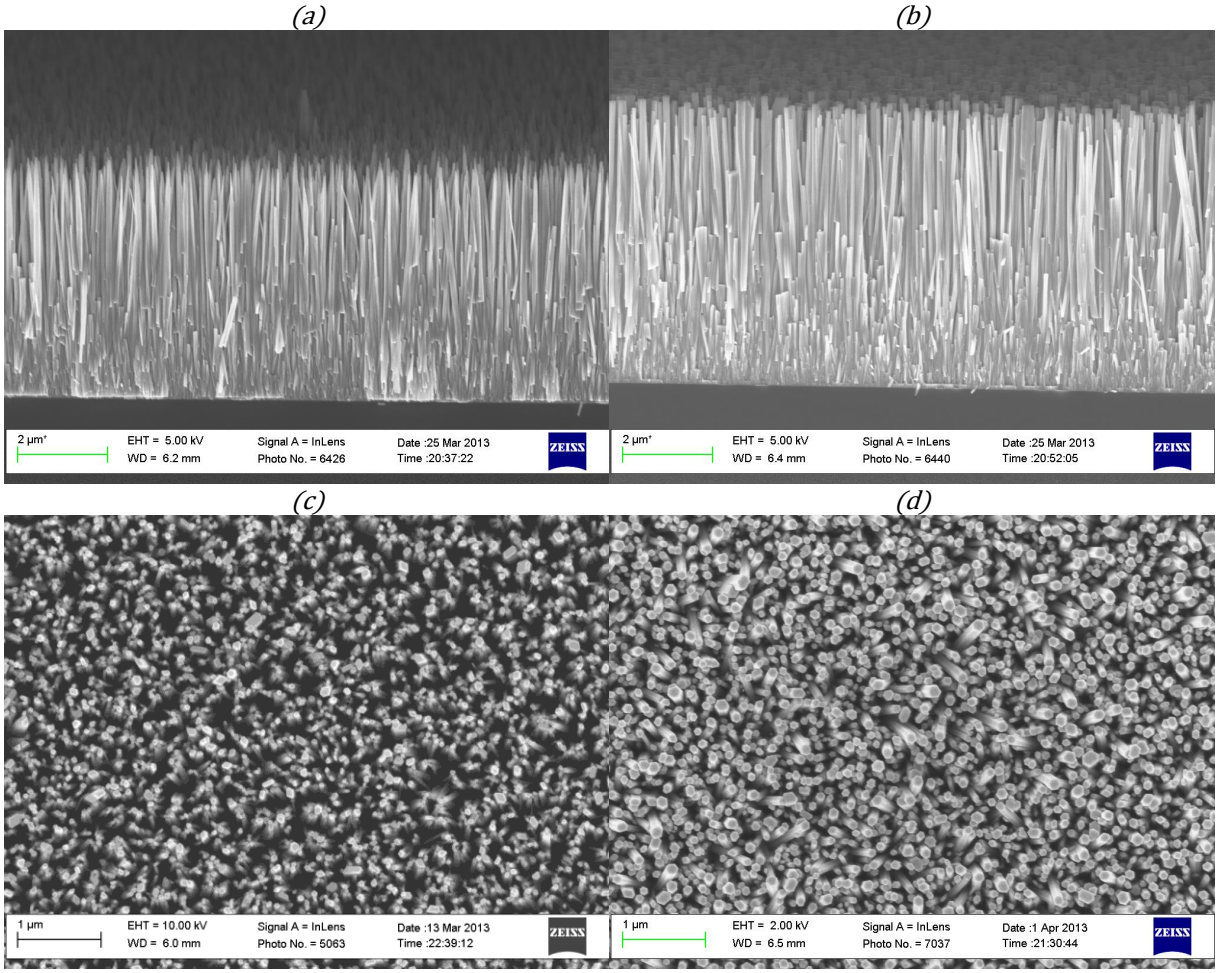

Figure 13 ZnO NW carpet grown using the optimized growing process. Various NW size (50 to 250nm of diameter and 4 to 5um of length) and densities (5×10^{8} to $10^{10}cm^{-2}$) obtained by tuning the reactant concentration and the growing time and temperature.

II.2.1.3. Synthesis and fabrication of ZnO NWs

The optimized hydrothermal ZnO NW growing process is efficient. It is fast (between 1 and 4 hours) and allows growing NW carpet on various substrates. But the addition of Ammonium and PEI makes the preparation and the growing techniques more difficult. Thus the manipulation and the setup are harder and the tuning of the NWs is more complex. Mastering this growing method can take time. However it is possible to grow ZnO NWs following the previous recipe without using Ammonium and

PEI. The growing principle and process are the same and the chemical reactions are identical. The preparation is easier but the NWs grown are a little bit different.

The non-addition of ammonium decreases the overall quantity of ammonium in the solution which is only supplied by HMTA. This may change a little the pH solution. But above all, the lack of ammonium allows the heterogeneous nucleation of zinc oxide in the bulk solution which consumes an important quantity of reactant useful for the growth of the NWs. In addition, the absence of PEI allows the homogeneous nucleation of zinc oxide in the bulk solution. It also results in a high super saturation level of Zn^{2+} ions in the solution. By consequence, the nucleation of ZnO in the bulk solution occurs and creates a lot of micro ZnO particles which precipitates and fall down similar to dust. Moreover these dusts consume a lot of nutrient in detriment of ZnO NWs. This plus the absence of HCHO on NW crystal facets lead to shorter and thicker NWs.

However this simple growing recipe, without ammonium and PEI, gave good results. But this requires some precautions to be taken to prevent ZnO particle deposition during the growth process. The NW length vary from 800nm to 1.5µm (Figure 14), the diameter varies from 100 to 500nm and the density is between 10^{10} and $10^{8}cm^{-2}$.

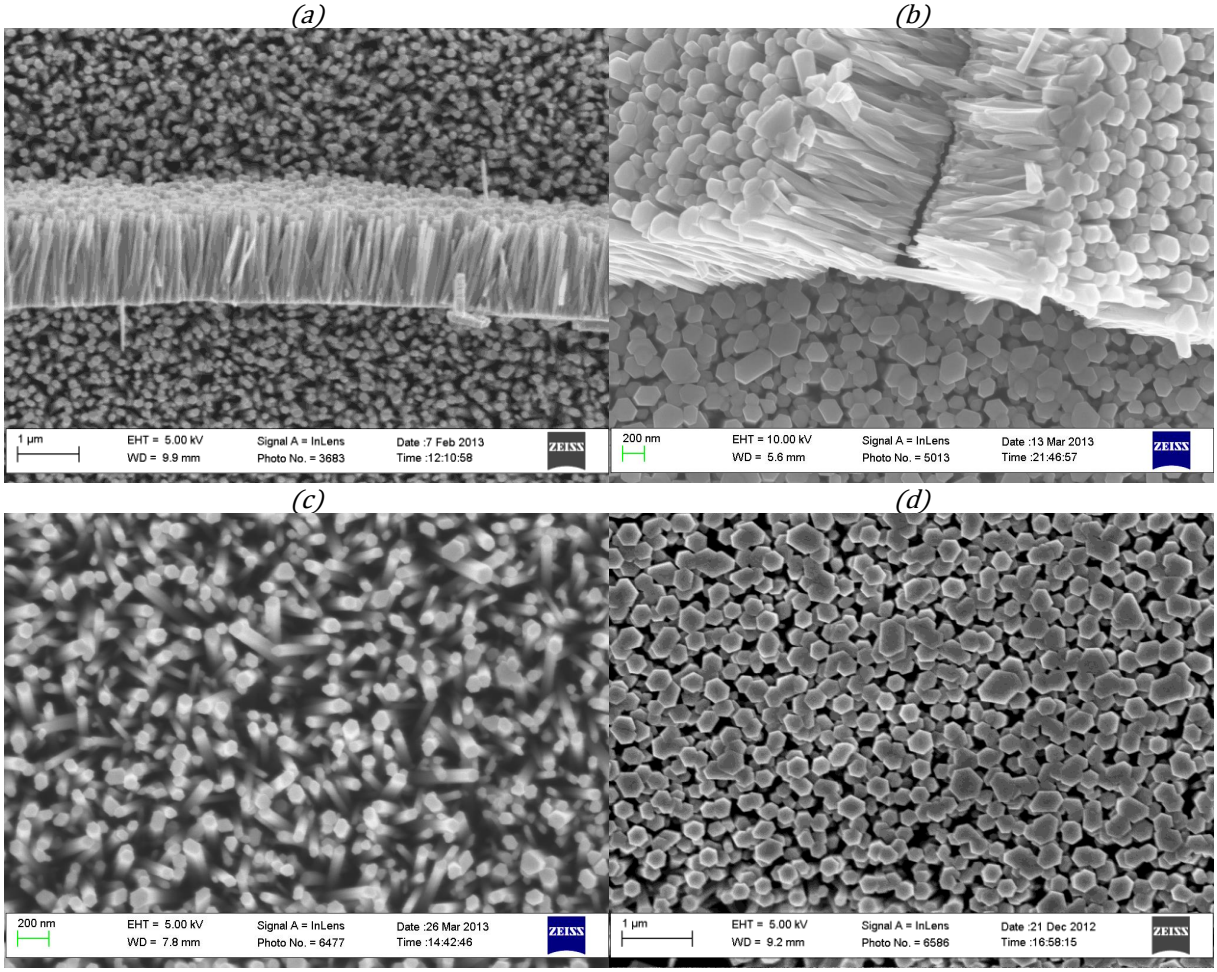

Figure 14 ZnO NW carpet grown using the simple growing process. Various NW size (100 to 250nm of diameter and 1 to 1.5um of length) and density (5×10^{8} to $5\times10^{9}cm^{-2}$) obtained by tuning the reactant concentration and the growing time and temperature.

II.2.2. Experimental setup

II.2.2.1. Preparation of the sample

The first step to grow ZnO NWs on a substrate is to prepare the substrate by cleaning it and depositing a ZnO seed layer with a thickness between 25 and 150nm. The role of the seed layer is to decrease the lattice mismatch between the substrate and the grown material. If the materials have two different crystal structures, to erase and adapt the crystals structures. Usually, on common substrates such as silicon (Figure 15) a 25nm ZnO seed layer is sufficient. But on certain material layers such as a silicon wafer with an Al_2O_3 thin layer it is necessary to add a 150nm ZnO seed layer. The reason is that Al_2O_3 can have a strong Boehmite crystal structure which can propagate through a thin ZnO seed layer and then create Boehmite ZnO structures on the top instead of ZnO wurtzite NWs. To deposit the ZnO seed layer, sputtering or ALD equipment's can be used in function of the desired thickness and quality. Then the substrate is attached to a sample holder such as a kapton film or a slice of glass. The ZnO seed layer can be patterned using photolithography process or a simple adhesive tape in our case to define growing surfaces and realize a selective growth.

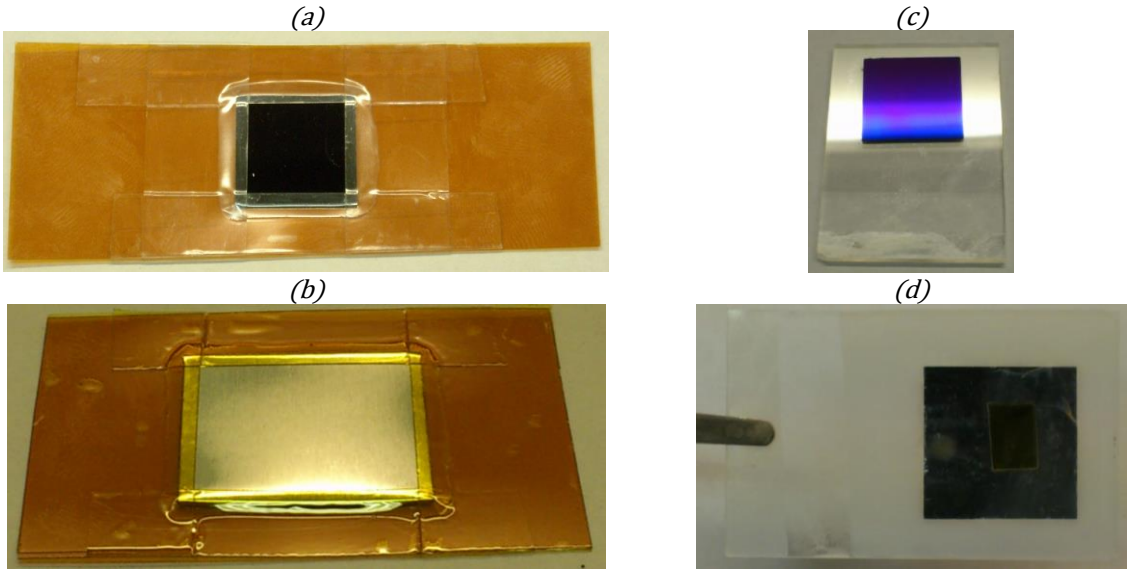

Figure 15 Different substrate layers for the growth of ZnO NWs. (a) A piece of silicon wafer attached on a kapton film using an adhesive kapton tape on the edges, (b) a piece of electro polished aluminum plate attached on a kapton film using an adhesive kapton tape on the edges, (c) and (d) a pieces of silicon wafer, with a ZnO seed layer, attached to a glass plate using a double side adhesive kapton tape.

II.2.2.2. ZnO NW growth

To grow good ZnO NWs it is important to respect a few points, especially using the simple recipe:

- After the decantation of the prepared solution, it is better to take the clear solution on the top using a pipe and not the dusts and mixture down the bottle (Figure 16a).
- To avoid any dust to deposit on the NW carpet the sample holder have be tilted face down in the bottle (Figure 16b) or floating face down on the solution (Figure 16c). The position of the sample in the bottle is very important using both recipes. In effect the concentration of nutrient can vary between the bottom and the top of the bottle. So the growing rate and the NW size can vary in function of the position of the sample in the bottle. Also when the sample is floating the concentration of reactant can vary between the edge and the center of the sample because of the near liquid-gas interface. Thus a noticeable difference in the NW size can appear on the edges.

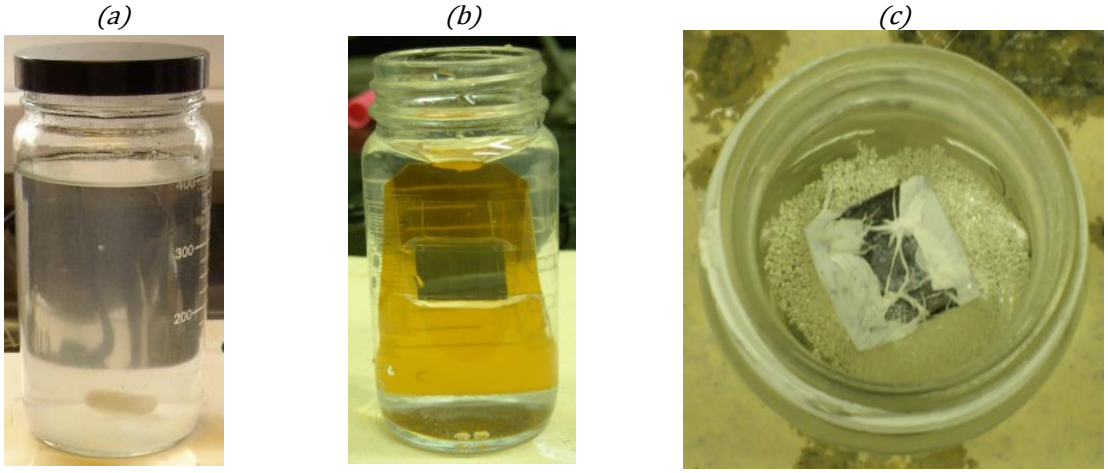

Figure 16 (a) Growth solution while decanting after magnetic agitation, (b) sample tilted face down in the growing solution and (c) sample floating on the top of the growing using Teflon tape.

- If dusts or defects are present on the seed layer, a quick ultrasound bath before the growth can detach dust and defects and thus improve the regularity and uniformity of the growth.

Finally, when the sample is correctly placed in the bottle, the growth can start putting the bottle in the oven and following the common or customized recipe according to the NW size and density desired.

II.2.2.3. ZnO NWs growing results

During the thesis, I synthetized ZnO NWs on pieces of silicon wafer with p-type and n-type doping (Figure 17a). In addition I synthetized on other various substrates such as hydro polished aluminum plates, aluminum foils, kapton films and slices of glass. The growing process is difficult to master to get perfect ZnO NW carpets but we finally controlled it. Thus we were able to grow good quality of ZnO NWs carpets on small piece of silicon wafer of $1cm^2$ and we succeeded to extend it on 2 inches wafer (Figure 17b).

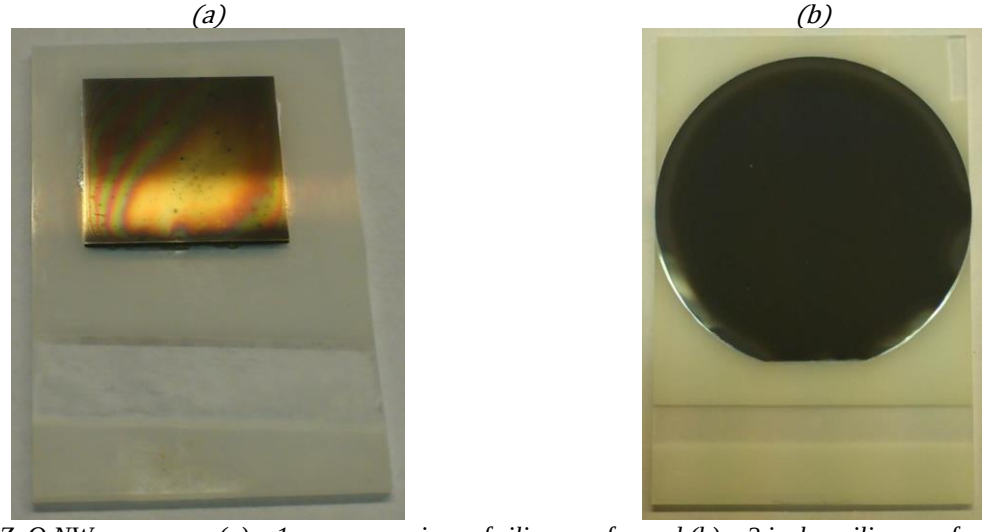

Figure 17 ZnO NWs grown on (a) a 1cm square piece of silicon wafer and (b) a 2 inches silicon wafer.

The biggest challenge was to grow perfect ZnO NW carpets with very few dusts, defects and contaminants. As shown on the Figure 18, various defects can grow on the sample (Figure 18a), dusts can be deposited everywhere using the simple growth process (Figure 18b) and contaminants altered the growth surface (Figure 18c).

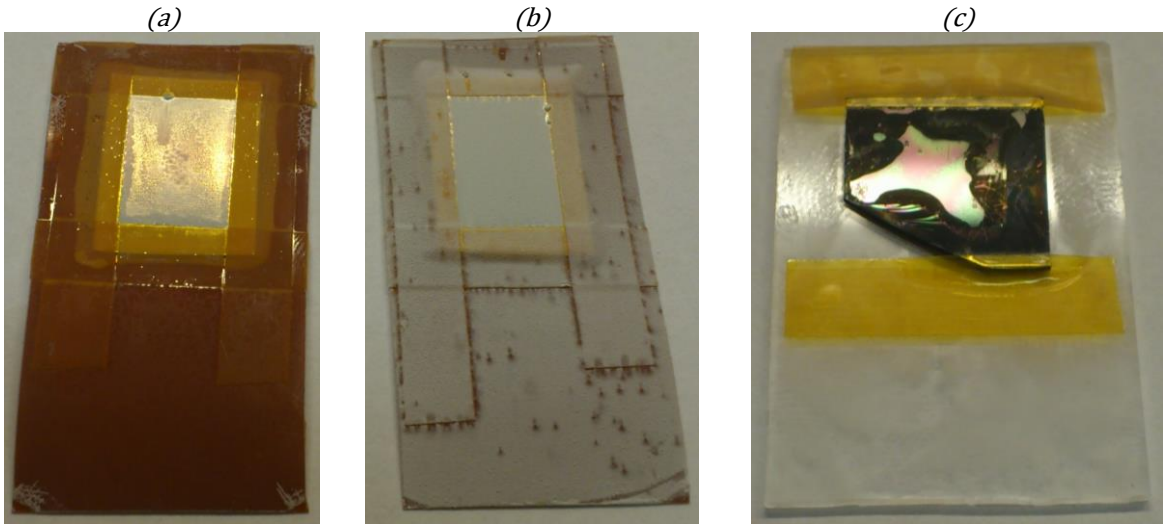

Figure 18 Sample growing issues. (a) Various macroscopic defects grown on the sample, (b) dusts deposited on the sample and (c) contaminants that spread on the sample.

II.2.3. Growth issues

During the growth process, many difficulties may occur. These problems are due to defects that can happen during the three steps of the fabrication of the NW carpet: On the first step during the preparation of the sample the seed layer can be imperfectly deposited at certain locations. It can be a lack of seed layer due to dusts or an adhesion problem of the seed layer (Figure 19a), or a hole due to a mechanical defect or a mechanical impact (Figure 19b) or a very small bubble below or in the seed layer (Figure 20). These problems will lead to a tiny hole with less or no NWs and it can even lead to the explosion of the seed layer which creates hole and dusts.

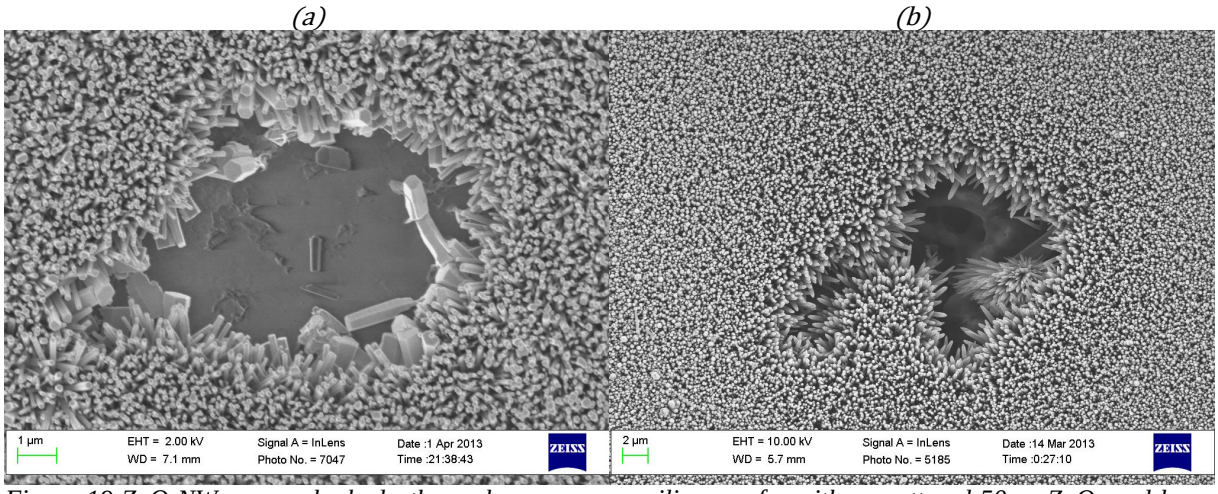

Figure 19 ZnO NWs grown by hydrothermal process on a silicon wafer with a sputtered 50nm ZnO seed layer (a) Seed layer hole and (b) silicon trough.

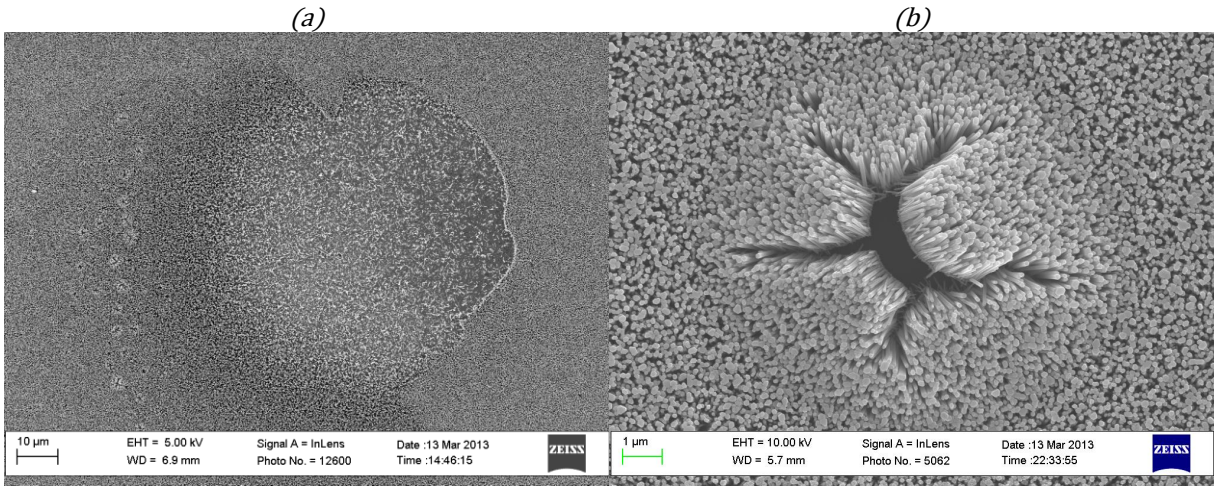

Figure 20 ZnO NWs grown by hydrothermal process on a silicon wafer with a sputtered 50nm ZnO seed layer (a) Growing problem due to a bubble and (b) growing problem because of a bubble under the seed layer.

Other defect can be formed during the growth itself. The sample can have some single NW which are bigger compare to the rest of the NWs (Figure 21a). Or it can have some localized cluster of NWs which grow like a flower over the carpet (Figure 21b). In these cases there is a local overgrow problem which is probably due to a small seed layer defect or a tiny dust. These defects can also be global. The NW defects can spread on a large scale with various NW sizes and densities randomly distributed (Figure 22a) or organized (Figure 22b). During the growing process, defaulting structures can grow because of a bad seed layer, contaminants and wrong reactant proportions. Thus can grow some ZnO horizontal (Figure 23a) and vertical (Figure 23b) boehmite plates [233] which can spread on the sample. These plates do not have a wurtzite structure and so they have bad or no piezoelectric properties. Thus, they change the mechanical and piezoelectric properties of the NW carpet which become less piezoelectric.

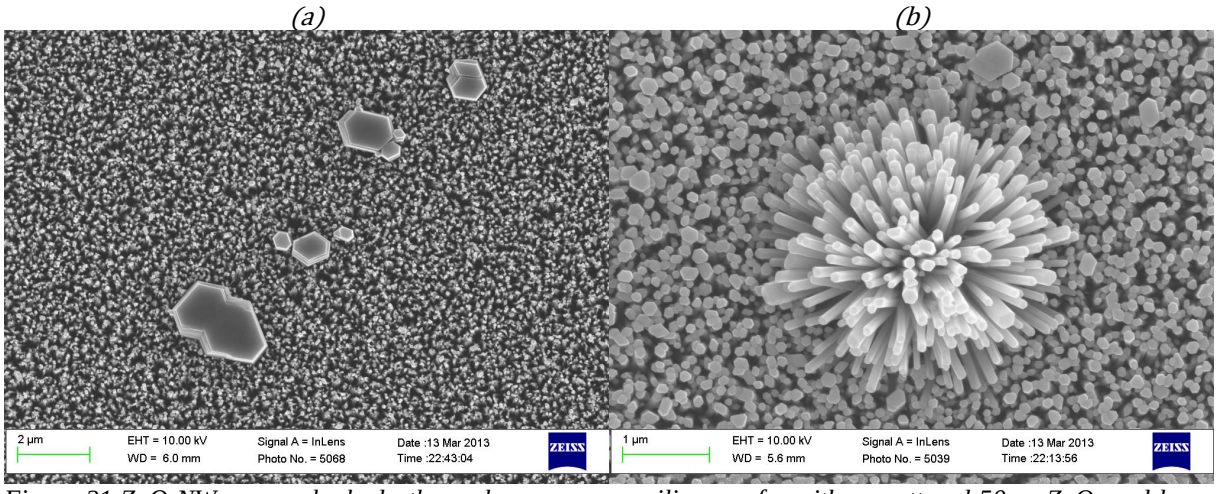

Figure 21 ZnO NWs grown by hydrothermal process on a silicon wafer with a sputtered 50nm ZnO seed layer (a) Single bigger NWs compared to the NW layer and (b) localized over growing cluster of NW.

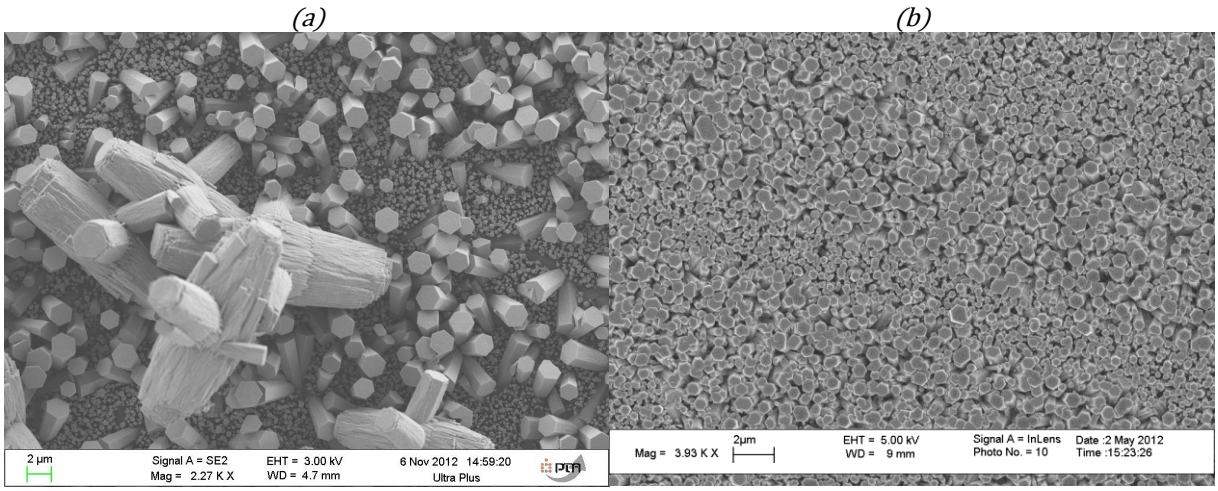

Figure 22 ZnO NWs grown by hydrothermal process on a silicon wafer with a sputtered 50nm ZnO seed layer (a) Random size growing problem and (b) organized size and density growing problem.

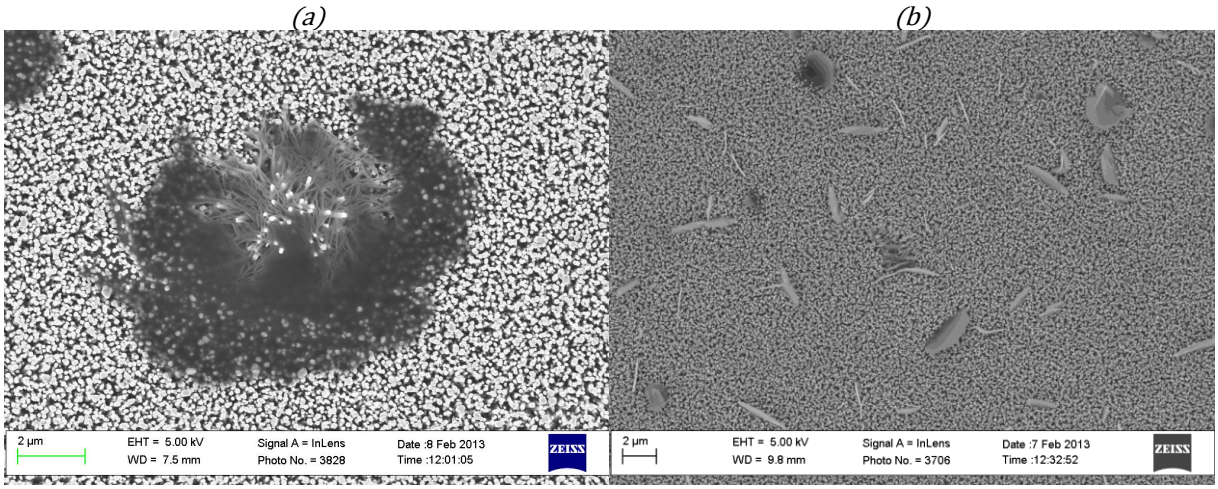

Figure 23 Hydrothermal ZnO NWs on silicon wafer with a sputtered 50nm ZnO seed layer (a) Horizontal and (b) vertical ZnO boehmite plates which grow and spread on the ZnO NW layer.

Finally, after the growth it is important to take care of the final cleaning process. Indeed if the NWs grown are thin and long they can bind together because of the capillarity forces (Figure 24a). So a Critical Point Drying process is required to avoid this phenomenon. It is also important to amply wash the sample with DI water to withdraw any particle (Figure 24b).

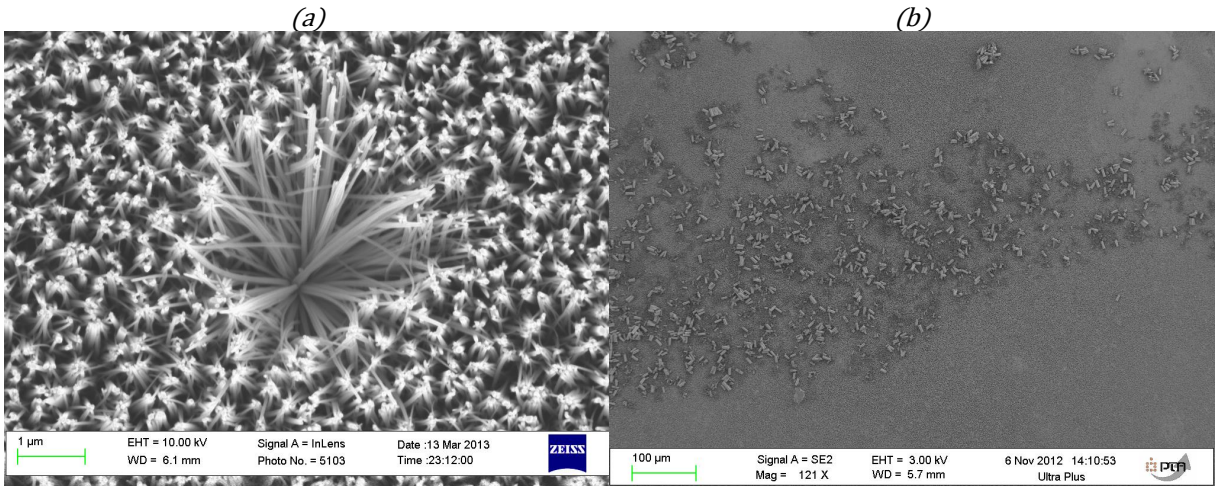

Figure 24 ZnO NWs grown by hydrothermal process on a silicon wafer with a sputtered 50nm ZnO seed layer (a) ZnO NW drying problem due to capillarity forces and (b) NW's dusts problem.

II.2.4. Growth on various surfaces and topologies

When mastered, the hydrothermal growing process of ZnO NW is very good to cover large surfaces of any substrate at low temperature and for a low cost. Despite the fact that it is difficult to grow perfect NW carpets without any defect, these defects can be minimized. Another interesting quality of this process is that it allows covering 3D patterns and structures with ZnO NWs (Figure 25). This multiplies the possibilities of integration of ZnO NWs and could lead to improved devices and new applications.

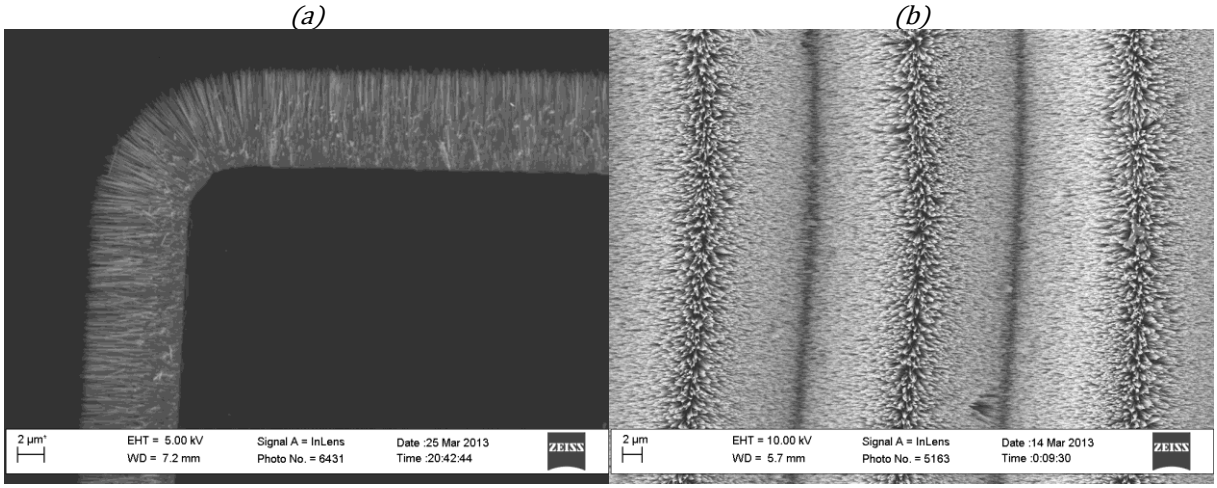

Figure 25 ZnO NWs grown by hydrothermal process on a silicon wafer with a sputtered 100nm ZnO seed layer (a) ZnO NWs grown on the edge of a sample and (b) ZnO NWs grown on a zig-zag surface.

II.3. Growth variability and distribution

Bottom-up growing processes does not allow fine control of the size of the NWs. As the electromechanical properties of the NW strongly depend on its dimensions, the statistical distribution of the size and geometrical properties of the NW array could have an impact on the performance of NW based sensors and energy harvesters. In the simulation works, we usually consider a network of NWs perfectly identical in size. This ideal case may seem quite simplistic and far from real devices. The most impactful geometrical parameter is the NW diameter which is reversely proportional to the potential generated at constant force applied laterally. In order to experimentally estimate this phenomenon, in collaboration with the CEA-Leti, we have analyzed the influence of the radius distribution from several samples. The study has been performed on ZnO NW grown at CEA (Figure 26a & b) by bottom up approach (MOCVD) and GaN NW synthetized at CHREA by top down techniques (Figure 26c and d).

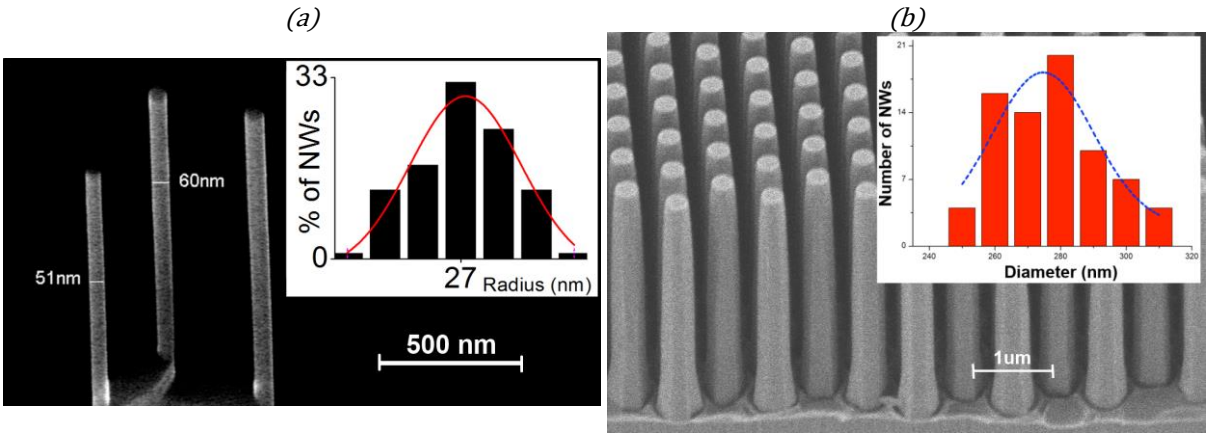

$$Gaussian\ function: \quad y = y_0 + A \times e^{-\frac{1}{2}\times\left(\frac{r-r_{average}}{\sigma}\right)^2}$$

y_0=-2.15095	y_0=2.1569
A=31.73509	A=16.050
σ=4.4076	σ=15.313
$r_{average}$=25.38102	$r_{average}$=274.72

Figure 26 Experimental Gaussian distribution and fit of the radius distribution of (a) a sample of ZnO NWs grown on sapphire substrate by MOCVD [234] *and (b) a top down GaN NWs sample.*

We have determined experimentally that the radius distribution of NWs followed a Gaussian distribution with an average radius of 27 nm and a standard deviation σ=4.4 for the ZnO NWs grown by MOCVD (Figure 26). While for the top down GaN NWs the average radius is 274nm and the standard deviation is σ=15.3. We also noted variations of the geometric shape of the NWs. Some NWs have a perfect wurtzite structure and therefore a perfect hexagonal geometry whereas others NWs have a deformed hexagonal geometry with some edges larger than others. The wurtzite structures can also be embedded into each other which can lead to one-dimensional structures with various shapes (Figure 14).

These variations of the size of the NWs can change the value and the distribution of the generated piezoelectric potential. This impact of this size distribution will be thoroughly investigated (II.4.1.3.). This can have a negative effect on the experimental devices [235] but also a positive effect if exploited in a clever way. One example of a positive effect will be mentioned later (III.2.2.) for an application as a force and displacement sensors [234].

II.4. Modeling of semiconductor piezoelectric NWs

II.4.1. Piezoelectric model of a NW under bending

It is essential for the study of ZnO NWs based devices to understand and calculate quantitatively, analytically as well as by numerical simulation, the piezoelectric potential generated by a NW in various configurations. The articles on the analytical calculation (based on the Lippmann theory of piezoelectricity [236]) and the finite element modeling of a ZnO NW are very few. The first notable proposal came from Professor Wang's group from Georgia Tech [210]. They proposed a model to calculate the potential distribution generated by a ZnO NW when subjected to bending forces. The NW is modeled by a cylinder, its diameter is 50nm and its length is 600nm. The NW is clamped at its root and a force of 80nN is applied at the top. A zero voltage is applied to its base. Subsequently other studies have investigated this problem using similar configuration [47], [235]. We will first use a similar configuration to compare our results.

II.4.1.1. Configuration

The modeled ZnO NW has a vertical c-axis, positioned orthogonally to a substrate connected electrically to the ground. From a mechanical point of view and provided that the NW has a length L large enough compared to its diameter, clamped in z=0 and free at the other end. The NW is supposed to have a perfect circular cross section. At the free end, at z=l, we apply a force F which is directed in the y direction, uniformly distributed over the upper surface and which causes bending of the NW. The NW and the associated system of axes are shown on Figure 27.

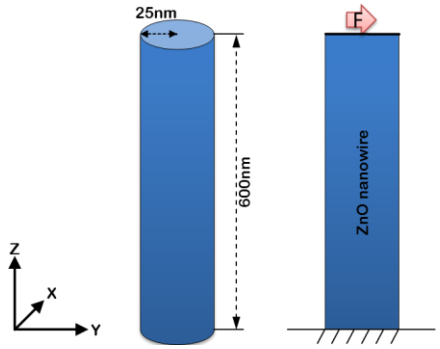

Figure 27 Schematic of a ZnO NW (l=600nm and r=25nm) under bending forces. It is clamped at root, free at the other end and a transversal force F is horizontally applied on the top side wall of the NW.

Here the analytical and finite element models are being developed in the framework of small deformations. This assumption is valid if the maximum radius of curvature ($R_{c\ max}$) of the bent beam satisfy $\alpha_{max} \geq 10L$ [237].

$$R_{c\,max} = \frac{Y.I_{xx}}{F.l} \geq 10.l \qquad \textit{Equation 37}$$

Where I_{xx} is the quadratic moment of the NW:

$$I_{xx} = I_{yy} = \int_{cercle} x^2 dr = \frac{\pi}{4} r^4 \qquad \textit{Equation 38}$$

For the chosen geometry, we determine the maximum amplitude of the applied force as:

$$F_{max} = \frac{Y.I_{xx}}{10.l^2} \qquad \textit{Equation 39}$$

The maximum amplitude of the force respecting the small strain assumption for NWs with length of 600nm and radius of 25nm is then F=10nN for ZnO and F=25nN for GaN. These forces are very low and so a study of the nonlinear case under high forces will be necessary (III.1.1.). But first we will keep the small deformation assumption and the linear mechanics for benchmarking with the literature. The material considered for the NW is ZnO. We used the values of the electromechanical and piezoelectric properties given by the COMSOL software library for bulk piezoelectric ZnO material.

II.4.1.2. Analytical calculation

Mechanical and electrical parameters of the problem are governed by four equations: the mechanical equilibrium equation, the equation of geometric compatibility, the constitutive equations of piezoelectricity and the Gauss equation [59]. The first two equations are purely mechanical equations whose solution determines the stress tensor T. In case we neglect the action of volume forces, the equation of mechanical equilibrium is:

$$\nabla T = 0 \qquad \textit{Equation 40}$$

As for the equation of geometrical compatibility it ensures that the strain tensor S derives a displacement field by imposing geometric constraints on S [238].

$$\frac{\partial^2 S_{ik}}{\partial x_j \partial x_l} + \frac{\partial^2 S_{jl}}{\partial x_i \partial x_k} - \frac{\partial^2 S_{jk}}{\partial x_i \partial x_l} - \frac{\partial^2 S_{il}}{\partial x_j \partial x_k} = 0 \qquad \textit{Equation 41}$$

where I, j, k and l are tensor index. The piezoelectric constitutive equations are (I.4.2.4.):

$$\begin{aligned} T_p &= c_{pq}.S_q - e_{kp}{}^t.E_k \\ D_i &= e_{iq}.S_q - \varepsilon_{ik}.E_k \end{aligned} \qquad \textit{Equation 42}$$

Finally, taking into account the presence of a free charge density ρ_e, the Gauss equation links the divergence of the electric displacement D_i to the charge density. But as a first approach we consider that there are no free charges in the ZnO undoped NW. This is equivalent to say that it behaves like a dielectric rather than a semiconductor. Thus we have:

$$\nabla . D_i = \rho_e = 0 \qquad \textit{Equation 43}$$

To facilitate the search for an analytical solution, we make two important assumptions. First, we use the simplified piezoelectric equations by applying the perturbation theory to (Equation 42). Thus it is possible to rewrite the piezoelectric equations for different orders of approximation [210]. We used the first order which takes into account the direct piezoelectric effect. The reverse effect of E on T is neglected. Thus the piezoelectric equations become:

$$\begin{aligned} T_p &= c_{pq}.S_q \\ D_i &= e_{iq}.S_q - \varepsilon_{ik}.E_k \end{aligned} \qquad \textit{Equation 44}$$

The first term is simply Hooke's law. S and T are linked only by the elastic properties of the material. Again, in order to facilitate the calculations, the second assumption is that the stiffness tensor is isotropic, which is realistic given the low anisotropy of ZnO. The stiffness matrix is:

$$s_{pq} = \begin{bmatrix} \frac{1}{c_{11}} & \frac{-\nu}{c_{12}} & \frac{-\nu}{c_{13}} & & & \\ \frac{-\nu}{c_{12}} & \frac{1}{c_{11}} & \frac{-\nu}{c_{13}} & & & \\ \frac{-\nu}{c_{13}} & \frac{-\nu}{c_{13}} & \frac{1}{c_{33}} & & & \\ & & & \frac{2(1+\nu)}{c_{44}} & & \\ & & & & \frac{2(1+\nu)}{c_{44}} & \\ & & & & & \frac{2(1+\nu)}{c_{66}} \end{bmatrix} \qquad \textit{Equation 45}$$

To determine the stress T, it is necessary to define the physical framework of the mechanical problem. We are assuming small deformations, the beam sections are therefore parallel. The beam model used is selected according to the form factor $\alpha=l/d$ of the NW. In our case the ZnO NW has a high form factor ($\alpha \geq 10$) which allows us to use the beam model of Euler-Bernoulli. If $\alpha \leq 10$, we cannot neglect the rotational inertia of the beam sections. It is then necessary to use other approaches such as the Timoshenko beam model. Mechanical stresses occur in the NW as a result of external mechanical forces applied to it. These are of two kinds: the bending force F_y which is applied to the surface of the free end and the binding reaction that appears at the clamped boundary edge of the beam (Figure 27). At the free end of the NW, the bending moment is zero, only the force applied is present. At the

clamped side (supposed as perfect), no displacement of the beam is possible. A force and a moment appear as a reaction to the force exerted on the free end. Thus the mechanical load tensor τ_i at the extremities of the NW is (Table 10).

Table 10 Stress tensor (a) at the free end of the NW and (b) at the clamped boundary of the NW.

(a)

$$\tau_{free\ end} = \begin{bmatrix} T_{xx} \\ T_{yy} \\ T_{zz} \\ T_{yz} \\ T_{xz} \\ T_{xy} \end{bmatrix} = \begin{bmatrix} 0 \\ F \\ 0 \\ 0 \\ 0 \\ 0 \end{bmatrix}$$

(b)

$$\tau_{clamped\ end} = \begin{bmatrix} T_{xx} \\ T_{yy} \\ T_{zz} \\ T_{yz} \\ T_{xz} \\ T_{xy} \end{bmatrix} = \begin{bmatrix} 0 \\ -F \\ 0 \\ -Fl \\ 0 \\ 0 \end{bmatrix}$$

In the general framework of a clamped beam, it has been shown that internal efforts depend only on the constraints T_{zz}, T_{yz} and T_{XZ} [239]. Thus, applying the empirical principle of Saint-Venant [240] to a clamped beam in flexion [241] and respecting the geometric compatibility equation, the internal stress tensor generated in the NW is of the following form [210], [235].

$$T_p = \begin{bmatrix} T_{xx} \\ T_{yy} \\ T_{zz} \\ T_{yz} \\ T_{xz} \\ T_{xy} \end{bmatrix} = \begin{bmatrix} 0 \\ 0 \\ -\frac{f_y}{I_{xx}}\, y(l-z) \\ \frac{F_y}{I_{xx}}\, \frac{3+2\upsilon}{8(1+\upsilon)} \left[r^2 - y^2 - \frac{1-2\upsilon}{3+2\upsilon} x^2 \right] \\ -\frac{F_y}{4I_{xx}}\, \frac{1+2\upsilon}{1+\upsilon} xy \\ 0 \end{bmatrix} \qquad \textit{Equation 46}$$

Then, following the Hook's law, the strain induced is:

$$S_q = s_{pq}.T_p \qquad \textit{Equation 47}$$

$$S_q = \begin{bmatrix} S_{xx} \\ S_{yy} \\ S_{zz} \\ 2S_{yz} \\ 2S_{zx} \\ 2S_{xy} \end{bmatrix} = \begin{bmatrix} \frac{\nu.F_y}{c_{13}.I_{xx}}\, y(l-z) \\ \frac{\nu.F_y}{c_{13}.I_{xx}}\, y(l-z) \\ -\frac{F_y}{c_{33}.I_{xx}}\, y(l-z) \\ \frac{F_y}{c_{44}.I_{xx}}\, \frac{3+2\upsilon}{4} \left[r^2 - y^2 - \frac{1-2\upsilon}{3+2\upsilon} x^2 \right] \\ -\frac{F_y}{c_{44}.I_{xx}}\, \frac{1+2\upsilon}{2} xy \\ 0 \end{bmatrix} \qquad \textit{Equation 48}$$

Equation 43 and Equation 44 give the direct piezoelectric phenomenon at the order 1. Thus the remnant electric displacement D^R is:

$$D_i^R = e_{iq}\,.S_q \qquad \textit{Equation 49}$$

From this equation, the three components of the remnant electric displacement are:

$$D_i^R = \begin{bmatrix} D_x \\ D_y \\ D_z \end{bmatrix} = \begin{bmatrix} e_{15}.2S_{zx} \\ e_{15}.2S_{yz} \\ 2.e_{31}.S_{xx} - e_{33}.S_{zz} \end{bmatrix} = \begin{bmatrix} -\frac{e_{15}.F_y}{c_{44}.I_{xx}}\left(\frac{1+2\upsilon}{2}\right)xy \\ \frac{e_{15}.F_y}{c_{44}.I_{xx}}\left(\frac{3+2\upsilon}{4}\right)\left(r^2 - y^2 - \frac{1-2\upsilon}{3+2\upsilon}x^2\right) \\ \frac{F_y}{I_{xx}}\left(\frac{2\upsilon e_{31}}{c_{13}} - \frac{e_{33}}{c_{33}}\right)y(l-z) \end{bmatrix} \qquad \textit{Equation 50}$$

From the remnant electric displacement we can derive the equivalent piezoelectric charge density ρ^R which is:

$$-\nabla.D^R = \rho^R \qquad \textit{Equation 51}$$

Thus the remnant charge density is:

$$\rho^R = -\nabla.D^R = \frac{\partial\overrightarrow{D^R}_x}{\partial x} + \frac{\partial\overrightarrow{D^R}_y}{\partial y} + \frac{\partial\overrightarrow{D^R}_z}{\partial z} = \frac{F_y}{I_{xx}}\left[2(1+\upsilon)\frac{e_{15}}{c_{44}} + 2\upsilon\frac{e_{31}}{c_{13}} - \frac{e_{33}}{c_{33}}\right]y \qquad \textit{Equation 52}$$

Recall that at the order 1, the electric displacement D_i in the NW is zero because the material is considered as a dielectric material with a density of free charges equal to zero. So we have the following equalities:

$$\nabla D_i = \nabla(e_{iq}.S_q + \varepsilon_{ik}^S.E_k) = \nabla(D_i^R + \varepsilon_{ik}^S.E_k) = 0 \qquad \textit{Equation 53}$$

It should be noted that it is the divergence of D^R rather than D^R itself that induces E. If we simply assume $\varepsilon.E=-D^R$, we would arrive at an absurd electric field with non-zero curl. Instead we can use the remnant equivalent piezoelectric charge ρ^R. Equation 53 will be transformed into an elementary electrostatic problem with the Poisson equation

$$-\nabla D_i^R = \rho^R = \nabla.(\varepsilon_{ik}^S.E_k) \qquad \textit{Equation 54}$$

It is very important to note that, in Equation 52, the remnant charge is independent of the vertical height z. Therefore, the electric potential is also independent of z. Physically it implies that the potential is uniform along the z direction except for regions very close to the ends of the NW. This means that the NW is approximately like a "parallel plate capacitor". The details of the calculation of the potential can be found in [210] in polar coordinates (r,θ) and using r_{NW} as the NW radius. They showed that the piezoelectric potential generated is:

$$V = \frac{F_y}{8.I_{xx}.\varepsilon_{r11}}\left(2(1+\upsilon)\frac{e_{15}}{c_{44}} + 2\upsilon\frac{e_{31}}{c_{13}} - \frac{e_{33}}{c_{33}}\right)\left(\frac{\varepsilon_0+3\varepsilon_{r11}}{\varepsilon_0+\varepsilon_{r11}}.\frac{r}{r_{NW}} - \frac{r^3}{{r_{NW}}^3}\right){r_{NW}}^3\sin(\theta) \quad (r < r_{NW}) \quad \textit{Equation 55}$$

$$V = \frac{F_y}{8.I_{xx}.\varepsilon_{r11}}\left(2(1+\upsilon)\frac{e_{15}}{c_{44}} + 2\upsilon\frac{e_{31}}{c_{13}} - \frac{e_{33}}{c_{33}}\right)\left(\frac{2\varepsilon_{r11}}{\varepsilon_0+\varepsilon_{r11}}.\frac{r_{NW}}{r}\right){r_{NW}}^3\sin(\theta) \quad (r \geq r_{NW}) \quad \textit{Equation 56}$$

Thus we can deduce from the piezoelectric potential equation that the maximum potential occurs at $r=r_{NW}$ and $\theta=90$.

$$V_{max} = \pm\frac{1}{\pi}.\frac{F_y}{\varepsilon_0+\varepsilon_{r11}}\left(2(1+\upsilon)\frac{e_{15}}{c_{44}} + 2\upsilon\frac{e_{31}}{c_{13}} - \frac{e_{33}}{c_{33}}\right)\frac{1}{r_{NW}} \quad (r = r_{NW}) \qquad \textit{Equation 57}$$

Equation 57 shows that, for a given applied force, the piezoelectric potential generated by a piezoelectric NW is inversely proportional to its radius and independent of its length. In linear mechanics, if we consider an anisotropic material having a Young's modulus Y, the maximum deflection of a clamped beam is connected to the force applied at the free end by the following relationship:

$$\delta_{max} = \frac{F_y . l^3}{3 . Y . I_{xx}} \qquad \textit{Equation 58}$$

Thus the maximum piezoelectric potential as a function of maximum deflection is:

$$V_{max} = \pm \frac{3}{4(\varepsilon_0 + \varepsilon_{r11})} \left(2(1+\upsilon) \frac{e_{15}}{c_{44}} + 2\upsilon \frac{e_{31}}{c_{13}} - \frac{e_{33}}{c_{33}} \right) \frac{{r_{NW}}^3}{l^3} \times \delta_{max} \qquad \textit{Equation 59}$$

In this case, at constant strain, the maximum piezoelectric potential is proportional to the cube of the aspect ratio a/L of the NW.

By studying the analytical solution of our problem, we can note that the electric potential is directly related to the size of the NW (radius and length). In the case of a NW of length l=600nm and radius r_{NW}=25nm undergoing a lateral force of 80nN, the analytical solution gives the following characteristic values: a maximum tensile stress of 3.91GPa, a deflection of 145nm of the NW corresponding to a maximum strain of 3% and a maximum value of the piezoelectric potential of 0.28V. These results are in agreement with the theoretical values found in the literature [47], [210]. Subsequently they will then be compared with the results of finite element simulation in the next section.

II.4.1.3. Finite Element Method simulation

To simulate the deformation of a piezoelectric NW we used COMSOL which is a Finite Element Method simulation software for solving common physical problems but also able to combine several domain of physics (multiphysics). There are four main steps before to simulate a problem: the choice of the geometry, materials selection, the physics and the boundary conditions, and finally the meshing of the structure. The study being in static mode, we worked in stationary regime.

The choice of the geometry strongly influences the simulation and must be close to the real geometry. COMSOL allows to model geometries from simple elements, but the software also allows to import more complex geometries from CAD software. The landmark chosen for modeling the NW is a 3D Cartesian coordinate system and the selected unit is the nanometer. As described in the previous section, the NW is treated as a cylinder and a border is defined on top of the NW in order to apply a force. The dimensions are the same as those used for the analytical calculation: 600nm in length and 25nm in radius (Figure 28).

Concerning the material selection, COMSOL has a large library of materials, but it is also possible to manually enter a new material with specific properties. For our simulations we used the bulk piezoelectric ZnO from the COMSOL's library to simulate the ZnO NW as a first approximation.

We have to choose the physics depending on the study needed. COMSOL proposes the main equations governing the general physics, but it is also possible to modify these equations and even add new ones. The studies were conducted using only the MEMS module of COMSOL. This module contains multiple physics including mechanical and electrical physics which are coupled in a sub-module of piezoelectricity. This sub-module of piezoelectricity is suitable for solving our problem. It is important to remember that the semiconducting properties of ZnO NW are reflected through its permittivity but in the model ZnO is described as a dielectric because the physics of semiconductors is not directly taken into account by the electrical module of COMSOL. We also specify in the software that we work in the linear regime and use the constitutive equation of piezoelectricity (Figure 6). It is also during this step that the boundary conditions of our system must be defined. These boundary conditions will be used by the software to calculate and converge to a solution to the problem. This calculation is performed by solving partial differential equations in a discrete manner. This step is the

most important, because each boundary condition ensures the existence and uniqueness of a solution. There are several boundary conditions in our problem:

- The density of free charges in the NW is considered as zero.

$$\nabla . D = \rho_e = 0 \qquad \textit{Equation 60}$$

- The side walls of the NW are considered as free to move
- The mechanical strain is fixed at the root of the NW. The goal is to cancel all degrees of freedom of the surface at the root of the NW, it is called fixed constraint or clamped.

$$\delta = 0 \qquad \textit{Equation 61}$$

- The potential is zero at the root of the NW. The electrical boundary condition is intended to give a reference value to the potential.

$$V = 0 \qquad \textit{Equation 62}$$

- The bending force is applied on the upper portion of the NW in the y direction. To keep the simulation comparable with the literature I will first consider a high lateral force of 80nN which is superior to the limit of the linear mechanical behavior (Equation 39). However I will first consider a linear physics and then I will address the non-linear case.

$$F_y = 80nN \qquad \textit{Equation 63}$$

The finite element method is based on a division of the space using a mesh. It is not necessary to use regular mesh and it is important to refine the mesh where parameters are expected to show large spatial variation (Figure 28). The more the mesh is fine the more the solution obtained by the finite element method is accurate and close to the "real" solution to the equations. However, the calculations could become longer and consume more PC memory. Special care must be taken, a not adapted mesh can create artifacts in the solution. For our structure we chose a tetrahedral mesh (Figure 28) with a 12nm maximum height and 10pm minimum height.

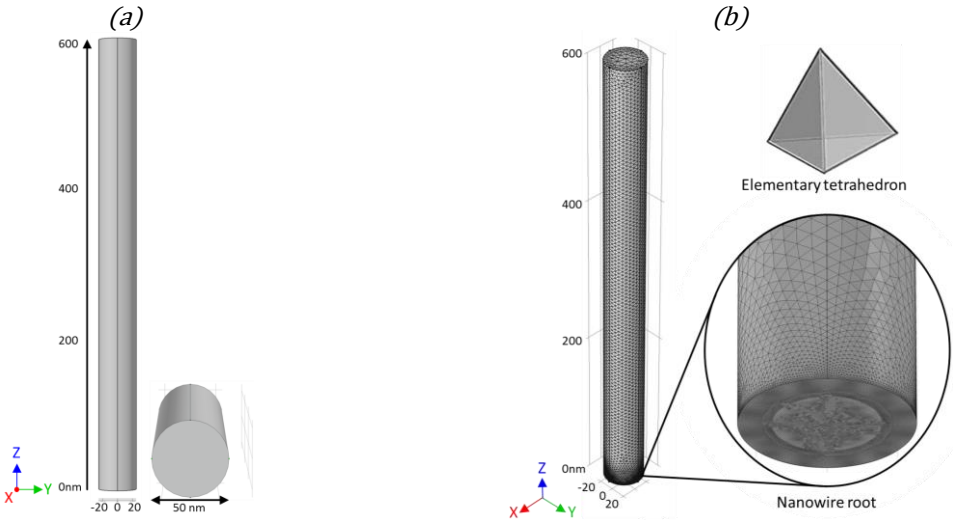

Figure 28 (a) Geometry of the ZnO NW used as a reference for the analytical calculation (l=600nm and r=25nm). (b) NW meshes containing 276 656 tetrahedrons with a mesh refinement at the root.

The simulation of a bended ZnO NW shows that the material stress is mainly concentrated at the base of the NW and distributed in an anti-symmetric way relative to the neutral section of the NW. The stress is mainly oriented along the z axis (T_z component Figure 29a). The lower part at the left undergoes traction (T_{max}=4.09GPa at 2nm from the NW base) and the lower part at the right undergoes compression (T_{min}=-4.11GPa at 2nm from the NW base). As suggested by the distribution of efforts

discussed above, the critical section is located at the clamped level where the stress is maximal. However, the analytical stress T is valid only away from the sections loaded, and the value of the stress calculated analytically is lower than the simulated value of the stress. Along the NW, the stress T_z decreases gradually as one move away from the anchor point of the NW (Figure 29a). However, we note a small anomaly at the anchor point due to the mesh size and where the stress seems to decrease locally. The distribution of the strain in the NW (Figure 29b) is similar to that of the stress and it deform of the NW (Figure 29c and d). Deformation occurs mainly near the anchor point of the NW, this part is strongly curved whereas the free end of the NW is straighter and suffers few constraints. Finally the maximum deflection of the NW ~130nm is considerable when compared to the NW length (l=600nm).

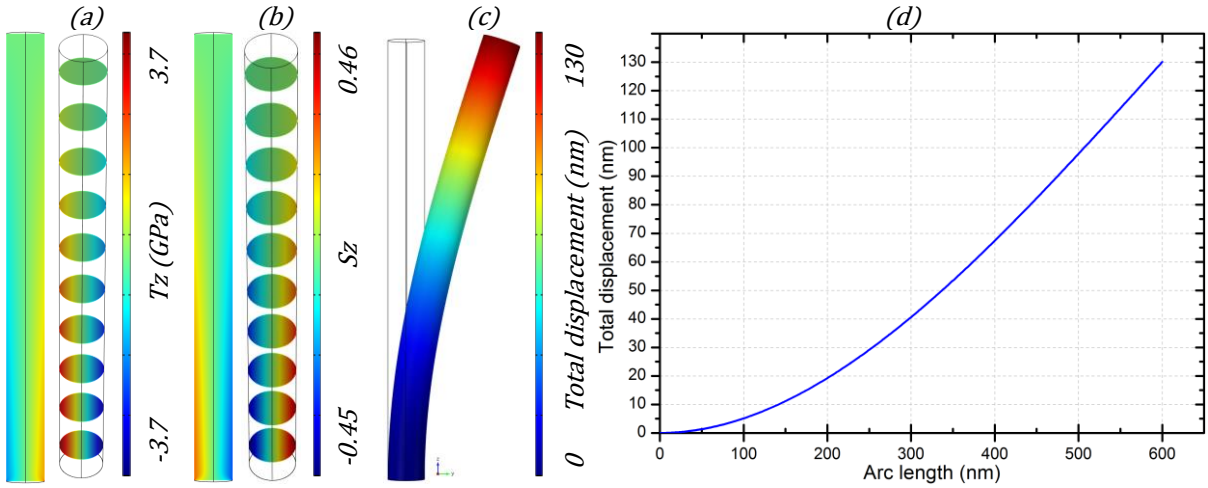

Figure 29 FEM simulation of a ZnO NW under bending. Z component of the mechanical (a) stress T_z and (b) strain, (c) total mechanical displacement and (d) Total mechanical displacement as function of the Z axis.

As mentioned before, the stress is mainly concentrated at the base of the NW. The charges of the piezoelectric NW will so come to accumulate where the constraints are present, which explains the electric displacement profile obtained inside the NW (Figure 30a). Indeed, in the equation of piezoelectricity, the electric displacement is directly related to stress. The result is a zero electric displacement along the neutral axis of the NW, and the latter increases as it approaches the lower sides of the NW. Thus, as for the stress, the maximum value of the electric displacement is located on the lower left and right sides of the NW (D_{max}=0.045C.m^{-2}). We note however that the electric displacement distribution in the X and Y components (Figure 30b and c) are negligible compared to the electric displacement in Z. Then, it generates the electric field represented in Figure 30d.

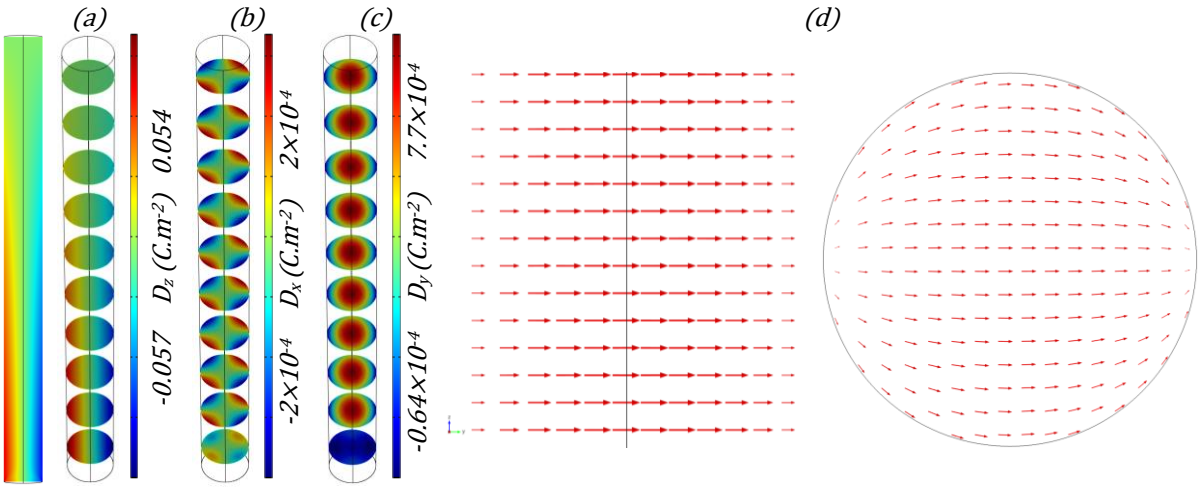

Figure 30 FEM simulation of a ZnO NW under bending. (a) Z component of the electrical displacement, (b) X component of the electrical displacement, (c) Y component of the electrical displacement and (d) electric field distribution in the YZ and XY middle planes.

Figure 31a shows the 3D pizoelectric potential distribution in the NW. We obtain equipotential surfaces along the side of the NW as predicted by the analytical model. On the central longitudinal section of the NW (Figure 31b) we observe an equipotential vertical distribution except at the ends of the structure. Indeed, on the curves representing the evolution of the electric potential along the NW's flanks in extension and in compression (Figure 31c) we see that near the free extremity of the NW (area where the force is applied), the amplitude of the potential is a little higher. Similarly, we note at the base a strong reversal of the electrical potential on an area of about 50nm. These observations are consistent with the finite element simulations of [47], [210].

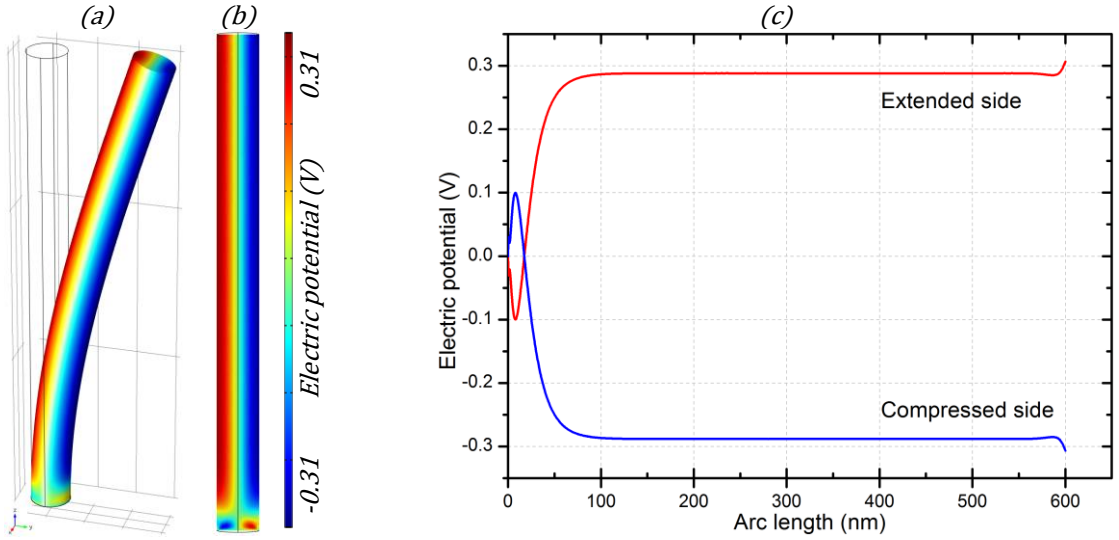

Figure 31 (a) 3D electrical potential distribution of a piezoelectric NW (l=600nm et d=50nm) under lateral bending force (F_y=80nN), (b) YZ cut view of the electric potential distribution and (c) evolution of the electric potential along the extended and retracted side walls of the NW as function of the Z axis.

In the central part of the NW, the electric potential generated is invariant along the z axis and anti-symmetric along the y axis (Figure 32). The potential varies almost linearly close to the neutral axis, then sharply decrease, which is consistent with the Equation 55 of the electric potential (r/r_{NW} - r^3/r_{NW}^3). The electric potential is uniform along the NW and equal to 289mV on the extended side and -289mV on the compressed side. Its distribution is somewhat similar to that of a plane capacitor.

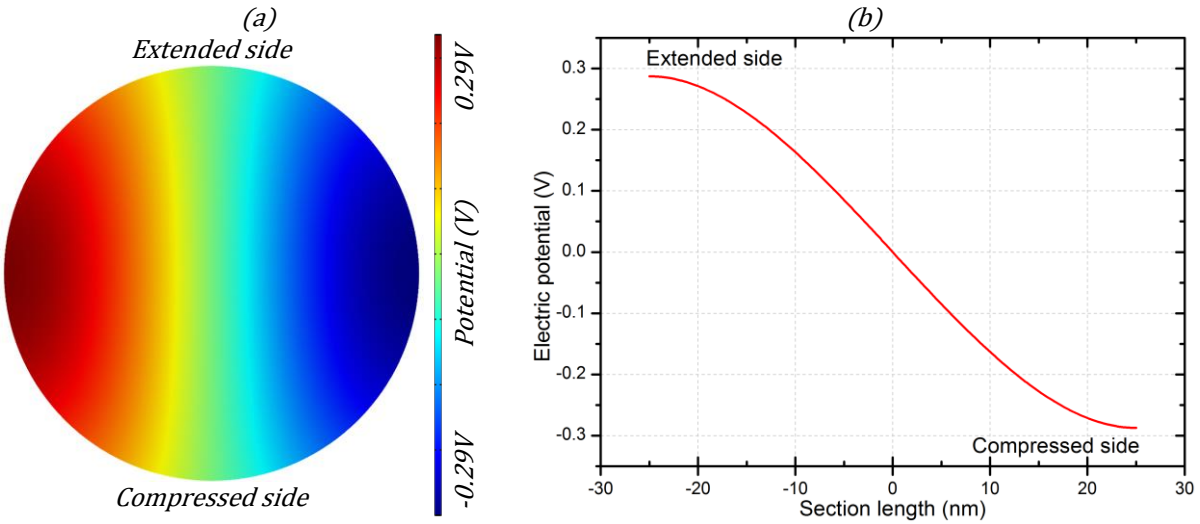

Figure 32 (a) XY middle cut view of the potential distribution of a piezoelectric NW (l=600nm and d=50nm) under lateral bending force (F_y=80nN). (b) Evolution of the electric potential across the middle of the NW as function of the Y axis.

II.4.1.4. Validity and accuracy of the potential profile

Similar FEM simulation have been addressed in the literature [47], [193], [210]. They show that for a similar ZnO NW (50nm of diameter and 600nm of length) similar results are obtained: under 80nN such NW generates a difference of piezoelectric potential around 0.6V and 0.8V (without neglecting the indentation phenomenon of the applied force) which is in the range of our results. The distribution of the potential is also similar with strong reversal at the NW base. In addition the analytical model of a bend piezoelectric NW is discussed and it shows that even restricting the piezoelectric equations to the first order and neglecting the reverse piezoelectric effect, the difference of potential between the analytical model and the FEM simulation, taking into account the full coupling of the piezoelectric equations, is smaller than 6% which is a very good result. Thus it confirms the validity of the model used and justifies the neglect of reverse piezoelectric effect for simple analytical calculations.

In order to fully understand the distribution of the piezoelectric potential generated by a bending force applied at the free end of a NW, it is important to note that the analytical formulation of the stress (T) is based on three simplifying assumptions:

- ZnO is considered as equivalent to an isotropic material.
- the reverse piezoelectric effect is not taken into account.
- T is determined using the principle of Saint-Venant [240].

The assumption of isotropy of the ZnO NW has in principle little influence on the results because ZnO is hardly anisotropic. The second hypothesis has some effect against the value of the generated piezoelectric potential. Analytical calculations do not take into account the reverse piezoelectric effect while the FEM simulation takes it into account. Therefore a portion of the difference in the piezoelectric potential generated between the analytical calculation and the FEM simulation is due to this aspect. Finally a small mesh can have an effect on the exact value of the piezoelectric potential generated, especially close to the base of the NW where the 3D distribution of the strain and the electric potential is complex. Therefore we used a fine mesh on the NW and a refined one at its base (Figure 28b) to get accurate and reliable results of the piezoelectric potential distribution. Table 11 compares these results with those in the literature.

Table 11 Comparison of the results of analytical calculation, FEM simulation and references of the bending model of a ZnO piezoelectric NW of 600nm length and 50nm diameter bended by a lateral force of 80nN. The maximum stress and strain have been taken 2nm from the NW base to avoid any boundary effect.

	Maximum stress	*Maximum strain*	*Maximum displacement*	*Maximum potential*
Analytical calculation	*3,91GPa*	*3 %*	*145nm*	*280mV*
FEM simulation	*4.09 GPa*	*3 %*	*130nm*	*290mV*
Georgia Tech [210]	-	-	*145nm*	*268mV*
Max Planck Inst [47]	-	-	*133nm*	*300mV*

In general our results are fairly close to the literature which can be explained by the fact that we use the same theories and simulation tools. Note that the spread between our values extracted from analytical calculations and FEM simulation are very close (error smaller than 3.6%). This error is mainly due to the simplification at the order 1 of the piezoelectric equations in the analytical model. Indeed, Professor Wang's group study [210] shows that on average the simplification at the order 1 induces an error on the analytical calculation lower than 6% compared to a fully coupled piezoelectric system . In our case this error is 3.6%.

Finally the difference of the piezoelectric potential at the ends of the NW has still not be clearly explained. The increase in potential at the free end of the NW can be explained by the effect of the local stress created by the force applied on this region. This phenomenon was not considered in the analytical expression of the internal stress in the NW because we used a general term whereas this effect is a phenomenon of local deformation of matter. Instinctively, it is understood that the local stress is a little stronger in the place where the force is applied than in the rest of the NW. But the strong inverted piezoelectric potential at the root of the NW is more surprising. Indeed, this reversal of the piezoelectric potential at the NW's root is not predicted by the analytical model. This is due to the fact that we have determined the stress T with the principle of Saint-Venant. However, it is important to note that the principle of Saint-Venant states that the form of T is valid away from areas of application of external mechanical stresses [59]. That is to say not close to the free end where the force F_y neither near the NW clamp where it undergoes a reaction which is composed of a force and a moment. In practice, this approximation is valid in remote zones far from the loaded sections up to 2 or 3 diameters [239] that is to say at 100nm from the clamp and the free end. Therefore it is normal that our model of the stress in the NW does not show this strong inversion. But it can be explained by carefully observing the forces experienced by the NW. The stress tensor at the extremities of the NW (Table 10) shows that the reaction force R_y at the base is opposite to that applied at the free end, which is at the origin of the inversion of the piezoelectric potential. In addition, the torque induced M_{yz} further increases the stress in this area. The study of the components Y (Figure 33a) and YZ (Figure 33b) of the stress in the NW shows that it is mainly concentrated in a 20 to 30nm high region at the base of the NW. The simulation of the same piezoelectric NW using two fixed constraint points and a roller area (slipping contact, without shear forces) as bottom boundary conditions instead of a fixed constraint surface boundary condition shows that the absence of reaction forces at the root of the NW (Figure 33c) lead to a distribution of the piezoelectric potential without inversion at the root (Figure 33d). However, this would rather concern the simulation of NW grown on a stretchable substrate for instance.

To conclude, the shear effect at the clamped end of the NW is causing the piezoelectric potential inversion at the NW root. In this area, potential is larger than in the rest of the NW due to the high stress induced. However, this potential inversion cannot fully develop at the root of the NW because of the ground boundary condition imposed on the clamped surface and which represents a grounded substrate. The use of an insulating or poorly conductive substrate has a huge impact on the inversion of potential that will be discussed in III.1.3. .

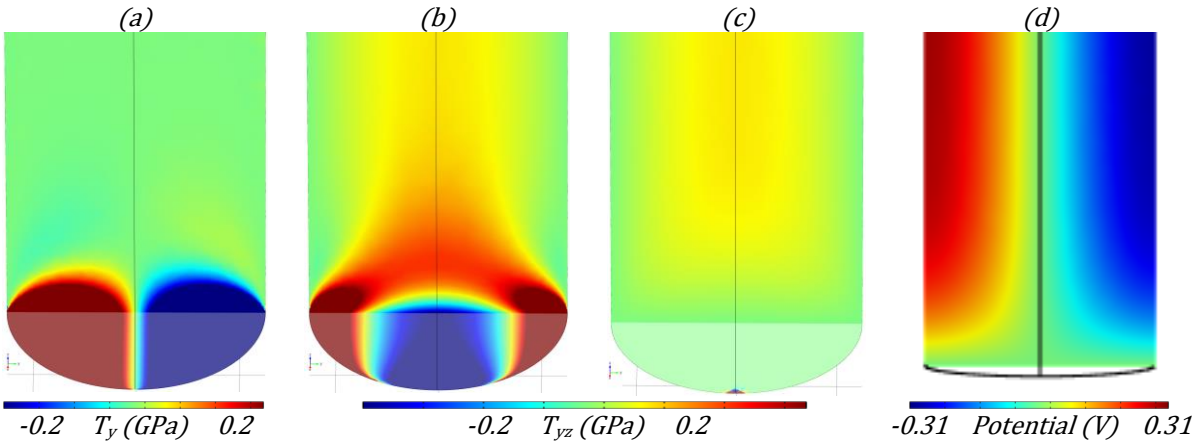

Figure 33 (a) Y component of the stress tensor at the root of a NW using a surface fixed constraint boundary condition. (b) YZ component of the stress tensor at the root of a NW using a surface fixed constraint boundary condition and (c) using a two point fixed constraint with surface roller boundary condition. (d) Electrical potential at the root of a NW fixed using a two point fixed constraint with surface roller boundary condition.

II.4.2. Scaling rules of ZnO NW

Now that we modeled the bending behavior of a piezoelectric NW using FEM simulation, it is possible to determine the influence of the morphology of the NW on the value of the electrical potential generated. Several parameters will be evaluated as the length, the radius and therefore the aspect ratio of the NW.

First, we note that the larger the radius of the NW is, the lower is the electrical potential generated on the sidewalls (Figure 34a). The curve of the maximum electric potential as a function of the radius, expressed as a logarithm (Figure 34b) decreases linearly. Therefore the variation law of the electrical potential as function of the NW radius follows an equation of the type 1/r, the potential is inversely proportional to the radius which is consistent with Equation 56.

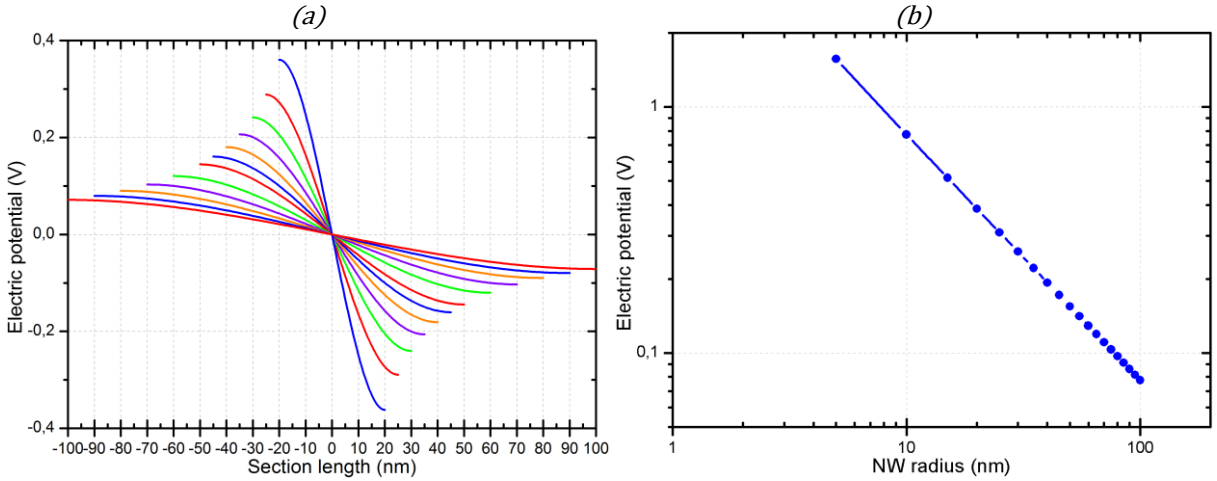

Figure 34 FEM simulation of the evolution of the electrical potential generated by a clamped piezoelectric NW (r=25nm, l=600nm) bended by a lateral force of F=80nN applied at its free end as function of the NW radius. (a) Potential profile along the y axis at the middle of the NW at z=300nm and (b) logarithm of the maximum positive potential on the extended side of the NW.

In contrast, we note that the length of the NW does not affect the electrical potential generated in the NW (Figure 35). Indeed if the NW is longer, then it is easier to bend and so the deformation should increase. But as it is longer, the deformation is distributed over a greater length and so the strain and the potential finally remain the same.

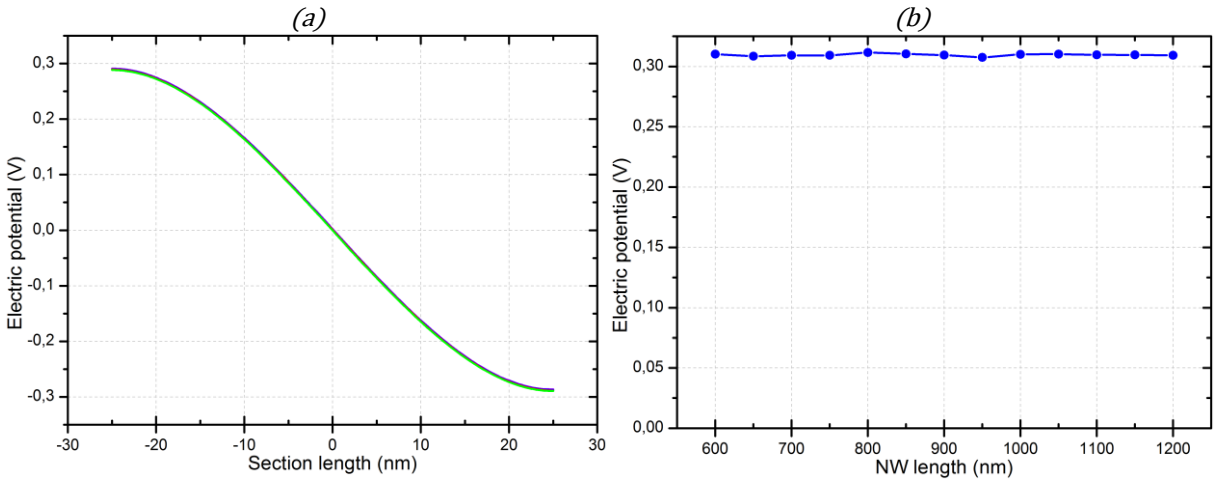

Figure 35 FEM simulation of the evolution of the electric potential generated by a clamped piezoelectric NW (r=25nm, L=600nm) bended by a lateral force 80nN applied at its free end as function of the NW length. (a) Potential along the y axis at z=300nm and (b) maximum of positive potential on the extended side of the NW.

Finally, the evolution of the electric potential as a function of the applied force is linear (Figure 36a). The potential is proportional to the force applied. This was provided by the study previously conducted. But keep in mind that this is only valid with the assumption of small deformation in the linear mechanics regime. In the case of an application of high forces and large displacement, these calculations and simulations are no longer valid and a non-linear mechanical model must be used. The influence of nonlinear phenomena can be large and so the result could be highly modified. That is why we have continued to study a valid non-linear model for large deformations in the next chapter (III.1.1.). This non-linear regime is necessary for realistic targeted applications.

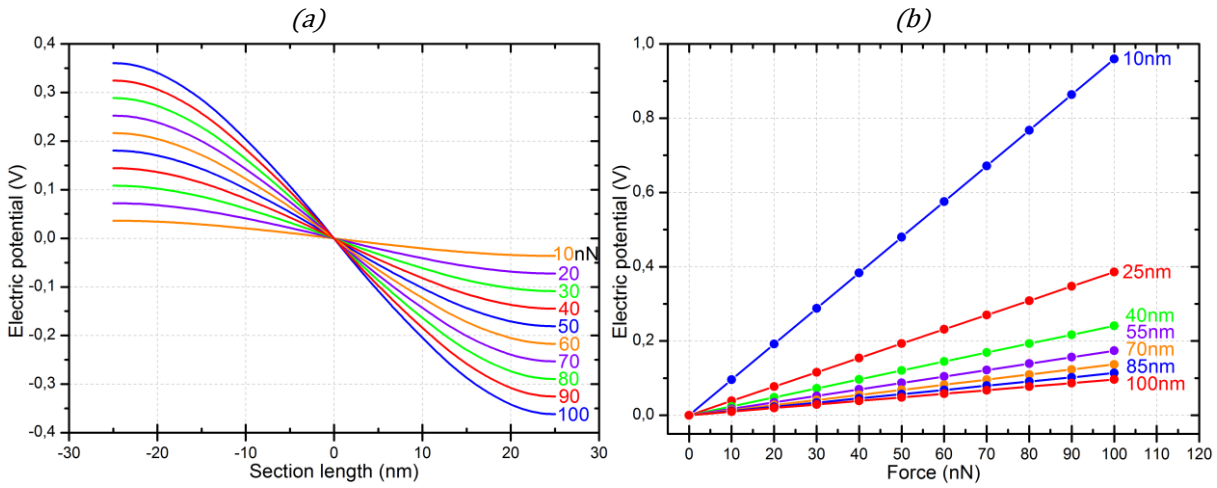

Figure 36 FEM simulation of the evolution of the (a) potential profile along the y axis at z=300nm and (b) maximum of positive potential on the extended side of a clamped piezoelectric NW (r=25nm, l=600nm) as a function of the NW radius, and bended by different lateral forces applied at its free end.

II.5. Near field characterization

II.5.1. Introduction to NW characterization

It exist a large panel of methods and equipment to characterize the physical properties of materials such as:

- SEM (scanning electron microscopy) and STEM (scanning transmission electron microscope) for the morphology characterization
- EDX (energy dispersion of X ray) and XPS (photoelectron spectroscopy) for the chemical composition characterization.
- XRD (diffraction of X ray) and the Raman spectroscopy for the structural characterization.
- UV-visible SP (spectrophotometry) and PL (photoluminescence) for the optical properties characterization.
- Photo current spectroscopy, the cathodoluminescence and the electroluminescence for the electro-optic characterization.
- Probe station and microelectronic chip for the electrical characterization
- MEMS and NEMS specific set-ups and structures for the electromechanical characterization [242], [243]

To characterize the electro-mechanical coupling properties of piezoelectric semiconducting NWs, the AFM seems an adapted and good characterization tool that can perform different kind of measurements such as topologic, electrical and mechanical characterization as well as piezoelectric characterization. The AFM is adapted for the sensing and actuation of nanostructures, it is versatile and convenient for small laboratories. For these reasons we firstly focused our study on the AFM characterization of piezoelectric semiconducting NWs.

The Atomic force microscopy (AFM) or scanning force microscopy (SFM) is a very high-resolution type of scanning probe microscopy. G. Binnig et al. invented the first AFM and reported its working principle in 1986 [244]. It is one of the foremost tools for imaging, measuring and manipulating matter at the nanoscale. It can measure the three dimensional topography as well as physical properties of a specimen surface by a sharpened probe to create an image with very high demonstrated resolution of fractions of a nanometer (0.1nm). This value is more than 1000 times better than the optical diffraction limit. Unlike traditional microscopes, AFM does not depend on electromagnetic radiation, such as photon or electron beams.

As shown on Figure 37, the AFM is composed of a micro-scale cantilever with a sharp tip (probe) at its free end that is used to scan the sample surface. Usually, strong and sharp tips made of silicon or silicon nitrides with a radius of curvature of several nanometers (typically 30nm) are used to scan the sample surface. When the tip approaches the sample and is close enough to the surface, the interaction between the tip and the sample lead to a deflection of the cantilever according to Hooke's law. The responsible force field consists of the mechanical contact force, the Van der Waals forces, capillary forces, chemical bonding, electrostatic forces, magnetic forces, the solvation forces etc. and vary with the sample surface. Typically, the cantilever deflection is measured by using a laser spot reflected from the cantilever's top surface into an array of position sensing photodiodes detectors. Other methods can be used such as optical interferometry, capacitive sensing or piezoresistive cantilevers. The scanner and the cantilever are driven using piezoelectric elements allowing accurate and precise movements. An image of the sample surface is then reconstructed by monitoring the precise motion of the probe as it is scanned over the surface. In some specific operation mode, electric potentials can be scanned

using conductive cantilevers and currents can be measured through the tip to probe the electrical conductivity or transport properties of nano objects for example.

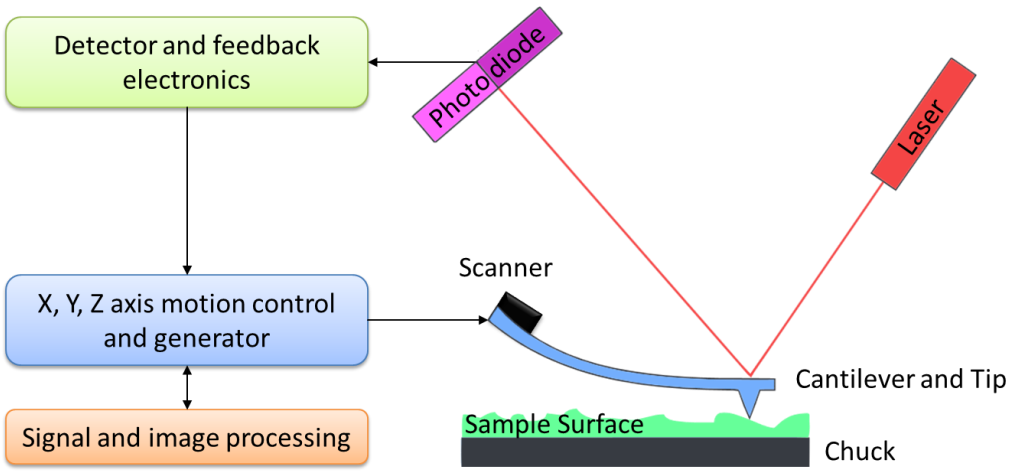

Figure 37 Block diagram of atomic force microscope using beam deflection detection. As the cantilever is displaced via its interaction with the surface, the reflection of the laser beam will be also displaced on the surface of the photodiode.

In our study we used two different systems. In IMEP-LAHC we used a Veeco (Bruker) Dimension 3100 commercial AFM system and nanoscope IV electronics with a three dimension closed-loop feedback configuration. This configuration is made up of three piezoelectric crystals, each responsible for scanning in the x, y and z axis. In professor Wang's group in Georgia Tech we used a MFP-3D AFM system from Asylum Research.

II.5.2. AFM characterization scanning using a tip on vertical NWs

The characterization of the electromechanical and piezoelectric properties of ZnO and GaN NWs using an AFM has been firstly investigated by the professor Wang's Group in Georgia Tech. They have scanned vertically grown ZnO NWs on a conductive substrate, using a Pt conductive AFM tip and they monitored the current and the potential generated by the NWs. This characterization method is based on the piezoelectric and semiconducting properties of ZnO NWs. In contact mode, a constant normal force of 5nN is maintained between the tip and sample surface. The tip scanned over the top of the ZnO NWs and the tip's height is adjusted according to the surface morphology and local contacting force. Then the output voltage across an external resistive load (R_L=500MΩ) is continuously monitored as the tip scans over the NWs.

Experimentally, both the topography image and the corresponding output voltage images across the load can be recorded simultaneously when the AFM tip is scanned over the NW arrays. Thus many sharp output peaks are observed where the potential peaks are 6mV, around 50 time higher than the noise level, and their positions correspond to NWs. They noted that the output voltage was negative and, by examining the topological profile of a NW and its corresponding output potential, they observed a delay for the voltage output signal, which means that there is no electric power output when the tip contact first the NW, but a sharp voltage peak is generated when the tip is leaving the NW. In addition they noted that the output voltage signal is proportional to the NW size. Following further investigation they also noted that the output signal is present only for piezoelectric NWs. No electrical output was recorded for tungsten oxide, silicon and metal NWs, neither for carbon nanotubes. Friction or contact potential did not seem to play a role in the observed output power. Finally, to generate electricity, the contact between the tip and the NW needed to be Schottky [245].

The Schottky contact between the AFM tip and ZnO NW is the key of this phenomenon which creates, accumulate and output charges through a NW.

The lateral force applied at the free end of the NW by the AFM tip scanning in contact mode bend the ZnO NWs similarly to the case of study of II.4.1. The bending force deflects the NW and generates a strain field with extended and compressed surfaces. As a result, a piezoelectric potential distribution is generated in the NW where the extended side exhibit a positive potential and the compressed side a negative one. The first step is a charge accumulation process, when the conductive AFM tip touches the extended surface of the NW (with positive potential), the Pt tip / ZnO NW Schottky junction is negatively biased. So the reverse biased Schottky diode bloc the current to flows across the interface and charges accumulate. The next step is the charge releasing process. When the AFM tip contacts the compressed side of the NW, the Pt tip / ZnO NW Schottky junction is positively biased. Thus the Schottky diode let the current flow and it produces a sudden increase in the output electric current. This current is the result of the junction potential difference driven flow of electrons from the semiconducting ZnO NW to the Pt tip. Then the flow of the free electrons from the loop through the NW to the tip will neutralize the charges distributed in the NW volume due to the piezoelectric effect and thus screen and reduce the magnitudes of the piezoelectric potential.

These experiences and their interpretation have been subject to debates and questions [47], [193]. But after further investigations and using different materials [245], NWs and doping [246] this phenomenon has been more precisely explained and developed [247]. Now it is accepted and applications based on it have been proved [248].

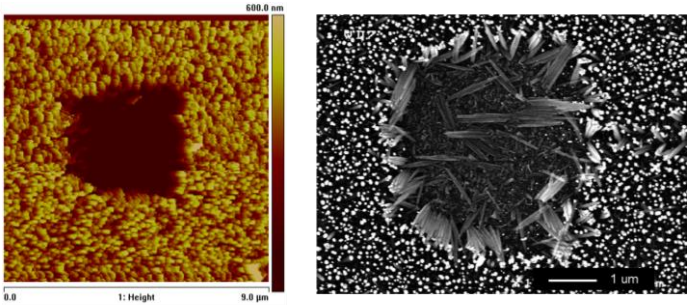

Figure 38 AFM and SEM top view image of a GaN NW array vertically scanned by an AFM when applying to much pressure on the NWs [249].

This method has been taken over and operated by several research groups. In a first time we used it to characterize GaN NW [249], but this characterization technique has many drawbacks: first it is difficult to control the applied force which makes it most often destructive or at least damaging (Figure 38). Secondly, it is very difficult to control the exact contact between the AFM tip and the NW. In fact, the applied force is imprecise and transitory what makes electromechanical and piezoelectric characterizations inaccurate. To remedy this lack of control and extend the characterization possibilities, in a previous Ph.D. Xin Xu from IMEP-LAHC laboratory proposed a significant improvement of this characterization method [1]. It consisted in cutting a sample of vertical NWs in two and tilt it at 90° to study NWs present on the edge. Thus it is possible to locate the NWs under the AFM. The horizontal arrangement of NWs under the AFM tip allows better control of the applied force and its position on the NWs in a stationary or dynamic mode which offers greater opportunities for AFM characterization.

II.5.3. AFM characterization using a lateral approach

AFM characterization methods of lateral beams [250] and lateral NWs [1] have been developed in the laboratory in order to improve the mechanical, electrical and piezoelectric characterization of such one-dimensional nano objects. That thanks to a thinner and better controlled AFM approaches of these nano objects, which is essential for their characterization and understanding.

II.5.3.1. Mechanical characterization

MEMS and NEMS have, as their name suggests, mechanical parts and systems. In order to better understand their operation, it is imperative to know their mechanical characteristics. With regard to piezoelectric NGs for example, it is important to characterize the mechanically active part of the system, that is to say the piezoelectric NWs. For this, two characterizations have been developed and realized.

- The calculation of the NW bending as function of the applied force.
- The calculation of the Young modulus of NWs.

a.Flexion of a NW

Firstly we studied the NW bending as function of the applied force. To proceed we considered the following setup:

- The NW has a hexagonal section with a diameter d and a length l.
- The NW is clamped at one extremity and free at the other one.
- We apply a lateral force on a small surface located along the NW (Figure 39a).

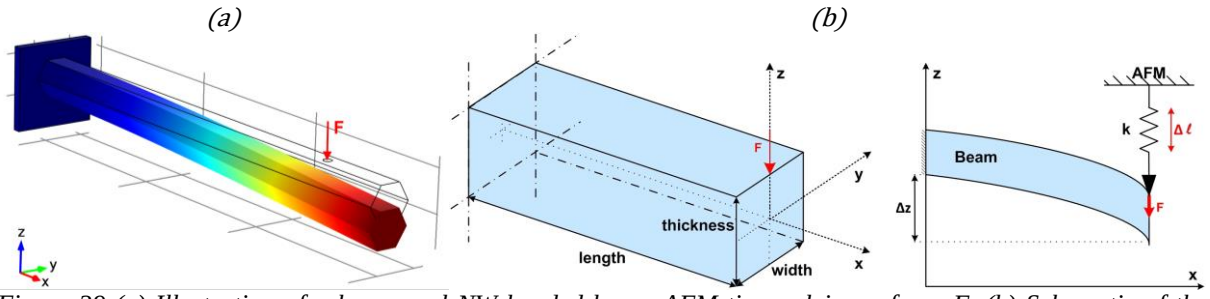

Figure 39 (a) Illustration of a hexagonal NW bended by an AFM tip applying a force F. (b) Schematic of the mechanical problem considered [250].

Considering the geometry of the problem, we calculated the deflection of the NW using the theory of beams and the Euler-Bernoulli equations. From these equations we have:

$$\frac{d^2}{dx^2}\left(Y.I_y.\frac{d^2u}{dx^2}\right) = F \qquad \textit{Equation 64}$$

where Y is the Young's modulus, u the position along the NW axis, I_y the moment of inertia of the NW and F the applied force.

considering the hexagonal structure of the wurtzite ZnO NW, the associated inertia moment I_y is:

$$I_y = \frac{5\sqrt{3}.a^4}{16} \qquad \textit{Equation 65}$$

where a is the hexagon edge.

then, using the following boundary conditions:

$$u|_{x=0} = 0\ ;\ \frac{\partial u}{\partial x}|_{x=0} = 0\ (fixe\ end) \qquad \textit{Equation 66}$$

$$\frac{\partial^2 u}{\partial x^2}|_{x=l} = 0\ ;\ \frac{\partial^3 u}{\partial x^3}|_{x=l} = 0\ (free\ end) \qquad \textit{Equation 67}$$

where L is the NW length.

we can solve the Equation 64 and express the NW flexion as function of the applied force:

$$\Delta z = F.\frac{(3.l.x^2 - x^3)}{6.Y.I_y} \qquad \textit{Equation 68}$$

where x is the distance from the NW root where the force is applied.

thus if we apply the force at the end of the NW we have:

$$\Delta z = \frac{F.l^3}{3.Y.I_z} \qquad \textit{Equation 69}$$

in addition we modeled the AFM cantilever by a spring (Figure 39b), and then extended our calculation to link the applied force F to the deflection of the AFM cantilever:

$$\Delta l_{AFM} = F_{AFM}/k_{AFM} \qquad \textit{Equation 70}$$

where Δl is the AFM cantilever deflection, F the force applied by the AFM and k the spring constant of the AFM cantilever.

Using an AFM, we can make approach-retract curves of the AFM tip on samples, NWs in this case. As a result, we obtain the graph of the position of the AFM tip as a function of the position of the AFM head. From this data we can calculate the deflection of the NWs and we can extract the NW Young's modulus. The methodology is described as follows:

- At first, we note the initial position of the AFM tip. It is a constant that we will use later to determine the relative change of the AFM tip position. We call this constant: Z_{tip_0}
- The displacement of the NW: (ΔZ_{NW}) relative to its original position is equal to:

$$\Delta Z_{nanowire} = Z_{Piezo} - \left(Z_{tip} - Z_{tip\_0}\right) \qquad \textit{Equation 71}$$

where Z_{piezo} is the displacement of the AFM head. We do not subtract the initial position of the piezoelectric AFM head because its position is relative and the AFM considers it equal to zero at the beginning of the approach-retract curve.

- Then knowing the AFM tip spring constant (using the AFM Thermaltune function for example) we calculate the force that the AFM tip applies on the NW: (F_{tip}).

$$F_{tip} = k_{tip} \times \left(Z_{tip} - Z_{tip\_0}\right) \qquad \textit{Equation 72}$$

where k_{tip} is the AFM tip spring constant.

- In this way we obtain the graph of the NW bending as function of the force applied by the AFM tip. At this level, the key parameter is the slope of the graph: k_{slope}

$$k_{slope} = \frac{F_{tip}}{\Delta Z_{nanowire}}\ or\ before\ \frac{F}{\Delta z} \qquad \textit{Equation 73}$$

If we apply the force at the free end of the NW we have:

$$k_{slope} = \frac{F_{tip}}{\Delta Z_{nanowire}} = \frac{3.Y.I_z}{l^3} \qquad \textit{Equation 74}$$

Thus we can extract the NW Young modulus:

$$Y = \frac{k_{slope}.l^3}{3.I_z} \qquad \textit{Equation 75}$$

However, what will happen if we do not apply the force at the free end of the NW? In fact in all cases we must consider that the length of the NW used in the calculation is the distance from the anchor to the applied force. And then we can extract the Young's modulus. This because when we measure the deflection of the NW with the AFM, we only measure the deflection were the AFM tip is located.

$$Y = \frac{k_{slope}.u^3}{3.I_z} \qquad \textit{Equation 76}$$

where u is the length from the NW anchor to the point of application of the force by the AFM along the NW.

b.Young's modulus measurement

To carry out a measurement of the Young's modulus of a horizontal NW as described above we used the following procedure: the samples are vertically mounted on the edge of an aluminum metal support using silver paste. Then the support is tilted at 90° in the AFM. Then we perform a topological image of the edge of the sample to identify NWs position. This step is quite difficult because of the configuration of the sample to be imaged which has a hard region (the substrate), thin and flexible NWs and air around. Once the topological image is obtained we realize approach-retract curves along the NWs or the other nano objects imaged (Figure 40a).

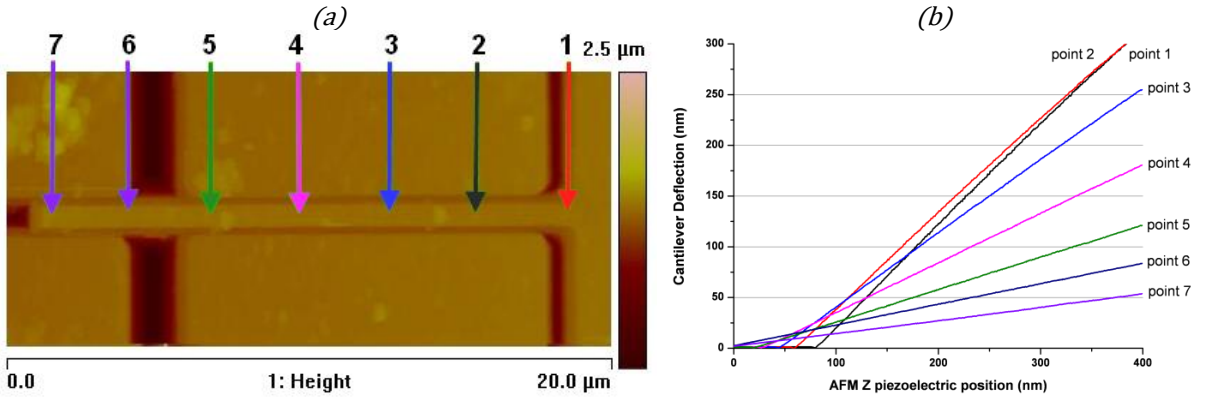

Figure 40 (a) AFM image of a nanoswitch with the AFM tip position where approach-retract curves have been performed. (b) AFM approach-retract curves preformed on points from 1 to 7 [250]

The approach-retract curves (Figure 40b) show the tip cantilever deflection as a function of the AFM Z piezoelectric actuator position. During the approach, the AFM head goes down on the sample. The cantilever does not deflect until it touches the sample. We observe a flat part on curves 1 to 5. The shift and the absence of this flat part on curves 6 and 7 indicate that the sample is tilted. After touching the sample, the AFM head approach is compensated by the cantilever deflection at curve 1 and by the beam deflection at curve 7. So in the curve 1 the slop angle of the curve is about 45° because there is no beam to absorb the cantilever deflection (after it touches the sample). Conversely in curve 7 a part of the AFM head movement is compensated by the beam deflection. So the tip cantilever deflection is lower and the slope of the curve is lower than the previous curves.

Recent studies have shown a difference of opinion about the effect of diameter on NW's Young's modulus. Indeed, some argue that this value decreases with diameter [251]–[253], while others claim the opposite [254], and some other think that there is no effect [255], [256]. A mechanical characterization will allow getting an idea of the mechanical behavior of our NWs. To do this, two samples of GaN NWs fabricated by two different approaches, one by a plasma etching and the other one by MOCVD have been analyzed. The substrate used for these two specimens is sapphire and the

growth was performed according to the [111] direction. The Figure 41a&b and Figure 41d&e show the AFM and SEM images of these samples.

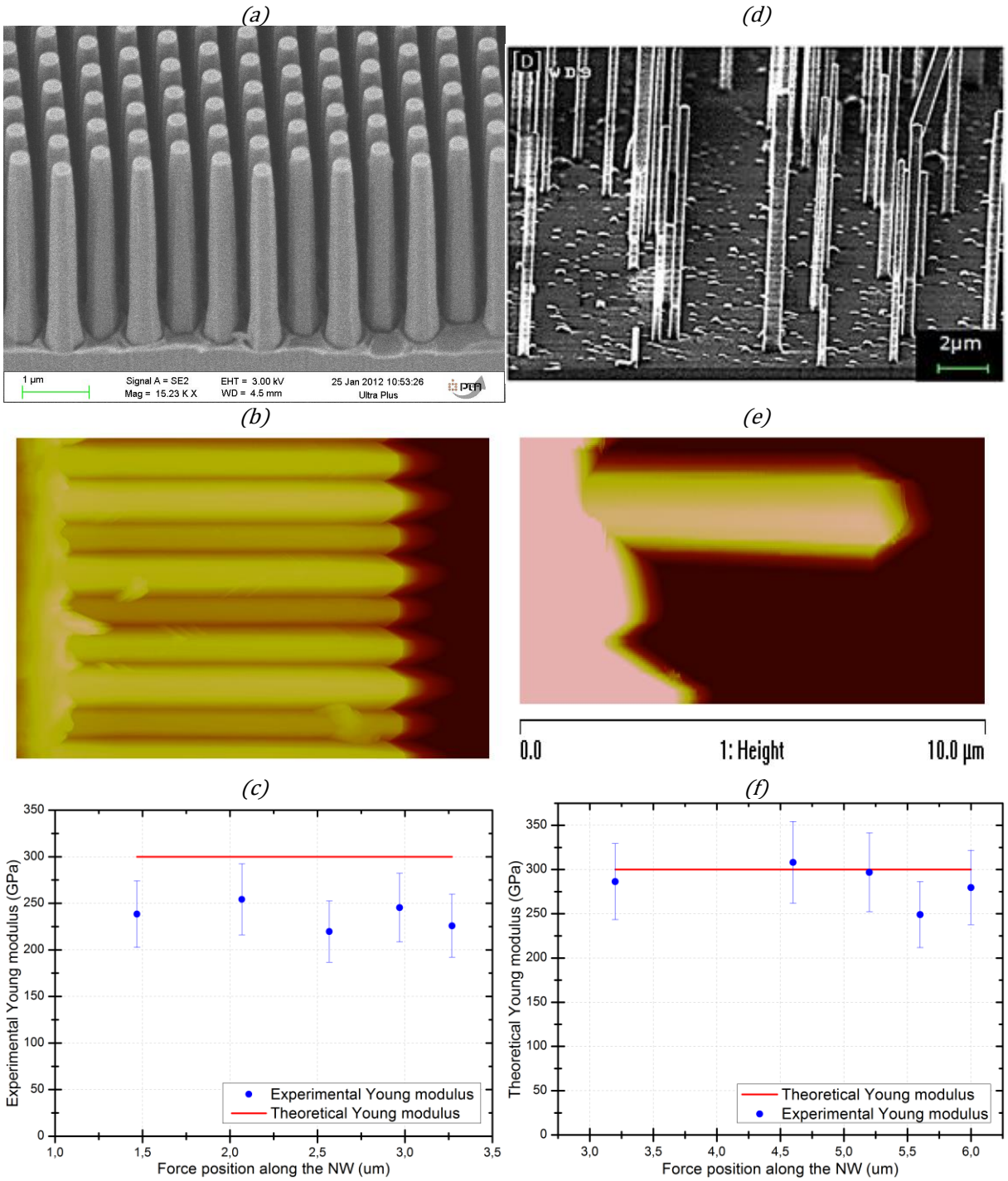

Figure 41 SEM image, AFM image and Young modulus extraction from AFM approach-retract curves for (a), (b) and (c) a top down GaN NWs and (d), (e) and (f) a MOCVD GaN NWs. Theoretical NW Young modulus value: 300 GPa [200], [253].

Figure 41c & f show the results of the characterization of the Young's modulus of the two GaN NWs samples. The estimated error on these measures is the following:

$$\frac{\Delta Y}{Y} = 3\left|\frac{\Delta l}{l}\right| + 4\left|\frac{\Delta w}{w}\right| + \left|\frac{\Delta F}{F}\right| + \left|\frac{\Delta z}{z}\right| \qquad \textit{Equation 77}$$

where l is the length, w the width, Y the Young modulus, F the force and z the AFM vertical displacement.

Thus we obtain the experimental values of the Young's modulus of these samples:

Table 12 Young modulus characterization results and estimated errors.

Sample	*Length*	*Diameter*	*Force*	*Displacement*	*Young's modulus*
Top down GaN	*l=3.5µm* *Δl=100nm*	*w=275nm* *Δw=6nm*	*ΔF/F=3%*	*Δz/z=3%*	*Y=236 ±33 GPa*
MOCVD GaN	*l=7µm* *Δl=175nm*	*w=358nm* *Δw=8nm*	*ΔF/F=3%*	*Δz/z=3%*	*Y=283 ±44 GPa*

The Young's modulus obtained for these two samples are slightly lower than a theoretical GaN NW value of 300GPa and slightly higher than the bulk value. Our results are in agreement with those obtained by [200], [253]. In their works, they experimentally demonstrated that NWs having diameters greater than 84nm have a Young's modulus close to the theoretical value. Several reasons may explain our difference. First, the quality of growth of the NWs can cause the formation of a significant amount of defects and stress which are responsible of the decrease of mechanical properties. Another explanation could be the lattice mismatch between GaN NW and the sapphire substrate; this can cause a residual stress between the substrate and the NW. This constraint may reduce its mechanical properties. On the other hand, the estimation of the length and diameter of the NWs added to the not clear limit of the anchor could be a source of error. According to the formula of quadratic moment (Equation 65), the diameter is raised to the power 4. Thus even a small error of these values may result in a big error on the measurement of Young's modulus. Finally, other phenomena can come into play such as a small indentation of the NWs [250]. One way to reduce these errors is to perform a series of measurements on a large number of NWs.

To validate these experiments, we simulated the mechanical behavior of the top-down GaN NWs. We made bending tests and we compared the experimental results with models having a hexagonal or cylindrical geometry (Figure 42). Indeed it is common to use a cylindrical geometry to simulate NWs [47], but the results show that this approximation is not valid in the case of a fine mechanical characterization. Thus the force-bending curve obtained with the hexagonal geometry overlaps our experimental values whereas the cylindrical geometry has a relatively large error.

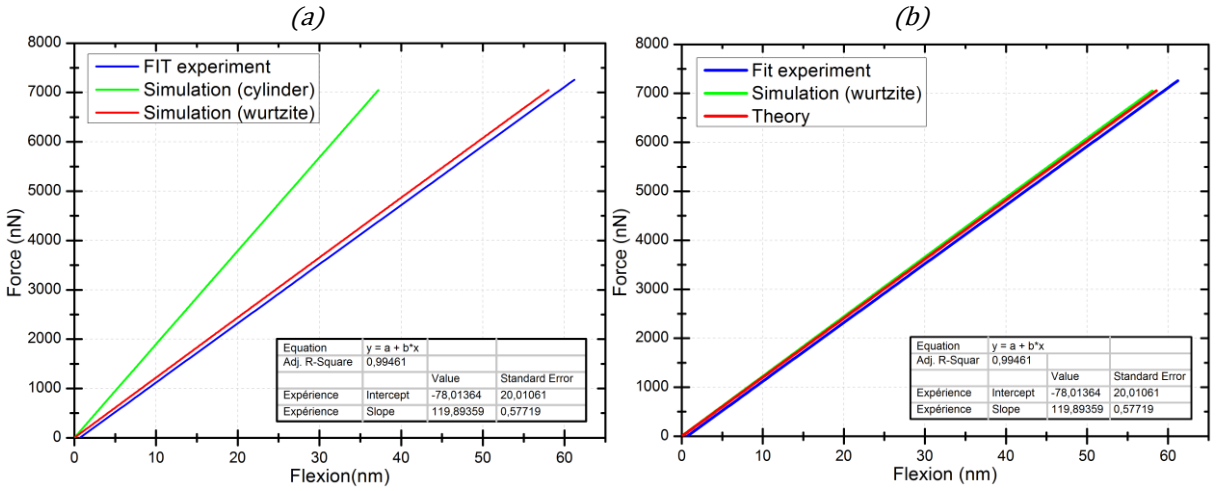

Figure 42 Curve of the force as function of the NW deflection. (a) Comparison between NW having a cylindrical and hexagonal geometry and (b) comparison between the theoretical calculation, FEM simulation and experimental results.

c.Discussion

In summary, we presented an AFM method for measuring the Young's modulus of one-dimensional micro and nano structures. In addition we developed a theoretical model, using classical mechanics, which is in agreement with the experimental results. This technique has two benefits. First, it allows

measuring the Young's modulus without destroying the sample. Two, it can easily be applied to many structures such as NWs and nanobeams for example. One disadvantage is the error in the evaluation of the dimensions of the structure which generates a significant error in the final results of Young's modulus. An accurate estimation of the dimensions of the object characterized is necessary beforehand. For now, because of the large range of uncertainty, it is impossible to distinguish any size effect on the mechanical properties of the ZnO and GaN NWs that we studied their average Young's modulus remains similar to that of bulk material.

II.5.3.2. Piezoelectric characterization

The same lateral configuration can be used to analyze piezoelectric properties using a conductive AFM tip. NW bending induces a local electric potential via the direct piezoelectric effect. It is then possible to measure the properties of the electrical circuit created by means of a voltage amplifier and an oscilloscope for example and then extract the piezoelectric potential generated (Figure 43).

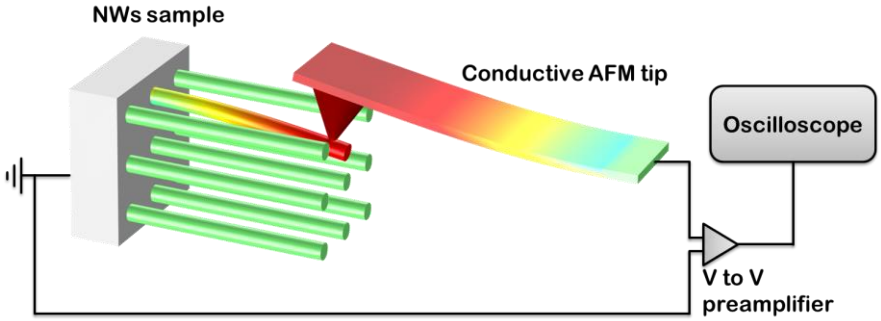

Figure 43 Schematic of the AFM experimental setup

However in order to correctly choose the measurement parameters, some modeling is required.

a.Equivalent electrical circuit of piezoelectric semiconducting NWs

First, to extract the piezoelectric properties of piezoelectric semiconductor NWs from the AFM characterization electrical circuit we need to establish the equivalent circuit of a NW and determine its impedance. Thus we consider a cylindrical single crystal of ZnO as NW, with perfect circular section, a length l and radius r as r<<l. The NW is oriented along the z axis coincident with the c-axis of the crystalline lattice of the ZnO. The NW is clamped at the root and free at the other end. It is subjected to a compressive force F (directed along the z axis) which is considered uniform. Given the NW dimensions, the T_{ij} stress tensor components are all zero except T_{33}=F/A. Therefore we assimilate the NW to a bar in mode 33. The NW is electrically contacted at both ends. It is electrically connected to an external load Z_{out} representing the output circuit. As only the deformation mode 33 is taken into account, the quantities are uniform in x and y. The device receives an external input of mechanical energy from the compressive force F. This energy is stored in the NW in elastic form and results in deformation thereof. Due to the piezoelectric properties of ZnO, a portion of the mechanical energy is converted into electrical energy, a potential difference U appears between the electrodes and an electrical current I through the load Z_{out}.

There are many possibilities to represent and analyze the equivalent model of piezoelectric converters. For electrical engineering we need sufficiently simple and practical equivalent model of piezoelectric materials expressed only using electrical parameters. The best equivalent circuit that fits the typical piezoelectric converters impedance is the Butterworth-Van Dyke (BVD) model and its electrical dual circuit developed by Redwood [257]. Both of them are derived by simplifying the Mason [258] equivalent circuit and by making the best piezoelectric impedance modeling based on experiments and

electromechanical analogies. The simplest and most widely used equivalent circuit of piezoelectric converters is only applicable for relatively high mechanical quality factor piezoelectric converters where thermal dissipative elements, dielectric losses and internal resistivity are not taken into account. In the case of this work, a more general model has to be considered. Such a model is represented on Figure 44a considering a series resonant circuit and Figure 44b considering a parallel resonant circuit, where the red element represents the purely electrical nature of piezoelectric converters and the blue part represents the mechanical behavior. These equivalent series and parallel circuits are mainly used for the electrical to mechanical energy conversion and use the electromechanical analogy current to force and voltage to velocity where the motional current I_m is proportional to the force generated and the motional voltage V_m is proportional to the velocity. For the mechanical to electrical energy conversion the equivalent circuits with transformer separation between the electrical and electrical circuits can be used but they remain equivalent to the previous circuits.

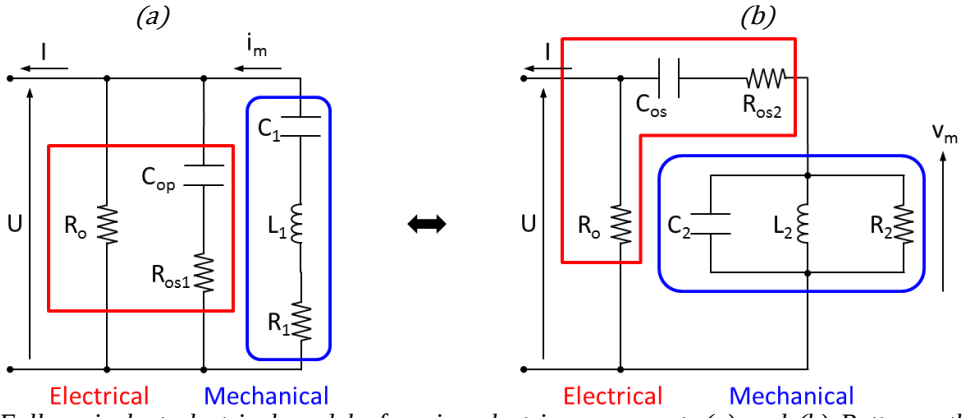

Figure 44 Full equivalent electrical model of a piezoelectric component. (a) and (b) Butterworth-Van Dyke piezoelectric converter model with dissipative elements (adapted from [257]*).*

In these models R_o represents the leakage resistance and $R_{os1} \approx R_{os2}$ the dielectric resistive loss. Usually for high quality piezoelectric ceramics R_o is in the range of 10 to 50MΩ and R_{os1} is in the range of 50 to 100Ω. Therefore, in most cases of high quality ceramics they are neglected, but because of the semiconductor nature of ZnO and GaN NWs R_o components must be considered. On the other hand the resistance R_{os} can be neglected because we are dealing with very small scale structures with low signal in quasi-static. The electrical capacitance $C_{os} \approx C_{op}$ represents the static capacitance of the clamped piezoelectric NW. Because we are working with nano structures then it needs to be considered. The mechanical behavior of the piezoelectric converter is represented by mechanical impedance which can be linearized around resonant frequencies and thus be represented by an RLC circuit. The values of R, L and C depend on the physical properties and dimensions of the ZnO NW. Thus the dissipative power loss R_1 represents the joint losses, frictions and material hysteresis-related losses (internal mechanical damping). The other components of the equivalent circuit are C_1 which represents the stiffness and L_1 which represent the motional mass of the piezoelectric.

The first application targeted is energy harvesting to power autonomous systems in natural or industrial and human environment. If the sources of mechanical energy are varied (moving fluid, vibration of structures, shocks, strains ...), their frequency ranges (a few Hz to several kHz) in any case remain far below the frequency of the first resonance mode a NW in compression and in bending (a few hundreds of MHz). In this case of NWs operating in quasi-static regime or at low frequencies, the equivalent circuit can be simplified. The L_1 impedance representing the effect of mass of the system approaches 0 and mechanical losses modeled by R_1 are negligible. Thus only remains C_1 which models the stiffness of the system. It was shown that C_1 is [235]:

$$C_1 = s_{33}.\frac{l}{A}$$ *Equation 78*

where s_{33} is the stiffness, L the distance between the two connections on the NW and A the contact surface of the connections. In addition ZnO is a semiconducting material, therefore the internal resistance R_o of the NW can be low and not negligible. The piezoelectric semiconductor NW is electrically characterized by its internal resistivity:

$$R_o = \rho.\frac{l}{A}$$ *Equation 79*

where ρ is the resistivity of the NW. Similarly the capacitance of the NW between the electrodes can be approximated by the simple calculation:

$$C_{op} = \varepsilon_0.\varepsilon_r.\frac{A}{l}$$ *Equation 80*

where ε is the permittivity. It is possible to model the circuit obtained in the form of a Thevenin or Norton generator. The Thevenin generator includes a voltage source V_m controlled by the applied force F in series with C_{op} and in parallel with R_o.

$$V_m = \varepsilon_0.\varepsilon_r.\frac{g_{33}}{C_{os}} \times F$$ *Equation 81*

where g is the piezoelectric coefficient. The Norton generator contains a current source I_m controlled by the applied force F in parallel with C_{op} et R_o.

$$I_m = \varepsilon_0.\varepsilon_r.g_{33} \times i.\omega.F$$ *Equation 82*

where i is the imaginary unit.

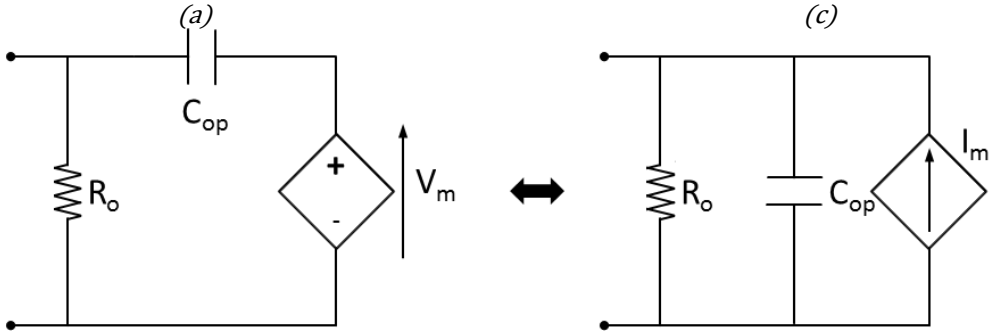

Figure 45 Low frequency equivalent circuit of a clamped-free piezoelectric beam in 33 mode using (a) a Thevenin generator and (b) a Norton generator (adapted from [257]*).*

In our cases, we can estimate the value of the resistance and the capacitance as shown in the Table 13.

Table 13 Calculation of the resistance and capacitance of a ZnO NW, with length l=600µm and radius r=25nm, with an electrical connection at its ends or on its flanks. The resistivity is considered between 1 and 10 Ω.cm. The flank is approximated as a plate capacitor of 50×500nm spaced by 50nm [47].

	Ends electrical connection	*Flank electrical connection*
R_{op}	*3< <30 MΩ*	*20< <200 KΩ*
C_{op}	8.21×10^{-20} *F*	3.94×10^{-17} *F*
τ	*~0.82 ps*	*~3.94 ps*

In these simple electrical models, we have to keep in mind that the electrical component values are highly dependent on the geometry of the NW, the material properties and especially its doping concentration.

However we can deduce several things from this simple reasoning:

- If we want to connect to a piezoelectric semiconductor NW a measuring device or energy harvester. Then, the input resistance of the device (Z_{out}) should be lower than the internal resistance of the NW. Otherwise the current will mainly pass through the NW.
- The input capacitance of any measurement system or energy harvester should be as low as possible to avoid losing the least possible charges in this capacitor. Indeed we have to keep in mind that in a nanoscale semiconductor, despite a strong doping, the volume of materials is very low and therefore the number of the dopants and charges is also low. 117 charges in a NW of 600nm length, 25nm radius and doped at $10^{17}cm^{-3}$.
- Finally, it is important to know the output impedance of energy harvesting devices to be able to adapt the input impedance of management energy systems in order to maximize the power transmitted and thus the energy really supply to the targeted device.

b.Piezoelectric NW-AFM tip circuit modeling

The characterization setup is composed of the NWs sample, the conductive AFM tip and the voltage amplifier. The electrical circuit formed can be broken down into several entities: the AFM tip-NW junction, the NW, the NW-substrate-external circuit contact and the voltage amplifier. This circuit is represented in Figure 46.

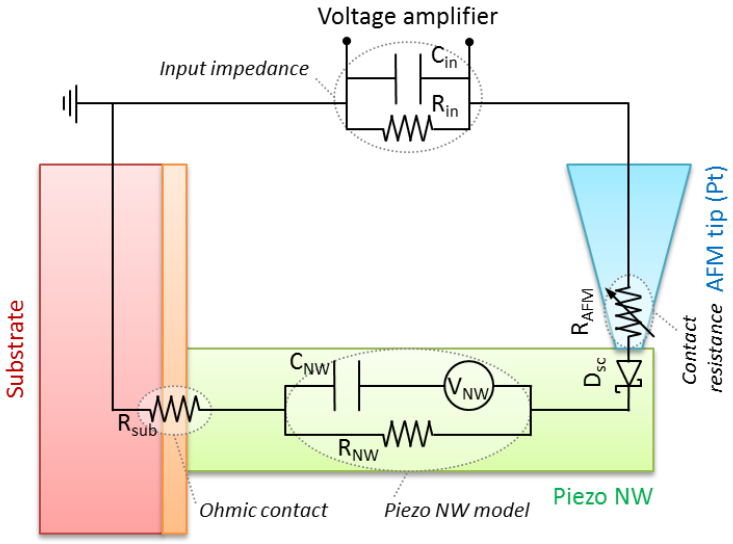

Figure 46 Schematic of the equivalent circuit of the AFM piezoelectric characterization set-up of a GaN NW.

In the case of a ZnO or GaN NW we can estimate some of these elements:

The conductive AFM tips are coated with platinum or a platinum and silicon alloy. When pressing a NW with one of these AFM tips, the electrical junction formed is characterized by two elements: First by a Schottky diode D_{sc} representing the AFM tip (Pt metal) - NW (GaN or ZnO semiconductor) contact. The nature of such a junction is known in microelectronics [145] and its behavior in the case of a ZnO NW and a platinum AFM tip was described by the research group at Georgia Tech (III.2.3.2.). We continued this study using GaN NWs to characterize this junction and demonstrate its strong application potential (III.2.3.2.). Secondly, by a variable contact resistance representing the electrical resistance of the contacts between the AFM tip and the NW which depends on multiple parameters such as the applied force, the rigidity of the material and the contact geometry. For simplicity, the tip-NW contact can be modeled as a sphere indenting a flat surface according to the Derjaguin-Muller-Toporov model [259]. However, it remains difficult to assess precisely this resistance since the parameters of the contact change on each NW measured. This resistance could be evaluated to 500Ω

in the best case [260], but after several successive measurements and damages, the AFM tip can be altered.

The piezoelectric semiconducting NW could be simply modeled by a current source in parallel with a capacitor and a resistor. In the case of a ZnO NW of 600nm length and of 50nm diameter, we approximated the value of these components (Table 13). Using the parallel plate capacitor approximation of a NW with lateral electrodes, the capacity of such a NW is estimated to $C_{NW}=3.94\times10^{-17}$ F. If a force of 80nN is applied at its free end, then the potential generated will be about $U_{NW}=0.3V$ and therefore the charges generated by the current source will be $Q_{NW}=C_{NW}\times U_{NW}=1.2\times10^{-17}C$ which correspond to 75 electrons. Concerning the internal resistance of hydrothermal ZnO NWs, their resistivity typically ranges from 10^{-2} to 10Ω.cm [38] which gives an internal resistance of about $R_{NW}=20k\Omega$.

The contact between the NW, the substrate and the measurement circuit varies depending on the substrate used and its doping. For simplicity we assume that the contact between these elements is ohmic in nature. But this is not always the case in practice, a PN junction may be present between a p-type substrate and n-type NWs (n-type ZnO NW on p-type Si wafer) or a Schottky junction may be present between a semiconducting substrate and a metal measuring system (n-type Si substrate connected with silver paste).

Finally the voltage amplifier can be seen as input impedance consisting of a resistor and a capacitor in parallel. The input impedance of the voltage amplifier we use is $R_{in}=100M\Omega$ and $C_{in}=10pF$. The impedance values of the measuring system are very important in this experiment. We tested several amplifiers and we arrived at the conclusion that the input impedance should be as low as possible. Indeed the more the input impedance of the amplifier used was high; the more the electrical signal was weak until no signal was finally measured. This is probably due to the low internal resistivity of the characterized ZnO and GaN NWs, but further investigations and researches are required to fully understand this phenomenon.

c.Piezoelectric potential measurements

Following initial characterization of piezoelectric NW in our laboratory [1] we searched to better understand the mechanisms involved in the bending of a piezoelectric semiconductor NW by an AFM tip coated with platinum.

First, using the AFM lateral characterization method, I characterized various GaN and ZnO NWs (Figure 47a). The results obtained are consistent with previous observations made by Xin Xu. When a force is applied along a NW and being bended, then an electric potential is measured (Figure 47b). Secondly the amplitude of the generated piezoelectric potential is proportional to the force applied (Figure 47c). Although the quantitative values differ from FEM simulations, the trend is consistent with them. Finally after consecutive deformations of the piezoelectric NW the potential generated decreases (Figure 47d). All these observations confirm the previous one described in [1].

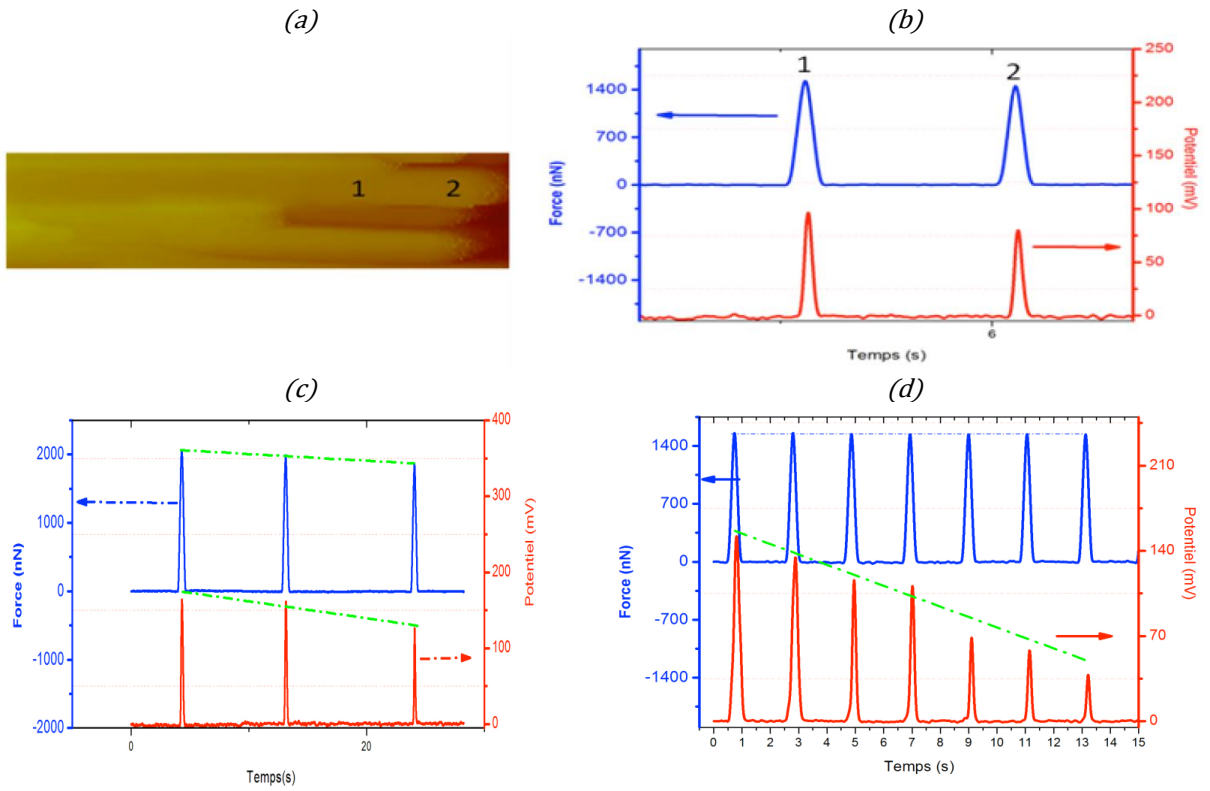

Figure 47 (a) AFM image of an intrinsic GaN NWs grown by MBE, (b, c and d) magnitude of the piezoelectric potential measured by AFM as function of the (qualitatively estimated) force applied.

Then we have characterized different GaN samples with different doping or a heterojunction (Figure 48). Overall we observed the same behavior and trends.

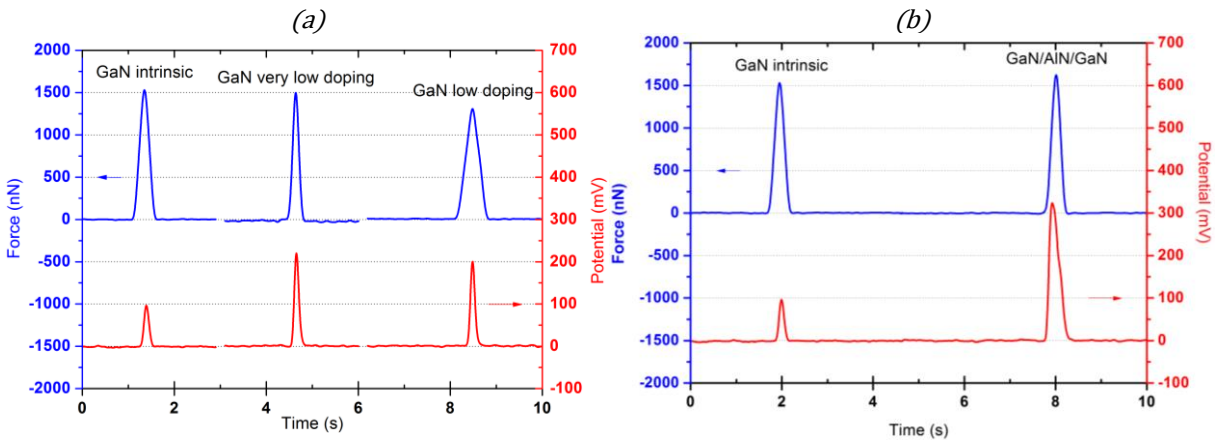

Figure 48 (a) and (b) Magnitude of the potential generated under an applied force (qualitatively estimated) for different GaN NWs (d=50nm and l=600nm) grown by MBE on Si wafer and AlN buffering layer with different doping concentration and structure. The force has been applied close to the end of each NWs.

For the moment the performed measurements vary a lot. Uncertainties and instabilities remains large and it is difficult to identify a repeatable and clear experimental trend about the electric potential generated by the NW having different doping. Because of this great variability of results between each sample, we focused on understanding the phenomena sample by sample. Further encouraging studies are ongoing on ZnO NW samples (Figure 49). Results are more accurate and repeatable.

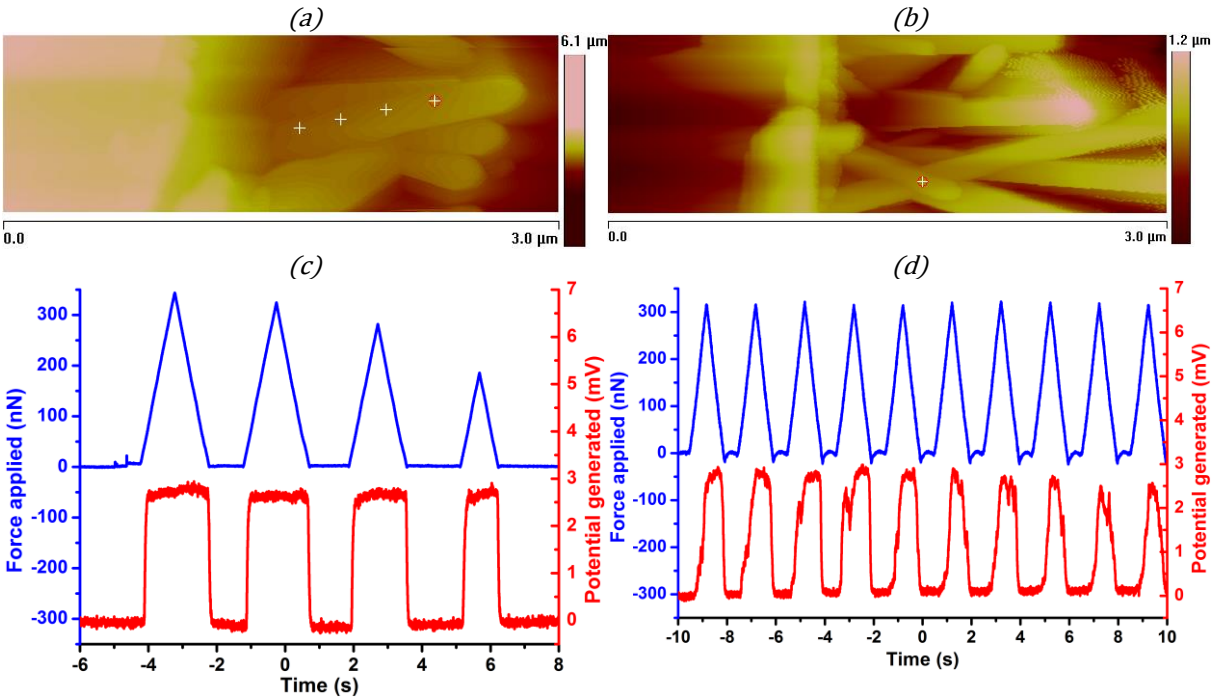

Figure 49 (a) and (b) AFM image, (c) and (d) magnitude of the potential generated under an applied force for different ZnO NWs (d=90nm and l=2um) grown by hydrothermal process on Si wafer. The force location is indicated on the images by the crosses.

The objective then, was to study the evolution of the electric potential and current as a function of time. But again, unfortunately, instability and variability of results is large from one NW to another in the same sample.

Overall, the uncertainties remain large on this type of measure. Several effects can be involved: thermal drift of the AFM, state of the AFM tip and the nature and quality of its contact with the NW for example. Variability of the results is high on each NW in the same sample and between two equivalent samples, which is another important problem. So it is difficult to draw definite conclusions. The only solution seems to look for a better control of the parameters, for example by improving the uniformity of NWs and samples, and by understanding and controlling better the AFM measurement circuit. Some paths for improvement were initiated. The first was to study the growth of ZnO NWs in order to better control them and get better samples. The second was initiated at CEA by improving the identification and access to selected NWs using FIB etching selection.

II.5.4. PFM characterization of piezoelectric semiconductor NWs

II.5.4.1. PFM working principle

The AFM - PFM (Piezoelectric Force Microscope) mode measures the mechanical response when an electrical voltage is applied to a sample surface using a conductive AFM tip. In response to the electrical stimulus, if the sample has piezoelectric properties, it should locally expand or contracts. When the local piezoelectric response is detected as the first harmonic component of the tip deflection, its phase gives information on the polarization direction of the piezoelectric domain below the AFM tip. In addition the detection of the lateral components of tip vibrations can provide information on the in-plane surface displacement, known as lateral PFM. Finally, the electromechanical PFM response can be probed as a function of the AC bias or the DC bias of the tip, providing information on the piezoelectric coefficients and the polarization switching in ferroelectrics respectively.

PFM requires detection of small tip displacements induced by relatively high amplitude and frequency voltages measured at the same frequency as the driving voltage. Any instrumental crosstalk between the drive and the response will create a parasitic PFM background that can easily screen the sample PFM response, especially for materials having weak piezoelectric coefficient. In addition, small cantilever displacement implies a very small signal-to-noise ratio. Therefore the piezoelectric signal is most frequently detected by a lock-in amplifier connected to the deflection of the AFM cantilever. By employing an oscillating electric field, low-frequency noise and drift can be eliminated from the measurement. Minimizing the crosstalk between the driving voltage and the response requires reliable and accurate microscope mechanics, electronics and experimental setup.

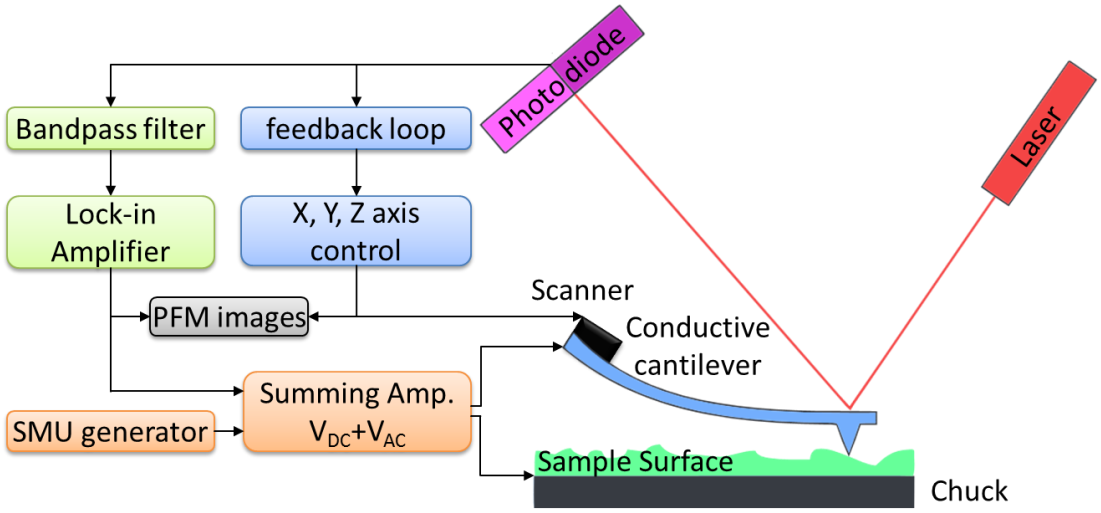

Figure 50 Schematic of the full PFM mechanism.

The relationship between strain and applied electric field is described by the piezoelectric matrices (I.4.2.3.). Generally the most important piezoelectric coefficient for vertical PFM is the d_{33} component, since it links directly the vertical motion of the cantilever. The voltage applied to the tip V_{tip} is:

$$V_{tip} = V_{dc} + V_{ac}\,cos(\omega t) \qquad \textit{Equation 83}$$

where V_{dc} is the direct voltage applied to the AFM tip, V_{ac} the alternative voltage applied to the AFM tip and ω the pulsation.

This induces a piezoelectric strain in the material that causes cantilever displacement z due to piezoelectric effect:

$$z = z_{dc} + A(\omega, V_{dc}, V_{ac})\,cos(\omega t + \varphi) \qquad \textit{Equation 84}$$

where z_{dc} is the cantilever displacement due to the direct voltage, A the AC amplitude which usually should be higher than 30-50pm to be detected and φ the phase difference.

When the AC voltage is driven at a frequency well below the contact resonance frequency of the cantilever, this expression becomes

$$z = d_{33}.V_{dc} + d_{33}.V_{ac}\,cos(\omega t + \varphi) \qquad \textit{Equation 85}$$

Thus the magnitude of the PFM oscillating response is a measure of the magnitude of d_{33} and the phase is sensitive to the polarization direction of the sample. The direction of sample polarization determines the sign of the response. If the polarization is parallel and aligned with the applied electric field, the piezoelectric effect will be positive, and the sample will locally expand. On the contrary, an anti-parallel polarization and electric field will shrink the sample. Thus the phase of the cantilever provides an indication of the polarization orientation of the sample.

II.5.4.2. Experimental tests and issues

This AFM characterization mode seems to perfectly match our need for piezoelectric NW characterization. Thus we developed PFM in order to better understand and characterize the ZnO and GaN NWs. However this method is difficult to use for the characterization of three-dimensional nano-object, having depth and constituted of low coefficient piezoelectric materials such as ZnO or GaN NWs as compared to a PZT thin film. The first experiments that we conducted highlighted numerous difficulties and obstacles to the PFM characterization of piezoelectric NWs.

Firstly the depth of a NW forest is a real obstacle to PFM measurements. Indeed it is very difficult to achieve a top view PFM image of a NW carpet because you cannot follow their profiles but only touch their ends. Measures exist on large ZnO nano-pillars well organized [207], [261] but no measures have yet been made on NWs of few tens of nanometers in diameter as our samples. In addition it is difficult to interpret measurements and to separate the PFM signal from the influence of the movement of the NWs (**Erreur ! Source du renvoi introuvable.**). The piezoelectric potential generated by the urvature of the NWs can influence the PFM measures and involve other phenomena. But especially the influence of topology on the PFM measurement is very high because of its impact on the surface and the quality of the contact between the AFM tip and the sample and on their electrostatic coupling.

The quality of this electrical contact is very important for the quantitative extraction of the value of the piezoelectric coefficients. The solution to all this will be not to make a PFM image, but only a PFM measure at a specific point by standing at the extremity of a NW. But again the NWs are so small that it is very difficult to stand at their end and stay on to perform PFM measurements while maintaining good electrical contact. We performed a PFM lateral characterization of NWs but the interpretation of results and the extraction of piezoelectric parameters are much more difficult because of the bending of the NWs.

The second difficulty is to perform a quantitative PFM measure on ZnO and GaN NWs. At first we had difficulties to calibrate our measurement system using reference samples supplied by the AFM manufacturer. PFM quantitative measures are highly dependent on the quality of the electrical contact between the AFM tip and the sample. To correctly extract a piezoelectric coefficient, it must be sure that the expansion or contraction of the material is observed due to the difference of electrical potential applied to the NW sample. If the electrical contact is bad then the voltage drop between the AFM tip and the sample measured will introduce an error of underestimation of piezoelectric coefficients measured. A poor contact may be due to a too low applied force, an AFM tip damaged or a thin film of water for example. The nature of the contact is also important because if it is not ohmic but Schottky such as between a ZnO or GaN NW and a platinum conductive AFM tip, then one must consider the threshold voltage of this diode. Finally, we must also take into account all elements of the measuring circuit which makes the calibration very important but difficult.

II.5.4.3. Solutions developed and investigated

Because of all these difficulties, the PFM signal of our first measurements was inaccurate and the values of piezoelectric coefficients extracted were very low. To overcome this we initially chose to amplify the PFM signal using the contact resonance frequency of the AFM tip. In addition, to limit the effect of the topology we used the PFM mode called DART [262] developed by Asylum Research to track, using two lock-in, the changes of the contact resonance frequency due to topology. Then we worked on the structure of the sample. We tried to fix the NWs to prevent them to move while applying reasonable force to obtain a good electrical contact. For this we spincaoted PMMA on NWs,

then we etched them using O2 plasma to adjust the level of PMMA. We also sputtered a thin layer of gold on top of the samples without covering the sides of the NWs to achieve a good ohmic contact between the AFM tip and the NWs. We encountered numerous difficulties, particularly when adjusting the level of PMMA, which etching after etching refine the end of the NWs. However, despite the use of these advanced PFM techniques and sample preparation we did not get convincing results until now.

A technique commonly employed is to disperse the NWs on a substrate in order to characterize them [30], [36], [263]–[265]. For this, we studied the dispersion of our NWs on Si wafers, using ultrasound we adapted the dilution of the NWs. In order to electrically characterize piezoelectric semiconductor NWs we have created a chip to connect by ebeam lithography some NWs, previously scattered, to electrical contacts that were deported on the outside of the chip. Thus it is possible to electrically characterize the NWs using a probe station. In addition to this we have also developed an AFM chuck to electrically characterize these chips while using the AFM. This chuck and board works with DIL sockets allowing connecting 24 electrical signals on a chip by wire bonding. We can then characterize electrically piezoelectric NW while applying a local mechanical stress or a deformation using the AFM (Figure 51).

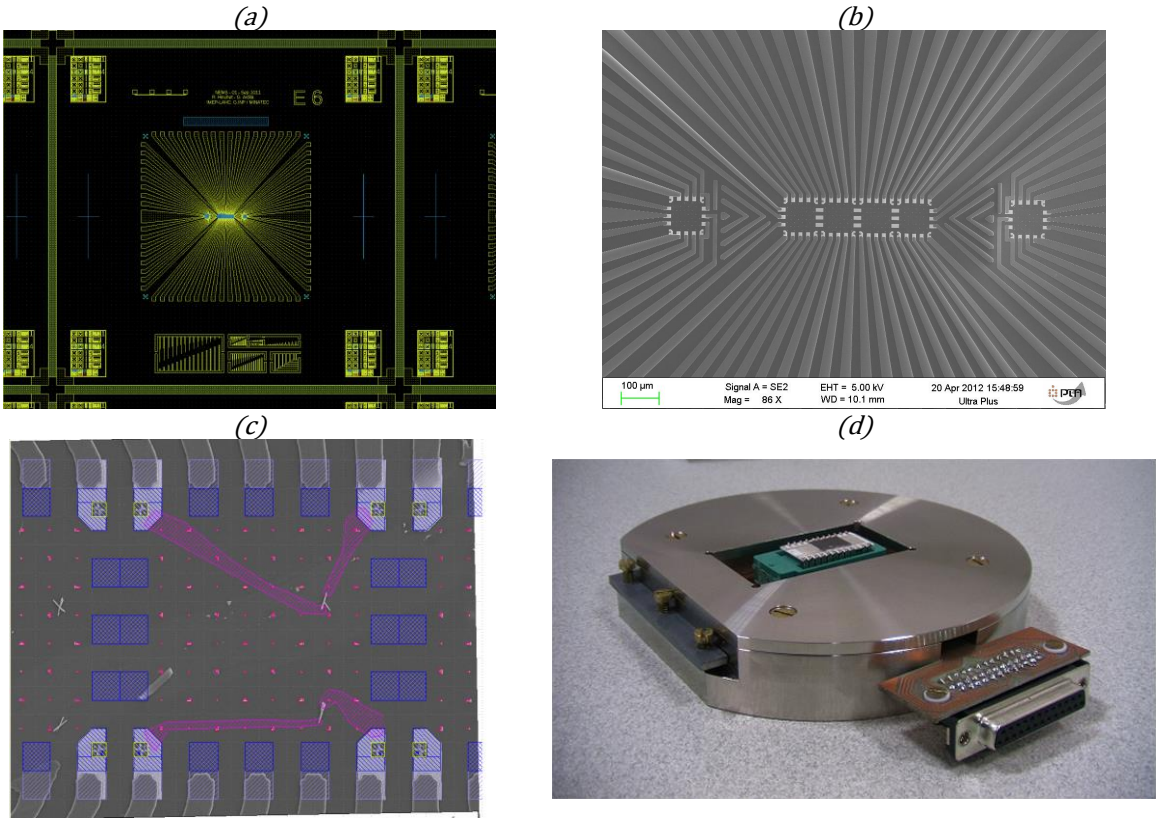

Figure 51 (a) Design and mask of the electrical characterization chip, (b) SEM image of the fabricated chip, (c) SEM image and mask of the connection of ZnO NW using ebeam lithography and (d) photo of the AFM electrical characterization chuck.

Using these tools, the possibilities of electrical and piezoelectric characterization of piezoelectric semiconducting NWs are very interesting. However due to delays and the lack of time this project have been delayed and paused. Unfortunately the time invested in the development of these characterization techniques did not lead to results yet, but the interest of this project of electrical and piezoelectric characterization remains intact and I remain convinced that this project will lead to interesting results.

II.6. Conclusion

In summary, in this chapter we have introduced the most common fabrication processes used to grow ZnO and GaN NWs. Top down approaches allow a better control of the regularity of the NWs in terms of size, shape and position but with actual technology, it is very challenging to fabricate NWs with diameters lower than few tens of nm. On the other hand, bottom up processes are standard methods to obtain ZnO and GaN NWs, allowing the fabrication of NWs with high aspect ratio and diameter in the range of a few nanometers. But those methods lead to larger distribution in sizes (including height) while the position and organization of the NWs is poorly controlled and usually random.. We have presented MBE that is a growth method used to grow the high quality GaN NWs studied in this thesis. We have also deeply investigated the hydrothermal growth of ZnO NWs which allows the growth of ZnO NWs at low temperature (<100°C) on large various substrates. Hydrothermal ZnO NWs have more crystallographic defects than other methods but it is scalable and convenient to use while being IC compatible. While it is difficult to grow large and regular ZnO NWs arrays with as less as possible growing defects, dusts and contaminations (chemical or structural), we succeed to grow ZnO NWs arrays with different profile (flat, corner, zigzag) on various substrates (Si wafer, Al foil, Kapton film and Glass) and various sizes (from $1cm^2$ to 2 inches wafer size).

To deeper understand the electromechanical behavior of ZnO and GaN NWs and evaluate their potential, we have developed both analytical and FEM simulation models of a ZnO NW bent by a lateral force applied at the top of the NW. Thanks to the analytical model we understood the piezoelectric physics mechanism occurring in an individual NW under bending. In complement, the FEM simulations gave accurate estimate of the piezoelectric potential distribution in the NW. The confrontation of the analytical and FEM simulation models showed small differences due to the simplification of the piezoelectric equation to the first order in the analytical study and small edge and mesh effects in the FEM simulation. We noted that there is an inversion of the potential at the base of the NW where the electric potential is strong and which is due to the shear stress generated by the bending force. Extensive parameter screening was carried out to define scaling rules which are of importance for device performance prediction and optimization. We have shown that the potential generated increases linearly with the force applied while it strongly increases when the radius decrease and remains constant with the NW length. Thus these scaling rules allow optimal design of ZnO NWs based devices in view of specific applications such as artificial skin sensors.

Finally to later use and integrate piezoelectric NWs into functional sensors and energy harvesters we have characterized experimentally the electromechanical properties of individual ZnO and GaN NWs. We have chosen to use an original AFM lateral setup developed at IMEP-LAHC to perform mechanical and piezoelectric characterization of bottom up ZnO and top down GaN NWs. This unique setup allows an easier and better control of the force applied on the piezoelectric NWs. Our investigations show that there is no size effect on the mechanical properties of these NWs. Thus there is no impact of the downscaling to the nanometer range of the mechanical properties. We then studied the piezoelectric characteristics by bending individually NWs and measuring at the same time the potential generated using a conductive AFM tip. The overall results confirm that the potential generated varies linearly with the force applied. In addition, undoped GaN NWs seems to generate more electric potential than the doped one. Interestingly, highest voltages have been observed on individual GaN NWs with multiple AlN heterojunctions. To provide further insight in the piezoelectric properties of individual NWs, different electrical modes (such as PFM) have been initiated and could give important complementary results in the future.

Chapter III. Piezoelectric NW based force sensors

The better understanding of the properties of piezoelectric NWs opens new perspectives of application of the piezoelectric phenomenon. Especially, the control of the piezotronic effect at nano scale allows the development of improved performing mechanical sensors for example. But in order to properly use and integrate semiconductor piezoelectric NWs we need to investigate various parasitic effects. The piezoelectric behavior of semiconductor piezoelectric NWs changes under nonlinear strain generated when using high forces. The surrounding environment of the NWs modifies the generated electric potential distribution. Finally the NWs growth could generate defects, doping and size fluctuations in the SC NWs. The free carriers generated by the defects and the doping in the semiconductor piezoelectric NWs screen the piezoelectric effect and drastically decrease the generated piezoelectric potential whereas the size variations of the NWs can change the potential. Nevertheless it is possible to overcome these problems and even use them to customize piezoelectric and piezotronic devices. We modeled mechanical sensors based on the electric potential measurement generated by a force, a pressure or a displacement thanks to the direct piezoelectric effect. Thus semiconductor piezoelectric NWs mechanical sensors can achieve a very high force, pressure and displacement sensitivity selecting the NWs size and space resolution. But it is also possible to build a force sensor based on the measurement of current variation through a Schottky junction, the variation of the Schottky barrier height being induced by the piezotronic effect. Such a device was characterized using an AFM and showed very good sensitivity to nano forces.

III.1. Semiconducting NWs related issues

ZnO and GaN NWs are complex electromechanical systems due to their piezoelectric and semi conductive properties. Thus, the classical models of piezoelectric systems are too restrictive to properly represent the phenomenon of mechanical energy conversion in these NWs. One of the major difficulties on modeling NW-based devices comes from the multi-scale problem. Depending on the application areas targeted and the processes involved, the size of ZnO NWs varies over several decades. Typically the length may vary from 500nm to 100µm and the diameter of 20nm to 1µm.

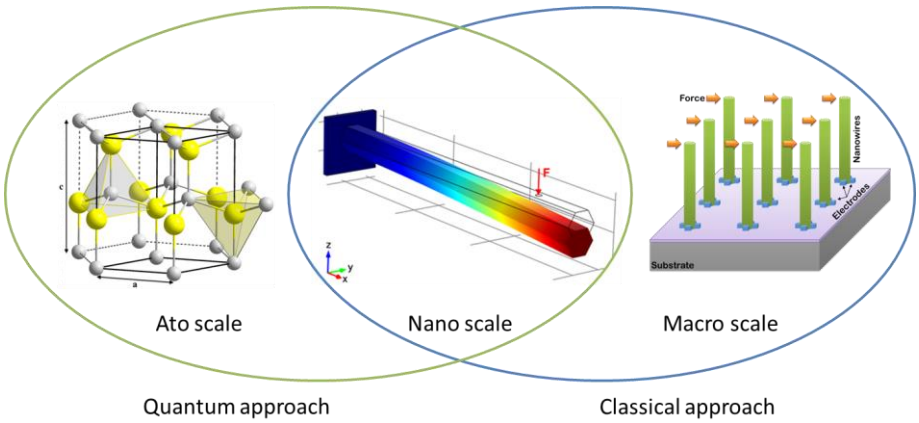

Figure 52 Domain of validity of the two modeling approaches: Quantum and classical, a multi scale problem (adapted from [235]*).*

The piezoelectric NWs that we use are at the border between classical and quantum mechanics, we have chosen initially to restrict ourselves to a classical formulation of the problem because it is simpler

to implement and interpret as a first approach. However, as we go along the understanding of the problem, the need to study the surface related effects. In order to investigate the realistic applications of ZnO and GaN NWs, it has been necessary to identify and gauge pitfalls and key parameters of the problem. One can distinguish three types of parameters: geometrical (r, l), material (N_d) and external (F, θ).

Firstly, in classical mechanics, deformations of structures subject to weak forces are considered as linear. But it is no longer valid when subjected to high stresses. They enter in a nonlinear deformation regime which can give very different results. It is therefore necessary to study the linear and nonlinear deformation regimes of ZnO and GaN NWs and understand their impact on the piezoelectric properties and the performance on potential applications.

Another key parameter to take into account for the modeling of NWs based devices is the statistical aspect of the NW growth process. This is directly related to the bottom-up fabrication processes that induce disparities in the length, diameter, shape and orientation of the NWs. The size distribution can have an impact on the overall behavior of the devices. For example it has been shown in the previous chapter that the amplitude of the potential in a piezoelectric NW under bending depends strongly on the form factor.

In addition, we have to consider the impact of the surrounding environment on the NWs. Mean the effect of the substrate and the possible buffering layers on which the NWs are grown. This may have an effect on the distribution of potential in the piezoelectric NW and especially at its base.

Finally, ZnO and GaN are also semiconductors used in microelectronics. Therefore it is necessary to consider the coupling between the piezoelectric and semi conductive properties, such as the impact of the presence of free charges on the piezoelectric conversion or the low internal resistivity.

III.1.1. Nonlinear model and scaling

III.1.1.1. The nonlinear case

In structural mechanics, several types of nonlinearities can be considered:

- Material nonlinearities due to the law of behavior of the solid. In most cases, this law can be expressed in the form of non-linear first-order differential equations.
- The geometric nonlinearities that occur in the problems of large displacements, large rotations and large deformations.
- Nonlinearities related to changing boundary conditions. This type of nonlinearity appears especially in problems of contact and friction between solids. These phenomena are described by inequalities and projection operations.
- Nonlinearities related to behavior instabilities that arise in the analysis of dynamic problems.

The geometric nonlinearities are associated with structures undergoing major displacements. The notion of major movement simply means that the key assumption on which is based the linear elasticity, the assumption of small perturbations is no longer valid. It stipulates that distorted and initial geometry should remain relatively close. But if a lateral force of 200nN is applied on the upper part of a NW with dimensions as l=600nm and r=25nm, we can notice that with a linear description, the FEM simulation converges to a solution (Figure 53a) where the NW undergoes a large displacement (300nm) and does not hold its shape, which is questionable.

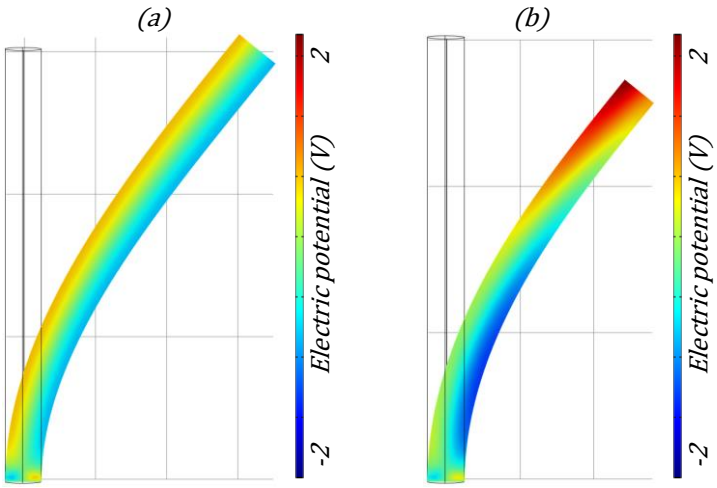

Figure 53 Distribution of the electric potential in a ZnO NW (l=600nm and r=25nm) under a bending force F=200nN. (a) Linear and (b) non-linear mechanical FEM simulation.

III.1.1.2. Nonlinear FEM simulation

We used a non-linear mechanical solver (preserving the geometry of our structure) in adequacy with the piezoelectricity module to resolve our problem. By applying this non-linear solver in previous case of very large displacement, we note that the geometry of the NW is perfectly preserved (Figure 53b). However there are significant differences in the electrical potential profile compared to the linear case. The analytical details of the numerical calculation are not discussed in this report because the non-linear piezoelectric equations system to solve our problem is very complex.

It is then possible to reconsider the reference case of a ZnO NW (l=600 nm, r=25 nm) clamped and undergoing a lateral force of 80nN on its upper part (II.4.1.3.). The non-linear simulation of this problem led to a solution of the electric potential distribution that is totally different from the linear case (Figure 54a & b).

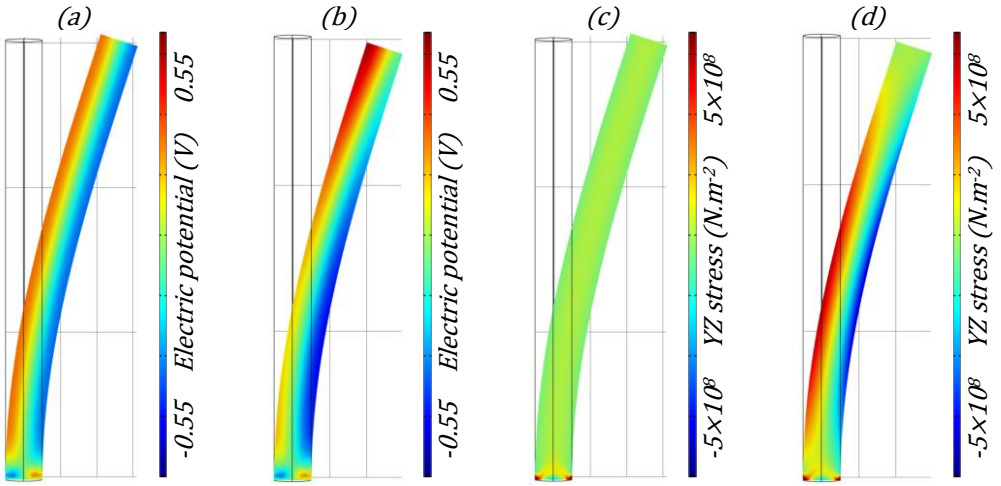

Figure 54 ZnO NW (l=600nm and r=25nm) under a bending force F=80nN. (a) Linear mechanics solution of the distribution of the electric potential and (b) nonlinear mechanics solution. (c) Linear mechanics solution of the distribution of the yz stress component and (d) nonlinear mechanics solution.

We distinguish significant differences in the electric potential profile of a NW between the linear case and the nonlinear case. In both cases the mechanical stress tensor T_x, T_y, T_{xz} and T_{xy} are the same, the main stress T_z is similar (>92%) and there is the shear stress at the clamped end of the NW. However, in the profile of the nonlinear case, we note in the middle of the NW an area where the stress component T_{yz} is strong while it was zero in the linear case (Figure 54c & d). This stress component

T_{yz} become as important as the principal stress component T_{zz} in the linear case. This means that there are two components for the electric displacement (D_y and D_z) and therefore an electric potential which does not depend only on y along the NW but now depends on y and z. Thus in the nonlinear case the positive potential values are located on the extended upper side of the NW and the negative potential on the lower compressed side of the NW. Indeed, in Figure 55a, it is observed that, with the non-linear solution, electric potential varies along the sides of the NW, unlike in the linear case where we observed an equipotential on these two faces. On the middle cross section of the NW (Figure 55b) the non-linear profile of the electric potential is shifted towards negative values in comparison with the electric potential profile of the linear case.

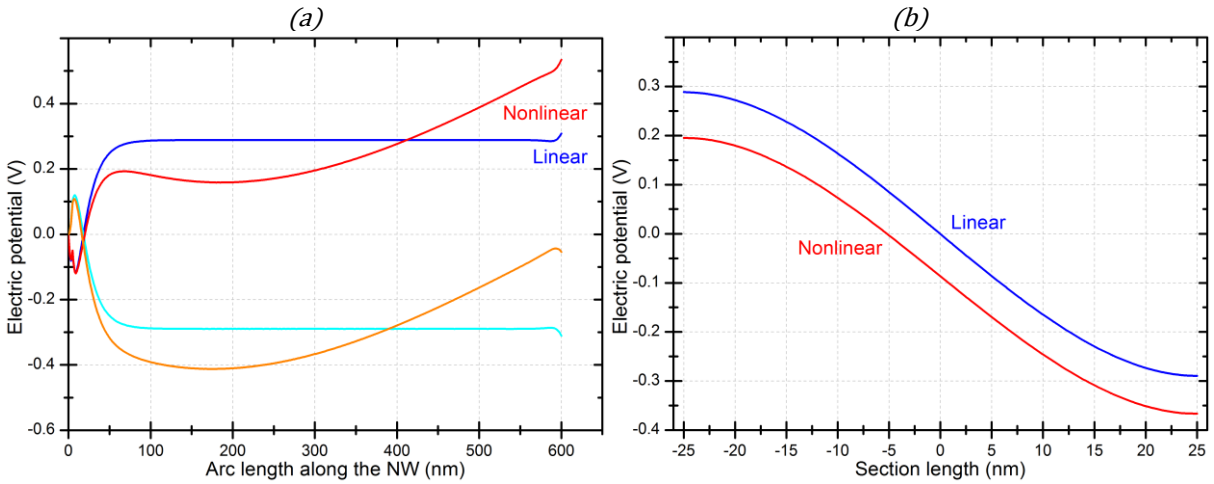

Figure 55 (a) Evolution of the electric potential along the extended and retracted side walls of the NW as function of the Z axis in the linear and nonlinear cases. (b) Evolution of the electric potential across the middle of the NW as function of the Y axis in the linear and nonlinear cases.

III.1.1.3. Validity of the linear model

The question now is to know when to use the linear or non-linear solution for the potential profile of a NW in bending mode (Figure 56).

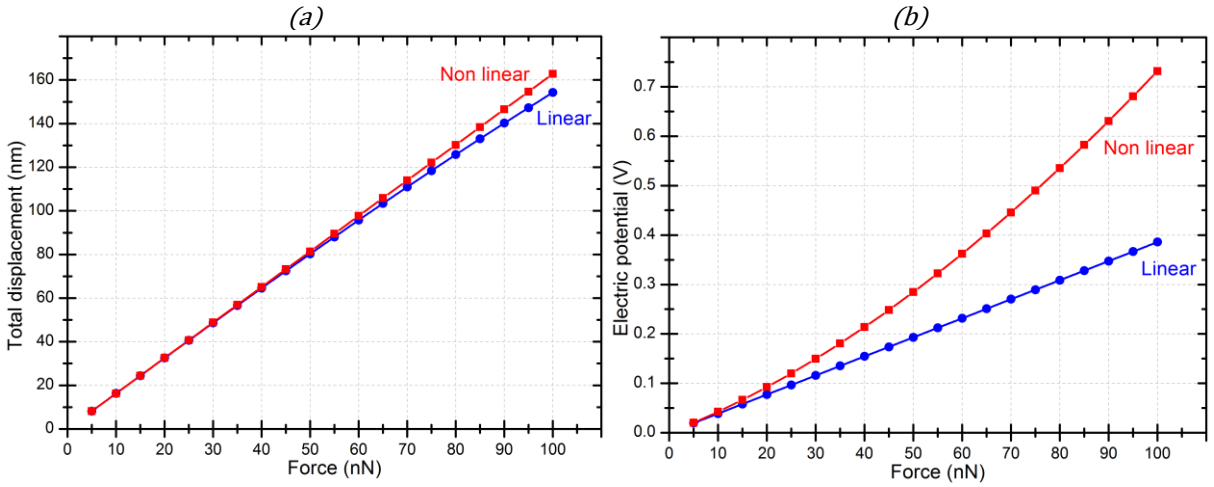

Figure 56 FEM simulation of the evolution of the (a) maximum displacement and (b) maximum of positive potential on the extended side of a clamped piezoelectric NW (l=600nm. r=25nm), as a function of the bending lateral forces applied at its free end, using linear and nonlinear mechanics solver.

For different forces we see that for the linear and non-linear solution, the displacement of the NW is almost identical until the force reach 50nN which is higher than the theoretical result previously addressed (Equation 39). But it is interesting to note that the piezoelectric potential generated is more

sensitive to the non-linear mechanical behavior and remains the same only for forces up to 10nN, which is more consistent with the Equation 39. So even for displacements of the order of the NW radius the piezoelectric potential generated is not linear and nonlinear resolution is required.

III.1.2. NW geometry effect

The ZnO and GaN NWs under study have a wurtzite structure with an hexagonal shape. So the NW does not have exactly a circular section but a hexagonal one. Previously we considered circular NWs to simplify the model but is necessary to investigate the effect of the hexagonal NW geometry on the amplitude and distribution of the piezoelectric potential in such NWs. Therefore we considered a hexagonal NW where the longer diagonal is equal to the diameter of the NWs previously considered. Then we studied this hexagonal NW using the same FEM simulation linear model (II.4.1.3.). Figure 57a and b show the piezoelectric potential distribution in a bended hexagonal NW. The maximum potential is 20mV higher than the potential generated by a circular NW of d=50nm and 25mV lower than a circular NW of d=43.3nm (Figure 57c) (which represents the narrower diameter of the honeycomb NW). In addition we noted that the inversion potential at the NW base is much stronger using the hexagonal shape. The influence of the mesh will be check first to be sure.

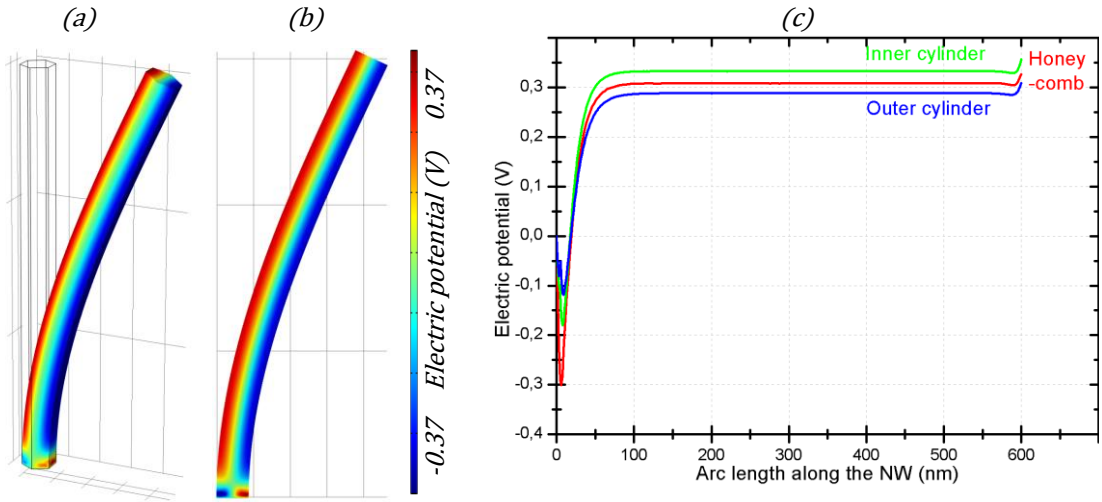

Figure 57 (a) 3D electrical potential distribution of an hexagonal piezoelectric NW (l=600nm et d=50nm) under lateral bending force (F_y=80nN), (b) YZ cut view of the electric potential distribution and (c) evolution of the electric potential along the extended edge of the NW as function of the Z axis and compared with two circular NW (r=25nm and r=21.5nm).

The middle cross section of the honeycomb NW (Figure 58a) shows that the potential distribution is still anti-symmetric relative to the y axis but the equipotential curve are not anymore parallel. The potential distribution is curved around the maximum and minimum potential pole.

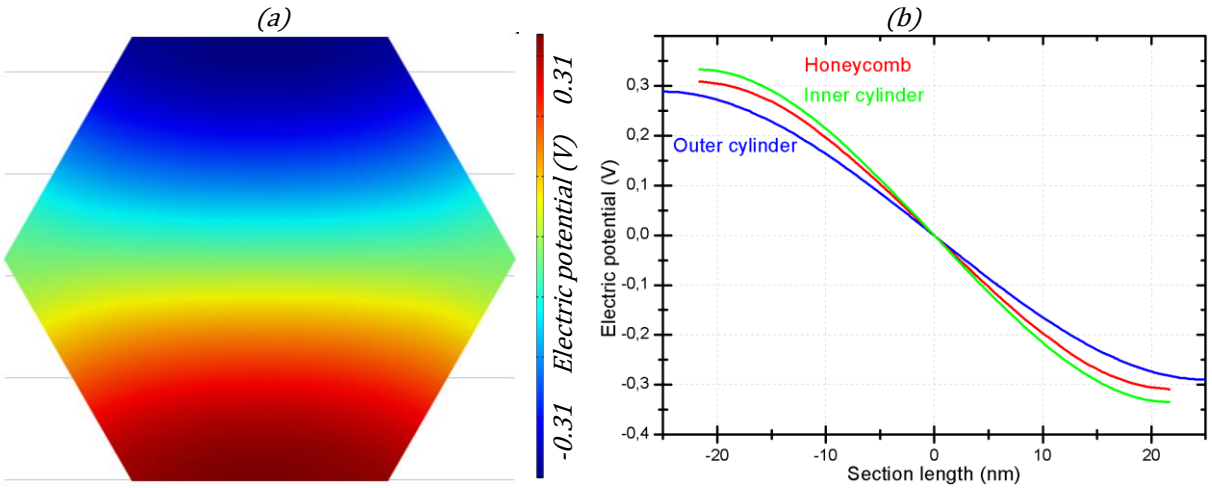

Figure 58 (a) XY middle cut view of the potential distribution of an hexagonal piezoelectric NW (l=600nm et r=25nm) under lateral bending force (F_y=80nN) and (b) evolution of the electric potential across the middle of the NW as function of the Y axis and compared with two circular NW (r_{out}=25nm and r_{in}=21.5nm).

Finally, the FEM simulation of a hexagonal NW demonstrates that the difference of potential between the circular and honeycomb NWs is small (≈6%). The piezoelectric potential generated by the hexagonal NW has almost the same potential distribution that of circular NW and its maximum value is equal to the potential generated by a circular NW of diameter d=46.7nm. So the circular shape approximation of wurtzite piezoelectric NWs leads to underestimate the potential generated by 6% which is equivalent to consider smaller cylindrical NW. But this aspect is negligible because of the growth variability and the Gaussian size distribution of the NW in experimental samples which have a bigger impact than the shape factor.

III.1.3. Role of the substrate and environment

As we saw about the electrical properties of NWs (I.4.3.5. c), the environment of the NW can greatly influence its electrical properties. That's why we will investigate the effect of the environment of the NW (substrate, seed layer and atmosphere) on the distribution of the piezoelectric potential generated by the NW under bending.

The FEM simulations of the distribution of the piezoelectric potential in a ZnO NW bended on a conductive substrate set to ground (Figure 31) shows that the potential is uniform along the NW similar to a plate capacitor and that there is a small area of potential reversing at the base of the NW which is due to shear forces. In Figure 59a we present the simulation results of the bending of a ZnO NW on a conductive silicon substrate surrounded by air. We note that the generated potential remains similar but the electric field lines are no longer concentrated in the NW but they extend into the surrounding air. The potential distribution remained similar to the previous case. A second simulation of a NW on an insulating substrate is presented in Figure 59b. In this case we see that the inversion of potential generated at the root of the NW is much stronger (8 times) and propagates further into the NWs and in the surrounding environment whereas the potential distribution in the upper part of the NW remains identical. This sharp increase is due to the fact that in the case of a conductive substrate, the ground boundary condition applied at the base of the piezoelectric NW greatly restricts the piezoelectric conversion of the high shear strain underwent at the root of the NW. This issue has already been noted by [266] when moving the ground boundary condition on the edge of the NW as grounded electrode.

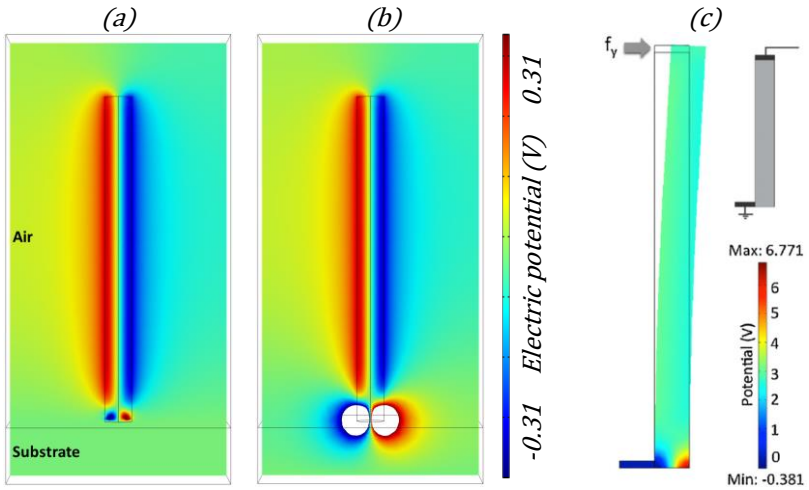

Figure 59 Distribution of the piezoelectric potential generated by a ZnO NW under bending (F=40nN), surrounded by air and clamped (a) on a conductive and grounded silicon substrate, (b) on an insulating silicon substrate. (c) Potential distribution in a bent ZnO NW grounded at the bottom left corner [266].

However in many cases such as the hydrothermal growth of ZnO NWs, a seed layer of about 50nm thick between the NW and the substrate is used to reduce the lattice mismatch of the materials and promote the growth of nanostructures. To consider this more realistic case, a 50nm thick seed layer was added to the model (Figure 60a). Adding the seed layer on a conductive substrate has the effect of separating the ground boundary condition from the NW root and its clamp boundary condition where shear stress occurs. This allows high mechanical stresses localized at the clamped level of the NW to be converted into electric potential depending on the thickness of the seed layer. The thicker the seed layer, the stronger the electric potential generated is. However, the seed layer is also constituted of piezoelectric ZnO. Therefore it will also undergo some mechanical stress and will generate a piezoelectric potential that will influence the overall distribution of the electric potential in the system. Thus we see that the inversion of the potential at the NW root extends and widens in the seed layer. This has been noted in [194] (Figure 60d) where the same phenomenon is present.

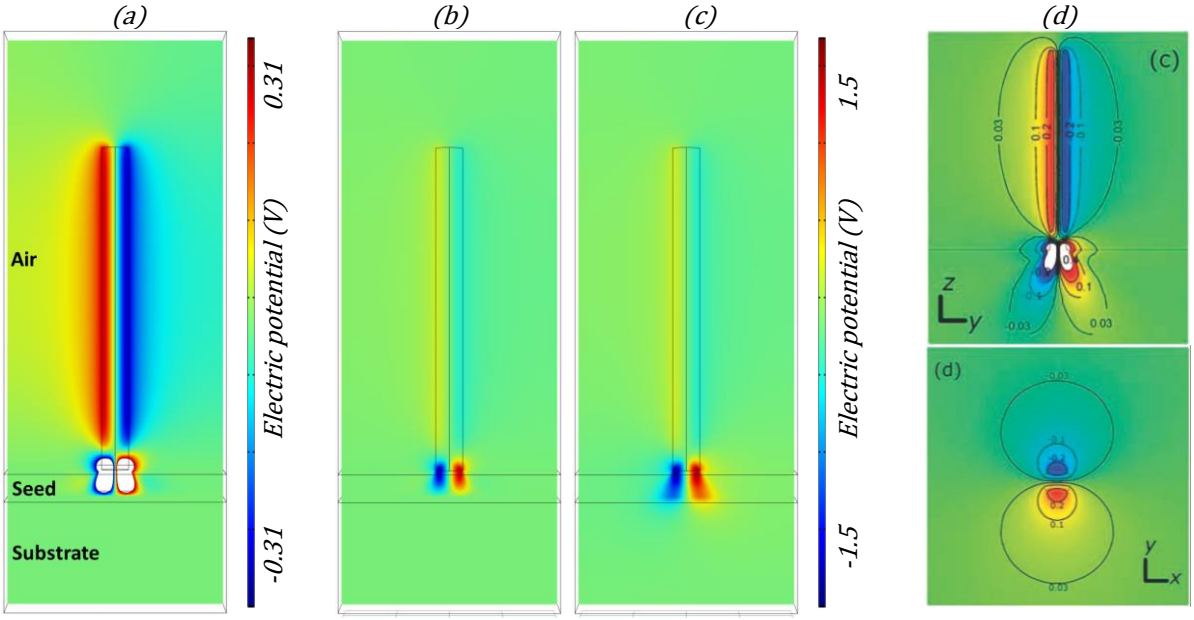

Figure 60 Distribution of the piezoelectric potential generated by a ZnO NW under bending (F=80nN), surrounded by air, clamped on a ZnO seed layer (w=50nm), (a) and (b) on a conductive and grounded silicon substrate and (c) on an insulating silicon substrate. (d) Potential distribution in a ZnO NW [194].

Finally, by comparing distributions of the piezoelectric potential generated by a bended ZnO NW surrounded by air, on a ZnO seed layer and on a conductive substrate (Figure 60b) or insulator (Figure 60c), it is noted that these distributions are relatively similar and in agreement with literature [194]. But the maximum potential at the base of the NW increase by 6% considering a ground substrate of Si and by 765% for a non-grounded substrate of SiO_2. The addition of a seed layer of 50nm increases this potential by 339% having a grounded substrate and by 368% if not grounded. They have a small equipotential along the NW and a strong inversion region at the root of the NW and stretched in the seed layer. Thus the electric potential extend distribution is quite different from that obtained by the simulation of a single NW without considering the surroundings (Figure 31). This has to be taken into account when conducting experiments and applications involving the piezoelectric potential generated at the root of the NW.

III.1.4. Screening effect

In the previous chapter we studied the behavior of purely piezoelectric ZnO NWs. However, ZnO NWs epitaxially grown are typically n-type doped due to unavoidable point defects and impurities [124], [125], [267]. Similarly GaN is also a semiconductor material with n-type intrinsic doping. Although the application of piezoelectricity in semiconductor devices has already been studied in GaN/AlGaN high electron mobility transistors (HEMTs) [268]–[270], the piezoelectric fields are constant in these devices as they are introduced by the interface strain which remain the same after fabrication. In contrast, the mechanical flexibility of piezoelectric compound NWs provides a more versatile platform to utilize the physics of piezoelectricity in semiconductors.

To model a semiconductor material with a significant amount of free charges, which are able to distribute all over the material masking the piezoelectric potential, the Lippman theory [52] cannot be directly applied. A model of this problem has been developed by Gao [194] in order to investigate the effect of doping on the piezoelectric behavior of laterally bent ZnO NWs. In addition few other studies also discussed the electric potential distribution when the thermodynamic equilibrium among free charge carriers is achieved for NWs with different doping concentrations [195], [271], [272].

In a ZnO NW (l=600nm and d=50nm) without free charges and bent by a lateral force of 80nN, the extended part of the NW exhibits a positive potential of 0.3V while the compressed part has an opposite potential of -0.3V (II.4.1.3.). When considering a semiconducting piezoelectric material, the free electrons and holes carriers redistribute according to the electric field created by the piezoelectric polarization. Thus in order to investigate the behavior of a bent NW, both the piezoelectric constitutive equation and the redistribution of electrons under thermodynamic equilibrium, given by the Fermi-Dirac statistics, must be taken into account.

The as-grown ZnO NWs are intrinsically n-type. In general, when the doping level is very low (on the order of $10^{14}cm^{-3}$) the density of free charge ρ_l is negligible compared to the equivalent piezoelectric charge density ρ_p. We can therefore neglect the contribution of free charges to the establishment of the electric potential. Nevertheless the donor concentration N_d varies according to the growth conditions with a typical concentration around $10^{17}cm^{-3}$ [267], [273]. This is the case of our non-intentionally doped ZnO NWs grown by hydrothermal process [274], [275] where the density of free charge can easily reach 10^{16} to $10^{17}cm^{-3}$. The consequence of this is that the electric potential decreases and falls to a value of 0.05V in the extended part of the ZnO NW. The negative part of the potential is preserved and reaches -0.3V. The decrease of the potential is due to the screening of the piezoelectric charge by free carriers. When the NW is bent, a charge density ρ_p (Equation 52) is created due to the

piezoelectric effect. This means that the potential is created by the polarizations of anions and cations in the NW; these charges cannot freely move as long as the strain is preserved. This charge is positive in the extended part of the NWs and results in a positive potential. This causes a lowering of the conduction band of the ZnO and decreases the energy levels [276]. On the contrary, a negative potential is established in the compressed part of the NWs and raises the levels of the conduction band. The free electrons in the conduction band occupying in priority the lowest energy levels; they will accumulate in the extended part of the NWs where the potential is positive and screen ρ_p. In the compressed part of the NW, a depletion region of free electrons is formed (Figure 61).

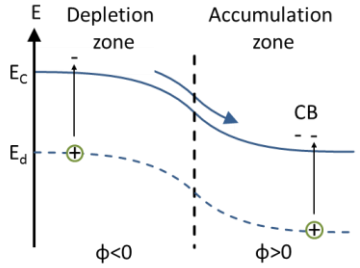

Figure 61 Effect of ϕ on the energy levels of the CB and the distribution of free charge carriers.

Articles [195] show that as the donor concentration N_d increases, the electric potential is almost completely screened at both sides. For a NW with a very high donor concentration $N_d>10^{18}cm^{-3}$, total neutralization of the piezoelectric potential occurs everywhere. Thus, a NW with a high concentration of free charge carriers is expected to exhibit a very small piezoelectric potential. This result is in agreement with the literature concerning the NG behavior under UV light [245].

III.2. Mechanical sensors

III.2.1. Introduction to mechanical sensors

The development of nano-newton force sensors to help and control the manipulation of micro and nano particles, objects or living cells has become a great technological challenge for advanced micro and nano assembly and future living cell manipulation. They have been widely explored in the fields of cell motility study [277], [278] and micro object manipulations [279], [280]. Micromanipulation with force control is an emerging area, indeed manipulating objects with higher dexterity could be facilitated by controlling the forces involved in the manipulation process. When manipulating micro and nano objects, especially delicate structures or biological materials that are fragile, pure position control is not adequate to ensure success and prevent damage to the object. Thus force control is often needed to achieve better manipulation results. Moreover, in applications such as individual cell based diagnosis or pharmaceutical test, obtaining force information is the main objective. Most of MEMS force sensor designs, as reported in [279], [280] use in-plane (lateral) sensing mechanism. From those one, microfabricated cantilevers have proven to be a reliable approach for monitoring biomolecular interactions [281]–[284]. Thus a lateral force-sensing cantilever can be used for force feedback on micro-probing, manipulation, positioning and cell separation.

The bending of a cantilever is related to the applied force. By monitoring its displacement, the amplitude of the applied force can be extracted. Several sensing methods can be used to detect forces: piezoresistive, capacitive and optical/laser detection. The optical method, mostly used in AFM, is based on focusing a laser spot on the cantilever and then monitoring the motion of the reflected light using a quadrant photodiode [285], [286]. This method is very powerful in measuring small

displacements, but it requires a highly accurate alignment of the optical system which can be complex. The tip of the cantilever should be larger than the laser spot size. The method therefore becomes very difficult when the size of the cantilever decrease [287] due to the low reflection of small cantilevers.

The capacitive method is based on the capacitance change when the structure is deformed and is the most widely used method in micro accelerometers and sensors for harsh environments. However the capacitive structures need to be completely isolated between two electrodes. Usually silicon-on-insulator (SOI) wafers or trench isolation are employed [288]. But, it is difficult to control the etching area to obtain a completely isolated structure at small scale. Moreover, the capacitive method requires complicated electronic circuits.

Piezoresistive transducers translate a force into a change in the value of a resistance. They are widely employed as sensing elements in pressure sensors, accelerometers, and cantilevers used as: nano mechanical sensors [289], binding force sensors [290] and bio-chemical mass sensors [291]. Recently, the developments of fabrication process have resulted into submicron piezoresistive cantilevers with pN resolution [292]. However, most of these force sensors are limited in their application because they employ vertical stack structures which can only detect the forces perpendicular to the wafer surface. In addition, to obtain high resolution, cantilever size has to be as small as the possible. So the fabrication of self-sensing piezoresistive thin cantilevers requires a technology that can create ultra-shallow piezoresistors on small cantilever.

Here we propose to use ZnO and GaN piezoelectric NW as force, displacement or pressure sensors. Compared to other technologies it has the advantages of being easier to build and integrate at nanoscale, it can be set up in 3D and very importantly, piezoelectric sensors can be self-powered.

III.2.2. Voltage measurement based force and displacement sensor

This parte has been done in IMEP-LACH with the intern M. Julien Keraudy who I co-advised and in collaboration with the CEA-LETI with the intern M. Julien Ferrera who I co-advised for the IMEP-LAHC part. We studied mechanical sensors based on the potential generated by strained piezoelectric NWs [234].

As explained before the generated potential depended on the force or displacement applied on the NW and also on its geometry and material properties. Thus it is theoretically possible to create a force or displacement sensor using piezoelectric NWs and measuring the piezoelectric potential generated. Such a sensor needs first to be investigated and fully evaluated in term of resolution, sensitivity and range of measurements. Of course we are aware of the actual challenge that represents the integration of such a piezoelectric NW as a nano sensor. But this kind of device have the advantage to be simple in principle, very small, tunable (thanks to the NW material and size), and self-powered because of its piezoelectric properties. In addition by scaling down piezoelectric materials, smaller forces are needed to bend the piezoelectric NW or nano-cantilevers.

Previously (II.4.) we related the geometrical and material dependent characteristics of NWs, their radius r, length l and piezoelectric coefficients d_{ij}, to the main figures of merit of the piezoelectric potential generated. This is applicable to mechanical sensors and we can define 3 working hypotheses: constant force (F), constant bending (δ) and constant pressure (P). Within this new frame, ΔV scaling with r was calculated for a given NW length at constant δ, F and P. Nevertheless the linear approximation is valid as long as $\delta<r$, with a generated potential difference (ΔV) in the range of several tens of mV only. Device applications require larger values of ΔV and δ, for which the linear approximation does not hold. Non-linear models were thus used which strongly modified the resulting

potential profile, with values routinely reaching several hundreds of mV (III.1.1.). Within this new frame, ΔV scaling with r was calculated for a given NW length of l=600nm at constant δ, F or P (Figure 62a). It highlights the necessity of contacting NWs in a bottom contact configuration, 30 nm above the substrate, which is effective for sensing applications with *ΔV* increasing linearly with *δ*, *F* or *P* in continuation with the linear model at small displacements (Figure 62b). Larger sensitivities would be achieved with a top-bottom contact configuration. However, such configuration remains technologically out-of-reach to date and would lose linearity for high forces.

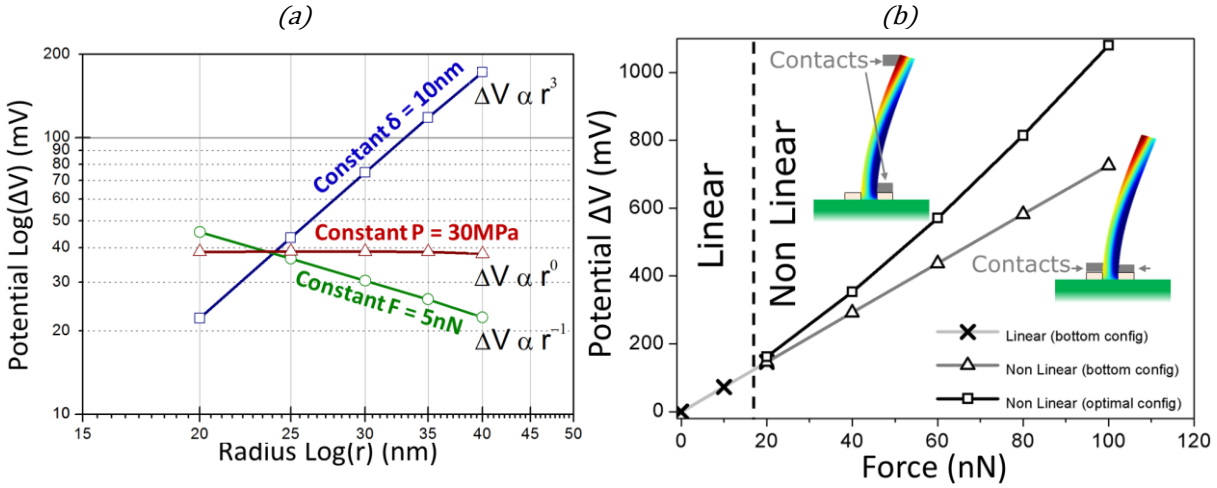

Figure 62 (a) Variations laws of ΔV(r) for a given NW length l (600nm). Different cases at similar NW deformation rates: constant F (5nN), constant δ (10nm) and constant P (30MPa). (b) ΔV(F) in the linear and non-linear cases. In bottom contact configuration, the potential increases following a linear law ($a=7.3\times10^6$ V/N), whereas in the "top-bottom" contact case, $\Delta V=bF+cF^2$ with $b=7.5\pm0.1\times10^6$V/N and $c=3\times10^{13}$V/N² [234].

To tackle the issue of improving sensitivities and integration densities beyond MEMS technologies, scaling of NW-based force (texture), displacement (position) and pressure (flow) sensors were simulated with our model. In the constant F or δ cases, a Gaussian dispersion of r, based on experimentally extracted distributions of ZnO NWs grown by MOCVD (Figure 26), induced the piezoelectric potential distributions of Figure 63 and the sensitivities calculated in Figure 64.

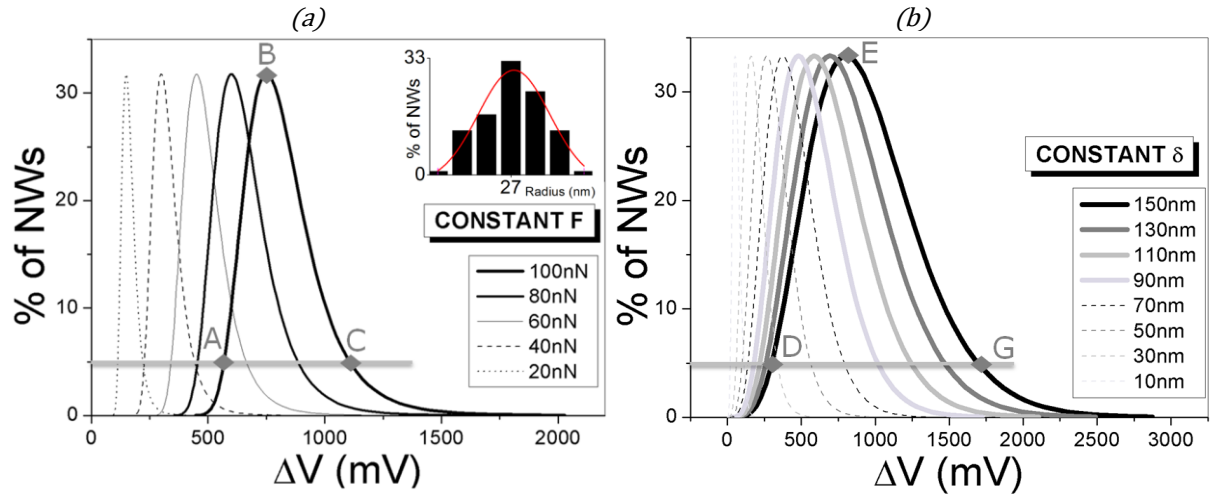

Figure 63 Normalized potential distributions for different values of (a) F applied on a matrix of NWs with the radius dispersion given in insert. The maximum B corresponds to 31% of r=24nm NWs. For 5% of NW, r=16 (C) or 32nm (A). And (b) δ applied to a matrix of NWs with the radius dispersion given in Fig.8. The maximum E corresponds to 33% of r=27nm NWs. For 5% of NW, r=19 (D) or 34nm (G) [234].

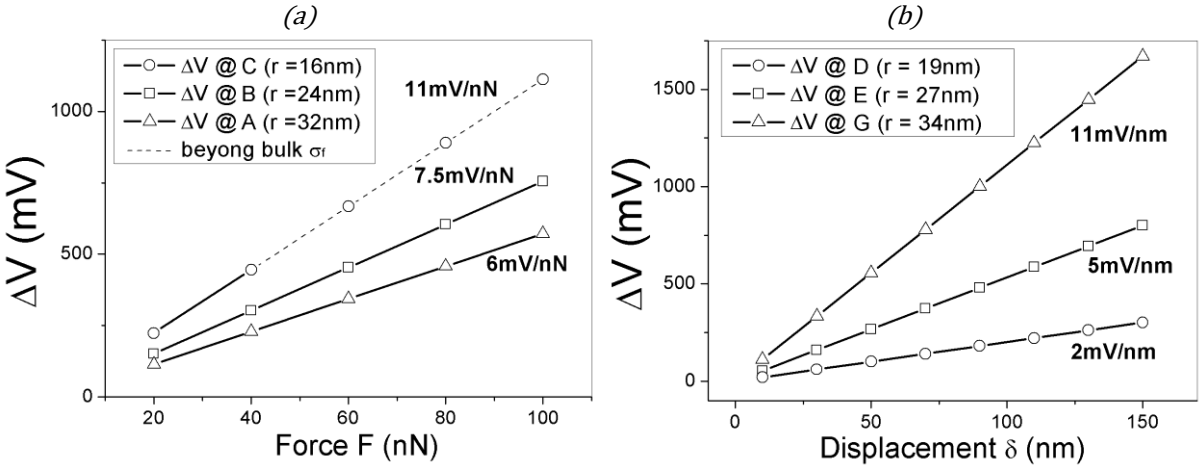

Figure 64 Sensitivities in mV/nN for various r NWs. (a) Lateral resolution drops by a factor of 2.6 between (C) and (B). The case 11mV/nN (r=16nm) may be questionable since beyond reported fracture strength (σ_f) of ZnO NWs for F>30nN. And (b) Lateral resolution also drops by a factor of 2.6 between (G) and (E). σ_f is not limiting in this case (large δ is applied on large r for highest sensitivities) [234].

The highest sensitivities, of the order of 10mV per nN or nm for the given example, were achieved by the NWs in the distribution that featured the smallest r for F sensing (point C in Figure 63a) and the largest r for δ sensing (point G in Figure 63b) respectively. Such high-sensitivity configuration is best suited for collective NW position sensors, since very few NWs contribute to the signal, which leads to a poor spatial resolution. However, for small r and large F, fracture stress σ_f limitations [198] should be considered. On the other hand, lower sensitivity with better spatial resolution may be exploited to calibrate displacement or force field sensors. In that case, many NWs contribute to the signal but sensitivity is divided by 1.5 and 2.2 respectively (points B and E in Figure 63). In the constant P case, all the NWs generated the same potential, independently of the r distribution. The sensitivity is then 1.3mV/MPa and limitations only result from the mechanical properties of NWs. Overall, the model demonstrates the very good performance of NW-matrix-based devices for pressure sensing. Interestingly scaling of GaN NWs to the same dimensions would result in lower sensitivities for F and P sensors (by a factor 2 and 3, respectively) but in almost identical sensitivities for δ sensor. As a result, ZnO is best suited for P and F sensors, whereas GaN may be favored for δ sensors based notably on its better mechanical properties and integration compatibility. In addition, since σ_f decreases as NWs become larger due to the presence of a larger number of structural defects [293], NWs are better suited to these applications than microwires, wherever large deformations are required.

III.2.3. Current measurement based force sensor

This part has been done in collaboration with Professor Z. L. Wang's group in Georgia Institute of Technology where I worked with M. Y. Zhou.

III.2.3.1. Working principle

The piezoelectric potential generated by piezoelectric NWs bent by a transvers force can be directly used to measure a force, displacement or pressure applied on it. But the piezoelectric potential generated can create new effects called piezotronic effects. To explore the piezotronic effect in a GaN NW under a transverse force we bend the end of a single NW using an atomic force microscope (AFM) tip. But this time we measured the current passing through the NW-AFM tip junction. According to the piezotronic effect, piezoelectric NWs can be used to transduce a shear/bending force into a dramatic current change through the NW. Owing to the local piezoelectric potential generated

by the applied force, the barrier height of the Schottky contact between a GaN NW and the platinum AFM tip can be modulated. Using this transduction mechanism, the transverse force can be correlated to the current. Thus it should be possible to realize a force sensor measuring the current passing through a Schottky junction placed on a piezoelectric NW. But this phenomenon is rather new and still needs to be deeper investigated. This section present the experimental demonstration and evaluation of the piezoelectric NWs to act as the main building blocks for micro-/nanometer-sized force sensor based on piezotronic effects.

III.2.3.2. Experimental characterization and modeling

For this experiment we used n-type Si doped GaN NWs. The n-type Si doped GaN NW array was synthesized by plasma assisted molecular beam epitaxy (MBE) on n-type Si (111) substrate (grown by Dr. R. Songmuang from CEA-CNRS Nanophysics and Semiconductors Group at Néel Institute) [294]. The Si cell temperature used for n-type doping was found to an electron concentration of ~2-5.$10^{19}$$cm^{-3}$ in epitaxially grown bulk GaN, as determined by Hall-effect measurements. Figure 65a shows that the NWs are vertically aligned with a uniform length of about 1.5μm.

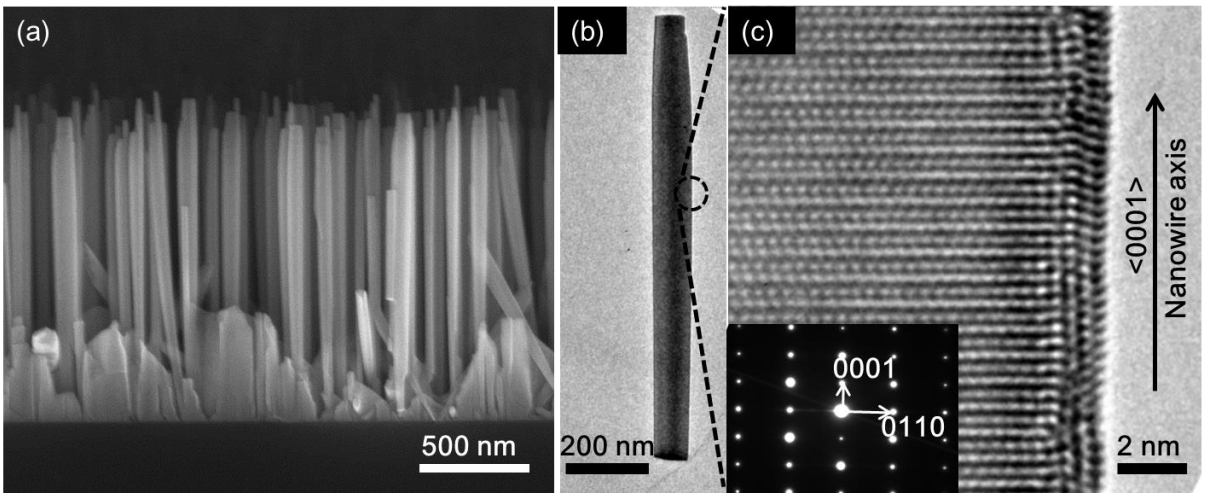

Figure 65 (a) 90˚ tilted SEM view of the vertically aligned GaN NW array grown on Si substrate. (b) Low magnification TEM image of a GaN NW. (c) HRTEM image and corresponding SAED pattern (inset) [248].

Low magnification transmission electron microscopy (TEM) image (Figure 65b) shows that the NW diameter is about 60nm. A corresponding high resolution TEM (HRTEM) image and selected area electron diffraction pattern (SAED) show that the as-grown GaN NWs are single crystalline with a wurtzite structure, and a growth direction of [0001] (Figure 65c).

In order to simulate transverse force conditions, we applied a bending force to the free end of a single GaN NW using an atomic force microscope (AFM), as shown in Figure 66a. To precisely position and control the AFM tip on the side of a single NW, we used the lateral AFM characterization procedure reported [1] and described in II.5.3.2.

In order to characterize the electric transport property under different transverse forces, three steps were applied to the experiments, as shown in Figure 66c. In the first step, the tip was engaged onto the free end of the NW with a preset force. The top curve in Figure 66c shows the applied force during the whole process. The applied force was increased by further deflecting the AFM cantilever. Secondly, after the applied force reached a preset value, the force remained constant during the dwell stage and the electrical measurements were initiated. In this stage, a sweeping bias between -2V and +2V was applied between the NW and the tip as shown in the middle curve in Figure 66c. The bottom curve is the current response to the applied bias. After the I-V measurements were performed, the AFM tip was

retracted from the NW. During both the force exertion stage and I-V measurement stages, any unstable conditions such as the tip sliding over the NW, or external disturbances such as mechanical drifting, can be easily differentiated by monitoring the continuity of the force as a function of time in the extend and dwell stage.

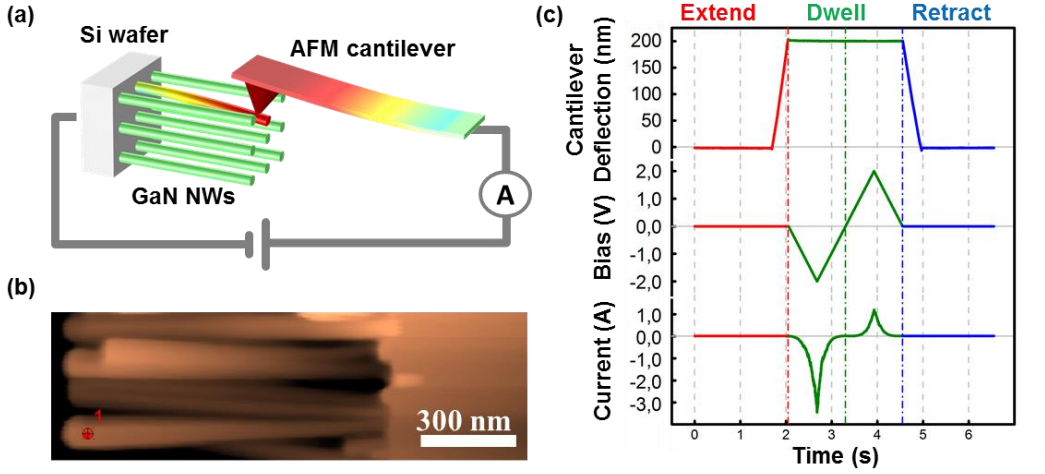

Figure 66 (a) Schematic of the AFM experimental setup. (b) AFM image of a 90° tilted GaN NW. The red mark on one of the NWs indicates the location of the AFM tip during the electrical measurement. (c) Illustration of the experiment process: from top to bottom, the cantilever deflection that is proportional to the applied force on the GaN NW; a bias applied between the AFM tip and the sample; and the corresponding detected current [248].

Prior to the I-V measurements, finite element simulations were done using the modeling linear method described in II.4.1.3. without considering the carrier concentration in the NW, to have a better understanding about the process. The free end of the NW is laterally pushed by the AFM tip with a force of 100nN. The length of the NW was set to be 1µm and the diameter was set to be 60nm. The strain generates a piezoelectric potential in a Ga-polar NW as shown in Figure 67a. It represents the simulated piezopotential distribution of a GaN NW with a growth direction of [0001]. The stretched side of the GaN NW exhibits a positive piezopotential with a magnitude of 0.063V. The compressed side of the GaN NW exhibits a negative piezopotential with the same magnitude as mentioned in II.4.1.3. This piezoelectric potential is proportional to the strain for small forces, as illustrated in Figure 67b. In order to verify the validity of the simulation results, we used the method described by [1] to measure the piezoelectric potential generated by the GaN NW using an AFM tip. As presented in Figure 67c, a positive piezoelectric potential was detected between the AFM tip and the magnitude of the piezoelectric potential is proportional to the force for the small forces applied in the experiments (200nN to 1000nN). Even if the quantitative values are different, the experimental and simulation trends are in agreement.

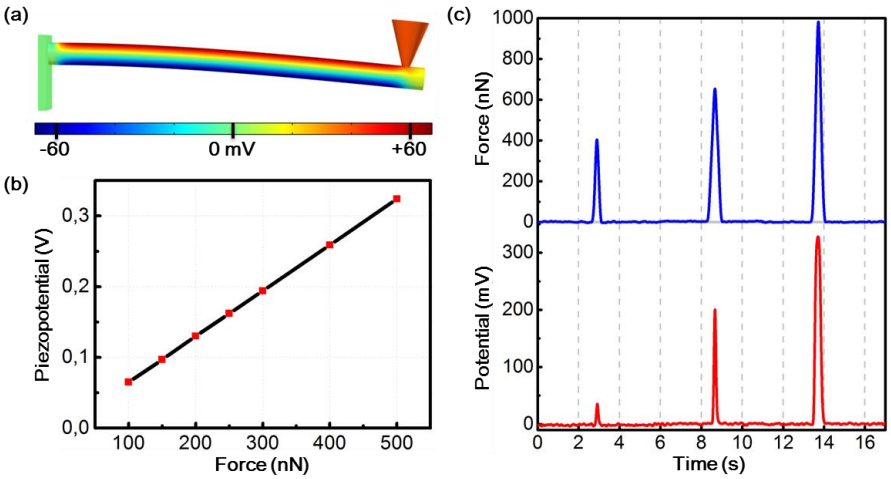

Figure 67 (a) Finite element simulation of the potential distribution at the surface of a GaN NW when subjected to a transverse force. (b) Positive piezoelectric potential generated in the NW as a function of the transverse force applied. The geometry of the GaN NW used in simulation is 1um in length, 60nm in diameter. (c) AFM measurements of the piezoelectric potential generated by a GaN NW under different bending forces.

In the subsequent I-V measurements, there are two metal-semiconductor contacts. One is the contact between the Pt coated AFM tip and GaN NW, while the other is between the silver electrode and the Si wafer. The work functions of the two metals are higher than the corresponding semiconductors' electron affinities. As a result, both contacts are Schottky contacts with different barrier heights. The Schottky barrier height (SBH, ϕ_B) of the Ag-Si contact is assumed to be much lower than that of the Pt-GaN one given that the work functions of Pt and Ag are 5.65eV and 4.26eV [97], respectively, and the electron affinities of GaN and Si are 4.1eV [295] and 4.05eV, respectively. The conduction band discontinuity between GaN NW and Si is negligible due to the 0.05eV difference in electron affinity and assuming a small difference of the doping concentration [294]. The energy band diagram is shown in Figure 68a.

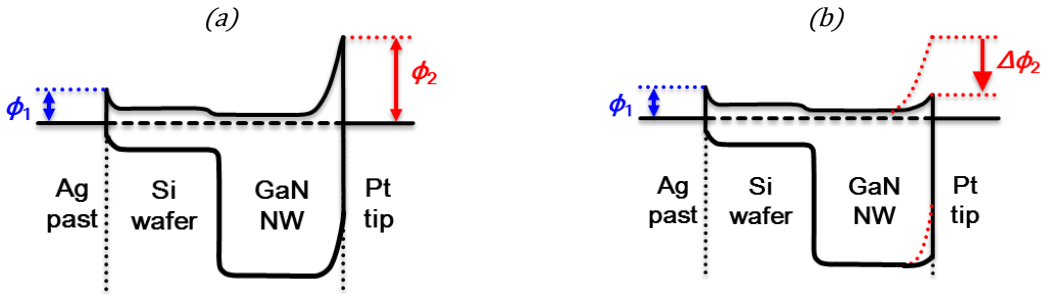

Figure 68 Energy band diagrams of the measured system to illustrate the Ag-Si Schottky Barrier Height between silver paste and silicon substrate (SBH ϕ_1) and the Pt-GaN (ϕ_2) at the contact between the AFM tip and the GaN NW (a) without and (b) with a piezopotential induced by an external forced ($\Delta\Phi$ means the change in the SBH) [248].

According to the piezotronic theory [276], a positive local piezopotential would lower the SBH, as illustrated in Figure 68b, subsequently increasing the current flow through the NW. Due to the Ag-Si contact opposite rectifying direction, the current flow from the Pt to the NW, defined as positive here, would be largely limited by the reversely biased Ag-Si Schottky contact, while the current in the reverse direction, defined as negative here, will be dominated by the Pt-GaN Schottky contact. Therefore, by monitoring the negative current, a change in SBH of Pt-GaN contact can be derived, and the applied force can be quantified.

Experimental results are shown in Figure 69. The current under negative bias dramatically increases as the force increases from 104 to 312nN. This asymmetric current change is mainly attributed to the

piezotronic effect as the piezopotential reduces the SBH between the Pt coated AFM tip and the GaN NW. Under positive bias, the current was largely limited by the reversely biased Ag-Si Schottky junction, which was not affected by the induced piezopotential.

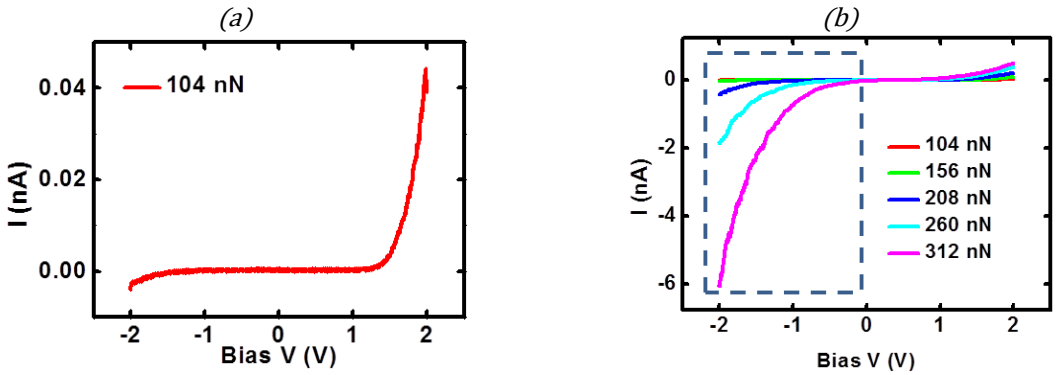

Figure 69 (a) Experimentally measured I-V characteristics under a constant transverse force of 104nN, and (b) at different forces ranging from 104 to 312nN [248].

During this process, the current was also influenced by the change of contact area of the AFM tip and the GaN NW. For simplicity, the tip-NW contact can be modeled as a sphere indenting a flat surface according to the Derjaguin-Muller-Toporov (DMT) model [259]. The contact area A can be approximate to:

$$A = \pi \left[\frac{Rr^*(F + |F_{adh}|)}{Y} \right]^{\frac{2}{3}} \qquad \textit{Equation 86}$$

where r is the AFM tip radius (20 nm), Y is the effective Young's modulus of the tip, F is the loading force, and F_{adh} is the tip–sample adhesion force which is experimentally determined to be 10nN [259].

As shown in Figure 70, using DMT model, the estimation of the influence of the external force on the area of contact shows that it is negligible compared to the detected current change

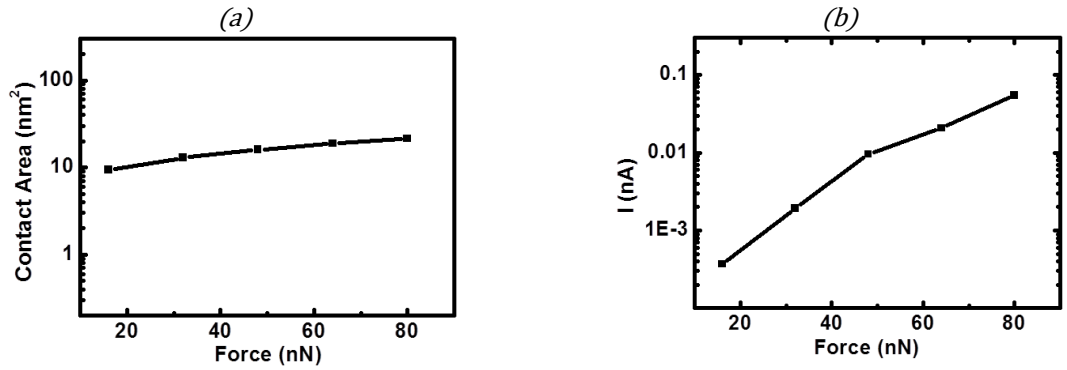

Figure 70 (a) Calculated contact area as a function of applied force. (b) Measured current as a function of applied force.

From experimental data, the current change was analyzed in both forward biased and reverse biased situations. As shown in Figure 71a, the current changes linearly with the force under forward bias, while exponentially with the force under reverse bias. In addition, the relative change of current in forward bias is very small compared to the change in reverse bias, as indicated in Figure 71b. The significant difference between the forward and reverse bias cases shows that the contact resistance is not the cause of the observed phenomenon; otherwise the trends of the two curves would be proportional. Therefore, it is fair to assume that the change of the Schottky barrier height is the dominant factor in our experiment

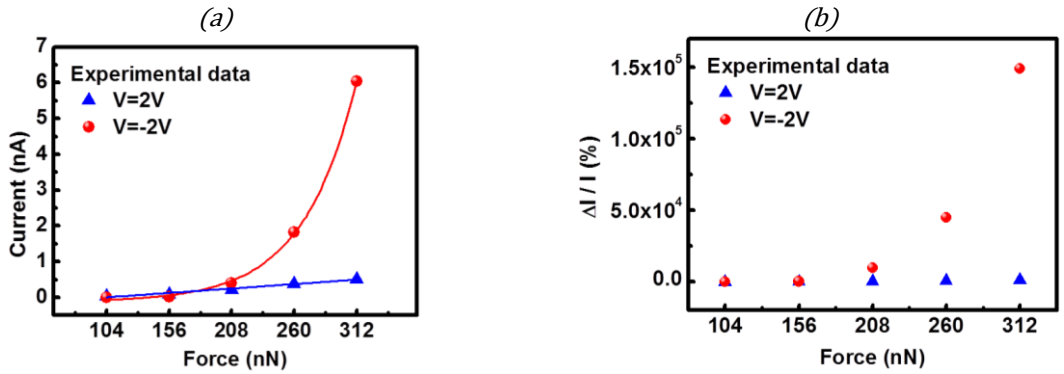

Figure 71 (a) Plot of measured current as a function of applied forces under forward bias (blue) and reverse bias (red) and their respective fitting curves. Red curve is an exponential fit, blue curve is a linear fit. (b) Plot of relative current change as a function of applied force.

To quantitatively calculate the SBH change under the applied transverse force, we employed the classic Schottky models to derive the change in SBH (Φ_B) from the I-V curve. By considering the high doping concentrations (>10^{17}cm^{-3}) of the GaN NWs and that all measurements were taken at room temperature, the thermionic-field-emission (TFE) models is most suitable for analyzing our experimental results [145]. In the TFE models, ln(I) is approximately proportional to V. By plotting ln(I)-V, we found that it has a good linearity as shown in Table 14 and Figure 72. Therefore, this indicates that the thermionic field emission process is dominant.

Table 14 Quality of linear fitting of experimental lnI-F data.

Force (nN)	104	156	208	260	312
Fit Slope	3.44495	3.17552	3.69889	3.22496	2.74963
Standard error	0.01029	0.01603	0.06906	0.01128	0.01229
Adjusted R-square	0.99153	0.98738	0.93177	0.98496	0.98166

In the TFE model the reversely biased current is described by:

$$I = \frac{A.A^{**}.\theta}{k}\sqrt{\pi.E_{00}\left[q.V + \frac{\phi_B}{cosh^2\left(\frac{E_{00}}{k.\theta}\right)}\right]} \times e^{\frac{-\phi_B}{E_{00}.coth\left(\frac{E_{00}}{k.\theta}\right)}}.e^{q.V\left(\frac{1}{k.\theta}-\frac{tanh\left(\frac{E_{00}}{k.\theta}\right)}{E_{00}}\right)} \qquad \textit{Equation 87}$$

*where A is the area of the Schottky barrier, A**is the effective Richardson constant, θ is the temperature, k is Boltzmann constant, q is the electron charge, ϕ_B is the distance between the Fermi energy of the metal to the bottom of the CB of the SC, E_{00} is the characteristic energy determined by the properties of semiconductor material.*

$$E_{00} = \frac{q.h}{4\pi}\sqrt{\frac{N_d}{m^*.\varepsilon}} \qquad \textit{Equation 88}$$

where h is the Planck's constant, N_d is the doping/impurity concentration, m is the tunneling electron's effective mass, and ε is the dielectric constant of the NW.*

Since the square root of V is negligible compared to the exponential term, under the safe assumption that the change in A** under strain is much smaller than the change in the SBH [145], $\Delta\phi_B$ can be approximated using the following expression:

$$\Delta\phi_B \approx -E_{00}.coth\left(\frac{E_{00}}{k.\theta}\right) \times ln\left(\frac{I}{I_0}\right) \qquad \textit{Equation 89}$$

where for GaN NW N_d=5×10^{17} cm^{-3}, m=0.2×m_0 = 1.82469145×10^{-31} Kg, the dielectric constant ε=8.9×ε_0, the characteristic energy E_{00}=9.84×10^{-3} eV and θ is the temperature equal to 300K.*

Based on this method, we can plot $\Delta\phi_B$ as a function of the applied force in Figure 72. The linear relationship is consistent with the piezotronic model described after.

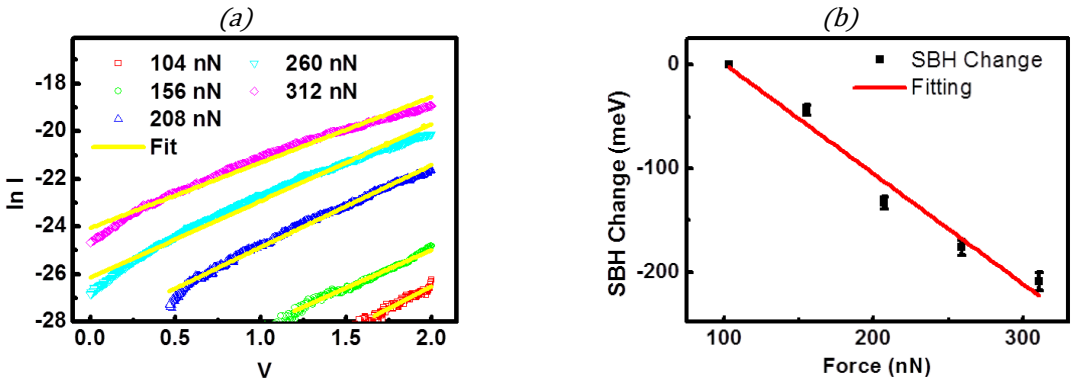

Figure 72 (a) Natural logarithm of the current vs voltage under reverse bias condition, as indicated by the dashed rectangle shown in Figure 69b and corresponding to the TFE model. (b) Calculated SBH change as a function of the applied force [248].

Indeed, according to previous reports about the theory of piezotronics, the induced SBH change is linearly dependent on the piezoelectric charge density ρ_{piezo} [276].

$$\Delta\phi_B \approx -\frac{q.\rho_{piezo}.{w_{piezo}}^2}{2.\varepsilon_{NW}} \qquad \textit{Equation 90}$$

where w_{piezo} is the width of the piezoelectric polarization charge layer.

Under bending, the piezoelectric charge density depends on the NW's electrical and mechanical properties, geometry and applied force [194] as described in Equation 91:

$$\rho_{piezo} = F\frac{r}{I_x.Y}[2(1+\nu)e_{15} + 2\nu.e_{31} - e_{33}] \qquad \textit{Equation 91}$$

where F is the applied transverse force, r is the NW radius, I_x is the momentum, E is the NW's Young's modulus, v is the Poisson ratio and e_{ij} are the piezoelectric coefficients

From Equation 87 to Equation 91, the transverse force could be linearly related to the change in the natural logarithm of the detected current Δln(I).

$$F \propto \rho_{piezo} \propto \Delta\phi_B \propto \Delta ln(I) \qquad \textit{Equation 92}$$

Figure 73 shows the sensitivity and response time characterized by AFM. First, a current change under certain working bias (V=-2V in this case), was recorded while increasing the transverse force by steps of 16nN. As shown in Figure 73a, the corresponding current, which is presented in semilog form, increased exponentially with applied force, consistently with the model stated above. Due to the exponential relationship between current and force, the NW has different sensitivities in different force ranges, where the sensitivity S_I is defined as $\Delta I/\Delta F$ meaning the variation of the current as the force is changed. In lower forces range (16 to 32nN), the sensitivity is about 0.5pA/nN; for larger forces range (64 to 80nN), the sensitivity is about 2pA/nN. From Figure 73a, since current change with increasing force can be clearly differentiated, it is fair to claim that the force resolution is better than 16nN.

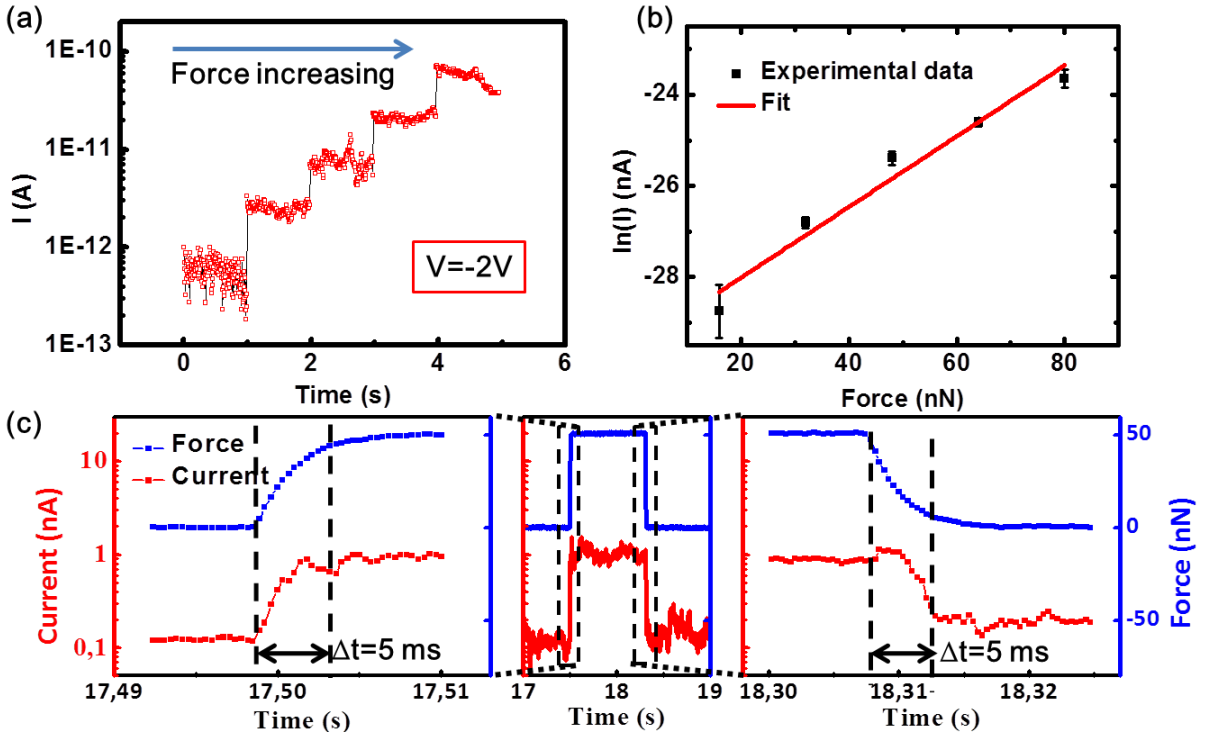

Figure 73 (a) Under constant applied voltage, the current passing through the GaN NW increased step-by-step as the applied force increased. (b) ln(I)-F curve demonstrating a linear relation between ln(I) and the applied force. (c) Time response of the current change as force changes (middle), with zoom on the response to the increased force (left) and deceased force (right) [248].

For practical applications, a sensor with a linear relationship between the input and output is preferred. Therefore, in our case, the ln(I) can be used as a metric to linearly represent the applied force. From the ln(I)-F fitting line in Figure 73b, the sensitivity defined as $\Delta\ln(I)/\Delta F$ meaning the variation of the natural logarithm of the current as the force changes, is calculated to be 1.24 ±0.13 ln(A)/nN by linear fitting. The response time was monitored by maximizing the sampling rate of the signal input channels of the AFM system. From Figure 73c, the current responds very well to the change in force for time intervals of 5ms, suggesting that the sensor has no remarkable delay in response at a frequency of 200Hz. In the piezotronic transduction process, the strain induced carrier redistribution and Schottky barrier change is much faster than mechanical deformation which is so the frequency limiting factor.

III.3. Conclusion

In this chapter, we have investigated and discussed the main piezoelectric semiconducting NW related issues that were not previously taken into account. We have shown that the nonlinear behavior of piezoelectric NW must not be neglected when considering high forces cases. Such nonlinear mechanics generates a non-linear piezoelectric potential distribution with the NW. The substrate and the buffer layer also play an important role in the distribution of the piezoelectric potential within NWs. For instance we have shown that the piezoelectric potential is multiplied by a 2.5 factor at the NW base and that it spreads through the substrate. Such a phenomenon could help to simplify device connections and increase sensitivity. It is important to consider all these aspects because they can strongly influence the piezoelectric field and thus affect the design of NW based devices. Finally the semiconductor properties of ZnO and GaN NWs should not be ignored because they can strongly decrease the electric potential generated in doped NWs and therefore decrease device performances.

Piezoelectric NW technology offers an ideal approach for integrated nanomechanical sensors array. The core of this technology, piezoelectric semiconducting NWs, is IC compatible, can be densely integrated and sensor signal is self-powered by the piezoelectric effect which generated an electric potential proportional to the applied force. The piezoelectric NW geometry can be tuned and respond to compression and bending which can potentially create a 3D force or displacement sensor.

We have investigated the theoretical capabilities of voltage force sensors based on GaN NW arrays. The main figures of merit were discussed in different working conditions (F, δ, P) corresponding to a wide variety of sensing applications. We concluded to several important trends concerning device design and material choice. Depending of the targeted application, the NW arrays response can be optimized by selecting the appropriate NWs size. We have shown that a high sensitivity, up to 10^7V/N should be accessible (allowing detecting nN forces, nm displacements or MPa pressures), which is a strong improvement considering comparable piezoresistive devices with sensitivity around 3×10^2V/N [296].

Experimentally we have demonstrated transverse force sensing capabilities of vertically aligned GaN NWs using piezotronic effect on the current passing through a metal-GaN NW junction. Using an AFM we have checked that by modulating the Schottky barrier height thanks to the piezoelectric phenomenon, the external transverse force could be linearly related to the natural logarithm of the current flow. The transverse force sensitivity is calculated to be 1.24 ±0.13 ln(A)/nN, with a response time less than 5ms, which are very impressive values. This nano-Newton force sensor demonstrates the potential for piezoelectric semiconductor materials to be used as the main building block for micro/nano sensor arrays.

Chapter IV. Piezoelectric NWs based mechanical energy harvesters

One of the new perspectives of the piezoelectricity at nano scale concerns the field of mechanical energy harvesting. Nowadays harvesting green and renewable energy from environment is one effective response to the power supply of autonomous systems needing from tens of µW to few mW [297]. Especially the mechanical energy is among the most abundant and reliable energy sources in our daily life, which is accompanying us regardless of the weather or temperature conditions. We differentiated three methods to harvest the mechanical energy using piezoelectric phenomenon. Firstly we can use vibrating piezoelectric nanostructures. But the mechanical resonance frequency of such devices is high (a few MHz) and thus difficult to be adapted to harvest mechanical energy from human sources, except probably from ultrasound. Secondly the energy harvesting device can work under compression cycles. We have studied a simple structure composed of semiconductor piezoelectric NWs immerged in a soft insulating polymer and packaged within bottom and top electrodes. To evaluate the performances of this simple structure we have developed an analytical model and we have performed FEM simulations to optimize it. We have fabricated prototypes using the hydrothermal growth of ZnO NWs and we have characterized those. Thirdly it is interesting to harvest the energy from movements using bending structures. Our simple design using vertical NWs allows also harvesting the bending movements of the substrate. Harvesting compressions and bending movements with a simple design is a strong advantage and has motivated the study of our design using models in the bending mode. Finally we have experimentally investigated this kind of device.

IV.1. Introduction to mechanical energy harvesting

IV.1.1. Harvesting mechanical energy

Ambient energy sources are diverse, particularly in the human environment. Mechanical sources are induced by various environmental phenomena or related to the human body and to the human activity. Indeed, the human body stores and dissipates a significant amount of energy [298] .It is important to note that the mechanical energy available in our environment has a wide spectrum of frequencies and time-dependent amplitudes. This type of energy is called random energy and can come from irregular vibrations, light airflow, noise and human activity. In addition to mechanical sources related to the environment or to the human being, thermal energy or electromagnetic radiation (light and high frequencies associated with wireless communications) in the environment could also be an exploitable source of energy. However, for the reasons given before (I.3.1.) we focus on the mechanical energy in this thesis.

Mechanical energy can take many forms: our environment is constantly subjected to vibration, pressure, forces, air and liquid flows. The magnitude of such energy could be small, which may exclude the application of some conventional energy harvesting technologies because the available mechanical force may not be strong enough to drive the generator. In addition, the frequency range of the available signal can be quite wide, but most of the energy is at low-frequency under 200Hz. Mechanical sources can come from the movements of the human body, natural or voluntary, but also of the ambient vibrations coming from surrounding machinery and human activity.

IV.1.1.1. Human body movements

The power dissipated by the human body is related to the power consumed by the body to perform a mechanical action multiplied by the performance of metabolic conversion. Indeed, at rest or during any activities, the human body converts energy expressed in calories per hour or Watts. Starner [298] has listed the calorific power consumption for different activities like sleeping , standing , playing piano , swimming (Table 15). For example, the calorific power consumed when driving a car is about 160W, and when swimming it goes to 580W. For the production of mechanical work, the human energy efficiency is not perfect; it goes with losses that come out as an exothermic emission. The corresponding conversion efficiency is estimated to 25 % which allows us to estimate the recoverable power. From the previous examples, while driving a car, the mechanical energy produced is only 40W and 150W for swimming.

Table 15 Mechanical energy from typical body motions [247]

Activity	Mechanical energy (W)
Walk	67
Upper limbs	3
Exhalation	1
Blood flow	0.93
Breath	0.83
Finger type	6.9-19 10^{-3}

IV.1.1.2. Vibrations from environments

Ambient mechanical vibrations are of various types: vibration, stress, shock and deformations. They are generally caused by machines, but can also be induced in the walls and floor by transports or weather for example (Table 16).

Table 16 Summary of several vibration sources [16], [299].

Vibration source	Acceleration ($m.s^{-2}$)	Frequency peak (Hz)
Car engine compartment	12	200
Base of 3 axis machine tool	10	70
Blender casing	6.4	121
Clothes dryer	3.5	121
Person tapping their heel	3	1
Car instrument panel	3	13
Door frame just after door closes	3	125
Small microwave oven	2.5	121
Wooden deck with foot traffic	1.3	385
Breadmaker	1	121
Windows next to a busy road	0.7	100
CD on netbook computer	0.6	75
Washing machine	0.5	109
Second storyfloor of busy office	0.2	100
Refrigerator	0.1	240
HVAC vents in office building	0.2-1.5	60

These resources are characterized by their frequency of vibration and their acceleration. A combination of theory and experiment [16] shows that about 200μW.cm^{-3} could be generated from vibrations that might be found in certain building environments. About noise, there is far too little power available from acoustic noise to be of use in the scenario being investigated, except for very rare environments with extremely high noise levels.

IV.1.1.3. A large range of applications

Many mechanical energy sources are available in our environment (Table 17), whether being vibratory or consisting of shocks, stresses and strains. The more the mechanical energy sources are numerous, varied and widely available, the more the number of potential application is great. The application examples are numerous and cover various sectors (Table 18). There are niche markets with strong potential of sympathy, large scale markets with high economic potential and emerging markets.

Table 17 Potential source of mechanical energy in our life environment for MEMS mechanical energy harvesters

Human body motion	• Breathing, exhalation • Blood flow & pressure • Walking, jogging • Arm and finger motion • Talking …
Transportation	• Automobile • Train, aircraft, boats • Tires, tracks, peddles, brakes, turbine, engines, vibration, noises …
Infrastructures	• Roads, bridges, tunnels • Farm, house structure • Control-switch, AC system • Water/gas pipes …
Industry	• Motors and robots • Compressors, pumps, chillers, fans • Vibrations, cutting and dicing, noise …
Environment	• Wind • Ocean currents and waves • Earth qurake, acoustic …

Table 18 The numerous potential application of MEMS mechanical energy harvesters in daily life.

Transport	• Monitor the tire pressure • Anticipate the failure of mechanical parts • Temperature or vibrations monitoring • Predictive maintenance
Industry	• predictive maintenance of machinery
Infrastructure	• Anticipate failures and cracks • Temperature or vibrations monitoring
Housing	• Wireless switches • Strain, temperature, light, cracks, presence wireless sensors
Health care	• Autonomous pacemakers • Independent hearing implants • Autonomous blood pressure sensors
Environment	• Monitoring parameters to help agriculture • Anticipate disaster (tsunami, volcano)
Defense and space	• Monitoring equipment and people • Border surveillance
Consumer electronics	• Reduce the frequency of reloads (MP3 player, remote control, ...)

IV.1.2. The mechanical energy conversion technology

IV.1.2.1. Mechanical energy harvesting technologies

To achieve a conversion of mechanical energy into electrical energy, several physical phenomena can be used. The most studied and used are piezoelectricity, electrostatics and magnetism. Each has some physical ability to convert and store energy depending on the principles and variables it involves. Piezoelectricity is the one that has the largest range of power densities and voltage attainable and

which is particularly suitable for the conversion of stresses, strains, shocks and vibrations into electric energy.

Each technology also has its advantages and disadvantages which is important to assess (Table 19). Piezoelectricity has many assets that are particularly suited to mechanical energy harvesting. Indeed ZnO and GaN piezoelectric NWs have the advantage of being compatible with the microelectronics industry, they generate high voltages and nanoscale piezoelectric coupling increases [29]. In addition the impedance of piezoelectric semiconductor NWs is lower than common piezoelectric ceramics. Finally, using nanostructures, it is possible to tune the structures and material to increase the overall properties of the piezoelectric layer in the manner of a fibrous composite material [59], [300].

Table 19 Advantages and disadvantages of electromagnetism, electrostatics and piezoelectricity for the mechanical energy harvesting [301], [302].

Technology	Electromagnetic	Electrostatic	Piezoelectric
Advantages	High coupling High output currents	Compatible with MEMS industry High voltages generated	Compatible with MEMS industry High voltages generated High coupling
Drawbacks	Difficult MEMS integration Low voltages generated Coils are resistive at low frequencies	Voltage source required High impact of parasitic capacitances Mechanical system needed	High impedance Mechanical strain Coupling coefficients linked to material
Energy density	High at macro level but decreases for smaller volume	Low at macro level but increases for smaller volume	High at macro level but may decrease at microscale due to materials properties
Maturity	High at macro but low at micro level	High at both macro and micro level	Average at both macro and micro
Scalability	Dificult for the material integration	Material integration is easy but structures are complex	Good even if material properties vary

IV.1.2.2. Energy transfer and conversion

Energy conversion is not perfect, a part of the energy can be dissipated as heat or radiation, for example. A simple way to optimize the conversion of mechanical energy into electrical energy is first absorbing a maximum of mechanical energy. Then it is necessary to maximize the energy conversion, and finally to transfer and adjust the electrical energy produced to the powered device. Thus there are three aspects to optimize (Figure 74).

- The transfer of the external mechanical energy to the energy conversion structures in the harvester. This is mainly a mechanical study.
- The yield of the mechanical to electrical energy conversion. This is a piezoelectric study and also a semiconductor study in our case.
- The transfer and adaptation of the converted electrical energy to the device. This requires an electronic study.

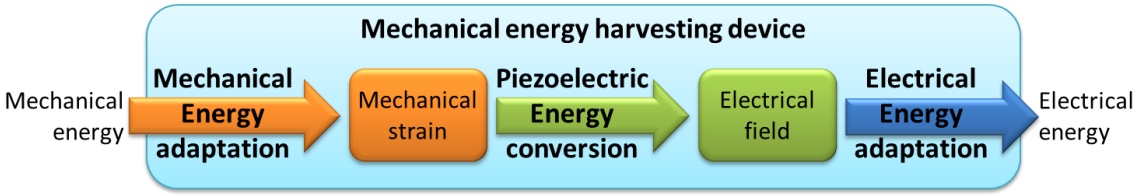

Figure 74 Diagram of the different stages of the conversion of mechanical energy into electrical energy by a piezoelectric mechanical energy harvesting device (1 mechanical energy adaptation, 2 piezoelectric energy conversion and 3 electrical energy adaptation).

In our project, we will focus on these three steps. In autonomous system a fourth step of electrical energy management is usually required. But the electronics adaptation requires knowing the specifications of the whole device and is widely studied in many laboratories as CEA LETI [303] or STmicroelectronics [304], [305] to create a unit adapting and managing different energy sources for various needs of electric energy.

IV.1.3. How to harvest mechanical energy?

IV.1.3.1. The input mechanical energy

As mentioned before (I.4.1.), piezoelectricity is closely related to mechanical stress. To get mechanical stress, it is necessary to subject a body to a significant force. This may generate deformations or movements which can be used to harvest mechanical energy.

- Deformations: it refers to harvesting the mechanical energy contained in the deformation due to the direct or indirect application of a force. If this force is applied briefly we speak of shocks and if it is applied over a longer period we speak of stress. Similarly we can identify direct deformations like walking on something or pressing button and the indirect distortions such as clothing or a tire when they are deformed.
- Movements: it refers to harvest the mechanical energy contained in the movements. This consists in harvesting the energy of vibrating body and accelerating movement. For this, we often proceed indirectly by transforming the variations (or accelerations) of different bodies into mechanical strain. For example vibrations, shocks or beatings could move a mass which deforms a piezoelectric beam.

Overall we can distinguish two types of mechanical energy harvesting devices, firstly those based on the use of shock, stress and mechanical deformation and secondly those which focuses on the harvesting and conversion of mechanical vibrations and accelerations (Figure 75).

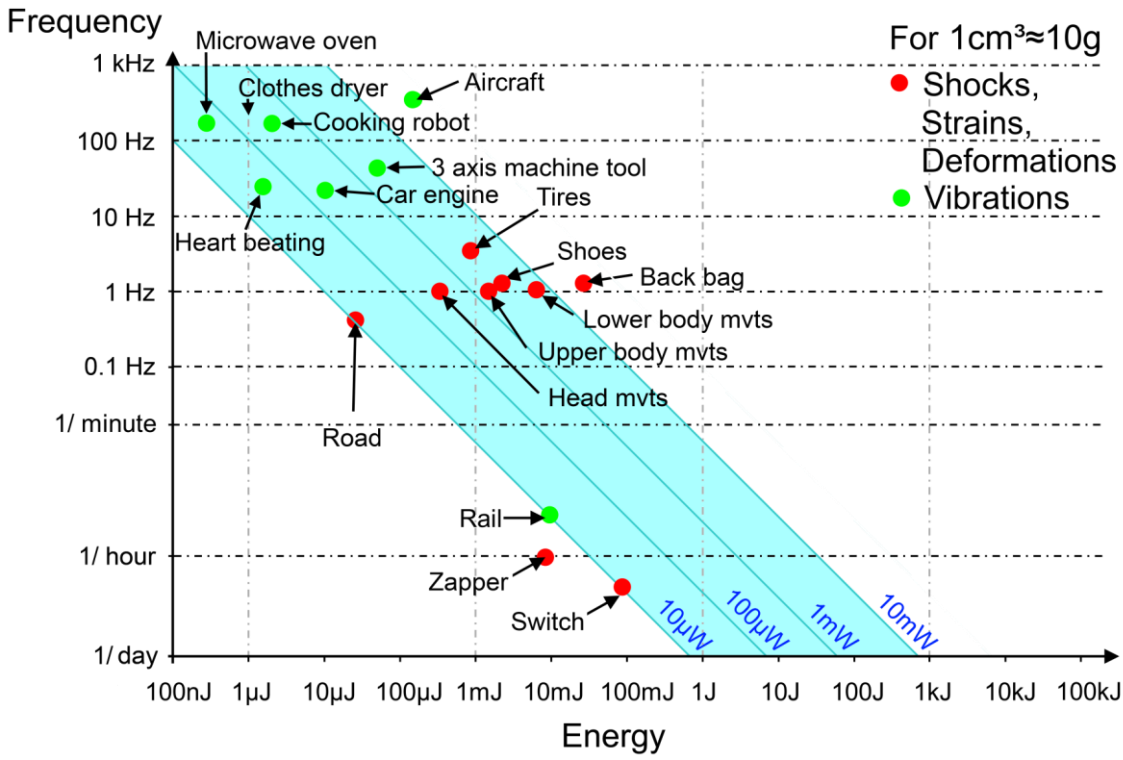

Figure 75 Type and amount of mechanical energy available in human activities (adapted from [306]*).*

These two different form of mechanical energy require different strategies to harvest their energy. So we can imagine different ways of designing a device incorporating piezoelectric NWs (NG) addressing a particular use.

1) The first kind of device comes from the direct application of force such as shock or stress on a solid body. We can put our device between this force and the body. It will be strained in the most efficient way possible (Figure 76a).
2) The second case is the use of indirect deformations. Fixing our harvester on a part under deformation undergo the deformation modes and then convert them into electrical energy (Figure 76b).
3) The third make use of movements. If the vibrations of a moving body are strong enough then they can deform the piezoelectric NWs themselves. If the vibrations are lower, then by attaching a weight to our device and connecting it to the body in motion, the mass inertia will create a strain in our piezoelectric material (Figure 76c).

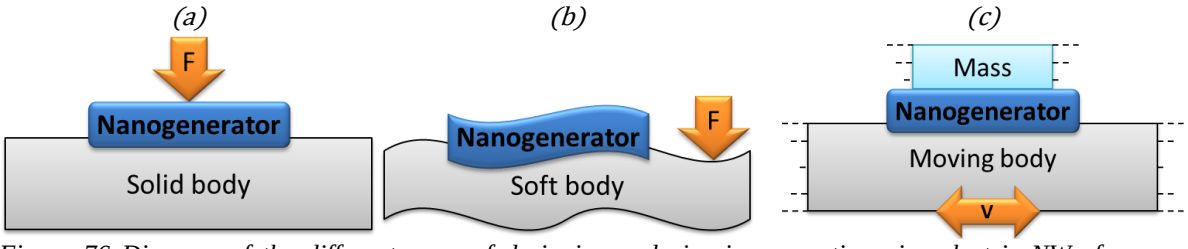

Figure 76 Diagram of the different ways of designing a device incorporating piezoelectric NWs for energy harvesting. (a) Device under direct axial deformation, (b) non axial deformation and (c) inertial deformation.

IV.1.3.2. State of the art of nanogenerators

I will introduce a brief state of the art of nanogenerator (NG), in particular the work done by the research team of Professor Z. L. Wang of Georgia Tech (USA) who is the pioneer in the field of NGs based on piezoelectric NWs [247]. We will discuss what types of NG structures were studied, comparing their advantages and disadvantages.

a.Vertically integrated NG (VING)

The first research team which investigated the mechanical energy harvesting using piezoelectric NWs was from Georgia Tech in 2006 [38]. They have designed a first mechanical energy harvester called NG using the same principle as the AFM top characterization method (II.5.2.). This first type of prototype has a vertical structure (compared to the substrate) and is called vertically integrated NG (VING). It is constituted of a ZnO NW array grown on an electrode. Then a zigzag (or with cones) platinum electrode is put on the top in order to act as an array of platinum AFM tips. Thus, following the same principle than the AFM top characterization method, electrical pulses can be harvested from the vibrations of the device. The main problems of this device are that it is very fragile, difficult to fabricate and can only harvest ultrasound vibrations (MHz) with a very small efficiency.

More integrated devices have been designed. First, NWs have been partially embedded in PMMA to protect then and make the NW matrix more robust. The platinum top electrode became flat to harvest vertical forces and to be easier to prepare and deposit. Thus the NG fabrication yield was better and its efficiency increased. But its global mechanism remained the same: the NWs are still gown on a bottom electrode with ohmic contact and the top electrode is made of platinum to keep the Schottky junction.

Following the improvement of the design, the structure of NG was improved. To avoid screening effects and current leakages the NW were fully embedded in PMMA making the NW insulated from the top electrodes. It increased the yield and the efficiency of the NG.

At the same time, designs have been thought and adapted for everyday life and human activity. NGs can be fabricated on a range of substrates, from polymers, semiconductors to metal, and from flat substrate to any substrate shape, because ZnO NWs can be grown at low temperature via a growing solution. Thus it has been possible to create radial NGs based on polymer fibers. The structure is still vertical compared to the substrate but the global shape of the NG allows the harvesting of mechanical energy in any direction around the fiber axis.

In addition innovative manufacturing methods have been tested. The goal was to develop easier fabrication methods, more adapted for large scale NG and industrial compatible. Prototypes mixing randomly piezoelectric NWs in an insulating medium such as PMMA have been investigated. Despite of the non-organization and missalignment of the NWs, a global vertical piezoelectric polarization can emerge and thus it is possible to harvest energy. This structure has the huge advantage to use a mixture of NWs in a polymer such as glue or painting which is very easy to use. But the performances of such a device are very low compare to others at this moment.

b.Laterally integrated NGs (LING)

Laterally integrated NG (LING) has been also investigated. This configuration has the advantage to use mainly the d_{33} mode of the piezoelectric NWs which is typically the higher coefficient. The same vertical NG structure have been used but tilted horizontally on the substrate. Thus as structure we have the piezoelectric NWs laying on the substrate between two electrodes. The main difficulty and drawback of this device lay in the horizontal growth of the NWs which is difficult. The efficiency of

these devices is similar to the VING but because of its structure and fabrication method, the density of NWs is usually smaller.

Here again, an industrial compatible fabrication method has been tested to make the fabrication of LING easier and more reliable. Using a brush and a solution with NW diluted in, it is possible to lay aligned NWs on a substrate. But the random polarization of the piezoelectric NWs will lead to low performances (the NW screening themselves). Nevertheless by pressing and at the same time sliding sample with a vertical array of NWs on the substrate we can lie down, align and polarize NWs in the same direction. The performances of this method are better than the previous one developed for VING devices but the manufacturing is trickier and it is still far less efficient than other LING. NG performances

Prof. Z.L. Wang's group improved the NWs quality and NG structure. Thus improvement after improvement they reached 20V [274] and then 58V and 134μA on open and short circuit conditions [307] using ZnO NWs. Nowadays various research teams are working on NGs such as the University of Princeton (USA), the University of Berkeley (USA), KAIST and Inha University (Korea), Tsing-Hua University (Taiwan) and various Chinese universities in partnership with the Beijing Institute of Nanoenergy and Nanosystems (China). They are developing prototypes using different structures and materials:

- GaN NWs [308]–[310]
- PZT microfibers (reaching 209V) [41], [218], [311]
- BaTiO3 pillar [33], [312]
- NaNbO3 NWs [313]
- PVDF nanofibers [42]
- CdS NWs [314], [315]
- InN NWs [316]

In France researches are focusing on ZnO VING devices as in Tours [48], [317] and Grenoble [300], [318]. The recent interest in NG is encouraging. Although most of the effort has been invested on proof of concept and fabrication of devices, very few references can be found on the theoretical analysis of the performances of such devices leading to optimization guidelines. A clear theory and strategy for mechanical energy harvesting using piezoelectric NW remains to be setup.

IV.1.3.3. Basics and core structure of the NG

There exist a multitude of NG structures possible leading to more or less optimized designs and efficient devices. However in any case we can identify some common basic structures that we can use and have to be studied. The core of the structure is the piezoelectric NW. First we have to identify the different means to mechanically and electrically contact the NWs:

Most of the time, NWs are grown vertically on a substrate. We can distinguish the:

- "Head" of the NW
- "Body" of the NW
- "Foot" of the NW

Then there are several possibilities to mechanically integrate the NWs:

- The "foot" and the "head" of the NW can be free or fixed.
- Release (Figure 77a) or support the body of the NW immerging the NW into a polymer matrix (Figure 77b).

Electrically we can contact the “foot” and / or the “head” of the NW using:

- an ohmic contact
- a diode contact
- an insulating contact

In any case, if we want to use the d_{33} mode of piezoelectric NWs which seems the most efficient in ZnO and GaN NWs, only one core cell structure makes sense: a piezoelectric NW with electrical contacts at its extremities (Figure 77a). This core cell can efficiently absorb mechanical strains and it remains technologically feasible. It would be more difficult putting electrodes along the NW for example. This core cell can be easily grouped and stacked to form large surfaces and volumes of NGs (Figure 77c).

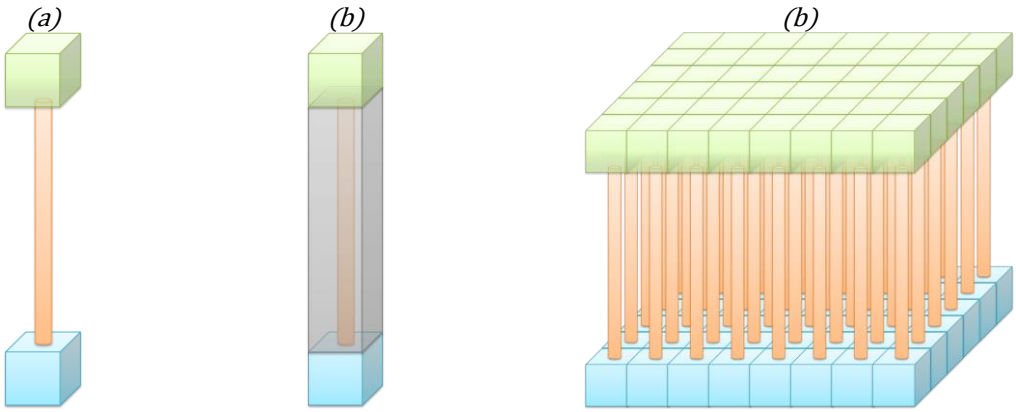

Figure 77 Diagram of (a) the NG core cell constituted of a NW connected at its ends and (b) with its body supported. (c) NG constituted of the assembly of numerous core cells.

In this work, the core cell was evaluated and optimized when integrated in different ways (VING or LING for example) and as a function of different mechanical.

IV.2. Resonant mechanical energy harvesting

First we investigate the dynamic behavior of piezoelectric NWs as the NG core cell to evaluate the potential of these structures in view of vibrating mechanical energy harvesting.

IV.2.1. Analytical study of the NW resonance frequencies

The resonance frequencies of cantilevers are well-known. The various modes of a single clamped beam are given by the following equations [319]:

$$f_1 = \frac{3.52}{2.\pi} \times \sqrt{\frac{Y.I_y}{m.l^3}} \qquad \textit{Equation 93}$$

$$f_2 = f_1 \times \frac{22}{3{,}52} \qquad \textit{Equation 94}$$

$$f_3 = f_1 \times \frac{61{,}7}{3{,}52} \qquad \textit{Equation 95}$$

where Y is the Young modulus, I_y the area moment of inertia, m the mass of the NW and l its length. Thus considering a cylindrical ZnO NW with a radius of r=25nm and a length of l=600nm, the

resonance frequencies are of the order of hundreds of MHz (f_1=118MHz, f_2=739MHz and f_3=2073MHz).

IV.2.2. Simulation of the piezoelectric NW frequency responses

We have confirmed the analytical calculation using FEM simulation only based on mechanical physics (f_1=118MHz, f_2=724MHz and f_3=1959MHz). However, because of the electromechanical coupling occurring in piezoelectric materials, the resonance frequency of such a NW could change. We performed a resonance frequency study of a ZnO NW including piezoelectric effect. The result (Figure 78a & b) shows that the resonance frequencies are slightly lower (f_1=98MHz, f_2=600MHz and f_3=1623MHz) but the order of magnitude remains the same. Then we have studied the evolution of the resonance frequency of such a NW by multiplying its length, diameter or size by a scaling factor α (Figure 78c). As expected an increase of the NW diameter increases its resonance frequency whereas the increase of its size or its length slightly reduces or decreases the resonance frequency respectively. But these solutions are not sufficient to lower resonant frequency in the order or lower than kHz and are difficult to setup because big or long NWs are difficult to grow keeping them vertical and aligned. As a result it confirms that the use of the resonance frequency of such a NW is restricted to few applications and devices working at hundreds of MHz which is not common for energy harvesting. In addition, in these cases the potential distribution change in the NW (Figure 78c & d) which can complicate even more the use of the resonance frequencies of piezoelectric NWs.

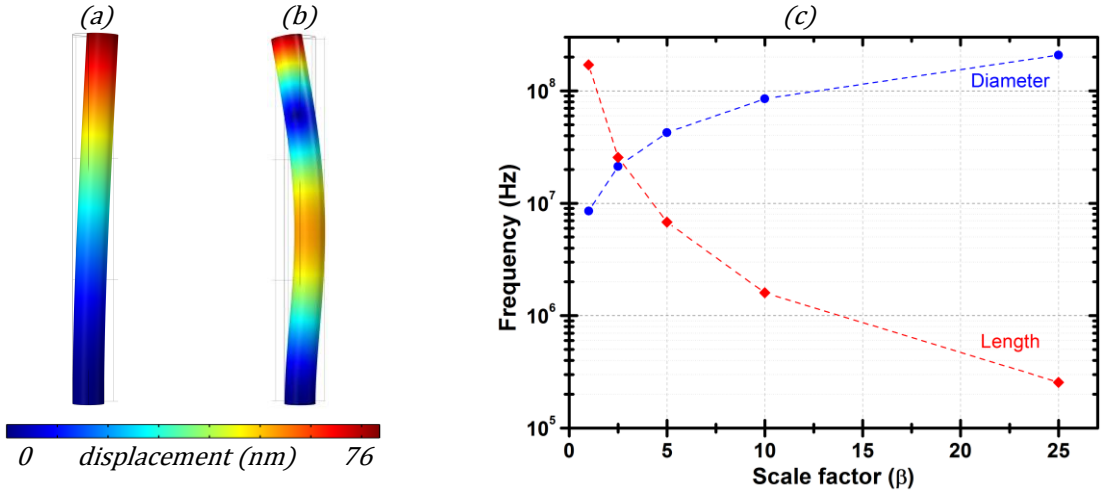

Figure 78 FEM simulation of the resonance frequencies of a ZnO NW (l=1000nm, r=25nm) including the piezoelectric effect. (a) Displacement shape at the first resonance frequency f_r=118MHz and (b) at the second resonance frequency f_r=723MHz. (c) Variation of the resonance frequency of the ZnO NW as function of the multiplication of its diameter d, length l or size (adapted from [320]*).*

IV.2.3. Application to resonant mechanical energy harvester

As described for a typical 50nm wide, 600nm long ZnO NW, the resonance frequency is found close to hundreds of MHz. Such a resonance frequency is too high for most present applications of mechanical energy harvesting, for which the range of frequencies of use is below 200Hz from human body and some structures, and around a few kHz from machines vibrations [321]. Even by tuning the NW dimensions it remains difficult to realistically reach these low frequencies.

Without considering any energy conversion, electrode position or dynamic problems, the non-adaptation of the resonance frequency of piezoelectric NWs to environment and human activity vibrations disqualifies the use of single piezoelectric NWs for this purpose. In addition the power

provided by a single NW is very small (typically 10 to 20pW for a ZnO NW with a length of 600nn and a diameter of 50nm [322]), so energy harvesting systems must be based on an ensemble of NWs. It is interesting to evaluate how the resonance frequency would change in such a case. The modeled structure is depicted in Figure 79a where vertical NWs are connected to a seismic mass. This kind of structure has been proposed in [323] and further realized, without considering any resonance effect, in [31].

FEM simulations have been used to calculate the influence on the resonance frequency of such parameters as the area of the array, the density of NWs and the weight of the seismic mass. Calculations were performed for ZnO. It was found that the simulation of a 1µm^2 area was sufficient (same resonance mode and frequencies) to represent the response of larger devices. Our reference structure consisted of a 100NW/µm^2 array with 1µm long NWs and a 1µm thick seismic mass. This density corresponds to 50nm wide NWs spaced by 50 nm. As expected the resonance mode of such a system is a little bit different compared to a NW. Because of its structure the seismic mass cannot bend and wave but only strafe laterally (Figure 79a). As shown in Figure 79b, the resonance frequency obtained is on the order of the MHz, but can be decreased by increasing the thickness of the seismic mass or by reducing the density of NWs. However, it seems very difficult to reasonably reach resonance frequencies lower than several tens of kHz. A resonance frequency of 6 kHz would require a density of 4 NWs/µm^2 (4×10^8 NW/cm^{-2}) and 100µm thick seismic mass which is not realistic. While it effectively increases output power, arranging NWs into resonant arrays should not provide a large design margin in terms of resonance frequency.

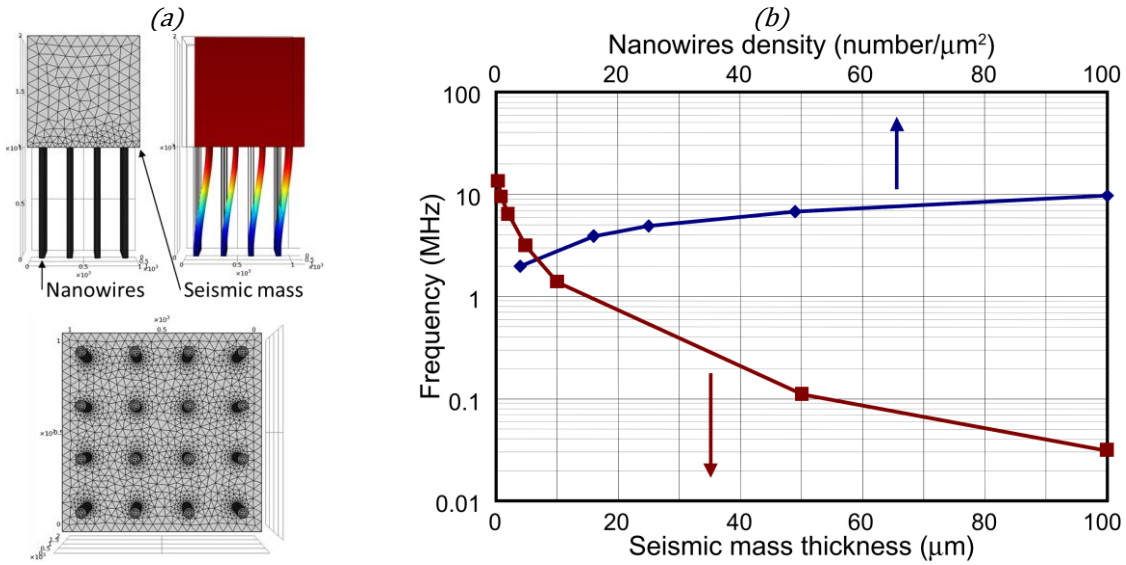

Figure 79 (a) View of the elementary cell simulated to calculate the resonance frequency of an array of vertical NWs connected by a seismic mass. The NWs are considered as fully clamped to a solid substrate at their bottom. The seismic mass is supposed to be made of tungsten. (b) Resonance frequency of the structure as a function of the thickness of the seismic mass and the number of NWs per µm^2 [320]

By grouping the NWs and using a heavy seismic mass on the top of them to decrease the resonance frequency of the whole system, the resonance remains again too high and not appropriate to harvest mechanical energy at low frequency. This without considering the problems related to the use of the piezoelectric potential distribution generated. Therefore a better approach seems to consist in considering real-time and quasi-static deformations, as developed in the next sections. These deformations could be encountered in low-frequency applications or when random mechanical inputs are available from the human body for example.

IV.3. Non resonant approach: axial compression mode

IV.3.1. Device structure and working principle

As shown in previous sections, various NG structures are possible and many have been tested. First of all we have to choose the best NG structure possible. To simplify the modeling, the fabrication, the characterization and the optimization of NG prototypes we will first focus on VING structures.

The main structure of VING devices consist in a vertical NW array with top and bottom electrodes. Then many possibilities are available, we can tune the mechanical and electrical contact at the root, along and at the end of the NW. The VING structure chosen was inspired from [31], [324] and is the simplest design developed to build NGs using piezoelectric NWs. This harvester can be divided into 3 parts (Figure 80a):

- First, a piezoelectric NW array that converts mechanical energy into electrical energy via the piezoelectric effect. This is the core of the device. In the following simulations we used undoped ZnO NWs but it could be adapted to other materials such as undoped GaN and AlN NW for instance.
- Secondly this matrix of NWs is immerged into an insulating layer which protects it from the electrical leakages and short circuits that could occur because of the n-type non intentional doping [274], [275]. Thus it increases the NG fabrication yield and makes it more robust. In this study we used PMMA soft polymer as interstitial material.
- Finally, top and bottom electrodes are used to collect electrical charges. Various metals or doped silicon can act as a bottom electrode. The electrical nature of this contact will be considered first as ohmic but depending on the material it could be PN or Schottky type. We will pay more attention to this contact in next sections by considering the seed layer (if used) and the nature of this contact.

Overall this first structure represents a good compromise between efficiency, robustness and feasibility. Its working principle illustrated in Figure 80b is the following: the mechanical forces and the impacts compress the piezoelectric NWs along their c-axis, thus generating a voltage difference ΔV across those due to the piezoelectric effect. This ΔV creates a displacement current where electrons flow I across the external circuit in order to compensate this potential difference. The thin insulating layer avoids current leakage and increases mechanical robustness. The voltage generated by the compressed NWs drives charges from the external circuit and accumulates them at the top and bottom electrodes, charging the capacitance and generating a current pulse. An opposite displacement current is generated when the force is released (Figure 80c).

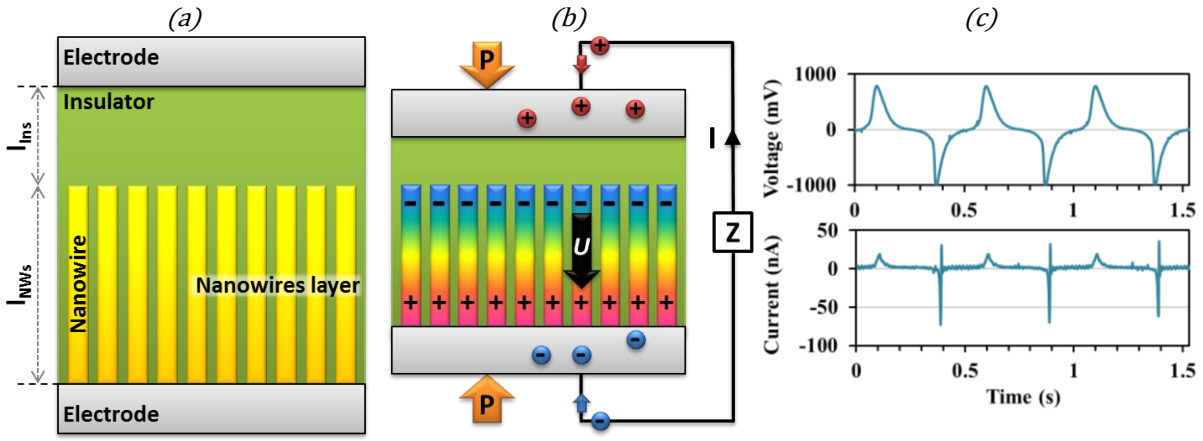

Figure 80 (a) Structure of the VING before and (b) working principle after vertical compression. (c) Experimental characterization result of a VING prototype under compressive force [300].

IV.3.2. Analytical approach

To build an analytical model approaching the NG behavior we first considered the NG as a capacitor under compressive forces. Then, classical linear mechanics and piezoelectric equations were used to derive simple expressions to estimate the overall energy conversion efficiency of the device (Figure 81). To proceed, we divided the energy conversion mechanism in 3 independent steps: mechanical energy transfer, mechanical to electrical energy conversion and electrical energy transfer to the output circuit. The total yield η_T is the product of the three individual step yields η_M, η_P and η_E respectively.

IV.3.2.1. Mechanical energy transfer

The first energy transmission step concerns the mechanical energy transfer from the top surface to the piezoelectric NW. We assumed that all the parts of the device were ideal layers with isotropic and constant both Young modulus (Y) and dielectric constant (ε). We assumed a regime of small elastic deformations where Hooke's law is valid. The piezoelectric NW layer was modeled as an ideal fiber composite material with a homogenous repartition of thin ZnO NWs. The properties of this composite layer were approached by weighting the PMMA and ZnO properties with their respective proportion (Y_{NWs}, ε_{NWs}). Within this model, pressing the device generates a stress T, perpendicular to the top electrode and uniform across the device layers. We assume the strain S in the composite layer as the strain in the piezoelectric NWs. During the compression process, part of the input mechanical energy is lost in the insulating layer. The yield η_M of the mechanical energy transfer was thus calculated as:

$$\eta_M = \frac{1}{1 + \frac{l_{Ins} \cdot Y_{NWs}}{l_{NWs} \cdot Y_{Ins}}} \qquad \textit{Equation 96}$$

where l_{NWs} is the thickness and Y_{NWs} the equivalent Young modulus of the NW composite layer (Figure 80), L_{Ins} and Y_{Ins} the top insulating layer thickness and Young modulus respectively.

depends on the thickness and Young's modulus ratios of the insulating and piezoelectric layers.

IV.3.2.2. Mechanical to electrical energy conversion

The mechanical to electrical energy conversion is based on the piezoelectric phenomenon. In the analytical model, we only considered the vertical strain S_z generated in the NW layer and the piezoelectric coefficient e_{33}. For simplification purposes, in-plane deformations due to Poisson ratio and tensorial effects represented by the e_{31} coefficient were not taken into account within this first approach. The potential difference V_{piezo} generated in the NWs was calculated. The generated

electrical energy was deduced as that of plate capacitor between the bottom electrode and a virtual electrode at the top of the piezoelectric NW layer. The resulting piezoelectric yield η_P was then:

$$\eta_P = \frac{{e_{33}}^2}{\varepsilon_{NWs}.(Y_{NWs} - T)} \qquad \textit{Equation 97}$$

where ε_{NWs} is the equivalent permittivity of the NW composite layer, e_{33} the piezoelectric coefficient of the NWs and T the stress in the NWs.

It depends on stress and piezoelectric properties. This expression is only valid for small stress T.

IV.3.2.3. Electrical energy transfer

The third step consists in calculating the electrical energy stored between the top and bottom electrodes, neglecting the voltage drop in the PMMA because of the 1D structure of the NG (dielectric loses mostly occurring in 3D). The corresponding energy yield η_E was then:

$$\eta_E = \frac{1}{1 + \frac{l'_{Ins}.\varepsilon_{NWs}}{l'_{NWs}.\varepsilon_{Ins}}} \qquad \textit{Equation 98}$$

where l' is the thickness of the VING structure after deformation (Figure 80).

It is the electrical analog of (Equation 96). It depends on the thickness and dielectric constant ratios of the insulating and piezoelectric layers.

IV.3.2.4. Optimization

Figure 81 summarizes this analytical model. With this global view of the system yield, it was possible to identify four optimization routes, which can be combined, and consist in engineering the structure or the material properties of the dielectric and piezoelectric layers.

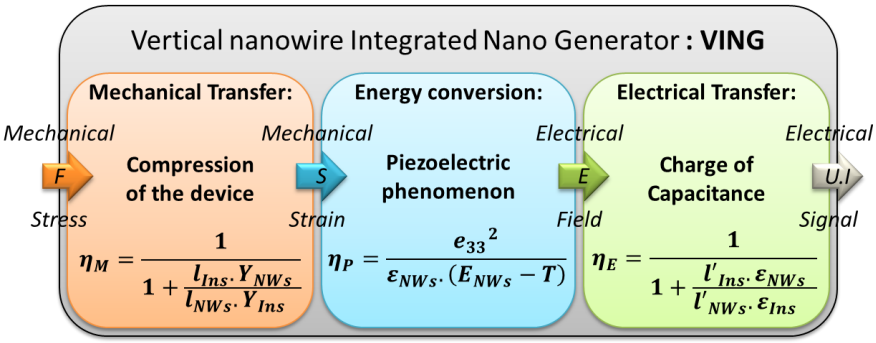

Figure 81 Diagram of the VING working principle. The yield (η) has been calculated for each step using the parameters of (Figure 80). l_x, Y_x and ε_x are the thickness, Young modulus and dielectric constant of layer x. The NWs layer is modeled as a uniform equivalent medium. T is the stress and e_{33} the piezoelectric coefficient relevant to this strain configuration (adapted from [325]*).*

Firstly, the thickness of the insulating layer needs to be as small as possible with respect to the piezoelectric layer without losing its insulating role between the NW and the top electrode. So the breakdown voltage of the insulating layer and the piezoelectric layer have to be higher than the piezoelectric potential generated in the NW. Secondly, the properties of the insulating material, Y_{Ins} and ε_{Ins}, need to be adapted. They are involved in the equivalent parameters used for the NWs layer. From analytical expressions of the yields above, it can be shown that the total yield can be put as a function of Y_{Ins}, and similarly as a function of ε_{Ins}, under the form:

$$\eta_T(Y_{Ins}) = \frac{1}{a + b.Y_{Ins} + \frac{c}{Y_{Ins}}} \qquad \textit{Equation 99}$$

where a, b and c are constants.

which goes through a maximum for optimum values of Y_{Ins}. Physically however, Y_{Ins} and ε_{Ins} cannot be optimized independently and it is necessary to consider the (Y_{Ins}, ε_{Ins}) couple for each material. Thirdly, we can tune the structure of the piezoelectric layer. Its equivalent Y and ε can be tuned by adjusting the NWs density. From the yield expression, decreasing the NW density should be beneficial as it decreases Y_{NWs} and ε_{NWs}. However it will decrease the available output energy. Finally, larger yields should be achieved with piezoelectric materials with large e_{33} coefficients [29] and small values of Y_{NWs} and ε_{NWs}.

The analytical model is appropriate to get a simple picture of the device behavior and general optimization guidelines. However, it misses several features, such as structural non-homogeneity, 3D effects and Poisson ratio influence, which can have a huge impact and will be studied by simulation in next section.

IV.3.3. FEM simulations

IV.3.3.1. NG core cell structure

To go further, we have performed FEM simulations of the full NG structure using COMSOL Multiphysics software. We considered small deformations, anisotropic materials and no fixe and free charges in the NW and in the insulator. The simulated structure consists in an array of NG elementary cells (Figure 82a) surrounded by air. The elementary cell structure consists of one ZnO NW immerged in a PMMA medium with top and bottom conductive electrodes. The reference cell includes a NW with radius r=25nm and length l=600nm, cell size is 100nm × 100nm × 700nm, the thickness of the PMMA layer above the NWs is l_{ins}=100nm. As boundary conditions we applied an electrical ground and mechanical fixed constraint condition to the bottom electrode. The normal displacement of the core cell sidewalls was set to zero using symmetry conditions. This is considered relevant for an elementary cell in the center of a large NG array. The top electrode of the NG core cell is rigid with floating potential. Finally a pressure of 1MPa is applied on the top of the cell. While the piezoelectric behavior of piezoelectric NWs under compression is understood [210] a wide range of potential amplitudes are observed in the literature for generating piezoelectric potential. In this study, we considered initially bulk materials properties, although several studies, sum up in [40], have shown that electromechanical and piezoelectric properties are enhanced at nanoscale, a further approach will be presented considering nanoscale effect.

First simulations were performed depending on the NG matrix size which is the number of elementary cells in the NG. Figure 82b shows the influence of the NG surface on its performances. The electric potential generated between the top and bottom electrodes (ΔV) increases from 20mV to 70mV as the NG matrix size increases from 1×1 cell to 15×15 cells, that is up to 225NWs (Figure 82c), and it converges to a maximum value of 80mV corresponding to the electric potential generated by one NG cell without taking into account edge effects and 3D dielectric losses (Figure 82 b & c). Figure 82d represents the piezoelectric potential distribution for 1 single cell and for a 15 × 15cells matrix, both surrounded by air. The piezoelectric potential generated from one NG cell is low (20mV) and it shows strong edge effects and 3D dielectric losses that are not representative of a cell behavior in the NG which is includes a large array. As the matrix size increases, edge effects and 3D dielectric losses

decrease. The piezoelectric potential saturates for a matrix size of around 200 NWs. Therefore, it is necessary to aggregate at least ensembles of 200 NWs to minimize these losses in NG.

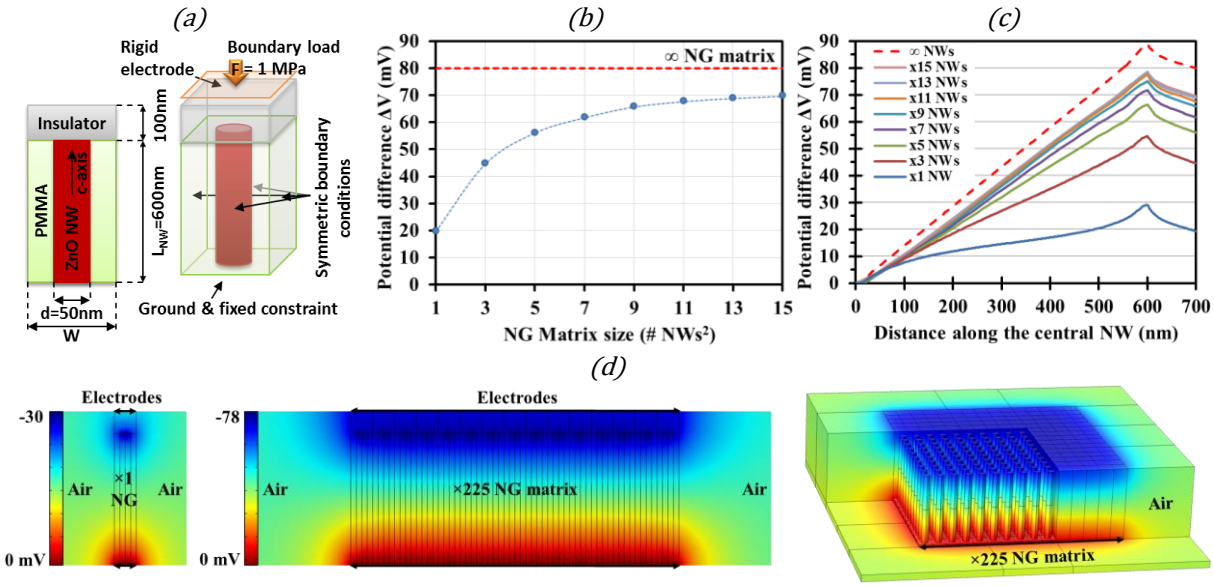

Figure 82 (a) Schematics of the geometry and boundary conditions used to perform FEM simulations on a NG core cell. (b) Evolution of the difference of electric potential generated at the top electrode by a NG surrounded by air as a function of the NG matrix size. The infinite NG matrix is calculated as one NG cell without edge effects and 3D dielectric losses. (c) Evolution of the electric potential generated through the central NW of various NG matrix sizes surrounded by air as a function of the distance from the NWs root at the bottom. (d) FEM simulation of the distribution of the electric potential generated by various NG matrix sizes embedded with PMMA, surrounded by air and strained under 1MPa, as a function of the NG matrix size [300].

In a second step, an extensive parameter screening was carried out based on the simulation of the core cell (Figure 82d) without surrounding air and edge effect. Parameters were varied around the reference NG cell dimensions in order to investigate optimization trends. Energy density per unit area was used to compare the results. We considered the coupling effect between the piezoelectric NW and the charged top and bottom electrodes. In static mode, this coupling decreased the generated piezoelectric potential by up to 40% due to the screening effect of the charges accumulated in the electrodes of the device.

IV.3.3.2. Evaluation of NG behavior and performances

The study of the influence of NWs density highlights several complex effects which are difficult to take into account in an analytical model. The density of NWs is measured by their distance relative to their diameter. For a NG core cell we have defined a ratio parameter α as the NW diameter d divided by the core cell width w.

$$\alpha = \frac{d_{NW}}{w_{cell}} \qquad \textit{Equation 100}$$

where α is the ratio parameter, d the NW diameter and w the NG cell width.

We distinguished two cases: a core cell on the edge of VING with free side wall movements and a core cell in the center with zero lateral movements. First, we simulated the total displacement Δl (Figure 83a). The difference with the analytical result is mainly due to the non-homogenous composition of the piezoelectric layer. Analytically, it was modeled as a composite layer with equivalent parameters obtained by linear combination. This is not precise enough for medium densities of NW as Δl is higher in the PMMA and smaller in the NW than expected (Figure 83a). Then, we studied the piezoelectric potential (V_{piezo}) (Figure 83b). Despite the influence of Poisson coefficient

[210] which should slightly increase V_{piezo} , the simulated results are one order of magnitude lower than expected because of the smaller Δl in the NW. Moreover, at low density, V_{piezo} is saturates due to mechanical 3D effects while the electrode potential decreases due to 3D electrostatic effects (Figure 83b). The largest output voltage is reached for a ratio α=0.5.

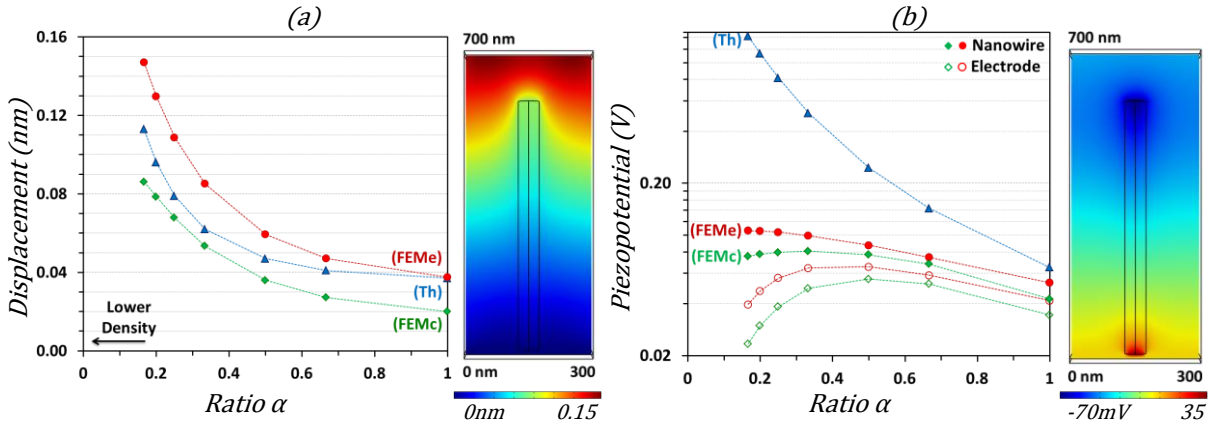

Figure 83 Analytical (Th) and FEM simulation results of a NG cell on the edge (FEMe) and in the center (FEMc) of VING structure as a function of the NW density as the ratio $\alpha=d_{NW} / w_{cell}$. (a) Total displacement at top Δl and cell cut view. (b) Piezopotential generated in the NW and between the electrodes, and cell cut view [325].

By decreasing the NW density, the cell capacitance is also decreased, as PMMA has a lower ε than ZnO (Figure 84a). The analytical model is very accurate at lower density (<1.5%) because the ε discrepancy on ε between PMMA and ZnO is much smaller (3.9 to 8.3) than that of the Young modulus (3 to 211GPa) which limits the error due to the non-homogenous structure. Finally, we plotted the surface density energy (Figure 84b). We obtained a maximum efficiency for a ratio α=0.5 which is quite different from the analytical model. This first comparison shows that 3D complex mechanical en electrical effects, which are difficult to take into account in a simple analytical model, are playing a major role.

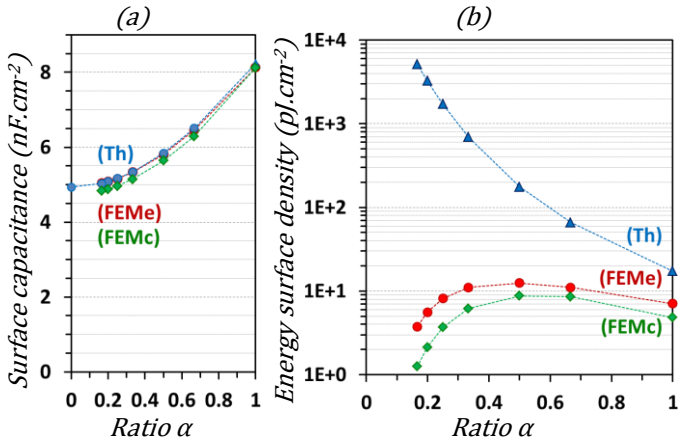

Figure 84 Analytical (Th) and simulation results of a NG cell on the edge (FEMe) and in the center (FEMc) of VING structure as a function of the NW density as the ratio $\alpha=d_{NW} / w_{cell}$. (a) Surface capacitance density and (b) Surface energy density as a function of the ratio [325].

From the yield expression in (Figure 81), the insulating layer should be as thin as possible. This was checked by varying PMMA thickness from 1nm to 1µm. The surface energy density (Figure 85a) is one order lower than expected due to the 3D phenomena described above. But the analytical model gives the correct optimization trend, proving to be useful in this case.

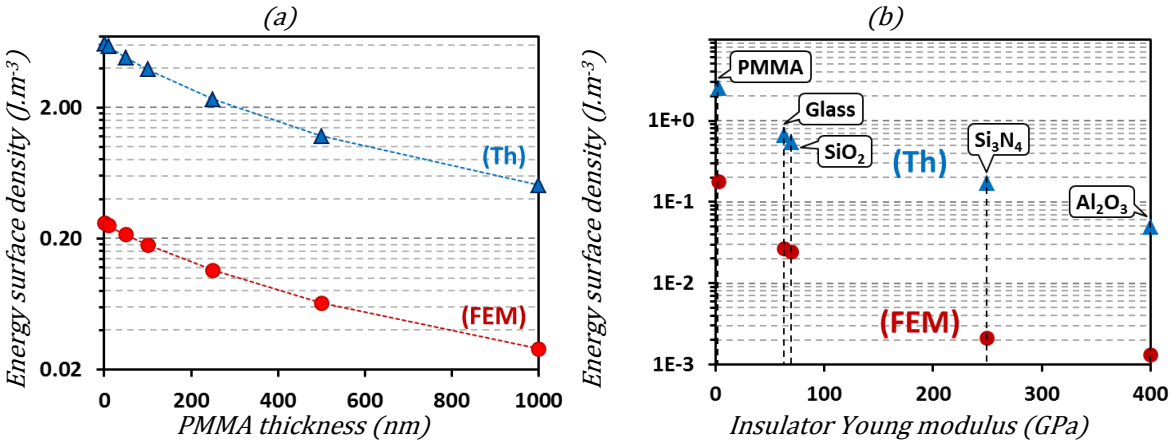

Figure 85 (a) VING surface energy density as a function of the insulator layer thickness. (b) VING surface energy density for different insulating materials listed in Table 20 ($\varepsilon_1 \in [3.9 ; 9.7]$, $Y_1 \in [3 ; 400GPa]$) [325].

Table 20 Mechanical and electrical parameters of different insulator (From the COMSOL library)

Insulators	PMMA	SiO_2	ZnO	Si_3N_4	Al_2O_3
Young's modulus (GPa)	3.0	73.1	111	250	400
Poisson's ratio	0.40	0.17	0.35	0.23	0.22
Relative permittivity	3.0	2.09	8.9	9.7	5.7

To investigate the optimal insulating material, we have tested different dielectrics with (Y_1, ε_1) couples corresponding to real materials (Figure 85b). PMMA, which features low Y and ε values, is better suited to our device than the other common dielectrics tested. Investigation through a broader range of materials would be required to find the best candidate for VING.

Globally it was found that 3D effects arising from the non-homogenous structure of this device were playing a major role, making precise analytical modeling difficult. In the range of geometries and materials tested, the optimum solution was obtained for a diameter to distance ratio α =1 and for a thin layer of PMMA. Further optimizations will need to consider the NG structure and piezoelectric material.

IV.3.3.3. Structure optimization

We found an optimized device structure using a thin (l_{ins}=100nm) PMMA insulating layer on top of the NWs and a medium density (α=0.5) of ZnO NWs. Using a thinner insulating layer is theoretically possible but it is difficult to fabricate keeping its electrical insulating role because of the mechanical solicitation and the "bumps" (topology). Several parameters and materials were investigated showing that PMMA is a good insulator for NG. The main issues were the dielectric losses and the non-homogenous structure of the NWs layer. The 3D dielectric losses occurred for low and medium NW density combined with a thick insulating layer, because the non-homogenous structure drives the strain field around the NWs. All these problems reduce the piezoelectric potential generated and the mechanical and electrical energy stored. However the capacitance and the electrical potential could be increased even more by using a thinner insulating layer and adapted NW density, to increase electrostatic coupling. Therefore, we propose a new structure (Figure 86) using various materials used in microelectronics such as Al_2O_3, Si_3N_4, or SiO_2 as top insulating layers. We will investigate and analyze the geometry and the materials used to improve the mechanical energy stored, the energy conversion and the electrical energy stored in the NG.

The insulating layer on the VING structure was divided in two parts: (layer 1) the insulator above the NWs and (layer 2) the interstitial insulator between the NWs. Considering the NG analytical models

developed previously (Equation 96 & Equation 98) we propose to use different materials for the top insulating layer and the interstitial insulating material so that mechanical and electrical energy storing mechanism are dissociated from piezoelectric energy conversion mechanism (Figure 81). This allows each term to be optimized separately. The idea is to reach high Young's modulus and permittivity for the top insulator and low Young's modulus and permittivity for the interstitial insulator, in order to maximize the energy stored in the NG. To decrease the effect of the non-homogeneous distribution of strain around the NWs we used a hard material like Al_2O_3 (Y=400GPa) as a top insulator. Then to increase the sensitivity of the piezoelectric NWs layer to small forces, we used a softer material such as PMMA as an interstitial insulator. As a result (Figure 86a), the deviation of the strain field in the structure significantly decreased and the strain was linearly distributed in the NWs layer, which is closer to the NG analytical model developed.

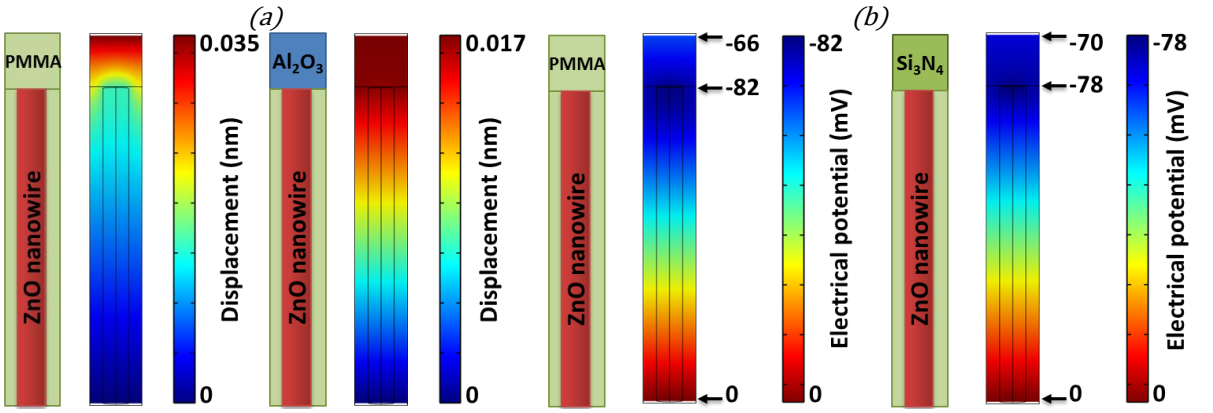

Figure 86 Schematic and FEM simulation of various NG structures (a) distribution of the displacement in a NG core cell with PMMA or Al_2O_3 as top insulating layer, (b) distribution of the electric potential in a NG core cell with PMMA or Si_3N_4 as top insulating layer.

This structure allows maximizing transmission of external mechanical energy to piezoelectric NWs which are the core of the NG. On the other hand, dielectric losses decreased the electric potential transmission from NWs to top electrode (Figure 86b) leading to a decrease of the stored electrical energy. Even if these losses are small and mainly occur for low NW density and thick insulating layer, we can minimize them by using a high permittivity (high-k) insulator. Among the insulators studied here, Si_3N_4 featured the best trade-off because of its large Young's modulus (250GPa) and relatively high permittivity (9.7).

IV.3.3.4. Design optimization

To further optimize this new design, we studied the effect of the NW density on the NG properties (Figure 87a). We computed the mechanical energy, electrical energy and total efficiency of the NG core cell as a function of NW density. A ratio α=1 corresponds a high NW density of $4\times10^{10}cm^{-2}$ and α=0.1 a low density of $4\times10^{8}cm^{-2}$. As expected from the previous study (IV.3.3.2.), the lower the NWs density, the higher the mechanical energy stored in the device for a given pressure (Figure 87b). This is due to the fact that the Young's modulus is much lower in PMMA than in ZnO. With a lower NW density, the proportion of ZnO decreases compared to PMMA, resulting in a smaller equivalent Young's modulus of the NWs layer. In the same way the capacitance is smaller (Figure 87c) due to the small permittivity of PMMA. Because of the dielectric losses and the deviation of the strain field around the NWs, a soft NW layer cannot generate maximum electric potential (Figure 87d) and electrical energy (Figure 87e). As a result, a lower NW density improved the storage of mechanical energy to the NG but reduced the electrical energy stored. In contrast, a high NW density increased the capacity to store electrical energy in the NG, at the expense of reduced mechanical energy storage. As

a result, NG efficiency goes through a maximum that results from a trade-off between the two mechanisms (Figure 87f).

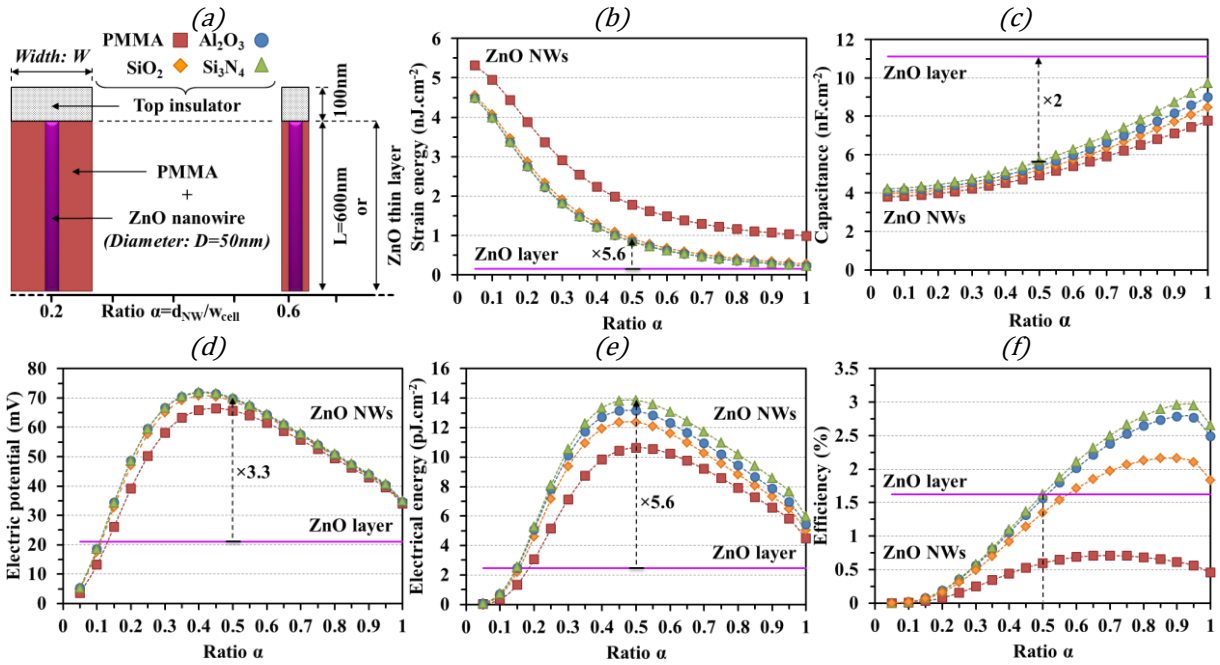

Figure 87 (a) Schematics of different NG structures using various materials (PMMA, SiO_2, Al_2O_3, and Si_3N_4) and NWs densities, (b) electrical potential, (c) capacitance, (d) mechanical energy, (e) electrical energy, (f) efficiency of a NG core cell. The comparison with a thin ZnO layer (-) has been done using the same FEM simulation and conditions.

Simulations show that the maximum of electrical energy produced by a NG under a given pressure of 1MPa was 14pJ.cm^{-2} and is achieved for an average NW density α=0.45. In this study different materials were tested and the maximum electrical energy peak varied only from α=0.45 to α=0.5 depending on their Young modulus and permittivity. A very low NW density can be considered as equivalent to one ZnO NW with the mechanical properties of PMMA, leading to a very low energy stored. On the contrary, a high ZnO NW density will correspond to a thin layer made of a material close to ZnO. In this case it is interesting to note that the efficiency of the piezoelectric mechanical energy harvester is close to the maximum but the output electrical energy is not, because of the low force sensitivity. Now for energy harvesting applications it is better to maximize the output electrical energy than the energy harvesting efficiency. Finally to evaluate the true advantage of the new structure, we simulated the electric potential generated by a NG constituted of a thin ZnO layer with the same thickness (600nm) and properties as the ZnO NWs. Under the same conditions, the ZnO NWs device generates an electric potential 3.3 times higher and a capacitance 2 times smaller than the ZnO layer device. Thus the electrical energy generated by NWs is 5.6 times higher compared to ZnO thin film due to the square of the voltage in the electric energy equation, and the efficiency is almost the same at α=0.5. This improvement of the output electrical energy while maintaining the same efficiency makes the NWs based NG more sensitive to small forces. It will generate an electrical energy equivalent to a thin ZnO layer but for a smaller applied force.

The new structures were then simulated to take full advantage of a smart combination of the mechanical properties of PMMA, electromechanical properties of Si_3N_4 and piezoelectric properties of ZnO. The core layer of the device was a NWs based structure acting as a piezoelectric composite material layer [326]. We then investigated the effect of NWs size on device performances. For a given NWs length of l=600nm, we increased the diameter d from 24 to 2400nm corresponding to a decrease

of the NW aspect ratio from 25 to 0.25. The decrease in NW aspect ratio reduces the density of mechanical energy stored and the electrical energy generated (Figure 88a & b) which both converged toward the values for a thin ZnO layer. Efficiency also decreased (Figure 88c).

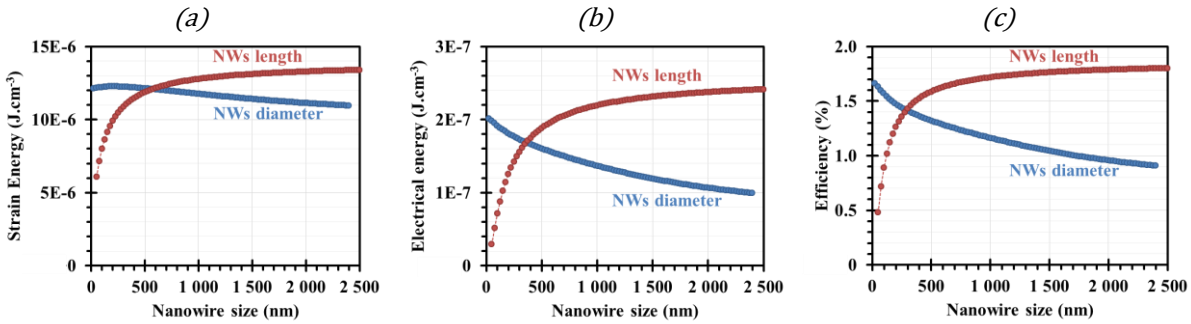

Figure 88 FEM simulation of a NG core cell using a ZnO NW embedded in PMMA with Si_3N_4 top insulator, a ratio parameter of 0.5 and under 1MPa. (a) mechanical energy, (b) electrical energy, (c) efficiency as function of the NW diameter at constant length l=600nm and as function of the NW length at constant radius r=25nm.

On the other hand, for a given radius of 50nm, we increased the NW length from 600nm to 2500nm with a NW aspect ratio changing from 12 to 50. As a result the density of electrical energy generated and the efficiency increased up to a maximum of 241nJ.cm^{-3} (corresponding to a power of 500nW.cm^{-3} if the pressure is applied at 1Hz) and 1.8% respectively. Such a piezoelectric ZnO NWs layer embedded in PMMA is very similar to fiber based composite materials [59]: in our case PMMA plays the role of the matrix material which is soft and sensitive to external strain while ZnO NW s plays the role of the reinforcement material while piezoelectric properties for the energy conversion. Such piezoelectric fibers are interesting for mechanical energy harvesting applications. But they are more complex because of the mix of the electromechanical and piezoelectric properties as well as for polarity issues. The resulting optimized structure consisted of thin and long piezoelectric NWs with an adequate density (α=0.5). In addition it is important to use a hard high k top insulating material. The design could be even better using a medium NW density and a zigzag top electrode [327] around each NW. The surface capacitance calculated for such a structure was increased by 2.8% and so was the electrical energy harvested.

IV.3.3.5. Piezoelectric material issue

Besides the improvement of the electromechanical structure of the NG, ZnO semiconducting properties can also be improved. Indeed the presence of ionized dopant atoms and of free carriers can decrease the piezoelectric potential generated by ZnO NWs because of the screening effect (III.1.4.). This could be an issue for energy harvesters as previous studies have reported doping concentrations above 10^{16} to 10^{17}cm^{-3} in ZnO NWs grown by hydrothermal chemical process [274], [275]. Hopefully, semiconductor structures tend to be mostly depleted at nanoscale [179]. Therefore, we simulated the influence of doping concentration on a ZnO NW using a fixed charge density. As previously, we used the bulk values for the piezoelectric coefficients. This means that we do not consider their increase at nanoscale. It was found that the electric potential decreases from 68 to 1.4mV as the doping level increased from 10^{12} to 10^{18}cm^{-3} at 1MPa, thus reducing dramatically the NG performances (Figure 89a).

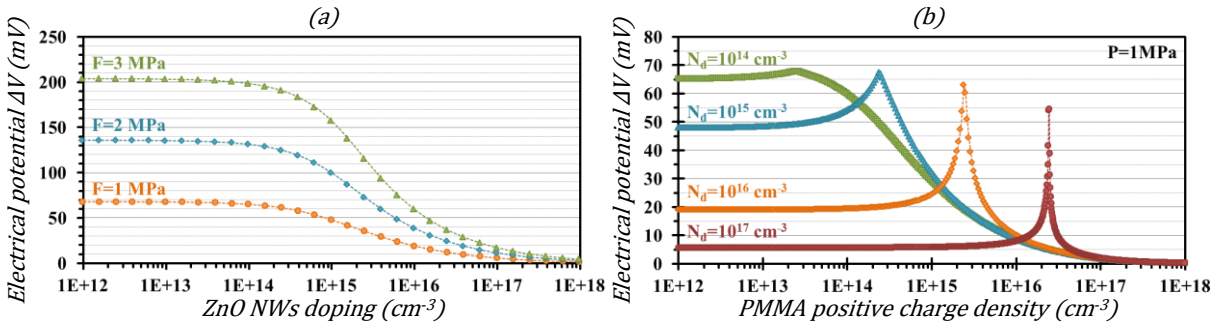

Figure 89 Piezoelectric and electrostatic FEM simulation of a NG core cell using a ZnO NW embedded in PMMA with Si_3N_4 top insulator and a ratio parameter of 0.5. (a) Difference of electric potential generated under various pressures, and as a function of the n type doping concentration of the ZnO NW. (b) Difference of electric potential generated under 1MPa for various doping concentration of the ZnO NW, and as a function of the p type doping concentration of the PMMA layer [300].

A similar effect also occurred using charged insulating layers [318]. However, studies [40] reported an increase of the piezoelectric coefficient of NWs at nano scale. For ZnO, by a factor close to 2 experimentally. Taking this factor into account in our models increased the piezoelectric potential from 70mV to 123mV, electrical energy from 13.9pJ.cm^{-2} to 42.5pJ.cm^{-2} (i.e. electrical power at 1Hz from 398nW.cm^{-3} to 1214 nW.cm^{-3}) and efficiency from 1.63% to 5.58%. These effects probably compensate part of the screening effect in NWs and allow NG to reach reasonable output voltage [307]. Nevertheless, by decreasing the quantity of free carriers and doping concentration in the NWs, it should be possible to decrease screening and thus increase the NG output voltage. Two strategies can be foreseen:

- Firstly, we can decrease the number of free carriers generated in the NW by improving its purity. Thus develop better growing technique is a key point. O_2 plasma or subsequent annealing process are also efficient on ZnO NWs [274] to cure the mechanical defects and oxygen vacancies which increase the number of free carriers and degrade ZnO NWs quality.
- Secondly, we can neutralize the charges in the NW using p–n junctions and depletion layers. Thus, using a p-type soft polymer like P_3HT instead of PMMA [328] between the NWs, it should be possible to cancel the screening effect from electrons in n-type ZnO NWs by depleting them from their free carries. When the quantities of n and p charges are equal, the potential reaches a maximum corresponding to the potential generated by a perfect depleted ZnO NW. However an excess of positive charges will again screen the potential. Figure 89b shows that the maximum peak of potential is very sharp and the main difficulty is to experimentally adjust the quantity of positive charges in the interstitial polymer to the quantity of n-type charges in the NWs to maximize the piezoelectric potential. In addition, the maximum peak is narrower as the n-type doping concentration of the NW gets higher. This solution is thus experimentally difficult to use and technologically challenging.

Finally, currently the equivalent circuit model of NG is being studied [329] to optimize the electrical energy adaptation. The influence of the NWs radius distribution on the electrical output is an interesting issue which is also under investigation [235]. One thing that has not been addressed here is the electrical signal adaptation and management problematic. This is a very important and complex step which can greatly influence the overall efficiency of NG. This issue should not be neglect and is currently subject to intense research [330].

The NG structure may appear challenging. Nevertheless we built NG prototypes and worked on the optimization of the NG fabrication process to get perfect and efficient NGs.

IV.3.4. Nanogenerator prototypes

IV.3.4.1. Technological process

The usual fabrication process is based on the liftoff method [331]. A liftoff process is used to pattern and stack all the NG fabrication steps: the seed layer deposition and the NW growth (Figure 90 steps 1 & 2), the PMMA spin coating (Figure 90 steps 3 & 4) and the Al top electrode (Figure 90 steps 5 & 6).

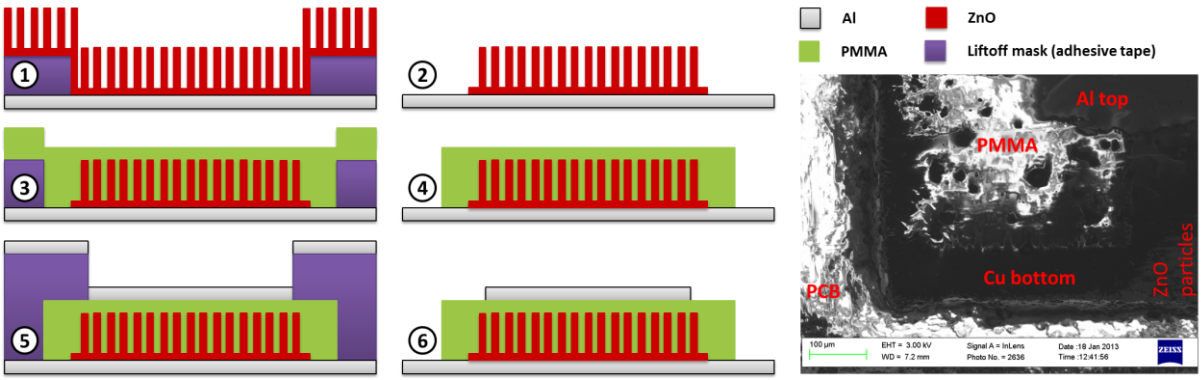

Figure 90 Diagram of the NG fabrication process using liftoff steps

Most of these fabricated layers are stacked. The multiplication of these steps tends to decrease the active NG surface and leads to complex, delicate and slow process. In addition it is a source of problems such as short-circuits because of the numerous manipulation steps generating dust and marks on the sample. Finally, the use of PMMA as matrix material makes it impossible to use photoresist for the deposition of the top electrode.

IV.3.4.2. Fabrication steps

Firstly we choose and prepare the NG substrate. To simplify the fabrication process we decided to use a conductive substrate such as doped silicon or Al plates. It is important to have a clean and plane substrate to ensure the good quality and conformity of the seed layer and thus avoid various problems (IV.3.4.3.). To do this we used polished n-type and p-type doped silicon wafer (Figure 15a) and electro-polished Al plate (Figure 15b). Other substrates have been tried such as commercial optical microscope glass slices (with bottom electrode Al layer) and manually polished metal plate but that did not work properly because of their high defects density and roughness. However Al foils worked fine using thick seed layers (100nm) and PMMA layer. Then to easily and safety manipulate the samples without damaging them we fixed them using adhesive tape on an inert sample holder such as kapton films (Figure 15a & b) and then glass slices (Figure 15c & d). The glass slices have the advantages to be stronger and more robust than kapton without reacting during all the fabrication process.

Following the NW growth (II.2. II.2.), to enhance the NG robustness and avoid short-circuits we spin coat a PMMA layer as thin as possible. In addition, after the optimization of the NG structures (IV.3.3.4.), we sputtered a thin Al_2O_3 layer over the PMMA to improve the NG performances.

Finally we sputter the top Al electrode (Figure 91a & b) and we connect the NG bottom and top electrodes using silver paste and copper wires (Figure 91c) or Al foil (Figure 91d).

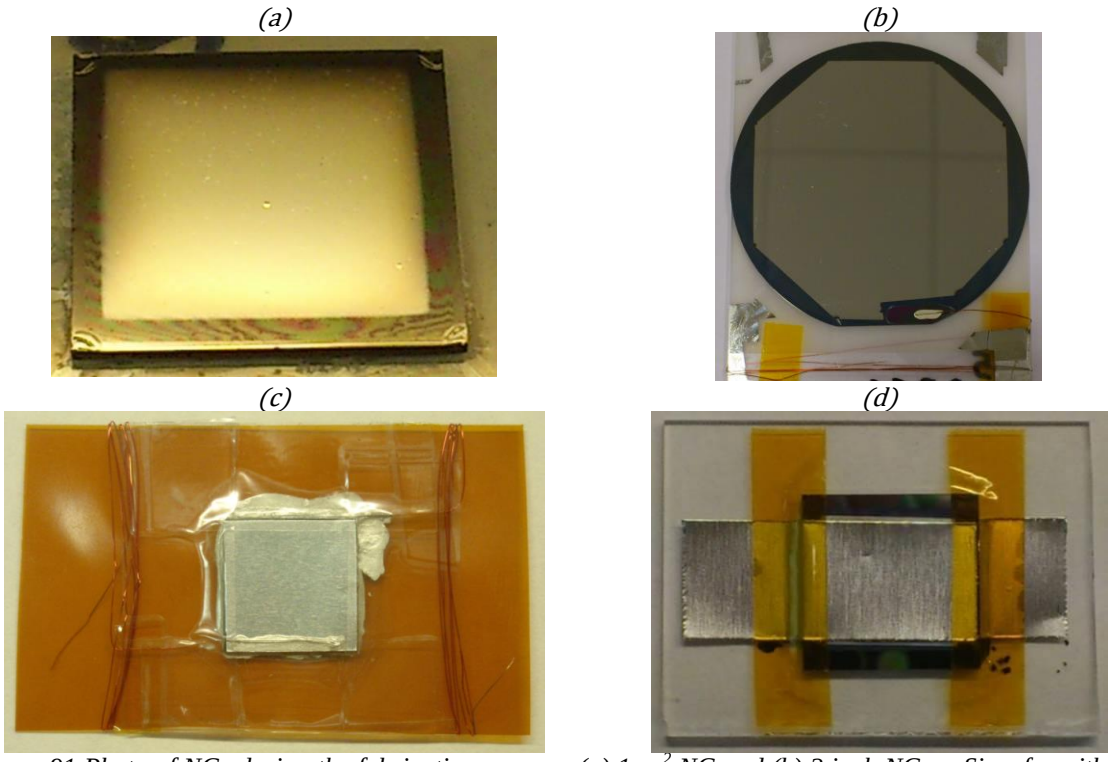

Figure 91 Photo of NGs during the fabrication process. (a) 1cm^2 NG and (b) 2 inch NG on Si wafer with top Al electrode deposited. (c) NG with a top Al protection plate and connected with silver paste. (d) NG connected with Al foils.

During all these fabrication steps, for fast and easy prototyping we used adhesive tapes to perform the liftoff process, the drawback is that it can damage and weaken the layers and devices or can introduce dust and defects on the device.

Figure 92 shows a cut view of a NG prototype fabricated. We can easily distinguish the structure of the NG (Figure 80a): the substrate and bottom electrode, the NW layer, the insulating layer and the top electrode. We can see that the main issue is the control of the homogeneity of NW layer and the penetration of the insulator in the NW layer which is very important for the improvement of the NG performances.

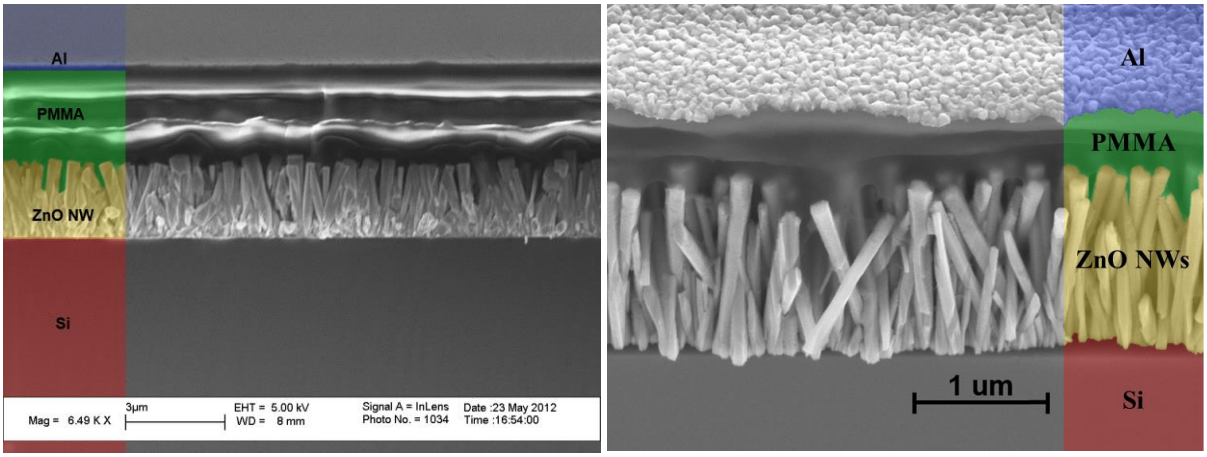

Figure 92 SEM images of the cut view of VING prototypes using ZnO NWs

IV.3.4.3. Fabrication issues

A mayor problem in the VING fabrication processes are short-circuits between the top electrode and the NW layer. It is very difficult to obtain an ideal device without these short-circuit while the yield is lower than 10%. We clearly identified several sources of short-circuits:

The roughness of the substrate (Figure 93a) is hardly covered with a constant thickness of PMMA as a top insulating layer. If the PMMA thickness is small, then the higher parts of the substrate will not be covered enough by the PMMA which will create some short-circuits. This makes the use of thick PMMA layer mandatory decreasing performance. Dusts and particles (Figure 93b) can appear at every step. If the dusts are bigger than the PMMA layer thickness, they will create a bumps which will not be covered by PMMA and will create short-circuits

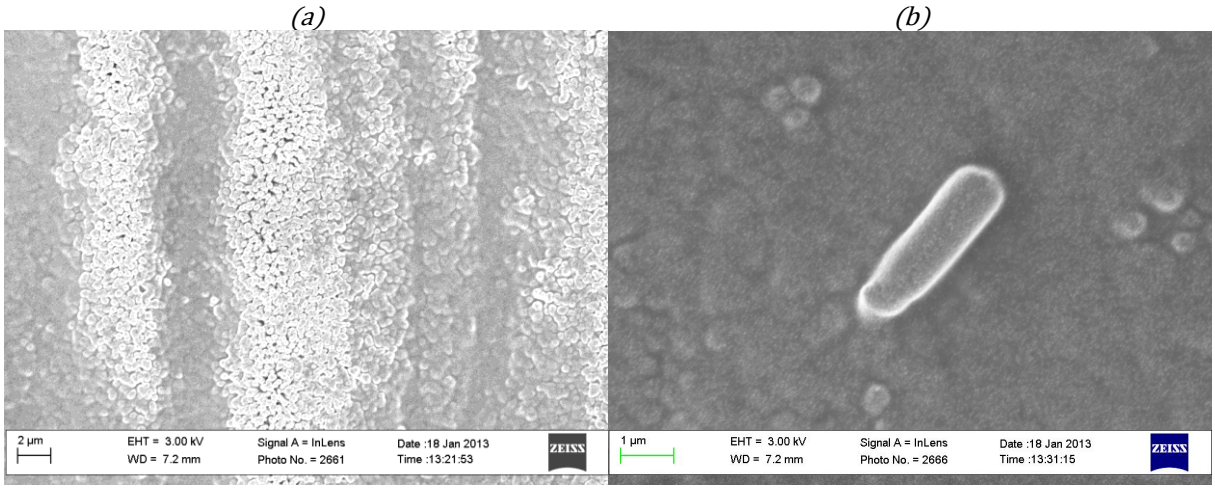

Figure 93 ZnO NWs covered with spin coated PMMA. (a) Roughness problem and (b) dust problem.

During the NW growth, some defects can occur (Figure 94a). It can be an overgrowth which will have the same effect as a hill. Or it can be undergrowth which will generate a hole. On the edge of this hole the PMMA thickness can be lower and create short-circuit. Poor control during the manipulation of the sample can create dusts and roughness (Figure 94b).

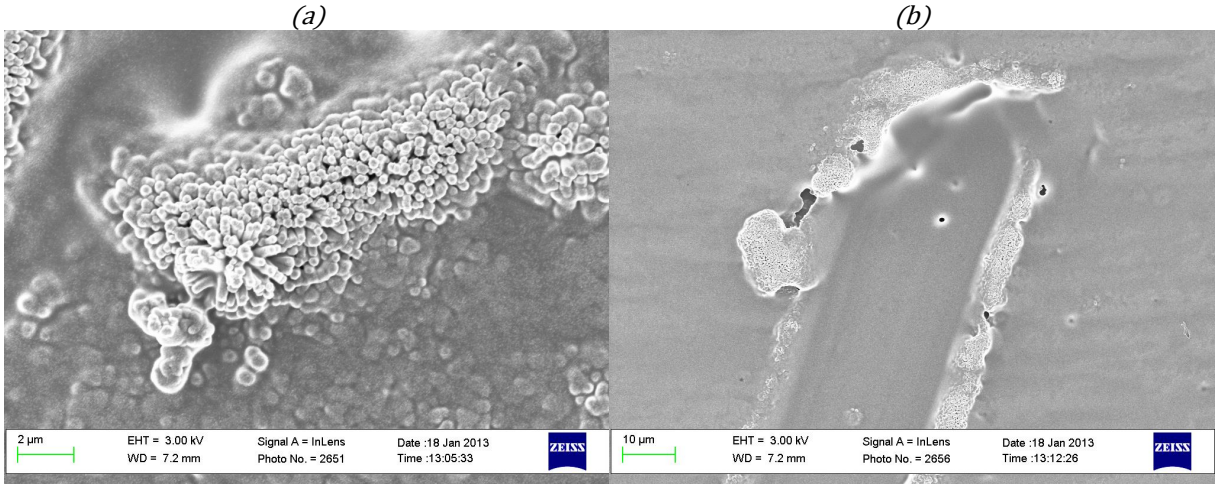

Figure 94 ZnO NWs covered with spin coated PMMA. (a) Growing defaults and (b) scratch during the manipulation.

IV.3.4.4. Fabrication improvements

Currently it seems impossible to avoid the short-circuit problems between the top electrode and the NW using the technology that we presently have at our disposal. Even if we deploy a huge effort to take care of the samples during all the fabrication process, defects still remains too numerous. So we use a second insulating layer between the bottom electrode and the NW seed layer. It seems easier to control the properties and quality of this layer as the first step on the NG fabrication process. Thus we should be able to increase the fabrication yield by managing the short-circuit problem with more efficiency.

We should be also able to process all the fabrication liftoff steps in only one step to simplify the fabrication of NG (Figure 95). In this case the problem is to control what happens at the edge and avoid short-circuits. We found few NW in the PMMA layer close to the edge and many particles. But the use of a bottom insulating layer can help to solve the short-circuit problem.

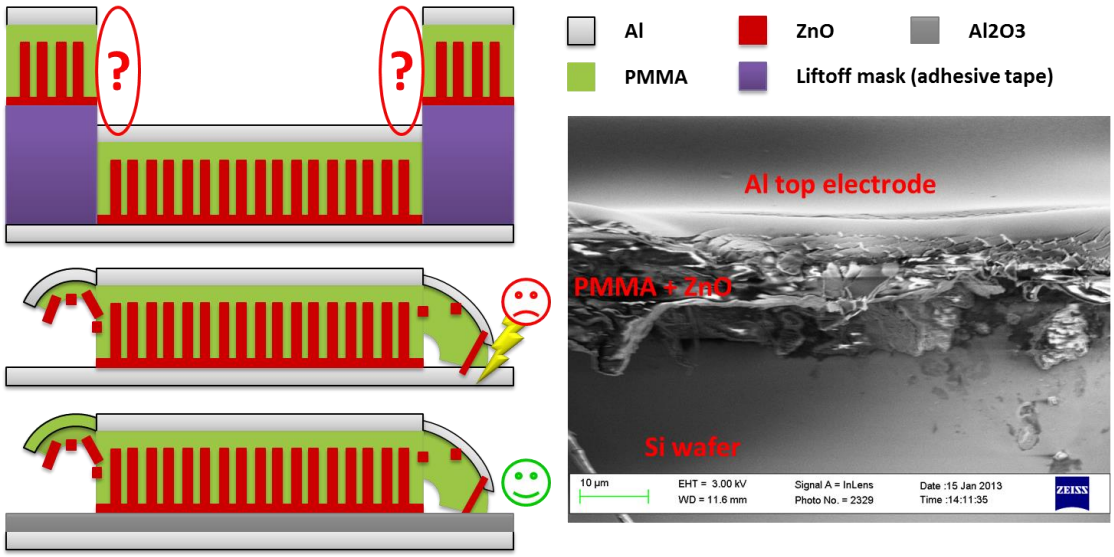

Figure 95 Problem on NG edge's considering only one liftoff process for the whole NG.

Using one liftoff process, the ZnO seed layer deposited is not uniform close to the edges because of the shadow effect. In this case, thinner seed layers (<100nm) could lead to the growth of various ZnO structures such as boehmite plate (II.2.3. Figure 23). These plates can be horizontal or vertical and have a non-aligned c-axis [233] and they will degrade the NG performances. During growth the boehmite plates spread everywhere on the sample and neutralize the overall vertical c-axis of the NW. The global structures become amorphous and the ZnO layer loses its piezoelectric orientation. We propose two solutions to this problem:

- Use another insulating layer material that does not generate boehmite structure instead of Al_2O_3. It requires investigation but can be helpful
- Sputter a thicker ZnO seed layer before the liftoff process.

IV.3.5. VING characterization in compression

To check that the NG fabrication is successful, several tests can be done. Since one of the biggest problem in current NG fabrication is short-circuits, the first parameter to check after fabrication is its resistivity. On prototypes we considered successful, resistivity was higher than 1MΩ. For lower values, current leakages start to be significant and the performances are not good. But, it depends of the device structures and the application. If the application generates a high strain, then the NG will

generate a high voltage and so the resistivity should be higher. On the contrary, smaller strain can operate NG with lower internal resistivity. Then, a simple pressure applied on the devices connected to a multimeter will show if it works or not. NG is supposed to be a supply power unit and so it should behave like a power source [332]. To be sure of this, a few simple measurements are required. First the voltage and the current of NG should be reversed when the NG is reversed. Then the potential of two NGs connected in series should add. Finally the current of two NGs in parallel should add.

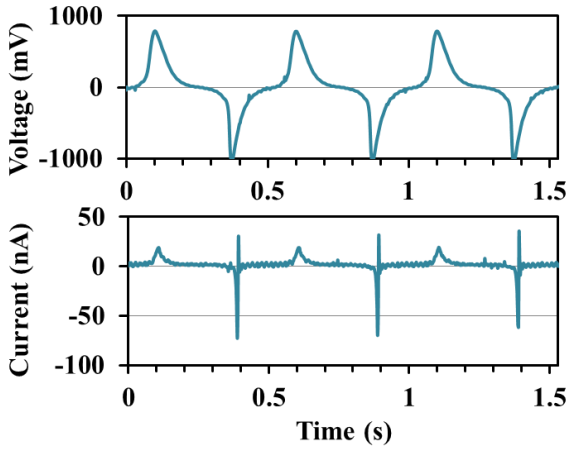

Figure 96 Voltage and current NG characterization under a compressive and periodical force [300].

We characterized the first NG prototypes using the Georgia Tech NG test bench (Figure 91). As shown on Figure 96, when applying a force on the NG in open circuit, the voltage increases and a current pic appears, then the voltage and the current decrease when the force is released. When the force is released, a symmetric voltage drop occurs and a strong and short pulse of current appears, then the voltage slowly decreases again. The main problem of this characterization is that we do not know the force applied on the NG and the input mechanical energy. Therefore to deeper investigate the NG operation and characterize in term of performance and potential application, we have developed a NG test bench (Figure 97). The characterization set-up is composed of a low frequency voltage generator which allows to generate various profiles of force on NGs such as sinusoidal, rectangular or triangular shapes. Then we amplify this signal to drive a piezoelectric actuator which applies the force on a very hard insulating chuck (in MACOR) compressing the NG. The applied force is measured thanks to a force sensor on top of the NG. Finally the NG signal V or I is amplified and displayed as a function of the time with the corresponding pressure signal on an oscilloscope or on a computer using an Analog to Digital Converter (ADC). To avoid as much as possible the noise and parasitic signal coming from the high voltage drive of the test bench piezoelectric ceramics we connected the test bench frame to the ground this divided the noise by a factor of 10 and thus insure a good Signal to Noise Ratio (SNR). Currently various ZnO and GaN NG prototype are under characterization.

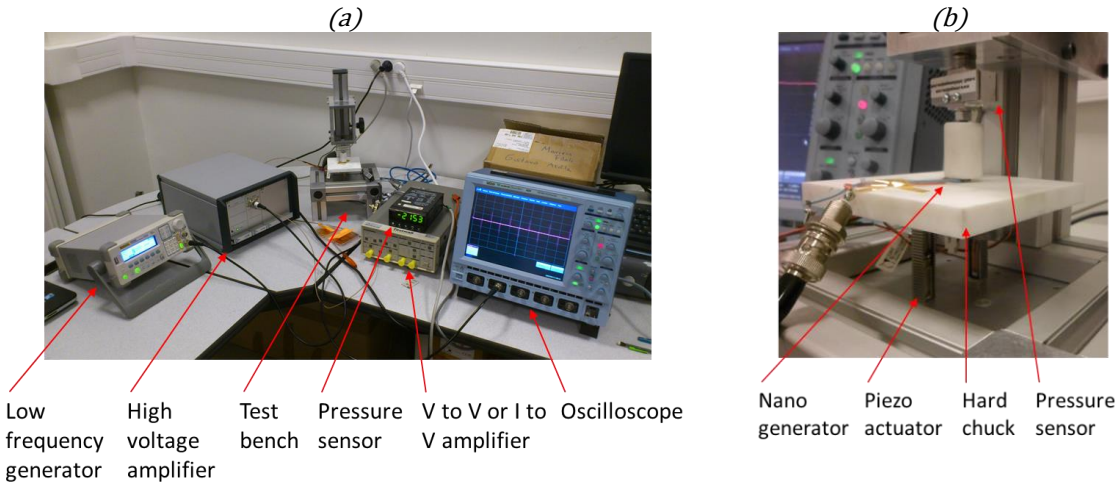

Figure 97 (a) NG test bench (b) NG characterization stage. The low frequency generator creates an electric signal which is amplify by the high voltage amplifier and then applied to the piezoelectric actuators of the characterization stage. These actuators transform the electric signal into a displacement signal which compresses the NG. Above the NG is positioned a force sensor which record the force signal applied to the NG. Finally NG and force sensors signals are display on an oscilloscope or a computer.

Everything is ready for the fabrication and development of VING devices. Use thin top insulating layer is one optimization rout for VING operating under compression. But what will happen when operating in bending? It is necessary to evaluate the performances of VING devices under bending.

IV.4. Non resonant approach: non-axial bending mode

In the previous sections we have studied how to design and build a NG to harvest the mechanical energy of deformations and strains generated by directly applying an external force on the NG. Now we propose to study the mechanical energy harvesting of indirect deformations and strain on NG. This means the NG is under bending or flexion.

IV.4.1. Working principle

In the case of a NG undergoing bending and flexion modes like on a membrane [333] or a beam far from their neutral axis, two main configurations exist:

- First, the piezoelectric NWs can be aligned on the substrate in the direction of the deformation (strain gradient) and connected. This configuration corresponds to LING devices (**Erreur ! ource du renvoi introuvable.**). In this case, the fabrication process of LING devices is different than VING devices but their overall structure and working principle remain the same: the deformations compress the piezoelectric NWs along their c-axis which generate a difference of potential between the electrodes. Therefore the global operation and behavior of LING device is similar to VING devices even if some differences exist.
- Secondly, the piezoelectric NWs can be aligned in a direction different than the deformations, the worst case being when the NWs are normal to the deformation direction. Keeping the same global NG structure, this case corresponds to a VING device under flexion (**Erreur ! ource du renvoi introuvable.**c).

In this section, we will focus on the performance evaluation of the NG previously designed (Figure 80) and optimized IV.3. to check how it would harvest bending and flexion modes.

IV.4.2. Analytical approach

We have previously evaluated NGs under compression (IV.3.). Here we extend the study to a flexion mode using a thin silicon membrane as a mechanical transducer, such a structure is taken as a case study to have a better insight in the multiphysics phenomenon involved. Such a characterization method has been developed since several years at IMEP-LAHC, both theoretically and experimentally for NEMS piezoresistive devices [333] and nanoMOSFETs [334]. In addition the fabrication of thin Silicon membranes (from few hundred nm to few tens of µm) is well controlled and many technological improvements have been developed in the context of the development of silicon-based SOI membrane micropumps with the startup EVEON [335]. Considering a Si membrane (25µm thick, 1cm edge) and applying a hydrostatic pressure of 1.8kPa, which is the limit of the linear deformation regime, we generate a force bending the membrane and thus compressing the NG cells from their sidewalls (Figure 98).

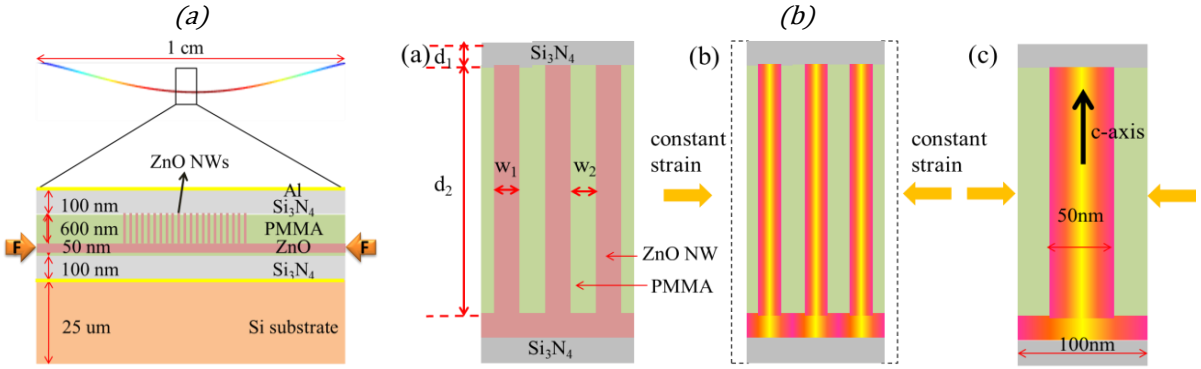

Figure 98 (a) Cross-section of a membrane with a VING, bended by a hydrostatic pressure P=1.8kPa and with a zoom on the structure. (b) Schematic of the laterally compressed VING structure with ZnO NWs (r=25nm, l=600nm). The cell width is w=100nm. When the membrane is bent, the NG is laterally compressed [336].

The main issue compared to previews studies is how the strain is transferred to the NW

When the device membrane is under flexion, the NG core cell is compressed laterally and extended along the c-axis (Figure 98). In the core cell, the energy conversion mechanism has been divided into 3 steps (Figure 81): mechanical energy transfer, mechanical to electrical energy conversion and the electrical energy transfer to the output circuit. In this case, in the first step, the input mechanical energy is different because of the lateral distribution of the strain in the NG core cell. If we consider the total mechanical energy $\mathcal{E}$ input in the NG core cell, the energy stored in the Si_3N_4 insulating layer (ξ_1), the energy stored in the NW / PMMA layer (ξ_2) and the mechanical energy in the NW (ξ_3). Thus, considering the principle of superposition of the layers which are uncorrelated, the mechanical energy transfer efficiency can be expressed as

$$\eta_m = \frac{\xi_3}{\xi_1 + \xi_2} \qquad \textit{Equation 101}$$

where ξ_1 is supposed to be a constant because of the very high young modulus of the Si_3N_4. Thus the major influencing factor is the ratio ξ_3/ξ_2, whose reciprocal varies with the volume ratio of NWs over the PMMA (related to the NW size and density) and with their Young modulus. Then the two next energy conversion and electrical transfer steps are similar to the compression case (IV.3.2.).

IV.4.3. FEM simulations

FEM simulations of the laterally compressed VING device were performed. The coupling between the mechanical, electrical and piezoelectric equations was considered for a core NG cell. The input impact described by the strain in the cell was calculated from a 2D model of the membrane (Figure 99a). Because the NW layer was much thinner than the membrane and far from neutral plane, the hydrostatic pressure generated constant lateral strain at sidewalls of each cell along the c-axis. We calculated that the NW/PMMA layer had a vertically homogeneous strain of -9.36×10^{-4} (within linear deformation) when the device is bent by a hydrostatic pressure of 1.8kPa, which is the limit of the linear deformation regime. The cell size was 100nm × 100nm × 850nm, with NW radius r=25nm and length l=600nm (Figure 99b) and we applied the strain underwent by the top layer of the membrane on the sidewall of the NG cell (Figure 99c). Young's modulus, Poisson's ratio and relative permittivity of the matrix material were varied around parameters of PMMA in order to investigate optimization trends. Several real insulating compounds were used as the matrix material. The potential generated and energy conversion was calculated for each material, as well as with a ZnO layer (the thickness is 118 nm) which has the same volume as the ZnO NW as a reference.

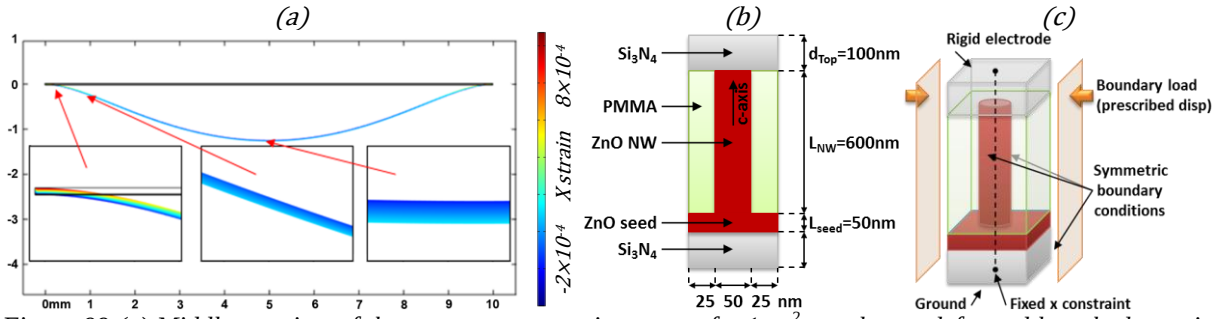

Figure 99 (a) Middle cut view of the x component strain tensor of a 1cm² membrane deformed by a hydrostatic pressure of 1.8kPa. (b) Structure of the laterally compressed NG reference cell and (c) FEM simulation boundary conditions used. Compression along the x axis (adapted form [336]*).*

IV.4.3.1. Evaluation and optimization of nanogenerator under bending

The analysis is focused on the displacement, the strain tensor component S_{xx} and the electric potential distributions. The effect of the hardness of the matrix material results in two different types of distribution for the displacement and the strain. When a soft matrix material (PMMA) was used, the matrix was more compressed than the NW as indicated by the displacement distribution (Figure 100a). The distribution of the strain tensor component S_{xx} (Figure 100b) shows that strain was concentrated in the matrix material instead of the NW. The opposite resulted when a hard matrix (Al_2O_3) was used (Figure 100c) and strain is concentrated in the NW (Figure 100d). This is consistent with the mechanical energy transfer efficiency (η_m) defined in section 3. As the Young's modulus of the matrix material increases, the efficiency increases. More mechanical energy is transferred into the core NW, influencing the final potential and energy generation.

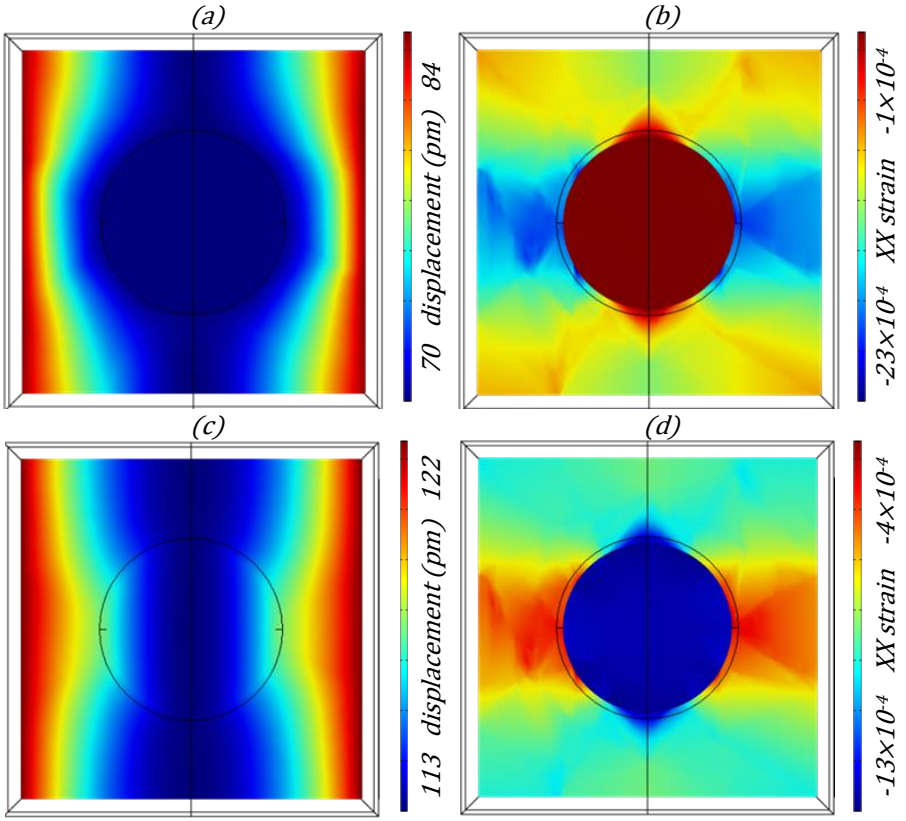

Figure 100 Horizontal middle cut view of laterally compressed VING, (a) total displacement and (b) XX strain component when using PMMA as insulator, (c) and (d) when using Al_2O_3 as insulator [336].

Several insulating matrix materials were considered to improve the NG performances. In the simulations, the total volume of ZnO was kept constant. The potential (Figure 101) was calculated along the central axis of the NG cell. From simulations, the potential generation ability of bulk ZnO (yellow line) is weaker than that of NW based NG cells. Zones (1) and (4) correspond to the Si_3N_4 insulating layers, where dielectric losses are unavoidable. Zone (2) corresponds to the thin seed ZnO layer, while zone (3) is corresponding to the NW layer. We identified 2 mechanisms involved in the conversion of the lateral strain into electric potential: first the lateral strain is converted into an electric field in the NW thanks to the transvers piezoelectric coefficient of the NW (d_{31}). Secondly the insulator matrix material is laterally compressed which increase its thickness, pushing the hard top insulating layer which vertically extend the NW if softer than the matrix material (or compress if harder). But this behavior is difficult to estimate and still under investigation. Globally, the NG cell with harder matrix materials (Al_2O_3, Si_3N_4) generated higher potential.

To clarify the energy transfer process, Young's modulus, Poisson's ratio and relative permittivity of matrix materials were varied independently. The former two parameters mainly influence the mechanical energy transfer and slightly affect the piezoelectric energy transfer. The relative permittivity affects the electrical energy transfer to the output circuit. Mechanical and electrical parameters of real matrix materials are listed in Table 20. First, the effects of Young's modulus and Poisson's ratio on the potential generation were compared (Figure 101c).

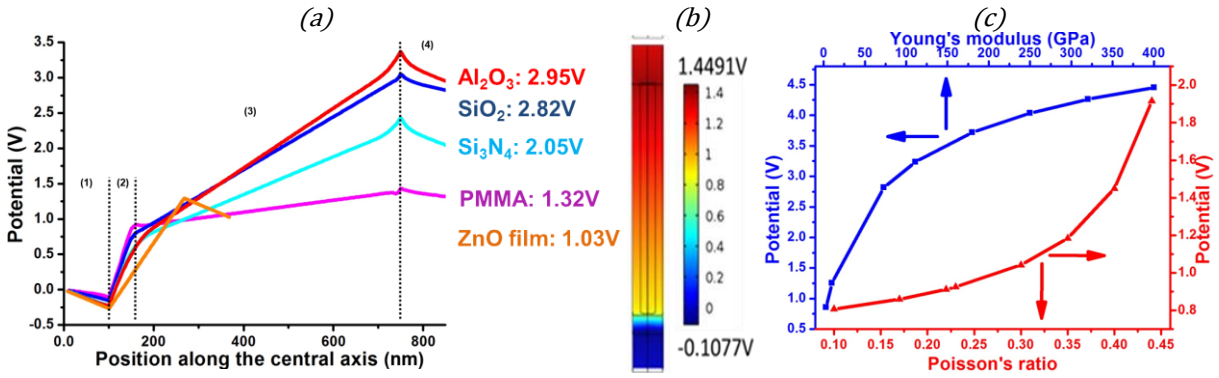

Figure 101 (a) Potential distribution with different matrix materials along the NW central axis. (b) Side view of the potential distribution with PMMA matrix. (c) Potential changing trend with the increasing Young's modulus and Poisson's ratio of matrix materials [336].

The curves were plotted against one parameter (Y for instance) while the two others (ε and υ for instance) were kept equal to that of PMMA. As the value of Young's modulus spans from 3GPa (PMMA) to 400GPa (Al_2O_3), the potential increases from 0.8 to 4.4V. In contrast, varying from 0.17 to 0.40, the change of Poisson's ratio only brings a potential difference of 1V. The relationship between the relative permittivity and the electric potential is more complex. In fact, the relative permittivity of the matrix material is not the direct factor that influences the electrical energy transfer process. Efficiency η_e decreases with increasing ε_{eq} of the matrix / NW compound. Here ε_{eq} is not a linear combination of the permittivity of the NW and the matrix. As a result, the potential curve reaches a maximum value when the permittivity is close to 2.5 (Figure 102a). Considering that the relative permittivity of real matrix materials varies from 2.09 (SiO_2) to 9.7 (Si_3N_4), the potential variation is less than 0.5V. In the simulation, the effect of Young's modulus is more significant than the effects of Poisson's ratio and relative permittivity.

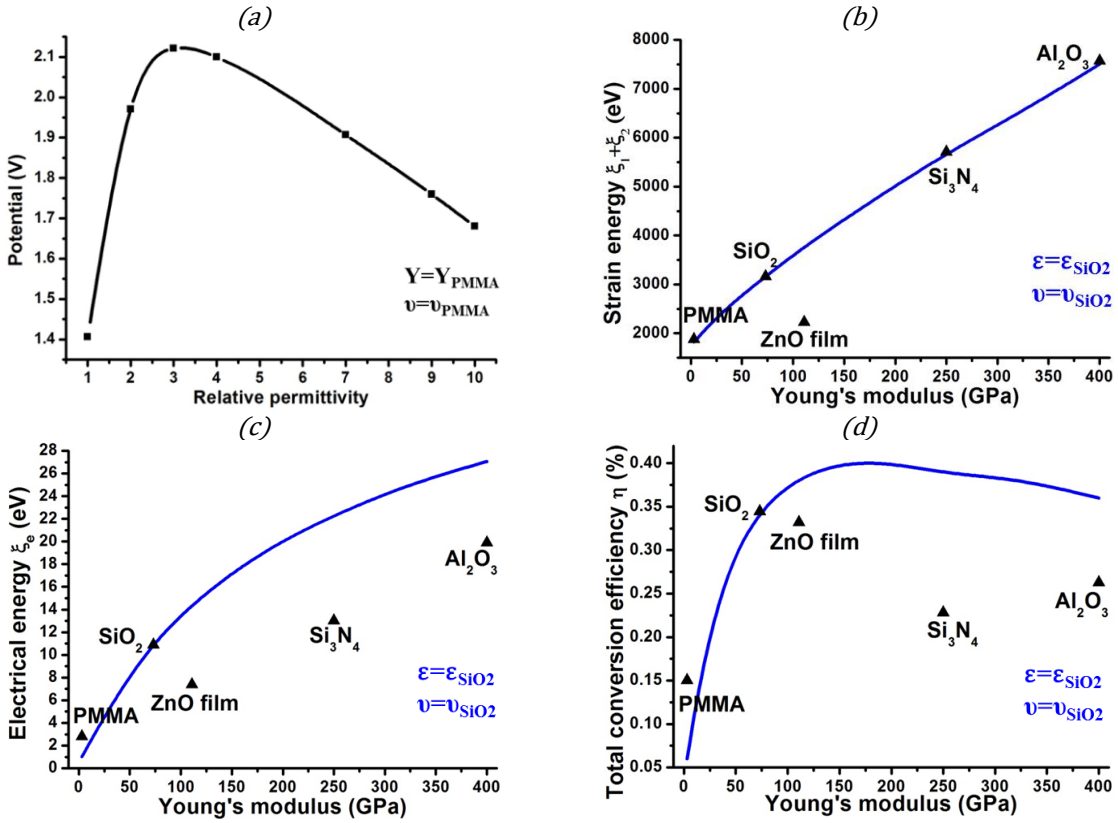

Figure 102 (a) Potential difference ΔV generated by the relative permittivity of the matrix materials having the Young modulus and Poisson ratio of PMMA. (b) Total strain energy, (c) total electric energy and (d) energy

conversion efficiency (per mechanical stimulus) as a function of the Young modulus of the matrix materials having the permittivity and Poisson ratio of SiO_2 and for few other matrix materials: PMMA Si_3N_4 and Al_2O_3 [336].

The relationship between Young's modulus and the energy transfer process is discussed in Figure 102. The solid line represents the simulation results of a material with fixed Poisson ratio (0.4) and relative permittivity (3.0) changing with increasing Young's Modulus, while the symbols represent simulation results for real matrix materials. At constant input strain, the strain energy is proportional to the equivalent Young's modulus of the matrix/NW compound, which means that more strain energy is needed to compress the NG cell with harder matrix material. With constant Poisson's ratio and relative permittivity, the total electric energy mainly benefits from the high mechanical energy transfer efficiency at high Y. For hard materials, large relative permittivity reduces the electrical energy transfer to the output circuit. For PMMA, the low relative permittivity decreased dielectric losses. Within the different materials investigated, SiO_2 achieved the highest conversion efficiency with low relative permittivity and medium hardness.

The design has to be a compromise between mechanical energy transfer and electrical energy transfer. Low mechanical energy transfer obtained with soft materials can be translated into a low sensitivity of the device to external forces. On the other hand, low electrical energy transfer obtained with hard material can increase the dielectric losses as they usually have high relative permittivity. Overall the LING structure could be more effective but it is more challenging and therefore we started with the fabrication and evaluation of VING prototypes where the geometry and the structure had been adapted for bending modes.

IV.4.4. Fabrication process of NG

This part has been done at Georgia Tech in collaboration with the Pr. Zhong Lin Wang by helping the Dr. S. Lee and Y. Lee in their research, where we participated to the fabrication and characterization of NG.

In order to fabricate several NG devices at the same time without any electrical problems, such as short circuit or electrical leakage we used the same design as in the previous section (IV.3.4.) with the addition of a bottom insulating layer of Al_2O_3. As substrate we used thin Al foil with a thickness of 18µm and purity of 99.5%. This substrate has the advantages to be low cost, thin, flexible and adapted for the NG fabrication (Figure 103).

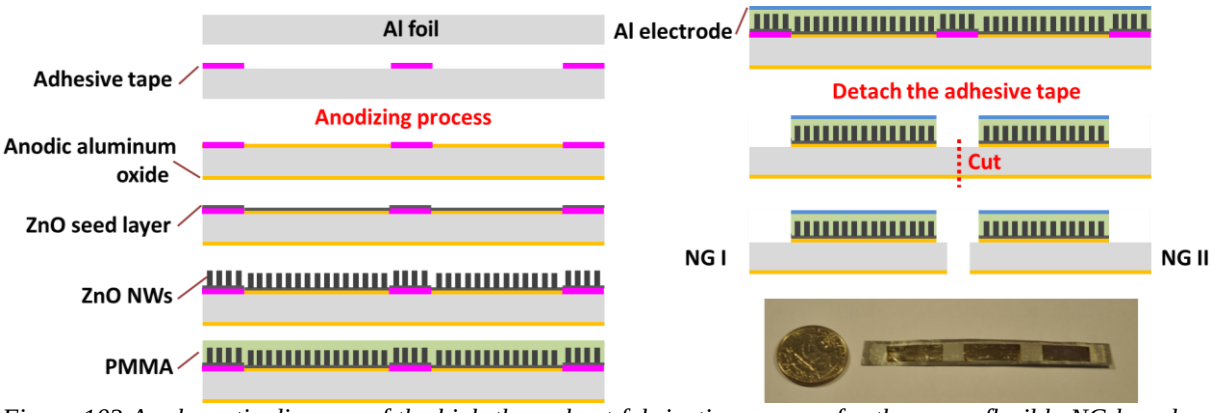

Figure 103 A schematic diagram of the high-throughput fabrication process for the super-flexible NG based on an AAO layer. Several NG devices are easily fabricated at the same time without any electrical problems, such as short circuit or electrical leakage [318].

First an adhesive tape was applied on the Al foil, and then the Al foil was anodized. In the anodization process, Anodized Aluminum Oxide (AAO) layers with nanometer pores were fabricated on both surfaces of the Al foil (Figure 104a). In order to cover up the AAO surface with nano-pores for the growth of ZnO NWs, 100nm thick ZnO seed layer was sputtered on the surface. The AAO layer was grown on the Al foil as an insulating layer, which created enhanced adhesion between the ZnO seed layer and the AAO due to not only the covalent bond by sharing oxygen atoms but also the increased surface contact area caused by the nanopores of the AAO layer compared to previous Georgia Tech's study [337]. In addition, since there was little difference in thermal expansion between them during the hydrothermal process, mechanically stable NG device was fabricated more efficiently. Then, ZnO NWs were grown on the seed layer by a hydrothermal process. The ZnO NWs were densely grown on the ZnO seed-coated AAO layer (Figure 104a). A thin layer of PMMA was spin-coated on the surface of the as-grown ZnO NWs to transmit the bending force to all NWs through the PMMA layer. A 50nm thick Al layer was sputtered on the surface of the PMMA layer, serving as the top electrode of the NG. Finally, by removing the adhesive tape and cutting the part previously covered by the tape, multiple NG devices were easily fabricated at once without any electrical problems, such as short circuit or electrical leakage.

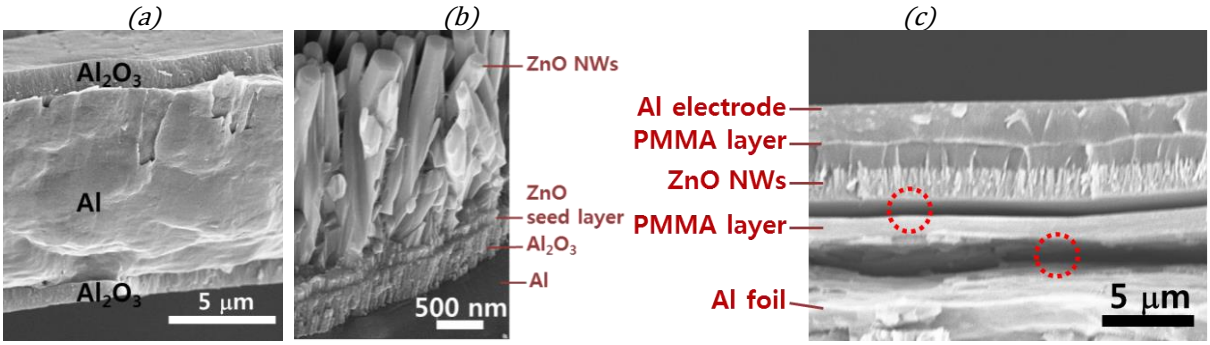

Figure 104 (a) Cross-sectional SEM image of the AAO layer on an ultra-thin Al foil by anodizing, (b) Cross section of the ZnO NWs on the ZnO seed-coated AAO layer. The diameter and the thickness of the ZnO NWs are about 300nm and 3μm respectively and (c) SEM image of the delamination occurred between PMMA layer and ZnO NWs or between PMMA layer and Al foil [318].

The cross section of the fabricated NG (Figure 105a) was observed by SEM as shown in Figure 105b. Figure 105c shows an optical image of the twisted super flexible NG with a thickness of about 16μm.

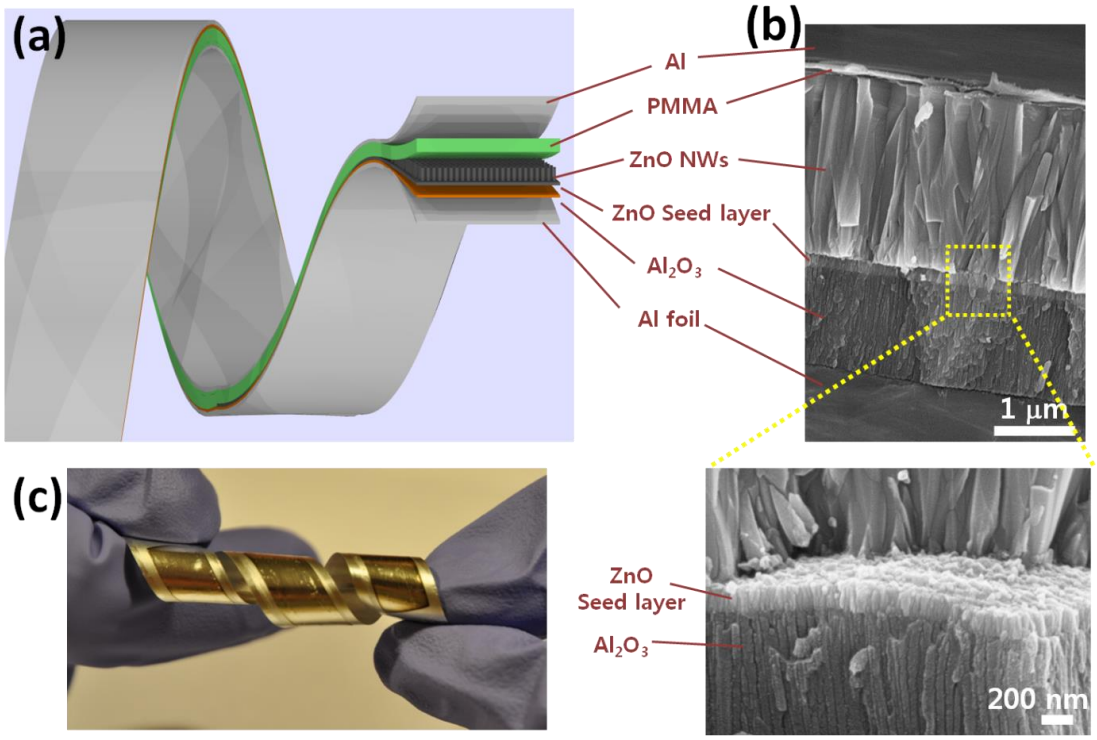

Figure 105 Super flexible piezoelectric NG (NG) (a) Scheme of the super-flexible NG based on an AAO as an insulating layer. The AAO layer was grown on an ultra-thin Al foil prior to the growth of ZnO NWs in order to lead to high-sensitivity and durability of the NG as well as good fabrication yield due to the covalent bonds by sharing oxygen atoms and the increased surface contact area by the nanopores of the AAO layer between the AAO and the ZnO seed layer. (b) SEM and the enlarged SEM images of cross section of the NG. (c) Optical image of the twisted super flexible NG [318].

IV.4.5. Bending characterization

The characterization of flexible NG focused on two aspects:

- The experimental optimization of the flexible NG
- The operation and application of the flexible NG

IV.4.5.1. Experimental optimization

In the study of flexible NG, we chose to use a bottom insulating layer made of AAO. This choice was motivated by the substrate chosen (Al foil) and the easy fabrication and good conformity of AAO layer.

The thin insulating layer plays a key role in the working mechanism of the NG by creating a high potential barrier between the ZnO NWs and the electrode. This barrier protects the NG from short circuiting, but it remains some electrical effects such as dielectric losses and screening effect that can affect the output performances of the NG. Also, since the NG acts as a charged capacitor, the capacitance of the device and the generated current vary with the thickness of the insulating layer. In order to investigate the effect of the thickness of the AAO layer on the NG, we carried out FEM simulation using a ZnO NW array of 15×15 (Figure 106a) for Al_2O_3 layer thicknesses of 100, 300, 600, 900, 1200, 1500, and 2000nm. The NG device was composed of PMMA, ZnO NWs, ZnO seed layer and Al_2O_3. As shown in Figure 106b, the simulation result shows that the difference of the voltage between the top and the bottom Al electrodes (ΔV) was slightly decreased as the thickness of the Al_2O_3 layer increased due to the dielectric loss in the insulator. In addition the capacitance of the Al_2O_3 layer is inversely proportional to its thickness, and the capacitance decrease leads to a drop in

the total capacitance of the NG device which is consistent with the previous optimization study of the top insulating layer (IV.3.3.3.).

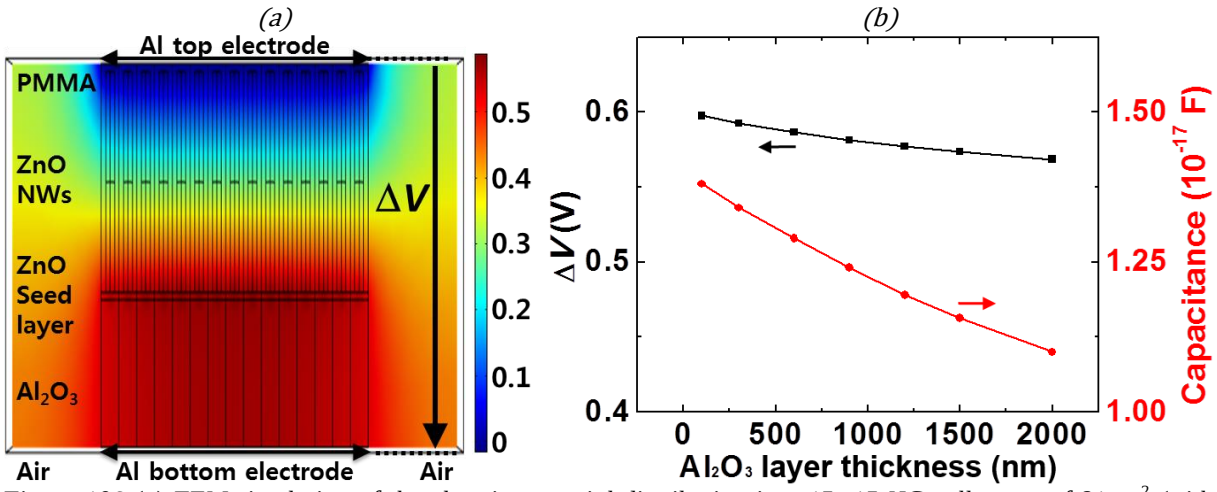

Figure 106 (a) FEM simulation of the electric potential distribution in a 15×15 NG cell array of 81μm² (with NG cell of w=600nm and NWs of d=300nm and l=3um). (b) potential difference and capacitance between the top and the bottom Al electrodes as a function of the thickness of the insulating AAO layer [318].

Before the experimental study, in order to exclude the effect of a change in capacitance under the external force, which could generate an output signals related to the measurement system, a device was prepared the device without ZnO NWs for comparison. The electric signal generated by the device was much smaller than that from the device with ZnO NWs (Figure 107a), and the result demonstrated that the signal was indeed from the piezoelectric effect of the ZnO NWs.

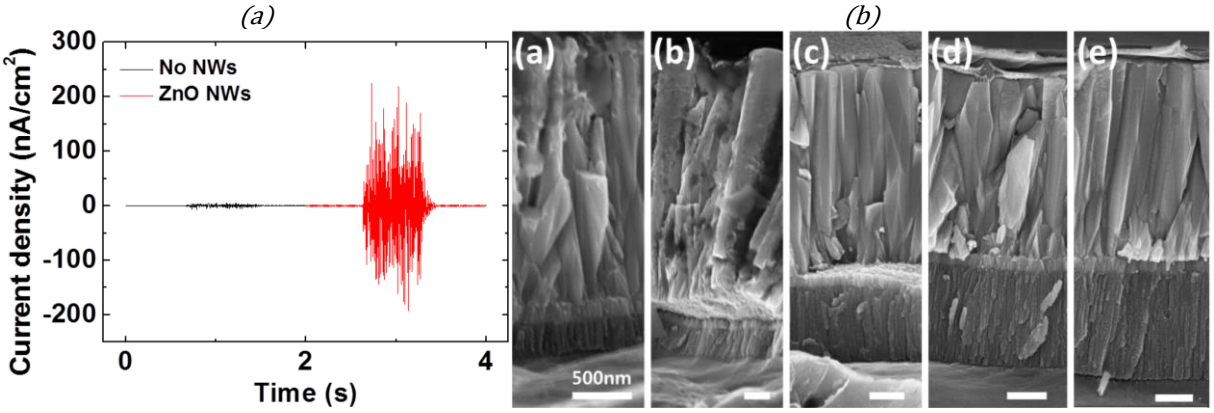

Figure 107 (a) Current density of the devices with and without ZnO NWs. Output currents of two devices were measured under the low-speed air flow (~1.5 m/s). (b) Cross section of NGs with different thicknesses of the AAO layers. By controlling the anodizing time of the anodization process, the thickness of the AAO layer was (a) 280, (b) 620, (c) 920, (d) 1220, and (e) 1440nm, respectively [318].

To demonstrate the simulation results, five NG devices with different AAO layer thicknesses of 280, 620, 920, 1220, and 1440nm, were prepared by controlling the oxidizing time (Figure 107b). To characterize the performance of the NG devices, the NG was tested by a controllable trigger setup, which could periodically bend and unbend under the same condition [338]. The NG was tested such that the ZnO NW layer was compressively strained. Firstly, when the thickness of the AAO layer was larger than 920nm, the output voltage decreased as the thickness increased, showing a similar tendency but in a higher proportion compared to the simulation results. As the thickness of the AAO layer increased from 920, 1220 to 1440nm the output voltage decreased from 0.11V, 0.09V and to 0.075V, respectively (Figure 108a). In addition, the output current showed a similar trend (Figure 108b) because of the role of the output voltage in the current equation I=dQ/dt=d(CV)/dt and the

capacitance decrease of the NG device as the thickness of the AAO layer increased. In general, the dielectric losses are affected by the dielectric constant of the material and the geometry of the device. In our case, considering the theoretical relative permittivity of Al_2O_3 and the 2D geometry of the NG, the effect of the dielectric losses should be minimal because of the high aspect ratio (≈625) of the width (1cm) to the thickness (16µm) of the NG device. Hence, there may be another reason for the decreased voltage output in our devices. Secondly, the NG with the AAO layer thinner than 920nm showed that the output voltage and the current increased with the thickness of the AAO layer unlike the simulation result.

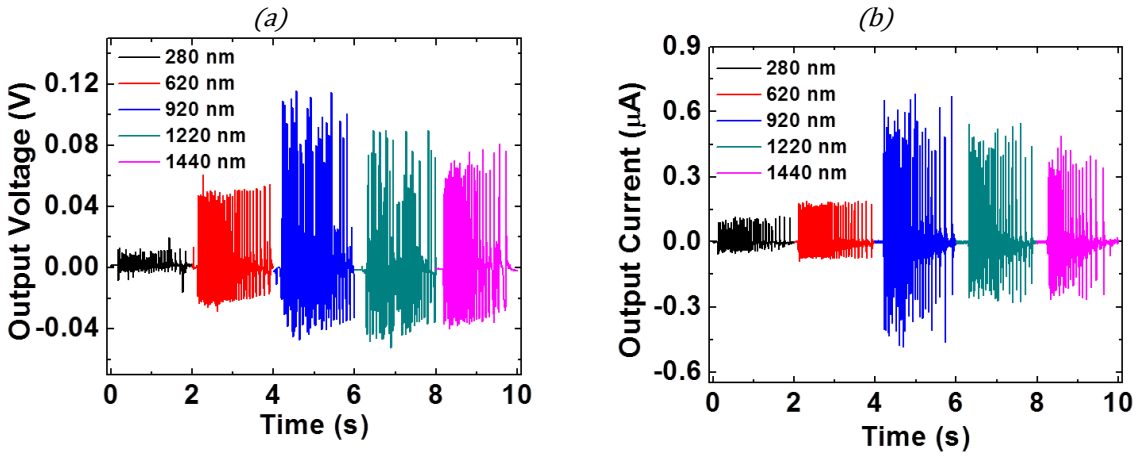

Figure 108 Dependence of the NG output performance on the thickness of the insulating AAO layer. (a) Experimental results of the output voltage and (b) current for the NGs with different thicknesses of the insulating AAO layer measured under the same experimental conditions [318].

The reason for the different tendencies between experimental and simulation results in this range is possibly due to a current leakage through the AAO layer. The AAO layer is probably not a perfect insulator and it may contain some structural defects and charge traps. Moreover, when the ZnO seed layer was sputtered on the AAO layer, some entered into the nanopores of the AAO layer, which led to reduction of the effective thickness of the insulating layer. Consequently, the current leakages might have occurred through the AAO layer due to hopping conduction mechanism between the ZnO NWs and the bottom Al electrode. Thereby reducing the leakage effect with the increased thickness of the AAO layer and enhancing the output performance.

In this study, the insulating AAO layer fabricated by the anodization process was not pure Al_2O_3. During the oxidizing process in sulfuric acid, Al^{3+} ions migrate from the Al across the Al/Al_2O_3 interface into the formed Al_2O_3 layer. While over half of the Al^{3+} ions contribute to the formation of the Al_2O_3 layer, the remaining Al^{3+} ions do not participate in the reaction with oxygen ions and eventually are dissolved into the acid solution [339]. At the end of the anodization process, the aluminum oxide layer contains impurities, including Al^{3+} ions [340]. As a result, they can screen the piezoelectric potential generated by the ZnO NWs. Since the ion quantity in the AAO layer increases with the volume of the AAO layer (at constant ion density), this screening effect is proportional to the thickness of the AAO layer. In order to investigate the effect of these impurities in the AAO layer, we measured the current leakages and calculated the resistances of the AAO layer and electron-beam-evaporated Al_2O_3 (Figure 109a). The resistance of the AAO layer was a few thousand times lower than that of the evaporated Al_2O_3 of equivalent thickness, and also the resistance of the AAO layer with a thickness of 300nm was larger than that with a thickness of 100nm. This means that the current leakage decreases as the thickness of the AAO increases. To understand the screening effect of the impurities, FEM simulation was performed as a function of the Al_2O_3 thickness from 100 to 2000nm

with various fixed charge densities (Figure 109b). The simulation result shows that ΔV gradually decreased with the increase of the Al_2O_3 thickness (and the increase in fixed charge density) due to the increased quantity of the fixed charges in the AAO. The graphs shows that this decrease in ΔV follows a higher rate compared to the preliminary study of Figure 106b. Because the influence from the current leakage is larger than that from the screening effect when the thickness of the AAO layer was thinner than 920nm, the output performance increased with the thickness of the AAO layer, which is different from the simulation result. Once the thickness of the AAO layer is larger than 920nm, the leakage effect is largely suppressed, so that the experimental trend agrees to the simulated trend.

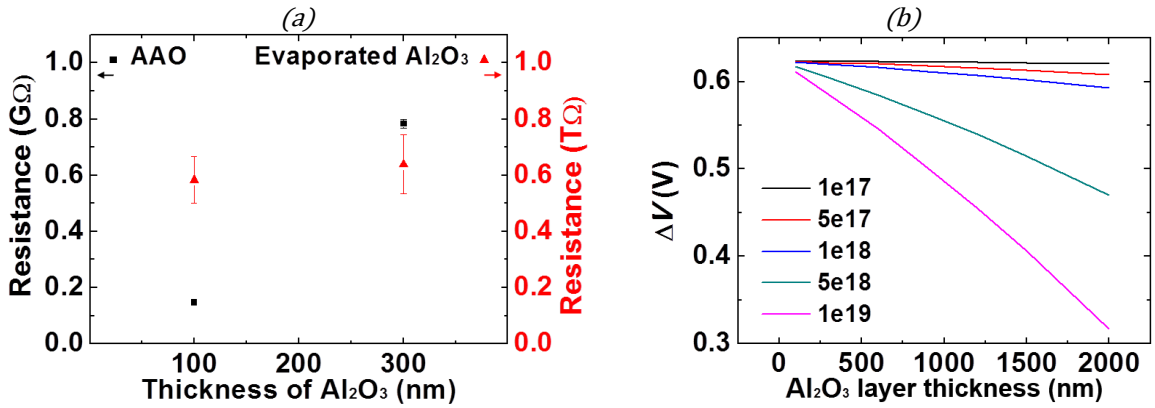

Figure 109 (a) Resistances of the AAO layer and evaporated aluminum oxide as a function of their thicknesses. (b) FEM simulation of ΔV generated by a 15×15 NG cell array as a function of the thickness of the Al_2O_3 layer with fixed charge density. The Al_2O_3 thickness varied from 100 to 2000nm and the simulation was performed at various fixed charge densities [318].

Nevertheless, despite the average insulating properties of AAO compared to evaporated Al_2O_3, AAO is more resistant than evaporated Al_2O_3 under bending. As already explained, its adhesion to Al foil and ZnO is better and its nanopore structures (Figure 110a) make it softer and generate less and smaller cracks than evaporated Al_2O_3. Thus AAO detach less (Figure 110b & c) and it can be grown on any surface shape [341] which make it more suitable for flexible NG.

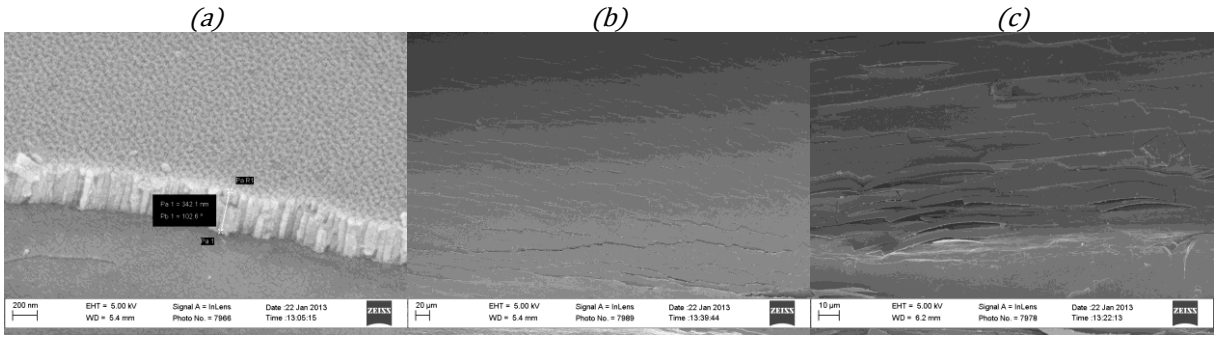

Figure 110 (a) SEM image of the nanopore structure of AAO layer, (b) AAO and (c) evaporated Al_2O_3 cracks and plates formed on NG insulating layer after flexion of the NG substrate.

IV.4.5.2. Operation and application of flexible NG

The performance of the NG with a 620nm thick AAO layer was measured by varying the bending direction under the same condition. Since the ZnO NWs were vertically grown onto the sputtered ZnO seed layer above the AAO layer, the top of the ZnO NWs has a positive potential when the NW layer is compressively strained or a negative potential when the NW layer is tensile strained. Therefore, if the decrease of the output voltage was caused by the screening effect from the current leakages and the impurities according to our assumption, the screening effect should vary with the bending.

Experimental results show that the output voltage and the current were about three times higher when the NW layer was compressively strained compared to when it was tensile strained (Figure 111).

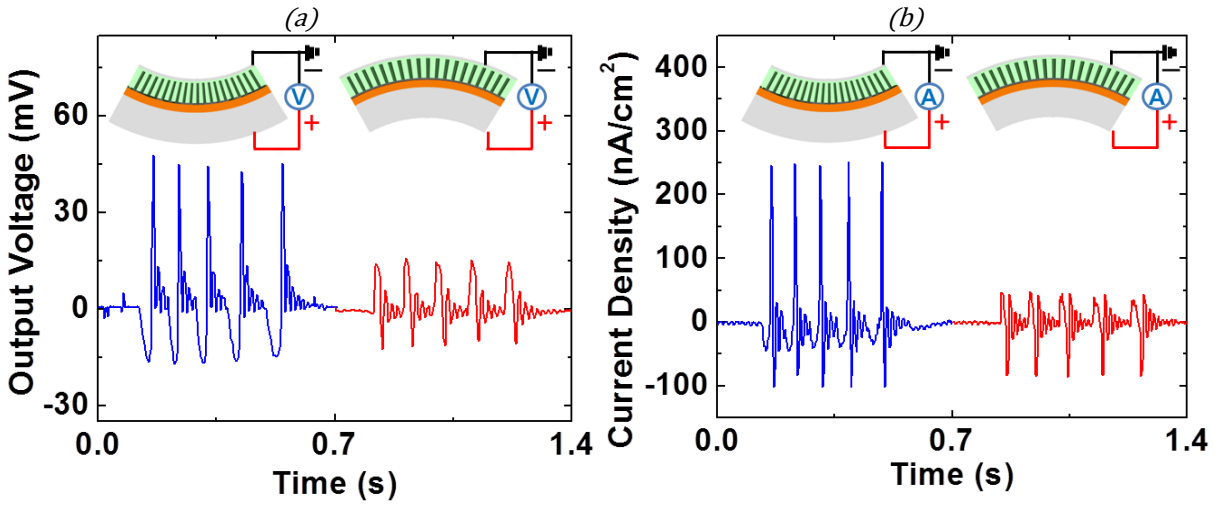

Figure 111 Output performance of the NG device depending on the bending direction. (a) Output voltage and (b) output current when the NG is compressively (inward bending) or tensile (outward bending) strain [318].

This behavior is not due to the large difference between the thicknesses of the bottom Al foil and the top Al thin film. The ZnO NW layer is located on the upper part of the NG, but the strain created in ZnO NW layer is not different between the compressive straining case (inward bending) and the tensile straining case (outward bending). This theory was excluded using FEM models, the strain across the ZnO NW layer showed the same amplitude regardless of the bending direction because the distance from the neutral axis to the ZnO NW layer does not change (Figure 112).

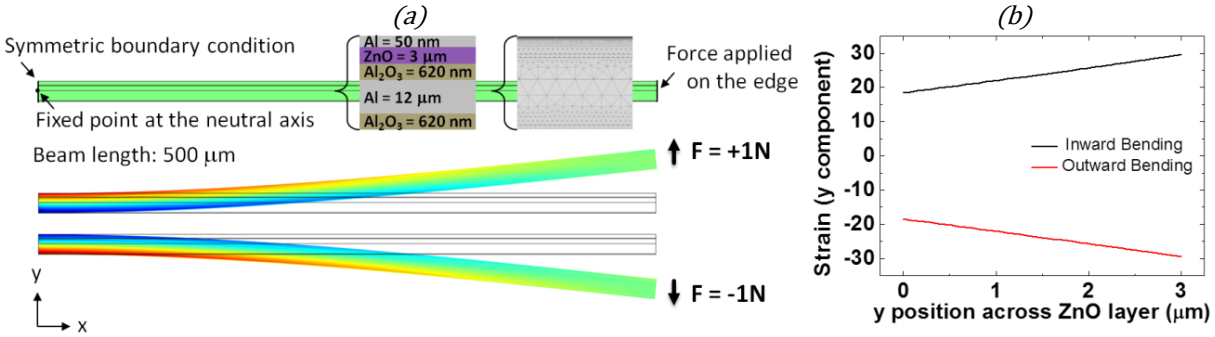

Figure 112 (a) FEM simulation of a NG composed of five layers. Considering the ZnO NW arrays grown on the substrate were close-packed, they were represented by a ZnO thin film to simplify the simulation. (b) Y strain in the ZnO layer while the NG is in inward or outward bending [318].

Therefore, the most dominant effect may be related to the screening effect near the bottom of the ZnO NWs. The bottom of the NWs has positive potential when the NW layer is tensile strained, which can be screened by the electrons coming from the current leakage through the AAO layer, as shown in Figure 113a. On the other hand, since the bottom of the NWs has a negative potential when it is compressively strained, the screening effect is significantly decreased (Figure 113b). This expected result agrees well with our observation.

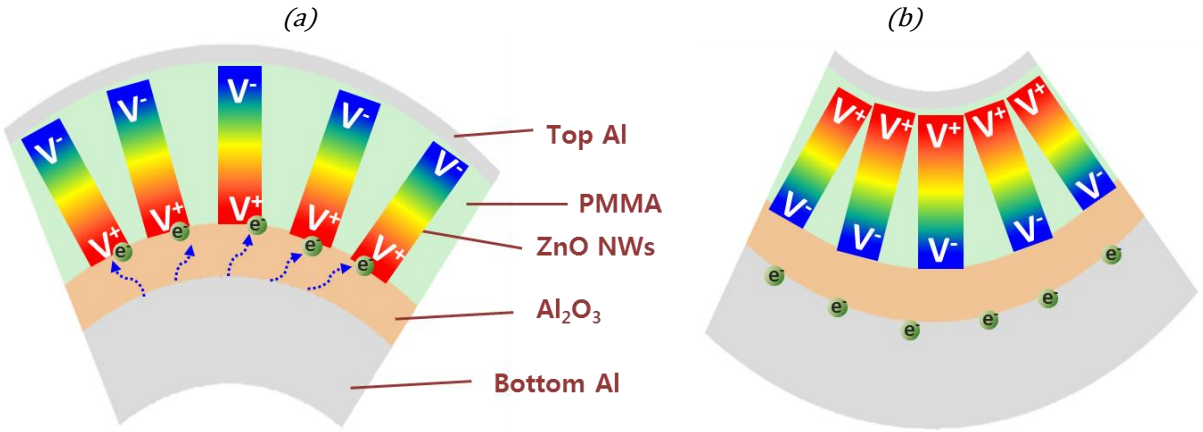

Figure 113 Analysis of the screening effect in a NG under (c) tensile strain and (d) compressive strain condition [318].

As application, the high sensitivity of super flexible NG enables us to measure even a slight local deformation on one's eyelid caused by the motion of the eye ball underneath when sleeping. The motion of the eye ball is associated with one's sleep pattern that consists of two types: non-rapid eye movement (NREM) sleep also known as quiet sleep and rapid eye movement (REM) sleep also known as active sleep [342]–[344]. Furthermore, since there are rich sensory and motor connections between the eye and the brain, the motion of the eye ball can provide valuable signs, associated with tiredness as well as brain activity [345]. To demonstrate the high sensitivity of the NG for detecting the local deformation on the eyelid according to the motion of the eye ball, a NG with active area of 3mm × 10mm was prepared. The device was attached to a right eyelid of a student, putting the top Al electrode face down on the eyelid in order to get the NW layer strained in compression during the eye ball motion for higher sensitivity (Figure 114a). The device was firmly attached on the eyelid with eyelash glue. The NG was driven by moving the eye ball from side to side, and the output voltage and current were measured under slow and rapid eye movement. While moving the eye ball from side to side, the NG is strained as the eye ball passes near the center of the NG, and then the NG is released as the eye reaches the other side. As a result, when the eye ball moves from left to right or from right to left, the output indicates one-cycle of an alternating signal caused by the piezoelectric potential; a single peak is detected while moving the eye ball from one end to the center of the NG, and the opposite peak is detected while moving the eye ball from the center to the other end of the NG. Figure 114b shows the output voltage of the NG measured under the slow motion of the eye ball (≈0.4Hz). The output voltage was observed as four-cycle alternating signals during four round-trips of the right eye. Furthermore, under the rapid eye movement (≈1.6Hz) of five round-trips, the measured output voltage clearly showed five-cycle alternating signals following the motion of eye ball (Figure 114c). The output current was then investigated according to the rapid and the slow eye movement (Figure 114d & e). However, each of one-cycle alternating signals in the output current could not be separately obtained under both the rapid and the slow eye movement; whenever moving the eye ball from side to side, portion of them showed one-cycle alternating signal while others showed either a positive or a negative peak. In other words, the signal generated by the motion of the eye ball in one direction was over covered by that from the following motion of the eye ball in the opposite direction due to the time-constant response of the NG output current. Thus, the output voltage can be effectively utilized to detect the eye ball motion for monitoring sleep pattern, tiredness, and possible brain activity for example.

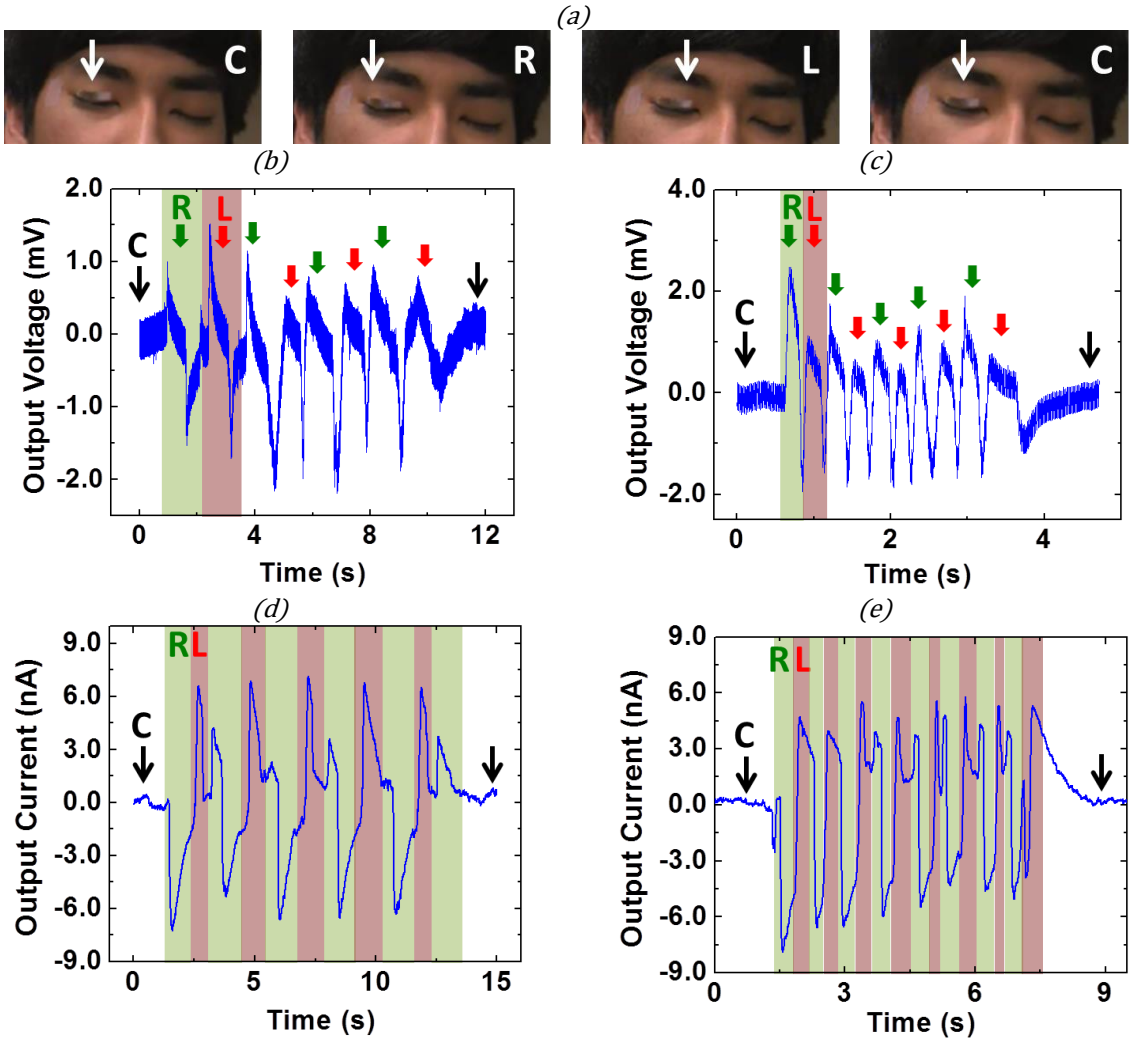

Figure 114 Super-flexible NG as an active sensor for detecting the motion of a human eye ball. (a) The NG attached a right eyelid was driven by moving the eye ball from right (R), center (C), and to left (L) or from L, C, and R. Output voltage measured under (b) slow and (c) rapid eye movement. Output current measured under (d) slow and (e) rapid eye movement [318].

IV.5. Conclusion

In conclusion, our energy harvesting study clearly demonstrates that piezoelectric NWs, such as ZnO and GaN NWs, are well adapted to mechanical energy harvesting only if properly integrated. Our dynamical study of typical ZnO NWs (few hundred of nanometers in length and tens to hundreds of nanometers in diameter) show that the mechanical resonance frequency is rather high, in the order of the MHz. Taking into account the piezoelectric phenomenon in the NWs, the resonance frequency slightly decreases but remains too high to harvest daily mechanical vibrations form human activity that lay in low frequency range. This conclusion still holds even by grouping the NWs or using a heavy seismic mass to decrease the resonance frequency of the whole system. Therefore we have focused our study to a more appropriate approach considering real-time and quasi-static deformations. These deformations could be encountered in low-frequency applications or when random mechanical inputs are available from the human body for example.

We have developed analytical models and FEM simulations of NG, to investigate electromechanical optimization of such devices (VING) with various insulating materials and geometries. After a deep analysis, we have proposed an innovative and efficient NG design [300]. When optimized, the

piezoelectric NWs layer of the NG is very comparable with piezoelectric composite material layer, having an optimum piezoelectric potential generated for long and thin NWs. The comparison between the optimized ZnO NWs based NG and a thin ZnO layer based NG under the same conditions proves the viability and the interest of using NWs for energy conversion applications like the mechanical energy harvesting. If we consider only the electromechanical nanostructure, the electrical energy harvested by the NG can be multiplied by a factor of 6, keeping the same efficiency than a thin piezoelectric layer and increasing the force sensitivity. While we have restricted our interest to ZnO, the models can be extended to other piezoelectric materials in form of NWs, nanobeams and nanofibers such as GaN [308], [309], $BaTiO_3$ [33], [312] and PZT [218], [311] between others. As for semiconductor piezoelectric NWs, the screening by ionized dopant strongly limits the performance for high doping, even under the assumption of full depletion. This degradation can only be partly compensated by the increase of piezoelectric coefficients which is expected at nanoscale [40]. Even if difficult to grow, undoped piezoelectric NWs seem the best option. To counter screening effects, NWs quality could be improved using plasma and annealing [274]. An alternative would be to deplete the NWs using positive charged matrix material such as P_3HT [328].

We have then investigated the fabrication of VING prototypes using the hydrothermal growth of ZnO NWs we have developed and that allowed us to realize large surface (up to $12cm^2$) devices. Fabrication is quite challenging due to short-circuit problems. During the NG fabrication process we have highlighted four mains obstacles that need to be tackled to obtain a good NG: the substrate roughness, the presence of dust and particles, growing defects and the importance of delicate manipulation control. Using only one lift-off process can help to increase the working NG yield but it was not enough. Therefore we advise to use a bottom insulating layer in addition of the top one, to better control the current leakages. To get even better performing NGs it is necessary to build the optimized structure which includes a composite PMMA-NW layer and a thin and hard top insulator.

In addition we have shown that the VING structure can be optimized to harvest bending modes. We have investigated various materials and we have defined optimization guidelines using different insulator matrix materials. Compared to PMMA previously defined as the best matrix material for NG operating in compression mode, an Al_2O_3 matrix material is better suited for NG operating in bending mode, improving the potential generated by two times and the electric energy by six times which is essential for energy harvesters. On the other hand SiO_2 should be preferred to maximize the energy conversion efficiency. The poor performance of this configuration can be explained by the fact that the strain is normal to the NW axis. Therefore, due to the Poisson ratio of the matrix material and the lower piezoelectric coefficients in transvers mode (d_{13}), the mechanical energy converted is lower. Although VINGs are not optimal in bending modes, they show reasonable performances. The most adapted structure in this case remains the LING consisting of a VING device stacked and tilted at 90°. As the fabrication of LING is difficult, we first investigated the fabrication of VING prototypes operating in bending mode. Similarly to the previous prototypes the fabrication is not easy mainly due to short-circuit problems. The addition of a bottom insulating layer allows the fabrication of long NGs ribbons. During the fabrication process of these devices we highlighted the important role of the bottom insulating layer and the strong influence of its electrical properties. Having a bottom insulating layer as thin as possible while keeping its insulating role is a key point to realize efficient NGs. In this case we compared AAO and evaporated Al_2O_3 as insulating layer. AAO showed lower electrical resistivity and thus larger leakage currents compared to evaporated Al_2O_3. Meanwhile they hold better the bending of the NG. Finally, functional prototypes were characterized through an original application example: a self-powered displacement sensor for eyes ball motion.

Conclusion and perspectives: Toward self-powered sensors

Smart systems are the combined result of advances in microelectronics leading to an increase in power, lower transistor energy consumption, the addition of new features (More than Moore), means of communication and especially its integration and application into our daily lives. The evolution of the field of smart systems is promising, and expectations are high in multiple fields of applications concerning the human activities and environment monitoring. But, victim of its success, the integration of more and more functions in smart system is leading to an energy issue where the autonomy of such smart systems is becoming to be the main issue. Therefore there is a growing need for autonomous sensors and power sources. Developing energy harvesters and self-powered sensors is one way to address this energy issue. Among the technologies studied, piezoelectricity has several advantages. It is compatible with the IC/MEMS industry, it generates high voltages (up to 100V [346]) and it has a high direct coupling efficiency between the mechanic and electric physics (up to 80% [347]). Among the piezoelectric materials, semiconductor piezoelectric NWs could be one of its strengths as they exhibit good piezoelectric properties and allows multiple integrations way in the IC industry. These improved piezoelectric properties, which could be due to mechanical effects (enhance Young modulus, flexibility) or electrical phenomenon, have to be investigated to get the best of piezoelectric NWs.

The main goal of this thesis was to study the electromechanical behavior of GaN and ZnO semiconductor piezoelectric NWs for mechanical sensor and energy harvesting applications. It is involving multiple physics (multiphyiscs): mechanic and electronic physics, but also piezoelectric and semiconductor physics. It is a multi-scale problem using nanostructures for macroscopic applications such as $1cm^2$ NG and map force sensor. This topic is rather new to the art. For this reason we had to develop the knowledge and tools necessary for the study of individual NW but also of assembly of NWs at different theoretical levels: conceptual, analytical and simulation, and at practical levels: fabrication, characterization and integration into devices.

To better understand how piezoelectric NWs could help to address this energy issue and to choose the best approach, we studied the piezoelectricity, the materials used and their properties. With the last progresses in synthetizing and optoelectronic characterization of ZnO and GaN NWs, those became very interesting. They are piezoelectric materials with good properties, compared to the best ferroelectrics, increasing at the nanoscale by more than 2 [29]. They have the advantage of being IC compatible, reasonably easy to synthesize by top-down and bottom-up approaches in form of semiconductor NWs which make them easier to integrate into today's technologies.

Therefore, we developed the hydrothermal growth of ZnO NWs (II.2.). Its control allowed us to grow ZnO NWs on various substrates (hard and flexible) with NWs diameters ranging from 50 to 250nm, lengths from 1 to 7µm and densities from 10^8 to $10^{10}cm^{-2}$. This is an essential step for the research and development of technology based on NWs. Then the other key point was to model and understand the behavior of piezoelectric NWs. So we have carried out an analytical study and FEM simulations of a bent ZnO NW. We have found a piezoelectric potential distribution comparable to the literature of ±0.3V under a lateral force F=80nN. We noted and explained the reversal potential at the base of the NW and addressed the scaling and sizing rules of these NWs where the piezopotential increases with the force and when the diameter decreases. Finally, in order to investigate the properties of ZnO and GaN NWs, we have developed and conducted mechanical and piezoelectric AFM characterization of NWs. The characterization of the Young's modulus of NWs larger than 100nm did not highlighted any

specific nano mechanical effect. The piezoelectric characterization demonstrated that an electric potential up to 300mV is generated when the NWs are deformed by forces of the order of the µN. This potential is proportional to the applied force, can saturate and depends on the properties of the NWs: piezoelectric coefficient, Young modulus and permittivity. Further development on characterization techniques is still required to quantitatively measure the piezoelectric coefficients of the small NWs considered in this work and to understand the role of free carriers, doping and structuration of the NWs on the potential generated.

With this basic understanding of the piezoelectric phenomenon in ZnO and GaN NWs, it is possible to design applications. However we have taken into account the phenomena that can disrupt or alter the piezoelectric effect. We modeled cylindrical and hexagonal NW geometry which has a negligible impact on the magnitude of the potential generated. Cylindrical NWs underestimate by 6% the potential generated by wurtzite NWs. Likewise, the non-linear behavior of the NWs subjected to large forces strongly affects the amplitude and distribution of the piezoelectric potential which increases. The environment and in particular the substrate, greatly influences the distribution and the magnitude of the piezopotential by more than 7 times, but only at the base of the NW. Finally, increasing the doping of the NW can entirely screen the piezoelectric potential and totally reduces it up to zero [300]. These effects are significant and must be taken into account during the design of devices using ZnO or GaN NWs. In the case of a force or displacement sensor based on the potential response of piezoelectric NWs, we have shown that the design, the sensitivity and the resolution of such a sensor is strongly influenced by these parasitic phenomena but they can be turned into advantages. For example the variability of the NWs diameters allows tuning the sensors sensitivity up to $10mV.nN^{-1}$ or increases its spatial resolution. Experimentally, it is possible to measure the current through a Schottky junction NW / metal to produce such a sensor. Thus using AFM we have demonstrated the feasibility of such a sensor reaching a sensitivity of $1.24\ ln(A).nN^{-1}$. We have highlighted the piezotronic effect consisting of the influence of the local piezoelectric potential on the band structure in semiconductors and their interfaces. This effect is very interesting and could lead to improved technologies such as highly sensitive UV sensors [348], [349] or our nN force sensor which is 3×10^4 times more sensitive than comparable devices [296].

Highly acclaimed in recent years, another application concerns the harvesting of mechanical energy based on piezoelectric NWs. Through a detailed study of this technology, we have highlighted the relevance of this approach for smart and or autonomous systems and sensors. Then we have studied and adapted the concept of mechanical energy harvesting to the use of piezoelectric NWs. This allows, in addition to the piezoelectricity advantages, a thin customization of structures and physical properties leading to new improvements. At first we have investigated the dynamical energy harvesting (IV.2.), but we realized that the resonance frequencies of such NWs were too high (few MHz) and it was very difficult to decrease them to values adapted to vibration of our daily environment (typically at frequencies below 200Hz). Thus, the quasi-static energy harvesting is another approach of the problem. We differentiated two cases: the axial solicitation of the NWs when the device is under axial compression and the transversal one when the device is under a bending force. These two cases are the best and the worst cases of compressing NWs and so they allow evaluating the NG performances of the design we have chosen. In the first case, using a simple analytical approach we were able to understand how it works and highlight potential optimizations guidelines. Then through FEM simulations we clearly understood all the advantages and disadvantages of this problem. We have shown using this model that the optimized structure consists of thin and long piezoelectric NWs with an adequate density (IV.3.3.4.). Thus NG based on ZnO

NWs could be more sensitive and generate up to 6 times more energy than a thin layer of ZnO with the same thickness and under the same force, in the manner of a composite material. In addition this could lead to a higher sensibility of NGs compared to standard micro mechanical energy harvesters, using PZT for example, allowing harvesting electrical energy from smaller forces and strains. Therefore optimizing the ZnO NG structure, at 1Hz under 1MPa it should be possible to harvest up to $500nW.cm^{-3}$ and up to $1.2\mu W.cm^{-3}$ taking into account doubling piezoelectric coefficients at nanoscale. In transversal solicitation (bending), the effectiveness of the device is lower than the compressive mode but remains greater compared to a device using a thin layer of ZnO with the same amount of piezoelectric material. During these studies, we have designed an optimized structure of NG and we have realized prototypes for compression and bending modes. To fully characterize these prototypes, we have developed a specific test bench and the first results are encouraging. The improvements are fascinating and such an electromechanical optimization of NG can be extended to other piezoelectric materials such as AlN and $BaTiO_3$ for example. Thus piezoelectric nano composite materials could lead to a great improvement in piezoelectricity.

Throughout this thesis, I have tried to build and direct the project with a realistic and practical approach responding to the primary questions: are piezoelectric NWs useful for self-powered sensors and mechanical energy harvesters? I demonstrated that they can bring great improvements in these fields in term of integration, structuration and sensitivity. This approach is necessary to convince on the interest and relevance of these researches. That is why this study is both global and as detailed as possible about this wide subject. Further investigations are still required to continue to improve these technologies. More accurate simulations taking into account the semiconductor physics in ZnO and GaN NWs are needed to optimize even more the NGs and the force sensors. The synthesis of low doped NWs and the fabrication of optimized NG must be developed to increase their performances and reach their full potential. In addition several issues should be addressed: What is the effect of the nonlinear piezoelectric behavior on the NG performances? Does the piezopotential generated saturate for high forces? But also what is the impact of charges and traps in the matrix material and how to turn the semiconducting properties of ZnO and GaN NWs into advantages? All that while improving the reliability, endurance and aging of NG. Furthermore to power future autonomous systems, multisource energy harvesters could harvest even more energy and so the integration of NG with other energy harvesters should be investigated [350], [351]. Such enhancements could overcome the poor perspectives of batteries and lead to an efficient duo, thank to adapted power management systems, to longer power supply future autonomous sensors. Thus piezoelectric semiconductor NWs, and especially ZnO and GaN NWs, could become a key technology for future energy harvesters and self-powered sensors. All this is fascinating and may lead to great improvements for future autonomous sensors.

References

[1] X. Xu, A. Potié, R. Songmuang, J. W. Lee, B. Bercu, T. Baron, B. Salem, and L. Montès, "An improved AFM cross-sectional method for piezoelectric nanostructures properties investigation: application to GaN nanowires.," *Nanotechnology*, vol. 22, no. 10, p. 105704, Mar. 2011.

[2] H. Sutter, "The Free Lunch Is Over A Fundamental Turn Toward Concurrency in Software," 2009. [Online]. Available: http://www.gotw.ca/publications/concurrency-ddj.htm.

[3] K. D. Wise, D. J. Anderson, J. F. Hetke, D. R. Kipke, and K. Najafi, "Wireless Implantable Microsystems: High-Density Electronic Interfaces to the Nervous System," *Proc. IEEE*, vol. 92, no. 1, pp. 76–97, Jan. 2004.

[4] A. M. Turing, "Intelligent Machinery, A Heretical Theory*," *Philos. Math.*, vol. 4, no. 3, pp. 256–260, Sep. 1996.

[5] J. Hassoun, S. Panero, P. Reale, and B. Scrosati, "A new, safe, high-rate and high-energy polymer lithium-ion battery.," *Adv. Mater.*, vol. 21, no. 47, pp. 4807–10, Dec. 2009.

[6] C. Buratti, A. Conti, D. Dardari, and R. Verdone, "An overview on wireless sensor networks technology and evolution.," *Sensors (Basel).*, vol. 9, no. 9, pp. 6869–96, Jan. 2009.

[7] J. M. Kahn, R. H. Katz, and K. S. J. Pister, "Next century challenges," in *Proceedings of the 5th annual ACM/IEEE international conference on Mobile computing and networking - MobiCom '99*, 1999, pp. 271–278.

[8] P. Volgyesi, G. Balogh, A. Nadas, C. B. Nash, and A. Ledeczi, "Shooter localization and weapon classification with soldier-wearable networked sensors," in *Proceedings of the 5th international conference on Mobile systems, applications and services - MobiSys '07*, 2007, p. 113.

[9] G. E. Blomgren, "Perspectives on portable lithium ion batteries liquid and polymer electrolyte types," in *Seventeenth Annual Battery Conference on Applications and Advances. Proceedings of Conference (Cat. No.02TH8576)*, 2002, pp. 141–144.

[10] F. Alessandrini, M. Conte, S. Passerini, and P. . Prosini, "Overview of ENEA's Projects on lithium batteries," *J. Power Sources*, vol. 97–98, pp. 768–771, Jul. 2001.

[11] C. O'Mathúna, T. O'Donnell, R. V Martinez-Catala, J. Rohan, and B. O'Flynn, "Energy scavenging for long-term deployable wireless sensor networks.," *Talanta*, vol. 75, no. 3, pp. 613–23, May 2008.

[12] S. Kang, S. Lee, and F. Prinz, "Size does matter: The pros and cons of miniaturization," *ABB Rev.*, no. 2, 2001.

[13] W. Y. Sim, G. Y. Kim, and S. S. Yang, "Fabrication of micro power source (MPS) using a micro direct methanol fuel cell (μDMFC) for the medical application," in *Technical Digest. MEMS 2001. 14th IEEE International Conference on Micro Electro Mechanical Systems (Cat. No.01CH37090)*, 2001, pp. 341–344.

[14] D. Friedman, H. Heinrich, and D.-W. Duan, “A low-power CMOS integrated circuit for field-powered radio frequency identification tags,” in *1997 IEEE International Solids-State Circuits Conference. Digest of Technical Papers*, 1997, pp. 294–295,.

[15] A. Nechibvute, A. Chawanda, and P. Luhanga, “Piezoelectric Energy Harvesting Devices: An Alternative Energy Source for Wireless Sensors,” *Smart Mater. Res.*, vol. 2012, pp. 1–13, 2012.

[16] S. J. Roundy, “Energy Scavenging for Wireless Sensor Nodes with a Focus on Vibration to Electricity Conversion,” BERKELEY, 2003.

[17] Yole, “MEMS industry evolution: from devices to function,” 2011.

[18] Isuppli, “MEMS Enters New Cycle of Double-Digit Growth,” *isuppli*, 2011. [Online]. Available: http://www.isuppli.com/MEMS-and-Sensors/MarketWatch/Pages/MEMS-Enters-New-Cycle-of-Double-Digit-Growth.aspx.

[19] Yole, “MEMS Devices Emerging MEMS report,” 2013.

[20] P. Harrop and R. Das, *Energy Harvesting and Storage for Electronic Devices 2011-2021*, IDTechEX. IDTechEX, 2011.

[21] S. Beeby and N. White, *Energy Harvesting for Autonomous Systems*. Artech House, 2010, p. 325.

[22] P. Yang, R. Yan, and M. Fardy, “Semiconductor nanowire: what’s next?,” *Nano Lett.*, vol. 10, no. 5, pp. 1529–36, May 2010.

[23] J. G. Lu, P. Chang, and Z. Fan, “Quasi-one-dimensional metal oxide materials—Synthesis, properties and applications,” *Mater. Sci. Eng. R Reports*, vol. 52, no. 1–3, pp. 49–91, May 2006.

[24] Y. Li, J. Xiang, F. Qian, S. Gradecak, Y. Wu, H. Yan, D. A. Blom, and C. M. Lieber, “Dopant-free GaN/AlN/AlGaN radial nanowire heterostructures as high electron mobility transistors.,” *Nano Lett.*, vol. 6, no. 7, pp. 1468–73, Jul. 2006.

[25] W. Wu, Y. Wei, and Z. L. Wang, “Strain-gated piezotronic logic nanodevices.,” *Adv. Mater.*, vol. 22, no. 42, pp. 4711–5, Nov. 2010.

[26] J. C. Johnson, H.-J. Choi, K. P. Knutsen, R. D. Schaller, P. Yang, and R. J. Saykally, “Single gallium nitride nanowire lasers.,” *Nat. Mater.*, vol. 1, no. 2, pp. 106–10, Oct. 2002.

[27] J. Zhou, Y. Gu, P. Fei, W. Mai, Y. Gao, R. Yang, G. Bao, and Z. L. Wang, “Flexible piezotronic strain sensor.,” *Nano Lett.*, vol. 8, no. 9, pp. 3035–40, Sep. 2008.

[28] R. Agrawal, B. Peng, E. E. Gdoutos, and H. D. Espinosa, “Elasticity size effects in ZnO nanowires--a combined experimental-computational approach.,” *Nano Lett.*, vol. 8, no. 11, pp. 3668–74, Nov. 2008.

[29] R. Agrawal and H. D. Espinosa, “Giant piezoelectric size effects in zinc oxide and gallium nitride nanowires. A first principles investigation.,” *Nano Lett.*, vol. 11, no. 2, pp. 786–90, Feb. 2011.

[30] M. Minary-Jolandan, R. A. Bernal, I. Kuljanishvili, V. Parpoil, and H. D. Espinosa, “Individual GaN nanowires exhibit strong piezoelectricity in 3D.,” *Nano Lett.*, vol. 12, no. 2, pp. 970–6, Feb. 2012.

[31] S. Xu, Y. Qin, C. Xu, Y. Wei, R. Yang, and Z. L. Wang, “Self-powered nanowire devices.,” *Nat. Nanotechnol.*, vol. 5, no. 5, pp. 366–73, May 2010.

[32] X. Duan and C. M. Lieber, “Laser-Assisted Catalytic Growth of Single Crystal GaN Nanowires,” *J. Am. Chem. Soc.*, vol. 122, no. 1, pp. 188–189, Jan. 2000.

[33] K.-I. Park, S. Xu, Y. Liu, G.-T. Hwang, S.-J. L. Kang, Z. L. Wang, and K. J. Lee, “Piezoelectric BaTiO(3) Thin Film Nanogenerator on Plastic Substrates.,” *Nano Lett.*, vol. 10, no. 12, pp. 4939–4943, Nov. 2010.

[34] D. Routkevitch, T. Bigioni, M. Moskovits, and J. M. Xu, “Electrochemical Fabrication of CdS Nanowire Arrays in Porous Anodic Aluminum Oxide Templates,” *J. Phys. Chem.*, vol. 100, no. 33, pp. 14037–14047, Jan. 1996.

[35] C. Majidi, Z. Chen, D. J. Srolovitz, and M. Haataja, “Spontaneous bending of piezoelectric nanoribbons: Mechanics, polarization, and space charge coupling,” *J. Mech. Phys. Solids*, vol. 58, no. 2, pp. 73–85, Feb. 2010.

[36] M.-H. Zhao, Z.-L. Wang, and S. X. Mao, “Piezoelectric Characterization of Individual Zinc Oxide Nanobelt Probed by Piezoresponse Force Microscope,” *Nano Lett.*, vol. 4, no. 4, pp. 587–590, Apr. 2004.

[37] J. Zhou, P. Fei, Y. Gu, W. Mai, Y. Gao, R. Yang, G. Bao, and Z. L. Wang, “Piezoelectric-potential-controlled polarity-reversible Schottky diodes and switches of ZnO wires.,” *Nano Lett.*, vol. 8, no. 11, pp. 3973–7, Nov. 2008.

[38] Z. L. Wang and J. Song, “Piezoelectric nanogenerators based on zinc oxide nanowire arrays,” *Science*, vol. 312, no. 5771, pp. 242–6, Apr. 2006.

[39] Y. Hu, Y. Zhang, C. Xu, G. Zhu, and Z. L. Wang, “High-Output Nanogenerator by Rational Unipolar Assembly of Conical Nanowires and Its Application for Driving a Small Liquid Crystal Display.,” *Nano Lett.*, vol. 10, no. 12, pp. 0–6, Nov. 2010.

[40] H. D. Espinosa, R. A. Bernal, and M. Minary-Jolandan, “A review of mechanical and electromechanical properties of piezoelectric nanowires.,” *Adv. Mater.*, vol. 24, no. 34, pp. 4656–75, Sep. 2012.

[41] X. Chen, S. Xu, N. Yao, and Y. Shi, “1.6 V nanogenerator for mechanical energy harvesting using PZT nanofibers.,” *Nano Lett.*, vol. 10, no. 6, pp. 2133–7, Jun. 2010.

[42] C. Chang, V. H. Tran, J. Wang, Y.-K. Fuh, and L. Lin, “Direct-write piezoelectric polymeric nanogenerator with high energy conversion efficiency.,” *Nano Lett.*, vol. 10, no. 2, pp. 726–731, Feb. 2010.

[43] Z. L. Wang, “Energy Harvesting Using Piezoelectric Nanowires-A Correspondence on ‘Energy Harvesting Using Nanowires?’ by Alexe et al.,” *Adv. Mater.*, vol. 21, no. 13, pp. 1311–1315, Apr. 2009.

[44] S. Kim, M. Chung, and S. Sohn, “Flexible Energy Conversion Device,” 2009.

[45] Z. L. Wang, X. Wang, J. H. Song, J. Zhou, and J.-H. He, “Nanopiezotronics,” 19-Mar-2007.

[46] Y. Shi and S. Xu, “Piezoelectric nanofibers, nanotubes, nanojunctions and nanotrees,” 2009.

[47] M. A. Schubert, S. Senz, M. Alexe, D. Hesse, and U. Gösele, “Finite element method calculations of ZnO nanowires for nanogenerators,” *Appl. Phys. Lett.*, vol. 92, no. 12, p. 122904, 2008.

[48] O. Graton, L. P. T. H. Hue, and M. Lethiecq, “Strategy of modelling and simulation of electromechanical conversion in ZnO nanowires,” *Adv. Appl. Ceram.*, vol. 44, no. 000, pp. 1–7, 2012.

[49] J. Curie and P. Curie, “Contractions et dilatations produites par des tensions dans les cristaux hémièdres à faces inclinées,” *Comptes Rendus l’Académie des Sci.*, vol. 93, pp. 1137–1140, 1880.

[50] J. Curie and P. Curie, “Développement, par pression, de l’électricité polaire dans les cristaux hémièdres à faces inclinées,” *Comptes Rendus l’Académie des Sci.*, vol. 91, pp. 294–295, 1880.

[51] J. Curie and P. Curie, “Sur l’électricité polaire dans les cristaux hémièdres à faces inclinées,” *Comptes Rendus l’Académie des Sci.*, vol. 91, pp. 383–386, 1880.

[52] M. Lippmann, “Principle of the conservation of electricity,” in *Annales de chimie et de physique série 5*, 1881, p. 571.

[53] T. Hahn, Ed., *International Tables for Crystallography*, vol. A. Chester, England: International Union of Crystallography, 2006.

[54] J. Yoo, K. Yoon, S. Hwang, S. Suh, J. Kim, and C. Yoo, “Electrical characteristics of high power piezoelectric transformer for 28 W fluorescent lamp,” *Sensors Actuators A Phys.*, vol. 90, no. 1–2, pp. 132–137, May 2001.

[55] M. J. Prieto, J. Diaz, J. A. Martin, and F. Nuno, “A very simple DC/DC converter using piezoelectric transformer,” in *2001 IEEE 32nd Annual Power Electronics Specialists Conference (IEEE Cat. No.01CH37230)*, 2001, vol. 4, pp. 1755–1760.

[56] A. Antonio, *Piezoelectric transducers and applications*, 2nd ed. 2008, p. 560.

[57] L. Carlioz, “Générateur piézoélectrique à déclenchement thermo-magnétique,” Institut National Polytechnique de Grenoble, 2009.

[58] W. Szlabowicz, “Contribution au dimensionnement et à la réalisation d’actionneur piézoélectrique à rotation de mode fort couple pour application aéronautique,” 2006.

[59] Q. Qin, *Advanced Mechanics of Piezoelectricity*, 2013th ed. Springer, 2012, p. 280.

[60] D. Parenthoine, L.-P. Tran-Huu-Hue, L. Haumesser, F. Vander Meulen, M. Lematre, and M. Lethiecq, “Modelling nonlinearity in piezoceramic transducers: From equations to nonlinear equivalent circuits.,” *Ultrasonics*, vol. 51, no. 2, pp. 109–14, Feb. 2011.

[61] F. Giraud, “Modélisation causale et commande d’un actionneur piézo-électrique à onde progressive,” Lille, 2002.

[62] W. G. Cady, *Piezoelectricity*. McGraw-Hill Book Company, Inc., 1946, p. 842.

[63] Y. Qi, N. T. Jafferis, K. Lyons, C. M. Lee, H. Ahmad, and M. C. McAlpine, “Piezoelectric ribbons printed onto rubber for flexible energy conversion.,” *Nano Lett.*, vol. 10, no. 2, pp. 524–8, Feb. 2010.

[64] Y. Qi and M. C. McAlpine, “Nanotechnology-enabled flexible and biocompatible energy harvesting,” *Energy Environ. Sci.*, vol. 3, no. 9, p. 1275, 2010.

[65] Z.-G. Ye, *Handbook of Advanced Dielectric, Piezoelectric and Ferroelectric Materials: Synthesis, Properties and Applications*, 1 edition. CRC Press, 2008, p. 600.

[66] J. Wang, C. S. Sandu, E. Colla, Y. Wang, W. Ma, R. Gysel, H. J. Trodahl, N. Setter, and M. Kuball, “Ferroelectric domains and piezoelectricity in monocrystalline Pb(Zr,Ti)O[sub 3] nanowires,” *Appl. Phys. Lett.*, vol. 90, no. 13, p. 133107, 2007.

[67] “Crystal Structure of Barium Titanate,” *Nature*, vol. 155, no. 3938, pp. 484–485, Apr. 1945.

[68] C. Millon, “Contribution à l’étude de procédés de réalisation de structures métal / PZT / métal sur silicium pour microsystèmes piézoélectriques,” INSA de Lyon, 2003.

[69] H. Lee, R. Cooper, K. Wang, and H. Liang, “Nano-Scale Characterization of a Piezoelectric Polymer (Polyvinylidene Difluoride, PVDF),” *Sensors*, vol. 8, no. 11, pp. 7359–7368, Nov. 2008.

[70] J. Kymissis, C. Kendall, J. Paradiso, and N. Gershenfeld, “Parasitic power harvesting in shoes,” in *Digest of Papers. Second International Symposium on Wearable Computers (Cat. No.98EX215)*, 1998, pp. 132–139.

[71] J. Tichý, J. Erhart, E. Kittinger, and J. Přívratská, *Fundamentals of Piezoelectric Sensorics*. Berlin, Heidelberg: Springer Berlin Heidelberg, 2010, p. 216.

[72] F. Qian, Y. Li, S. Gradecak, H.-G. Park, Y. Dong, Y. Ding, Z. L. Wang, and C. M. Lieber, “Multi-quantum-well nanowire heterostructures for wavelength-controlled lasers.,” *Nat. Mater.*, vol. 7, no. 9, pp. 701–6, Sep. 2008.

[73] Z. Zhong, F. Qian, D. Wang, and C. M. Lieber, “Synthesis of p-Type Gallium Nitride Nanowires for Electronic and Photonic Nanodevices,” *Nano Lett.*, vol. 3, no. 3, pp. 343–346, Mar. 2003.

[74] G. Zheng, F. Patolsky, Y. Cui, W. U. Wang, and C. M. Lieber, “Multiplexed electrical detection of cancer markers with nanowire sensor arrays.,” *Nat. Biotechnol.*, vol. 23, no. 10, pp. 1294–301, Oct. 2005.

[75] I. Vurgaftman and J. R. Meyer, “Band parameters for nitrogen-containing semiconductors,” *J. Appl. Phys.*, vol. 94, no. 6, p. 3675, 2003.

[76] L. C. Lew Yan Voon and M. Willatzen, “Electromechanical phenomena in semiconductor nanostructures,” *J. Appl. Phys.*, vol. 109, no. 3, p. 031101, 2011.

[77] P. Miller, “The Electrical Conductivity of Zinc Oxide,” *Phys. Rev.*, vol. 60, no. 12, pp. 890–895, Dec. 1941.

[78] C. Klingshirn, “ZnO: material, physics and applications.,” *Chemphyschem*, vol. 8, no. 6, pp. 782–803, Apr. 2007.

[79] S. J. Park, D.-Y. Jeon, S.-E. Ahn, S. Jeon, L. Montès, G.-T. Kim, and G. Ghibaudo, “Static electrical characterization and low frequency noise of a-InHfZnO thin film transistors,” *Thin Solid Films*, vol. 548, pp. 560–565, Dec. 2013.

[80] F. Fichter, “ber Aluminiumnitrid,” *Zeitschrift f r Anorg. Chemie*, vol. 54, no. 1, pp. 322–327, May 1907.

[81] W. C. Johnson, J. B. Parson, and M. C. Crew, “Nitrogen Compounds of Gallium. III,” *J. Phys. Chem.*, vol. 36, no. 10, pp. 2651–2654, 1932.

[82] H. P. Maruska and J. J. Tietjen, “THE PREPARATION AND PROPERTIES OF VAPOR-DEPOSITED SINGLE-CRYSTAL-LINE GaN,” *Appl. Phys. Lett.*, vol. 15, no. 10, p. 327, 1969.

[83] J. I. Pankove, E. A. Miller, and J. E. Berkeyheiser, “GaN electroluminescent diodes,” in *1971 International Electron Devices Meeting*, 1971, pp. 78–78.

[84] J. I. Pankove, E. A. Miller, D. Richman, and J. E. Berkeyheiser, “Electroluminescence in GaN,” *J. Lumin.*, vol. 4, no. 1, pp. 63–66, Jul. 1971.

[85] H. M. Manasevit, F. M. Erdmann, and W. I. Simpson, “The Use of Metalorganics in the Preparation of Semiconductor Materials,” *J. Electrochem. Soc.*, vol. 118, no. 11, p. 1864, 1971.

[86] S. Yoshida, S. Misawa, and A. Itoh, “Epitaxial growth of aluminum nitride films on sapphire by reactive evaporation,” *Appl. Phys. Lett.*, vol. 26, no. 8, p. 461, 1975.

[87] R. Dingle, D. Sell, S. Stokowski, and M. Ilegems, “Absorption, Reflectance, and Luminescence of GaN Epitaxial Layers,” *Phys. Rev. B*, vol. 4, no. 4, pp. 1211–1218, Aug. 1971.

[88] M. Ilegems, R. Dingle, and R. A. Logan, “Luminescence of Zn- and Cd-doped GaN,” *J. Appl. Phys.*, vol. 43, no. 9, p. 3797, 1972.

[89] S. Yoshida, S. Misawa, and S. Gonda, “Improvements on the electrical and luminescent properties of reactive molecular beam epitaxially grown GaN films by using AlN-coated sapphire substrates,” *Appl. Phys. Lett.*, vol. 42, no. 5, p. 427, 1983.

[90] H. Amano, N. Sawaki, I. Akasaki, and Y. Toyoda, “Metalorganic vapor phase epitaxial growth of a high quality GaN film using an AlN buffer layer,” *Appl. Phys. Lett.*, vol. 48, no. 5, p. 353, 1986.

[91] H. Amano, I. Akasaki, T. Kozawa, K. Hiramatsu, N. Sawaki, K. Ikeda, and Y. Ishii, “Electron beam effects on blue luminescence of zinc-doped GaN,” *J. Lumin.*, vol. 40–41, pp. 121–122, Feb. 1988.

[92] H. Amano, M. Kito, K. Hiramatsu, and I. Akasaki, “P-Type Conduction in Mg-Doped GaN Treated with Low-Energy Electron Beam Irradiation (LEEBI),” *Jpn. J. Appl. Phys.*, vol. 28, no. Part 2, No. 12, pp. L2112–L2114, Dec. 1989.

[93] H. Amano, T. Asahi, and I. Akasaki, “Stimulated Emission Near Ultraviolet at Room Temperature from a GaN Film Grown on Sapphire by MOVPE Using an AlN Buffer Layer,” *Jpn. J. Appl. Phys.*, vol. 29, no. Part 2, No. 2, pp. L205–L206, Feb. 1990.

[94] H. Amano, T. Tanaka, Y. Kunii, K. Kato, S. T. Kim, and I. Akasaki, “Room-temperature violet stimulated emission from optically pumped AlGaN/GaInN double heterostructure,” *Appl. Phys. Lett.*, vol. 64, no. 11, p. 1377, 1994.

[95] W. Mai, “Synthesis, characterization and application of ZnO nanomaterials,” GEORGIA INSTITUTE OF TECHNOLOGY, 2009.

[96] C.-Y. Yeh, Z. Lu, S. Froyen, and A. Zunger, “Zinc-blende–wurtzite polytypism in semiconductors,” *Phys. Rev. B*, vol. 46, no. 16, pp. 10086–10097, Oct. 1992.

[97] W. M. Haynes, Ed., *CRC Handbook of Chemistry and Physics*, 94th ed., vol. 129, no. 3. CRC Press, 2013, p. 2668.

[98] F. Bernardini, V. Fiorentini, and D. Vanderbilt, "Spontaneous polarization and piezoelectric constants of III-V nitrides," *Phys. Rev. B*, vol. 56, no. 16, pp. R10024–R10027, Oct. 1997.

[99] A. Ashrafi and C. Jagadish, "Review of zincblende ZnO: Stability of metastable ZnO phases," *J. Appl. Phys.*, vol. 102, no. 7, p. 071101, 2007.

[100] U. Özgür, Y. I. Alivov, C. Liu, A. Teke, M. A. Reshchikov, S. Doğan, V. Avrutin, S.-J. Cho, and H. Morkoç, "A comprehensive review of ZnO materials and devices," *J. Appl. Phys.*, vol. 98, no. 4, p. 041301, 2005.

[101] A. Rosa and J. Neugebauer, "First-principles calculations of the structural and electronic properties of clean GaN(0001) surfaces," *Phys. Rev. B*, vol. 73, no. 20, p. 205346, May 2006.

[102] M. Moseley, D. Billingsley, W. Henderson, E. Trybus, and W. A. Doolittle, "Transient atomic behavior and surface kinetics of GaN," *J. Appl. Phys.*, vol. 106, no. 1, p. 014905, 2009.

[103] S. D. Burnham and W. Alan Doolittle, "In situ growth regime characterization of AlN using reflection high energy electron diffraction," *J. Vac. Sci. Technol. B Microelectron. Nanom. Struct.*, vol. 24, no. 4, p. 2100, 2006.

[104] B. Daudin, J. L. Rouvière, and M. Arlery, "Polarity determination of GaN films by ion channeling and convergent beam electron diffraction," *Appl. Phys. Lett.*, vol. 69, no. 17, p. 2480, 1996.

[105] E. S. Hellman, "The polarity of GaN: a critical review," *MRS Internet J. Nitride Semicond. Res.*, vol. 3, no. 11, pp. 1–12, 1988.

[106] J. L. Rouviere, M. Arlery, B. Daudin, G. Feuillet, and O. Briot, "Transmission electron microscopy structural characterisation of GaN layers grown on (0001) sapphire," *Mater. Sci. Eng. B*, vol. 50, no. 1–3, pp. 61–71, Dec. 1997.

[107] D. Huang, P. Visconti, K. M. Jones, M. A. Reshchikov, F. Yun, A. A. Baski, T. King, and H. Morkoç, "Dependence of GaN polarity on the parameters of the buffer layer grown by molecular beam epitaxy," *Appl. Phys. Lett.*, vol. 78, no. 26, p. 4145, 2001.

[108] M. Seelmann-Eggebert, J. L. Weyher, H. Obloh, H. Zimmermann, A. Rar, and S. Porowski, "Polarity of (00.1) GaN epilayers grown on a (00.1) sapphire," *Appl. Phys. Lett.*, vol. 71, no. 18, p. 2635, 1997.

[109] P. Han, Z. Wang, X. Duan, and Z. Zhang, "Polarity dependence of hexagonal GaN films on two opposite c faces of Al[sub 2]O[sub 3] substrate," *Appl. Phys. Lett.*, vol. 78, no. 25, p. 3974, 2001.

[110] M. de la Mata, C. Magen, J. Gazquez, M. I. B. Utama, M. Heiss, S. Lopatin, F. Furtmayr, C. J. Fernández-Rojas, B. Peng, J. R. Morante, R. Rurali, M. Eickhoff, A. Fontcuberta i Morral, Q. Xiong, and J. Arbiol, "Polarity assignment in ZnTe, GaAs, ZnO, and GaN-AlN nanowires from direct dumbbell analysis.," *Nano Lett.*, vol. 12, no. 5, pp. 2579–86, May 2012.

[111] K. Hestroffer, C. Leclere, C. Bougerol, H. Renevier, and B. Daudin, "Polarity of GaN nanowires grown by plasma-assisted molecular beam epitaxy on Si(111)," *Phys. Rev. B*, vol. 84, no. 24, p. 245302, Dec. 2011.

[112] X. Kong, J. Ristić, M. A. Sanchez-Garcia, E. Calleja, and A. Trampert, "Polarity determination by electron energy-loss spectroscopy: application to ultra-small III-nitride semiconductor nanocolumns.," *Nanotechnology*, vol. 22, no. 41, p. 415701, Oct. 2011.

[113] M. D. Brubaker, I. Levin, A. V. Davydov, D. M. Rourke, N. A. Sanford, V. M. Bright, and K. A. Bertness, "Effect of AlN buffer layer properties on the morphology and polarity of GaN nanowires grown by molecular beam epitaxy," *J. Appl. Phys.*, vol. 110, no. 5, p. 053506, 2011.

[114] B. Alloing, S. Vézian, O. Tottereau, P. Vennéguès, E. Beraudo, and J. Zuniga-Pérez, "On the polarity of GaN micro- and nanowires epitaxially grown on sapphire (0001) and Si(111) substrates by metal organic vapor phase epitaxy and ammonia-molecular beam epitaxy," *Appl. Phys. Lett.*, vol. 98, no. 1, p. 011914, 2011.

[115] A. Dal Corso, M. Posternak, R. Resta, and A. Baldereschi, "Ab initio study of piezoelectricity and spontaneous polarization in ZnO," *Phys. Rev. B*, vol. 50, no. 15, pp. 10715–10721, Oct. 1994.

[116] R. T. Girard, O. Tjernberg, G. Chiaia, S. Söderholm, U. O. Karlsson, C. Wigren, H. Nylén, and I. Lindau, "Electronic structure of ZnO(0001) studied by angle-resolved photoelectron spectroscopy," *Surf. Sci.*, vol. 373, no. 2–3, pp. 409–417, Mar. 1997.

[117] K. Ozawa, K. Sawada, Y. Shirotori, K. Edamoto, and M. Nakatake, "Angle-resolved photoelectron spectroscopy study of the anion-derived dangling-bond band on ZnO($10\bar{1}0$)," *Phys. Rev. B*, vol. 68, no. 12, p. 125417, Sep. 2003.

[118] T. P. Chow and Ghezzo G, "SiC power devices," in *III-Nitride, SiC, and Diamond Materials for Electronic Devices*, Gaskill D.K., B. C.D., and Nemanich R.J., Eds. Pittsburgh: Material Research Society Symposium Proceedings, 1996, pp. 69–73.

[119] S. B. Zhang, S.-H. Wei, and A. Zunger, "A phenomenological model for systematization and prediction of doping limits in II–VI and I–III–VI[sub 2] compounds," *J. Appl. Phys.*, vol. 83, no. 6, p. 3192, 1998.

[120] H. Morkoc and U. Ozgur, *Zinc Oxide: Fundamentals, Materials and Device Technology*, 1 edition. Wiley, VCH, 2009, p. 488.

[121] D. Look, J. Hemsky, and J. Sizelove, "Residual Native Shallow Donor in ZnO," *Phys. Rev. Lett.*, vol. 82, no. 12, pp. 2552–2555, Mar. 1999.

[122] T. Minami, "Transparent conducting oxide semiconductors for transparent electrodes," *Semicond. Sci. Technol.*, vol. 20, no. 4, pp. S35–S44, Apr. 2005.

[123] D. Taïnoff, M. Al-Khalfioui, C. Deparis, B. Vinter, M. Teisseire, C. Morhain, and J.-M. Chauveau, "Residual and nitrogen doping of homoepitaxial nonpolar m-plane ZnO films grown by molecular beam epitaxy," *Appl. Phys. Lett.*, vol. 98, no. 13, p. 131915, 2011.

[124] C. G. Van de Walle, "Hydrogen as a Cause of Doping in Zinc Oxide," *Phys. Rev. Lett.*, vol. 85, no. 5, pp. 1012–1015, Jul. 2000.

[125] S. Cox, E. Davis, S. Cottrell, P. King, J. Lord, J. Gil, H. Alberto, R. Vilão, J. Piroto Duarte, N. Ayres de Campos, A. Weidinger, R. Lichti, and S. Irvine, "Experimental Confirmation of the Predicted Shallow Donor Hydrogen State in Zinc Oxide," *Phys. Rev. Lett.*, vol. 86, no. 12, pp. 2601–2604, Mar. 2001.

[126] C. G. Van de Walle and J. Neugebauer, “Universal alignment of hydrogen levels in semiconductors, insulators and solutions,” *Nature*, vol. 423, no. 6940, pp. 626–628, 2003.

[127] E. Lavrov, F. Herklotz, and J. Weber, “Identification of Hydrogen Molecules in ZnO,” *Phys. Rev. Lett.*, vol. 102, no. 18, p. 185502, May 2009.

[128] N. Nickel, “Hydrogen migration in single crystal and polycrystalline zinc oxide,” *Phys. Rev. B*, vol. 73, no. 19, p. 195204, May 2006.

[129] M. Wardle, J. Goss, and P. Briddon, “First-Principles Study of the Diffusion of Hydrogen in ZnO,” *Phys. Rev. Lett.*, vol. 96, no. 20, p. 205504, May 2006.

[130] A. Janotti and C. G. Van de Walle, “Hydrogen multicentre bonds.,” *Nat. Mater.*, vol. 6, no. 1, pp. 44–7, Jan. 2007.

[131] H. S. Kim, S. J. Pearton, D. P. Norton, and F. Ren, “Pulsed laser deposition of high-quality ZnO films using a high temperature deposited ZnO buffer layer,” *Appl. Phys. A*, vol. 91, no. 2, pp. 255–259, Feb. 2008.

[132] T. E. Murphy, D. Y. Chen, and J. D. Phillips, “Growth and electronic properties of ZnO epilayers by plasma-assisted molecular beam epitaxy,” *J. Electron. Mater.*, vol. 34, no. 6, pp. 699–703, Jun. 2005.

[133] D. C. Look, “Progress in ZnO materials and devices,” *J. Electron. Mater.*, vol. 35, no. 6, pp. 1299–1305, Jun. 2006.

[134] A. Y. Polyakov, N. B. Smirnov, A. V. Govorkov, E. A. Kozhukhova, S. J. Pearton, D. P. Norton, A. Osinsky, and A. Dabiran, “Electrical properties of undoped bulk ZnO substrates,” *J. Electron. Mater.*, vol. 35, no. 4, pp. 663–669, Apr. 2006.

[135] K. Kim, H. Kang, H. Kim, J. S. Lee, S. Kim, W. Kang, and G.-T. Kim, “Contact barriers in a single ZnO nanowire device,” *Appl. Phys. A*, vol. 94, no. 2, pp. 253–256, Jul. 2008.

[136] K. Subannajui, D. S. Kim, and M. Zacharias, “Electrical analysis of individual ZnO nanowires,” *J. Appl. Phys.*, vol. 104, no. 1, p. 014308, 2008.

[137] J. I. Pankove, “Luminescence in GaN,” *J. Lumin.*, vol. 7, pp. 114–126, Jan. 1973.

[138] F. S. Hickernell, “The piezoelectric semiconductor and acoustoelectronic device development in the sixties,” *IEEE Trans. Ultrason. Ferroelectr. Freq. Control*, vol. 52, no. 5, pp. 737–745, May 2005.

[139] A. Janotti and C. G. Van de Walle, “Fundamentals of zinc oxide as a semiconductor,” *Reports Prog. Phys.*, vol. 72, no. 12, p. 126501, Dec. 2009.

[140] A. Vaseashta, D. Dimova-Malinovska, and J. M. Marshall, *Nanostructured and Advanced Materials for Applications in Sensor, Optoelectronic and Photovoltaic Technology*. 2005, p. 425.

[141] A. Vincze, J. Bruncko, M. Michalka, and D. Figura, “Growth and characterization of pulsed laser deposited ZnO thin films,” *Cent. Eur. J. Phys.*, vol. 5, no. 3, pp. 385–397, Jun. 2007.

[142] V. R. Shinde, T. P. Gujar, C. D. Lokhande, R. S. Mane, and S.-H. Han, “Mn doped and undoped ZnO films: A comparative structural, optical and electrical properties study,” *Mater. Chem. Phys.*, vol. 96, no. 2–3, pp. 326–330, Apr. 2006.

[143] D. C. Look, D. C. Reynolds, J. R. Sizelove, R. L. Jones, C. W. Litton, G. Cantwell, and W. C. Harsch, "Electrical properties of bulk ZnO," *Solid State Commun.*, vol. 105, no. 6, pp. 399–401, Feb. 1998.

[144] D. a Scrymgeour and J. W. P. Hsu, "Correlated piezoelectric and electrical properties in individual ZnO nanorods.," *Nano Lett.*, vol. 8, no. 8, pp. 2204–9, Aug. 2008.

[145] S. M. Sze and K. K. Ng, *Physics of Semiconductor Devices*, 3rd Revise. Hoboken, NJ, USA: Wiley, Blackwell, 2006, p. 832.

[146] J. Goldberger, D. J. Sirbuly, M. Law, and P. Yang, "ZnO nanowire transistors.," *J. Phys. Chem. B*, vol. 109, no. 1, pp. 9–14, Jan. 2005.

[147] M. I. Daunov, R. K. Arslanov, M. M. Gadjialiev, E. V. Kortunova, P. P. Khokhlachev, and P. P. Shvansky, "Electrical and thermoelectric properties of ZnO under atmospheric and hydrostatic pressure," *Semiconductors*, vol. 40, no. 11, pp. 1255–1260, Nov. 2006.

[148] O. Schmidt, A. Geis, P. Kiesel, C. G. Van de Walle, N. M. Johnson, A. Bakin, A. Waag, and G. H. Döhler, "Analysis of a conducting channel at the native zinc oxide surface," *Superlattices Microstruct.*, vol. 39, no. 1–4, pp. 8–16, Jan. 2006.

[149] S. A. Studenikin, N. Golego, and M. Cocivera, "Carrier mobility and density contributions to photoconductivity transients in polycrystalline ZnO films," *J. Appl. Phys.*, vol. 87, no. 5, p. 2413, 2000.

[150] E. Schlenker, A. Bakin, T. Weimann, P. Hinze, D. H. Weber, A. Gölzhäuser, H.-H. Wehmann, and A. Waag, "On the difficulties in characterizing ZnO nanowires.," *Nanotechnology*, vol. 19, no. 36, p. 365707, Sep. 2008.

[151] Z. Fan and J. G. Lu, "Gate-refreshable nanowire chemical sensors," *Appl. Phys. Lett.*, vol. 86, no. 12, p. 123510, 2005.

[152] H.-W. Ryu, B.-S. Park, S. A. Akbar, W.-S. Lee, K.-J. Hong, Y.-J. Seo, D.-C. Shin, J.-S. Park, and G.-P. Choi, "ZnO sol–gel derived porous film for CO gas sensing," *Sensors Actuators B Chem.*, vol. 96, no. 3, pp. 717–722, Dec. 2003.

[153] D. Royer, E. Dieulesaint, and D. P. Morgan, *Elastic Waves in Solids I: Free and Guided Propagation*, 2000th ed. Springer, 1999, p. 374.

[154] I. Yonenaga, H. Koizumi, Y. Ohno, and T. Taishi, "High-temperature strength and dislocation mobility in the wide band-gap ZnO: Comparison with various semiconductors," *J. Appl. Phys.*, vol. 103, no. 9, p. 093502, 2008.

[155] Y. Hu, Y. Gao, S. Singamaneni, V. V Tsukruk, and Z. L. Wang, "Converse piezoelectric effect induced transverse deflection of a free-standing ZnO microbelt.," *Nano Lett.*, vol. 9, no. 7, pp. 2661–5, Jul. 2009.

[156] J. Molarius, J. Kaitila, T. Pensala, and M. Ylilammi, "Piezoelectric ZnO films by r.f. sputtering," *J. Mater. Sci. Mater. Electron.*, vol. 14, no. 5–7, pp. 431–435, 2003.

[157] E. Kohn, "Harsh Environment Materials," in *Comprehensive Microsystems*, 1st ed., Y. B. Gianchandan, O. Tabata, and H. Zappe, Eds. Amsterdam Elsevier, 2008, pp. 131–182.

[158] C. Fan, Q. Wang, L. Li, S. Zhang, Y. Zhu, X. Zhang, M. Ma, R. Liu, and W. Wang, "Bulk moduli of wurtzite, zinc-blende, and rocksalt phases of ZnO from chemical bond method and density functional theory," *Appl. Phys. Lett.*, vol. 92, no. 10, p. 101917, 2008.

[159] V. Siklitsky, "Semiconductors on NSM," *Ioffe Physico-Technical Institute*, 2007. [Online]. Available: http://www.ioffe.ru/SVA/NSM/Semicond/index.html.

[160] COMSOL, "COMSOL Multiphysics." Stockholm, 2013.

[161] D. Petersen, R. Link, O. Yeheskel, and O. Tevet, "A New Assessment Method for the Bulk Modulus and the Poisson's Ratio of Porous Ceramics," *J. Test. Eval.*, vol. 28, no. 3, p. 189, 2000.

[162] M. A. Moram, Z. H. Barber, and C. J. Humphreys, "Accurate experimental determination of the Poisson's ratio of GaN using high-resolution x-ray diffraction," *J. Appl. Phys.*, vol. 102, no. 2, p. 023505, 2007.

[163] J.-M. Wagner and F. Bechstedt, "Properties of strained wurtzite GaN and AlN: Ab initio studies," *Phys. Rev. B*, vol. 66, no. 11, p. 115202, Sep. 2002.

[164] D. Royer and E. Dieulesaint, *Ondes élastiques dans les solides, tome 1 : Propagation libre et guidée*. 1997, p. 328.

[165] A. Polian, M. Grimsditch, and I. Grzegory, "Elastic constants of gallium nitride," *J. Appl. Phys.*, vol. 79, no. 6, p. 3343, 1996.

[166] a. F. Wright, "Elastic properties of zinc-blende and wurtzite AlN, GaN, and InN," *J. Appl. Phys.*, vol. 82, no. 6, p. 2833, 1997.

[167] A. Sadao, *Properties of Semiconductor Alloys: Group-IV, III-V and II-VI Semiconductors*, 1 edition. Wiley, 2009, p. 422.

[168] B. Sen, M. Stroscio, and M. Dutta, "Piezoelectricity in wurtzite polar semiconductor nanowires: A theoretical study," *J. Appl. Phys.*, vol. 110, no. 2, p. 024506, 2011.

[169] T. Yao and S.-K. Hong, Eds., *Oxide and Nitride Semiconductors*, vol. 12. Berlin, Heidelberg: Springer Berlin Heidelberg, 2009.

[170] D. P. Norton, Y. W. Heo, M. P. Ivill, K. Ip, S. J. Pearton, M. F. Chisholm, and T. Steiner, "ZnO: growth, doping & processing," *Mater. Today*, vol. 7, no. 6, pp. 34–40, Jun. 2004.

[171] V. Bougrov, M. Levinshtein, and S. Rumyantsev, "Gallium Nitride (GaN)," in *Properties of advanced semiconductor materials : GaN, AlN, InN, BN, SiC, SiGe*, Michael E. Levinshtei, S. L. Rumyantsev, and M. S. Shur, Eds. John Wiley and Sons,Inc, 2001, p. 216.

[172] T. Hanada, "Basic Properties of ZnO, GaN, and Related Materials," in *Oxide and Nitride Semiconductors. Processing, Properties, and Applications.*, 12th ed., T. Yao and S.-K. Hong, Eds. Springer, 2009, pp. 1–19.

[173] A. Barker and M. Ilegems, "Infrared Lattice Vibrations and Free-Electron Dispersion in GaN," *Phys. Rev. B*, vol. 7, no. 2, pp. 743–750, Jan. 1973.

[174] L. Guo, Y. L. Ji, H. Xu, P. Simon, and Z. Wu, "Regularly Shaped, Single-Crystalline ZnO Nanorods with Wurtzite Structure," *J. Am. Chem. Soc.*, vol. 124, no. 50, pp. 14864–14865, Dec. 2002.

[175] B. Liu and H. C. Zeng, “Hydrothermal synthesis of ZnO nanorods in the diameter regime of 50 nm.,” *J. Am. Chem. Soc.*, vol. 125, no. 15, pp. 4430–1, Apr. 2003.

[176] Z. Wang, X. Kong, and J. Zuo, “Induced Growth of Asymmetric Nanocantilever Arrays on Polar Surfaces,” *Phys. Rev. Lett.*, vol. 91, no. 18, p. 185502, Oct. 2003.

[177] Z. L. Wang, X. Y. Kong, Y. Ding, P. Gao, W. L. Hughes, R. Yang, and Y. Zhang, “Semiconducting and Piezoelectric Oxide Nanostructures Induced by Polar Surfaces,” *Adv. Funct. Mater.*, vol. 14, no. 10, pp. 943–956, Oct. 2004.

[178] N. Wang, Y. Cai, and R. Q. Zhang, “Growth of nanowires,” *Mater. Sci. Eng. R Reports*, vol. 60, no. 1–6, pp. 1–51, Mar. 2008.

[179] B. S. Simpkins, M. A. Mastro, C. R. Eddy, and P. E. Pehrsson, “Surface depletion effects in semiconducting nanowires,” *J. Appl. Phys.*, vol. 103, no. 10, p. 104313, 2008.

[180] I. Levin, A. Davydov, B. Nikoobakht, N. Sanford, and P. Mogilevsky, “Growth habits and defects in ZnO nanowires grown on GaN/sapphire substrates,” *Appl. Phys. Lett.*, vol. 87, no. 10, p. 103110, 2005.

[181] D. Tham, C.-Y. Nam, and J. E. Fischer, “Defects in GaN Nanowires,” *Adv. Funct. Mater.*, vol. 16, no. 9, pp. 1197–1202, Jun. 2006.

[182] K. H. Lee, J. Y. Lee, Y. H. Kwon, T. W. Kang, J. H. You, D. U. Lee, and T. Kim, “Effects of defects on the morphologies of GaN nanorods grown on Si (111) substrates,” *J. Mater. Res.*, vol. 24, no. 10, pp. 3032–3037, Jan. 2009.

[183] Y. Ding and Z. L. Wang, “Structures of planar defects in ZnO nanobelts and nanowires.,” *Micron*, vol. 40, no. 3, pp. 335–42, Apr. 2009.

[184] B. W. Jacobs, M. A. Crimp, K. McElroy, and V. M. Ayres, “Nanopipes in gallium nitride nanowires and rods.,” *Nano Lett.*, vol. 8, no. 12, pp. 4353–8, Dec. 2008.

[185] R. Agrawal, B. Peng, and H. D. Espinosa, “Experimental-computational investigation of ZnO nanowires strength and fracture.,” *Nano Lett.*, vol. 9, no. 12, pp. 4177–83, Dec. 2009.

[186] K. A. Bertness, N. A. Sanford, J. M. Barker, J. B. Schlager, A. Roshko, A. V. Davydov, and I. Levin, “Catalyst-free growth of GaN nanowires,” *J. Electron. Mater.*, vol. 35, no. 4, pp. 576–580, Apr. 2006.

[187] B. Sieber, A. Addad, S. Szunerits, and R. Boukherroub, “Stacking Faults-Induced Quenching of the UV Luminescence in ZnO,” *J. Phys. Chem. Lett.*, vol. 1, no. 20, pp. 3033–3038, Oct. 2010.

[188] W.-H. Chu, H.-W. Chiang, C.-P. Liu, Y.-F. Lai, K.-Y. Hsu, and H.-C. Chung, “Defect-induced negative differential resistance of GaN nanowires measured by conductive atomic force microscopy,” *Appl. Phys. Lett.*, vol. 94, no. 18, p. 182101, 2009.

[189] H. M. Ng, D. Doppalapudi, T. D. Moustakas, N. G. Weimann, and L. F. Eastman, “The role of dislocation scattering in n-type GaN films,” *Appl. Phys. Lett.*, vol. 73, no. 6, p. 821, 1998.

[190] D. S. Wuu, W. K. Wang, W. C. Shih, R. H. Horng, C. E. Lee, W. Y. Lin, and J. S. Fang, “Enhanced output power of near-ultraviolet InGaN-GaN LEDs grown on patterned sapphire substrates,” *IEEE Photonics Technol. Lett.*, vol. 17, no. 2, pp. 288–290, Feb. 2005.

[191] H. Morkoc, *Handbook of Nitride Semiconductors and Devices*, Volume 1. 2008, p. 1311.

[192] C. Shi, P. M. Asbeck, and E. T. Yu, “Piezoelectric polarization associated with dislocations in wurtzite GaN,” *Appl. Phys. Lett.*, vol. 74, no. 4, p. 573, 1999.

[193] M. Alexe, S. Senz, M. A. Schubert, D. Hesse, and U. Gösele, “Energy Harvesting Using Nanowires?,” *Adv. Mater.*, vol. 20, no. 21, pp. 4021–4026, Nov. 2008.

[194] Y. Gao and Z. L. Wang, “Equilibrium potential of free charge carriers in a bent piezoelectric semiconductive nanowire.,” *Nano Lett.*, vol. 9, no. 3, pp. 1103–10, Mar. 2009.

[195] G. Mantini, Y. Gao, A. D’Amico, C. Falconi, and Z. L. Wang, “Equilibrium piezoelectric potential distribution in a deformed ZnO nanowire,” *Nano Res.*, vol. 2, no. 8, pp. 624–629, Aug. 2009.

[196] A. Hutson, “Piezoelectricity and Conductivity in ZnO and CdS,” *Phys. Rev. Lett.*, vol. 4, no. 10, pp. 505–507, May 1960.

[197] M. Y. Soomro, I. Hussain, N. Bano, E. Broitman, O. Nur, and M. Willander, “Nanoscale elastic modulus of single horizontal ZnO nanorod using nanoindentation experiment.,” *Nanoscale Res. Lett.*, vol. 7, p. 146, Jan. 2012.

[198] S. Hoffmann, F. Östlund, J. Michler, H. J. Fan, M. Zacharias, S. H. Christiansen, and C. Ballif, “Fracture strength and Young’s modulus of ZnO nanowires,” *Nanotechnology*, vol. 18, no. 20, p. 205503, May 2007.

[199] M.-R. He, P. Xiao, J. Zhao, S. Dai, F. Ke, and J. Zhu, “Quantifying the defect-dominated size effect of fracture strain in single crystalline ZnO nanowires,” *J. Appl. Phys.*, vol. 109, no. 12, p. 123504, 2011.

[200] R. A. Bernal, R. Agrawal, B. Peng, K. A. Bertness, N. A. Sanford, A. V Davydov, and H. D. Espinosa, “Effect of growth orientation and diameter on the elasticity of GaN nanowires. A combined in situ TEM and atomistic modeling investigation.,” *Nano Lett.*, vol. 11, no. 2, pp. 548–55, Feb. 2011.

[201] R. Calarco, M. Marso, T. Richter, A. I. Aykanat, R. Meijers, A. V D Hart, T. Stoica, and H. Lüth, “Size-dependent photoconductivity in MBE-grown GaN-nanowires.,” *Nano Lett.*, vol. 5, no. 5, pp. 981–4, May 2005.

[202] C. Soci, A. Zhang, X.-Y. Bao, H. Kim, Y. Lo, and D. Wang, “Nanowire Photodetectors,” *J. Nanosci. Nanotechnol.*, vol. 10, no. 3, pp. 1430–1449, Mar. 2010.

[203] J. D. Prades, R. Jimenez-Diaz, F. Hernandez-Ramirez, L. Fernandez-Romero, T. Andreu, A. Cirera, A. Romano-Rodriguez, A. Cornet, J. R. Morante, S. Barth, and S. Mathur, “Toward a Systematic Understanding of Photodetectors Based on Individual Metal Oxide Nanowires,” *J. Phys. Chem. C*, vol. 112, no. 37, pp. 14639–14644, Sep. 2008.

[204] F. Patolsky, G. Zheng, and C. M. Lieber, “Nanowire sensors for medicine and the life sciences.,” *Nanomedicine (Lond).*, vol. 1, no. 1, pp. 51–65, Jun. 2006.

[205] J.-S. Hwang, F. Donatini, J. Pernot, R. Thierry, P. Ferret, and L. S. Dang, “Carrier depletion and exciton diffusion in a single ZnO nanowire.,” *Nanotechnology*, vol. 22, no. 47, p. 475704, Nov. 2011.

[206] E. Latu-Romain, P. Gilet, N. Chevalier, D. Mariolle, F. Bertin, G. Feuillet, G. Perillat-Merceroz, P. Ferret, F. Levy, P. Muret, and A. Chelnokov, “Surface-induced p-type

conductivity in ZnO nanopillars investigated by scanning probe microscopy," *J. Appl. Phys.*, vol. 107, no. 12, p. 124307, 2010.

[207] H. J. Fan, W. Lee, R. Hauschild, M. Alexe, L. Rhun, R. Scholz, A. Dadgar, K. Nielsch, H. Kalt, A. Krost, M. Zacharias, and U. Gçsele, "Template-Assisted Large-Scale Ordered Arrays of ZnO Pillars for Optical and Piezoelectric Applications," no. 4, pp. 561–568, 2006.

[208] M. Minary-Jolandan, R. a. Bernal, and H. D. Espinosa, "Strong piezoelectricity in individual GaN nanowires," *MRS Commun.*, vol. 1, no. 01, pp. 45–48, Sep. 2011.

[209] S. Dai, M. Gharbi, P. Sharma, and H. S. Park, "Surface piezoelectricity: Size effects in nanostructures and the emergence of piezoelectricity in non-piezoelectric materials," *J. Appl. Phys.*, vol. 110, no. 10, p. 104305, 2011.

[210] Y. Gao and Z. L. Wang, "Electrostatic potential in a bent piezoelectric nanowire. The fundamental theory of nanogenerator and nanopiezotronics.," *Nano Lett.*, vol. 7, no. 8, pp. 2499–505, Aug. 2007.

[211] M.-T. Hoang, J. Yvonnet, A. Mitrushchenkov, and G. Chambaud, "First-principles based multiscale model of piezoelectric nanowires with surface effects," *J. Appl. Phys.*, vol. 113, no. 1, p. 014309, 2013.

[212] J. Chen and J. D. Lee, "Atomic Formulation of Nano-Piezoelectricity in Barium Titanate," *Nanosci. Nanotechnol. Lett.*, vol. 2, no. 1, pp. 26–29, Mar. 2010.

[213] M. Catti, Y. Noel, and R. Dovesi, "Full piezoelectric tensors of wurtzite and zinc blende ZnO and ZnS by first-principles calculations," *J. Phys. Chem. Solids*, vol. 64, no. 11, pp. 2183–2190, Nov. 2003.

[214] A. Mitrushchenkov, R. Linguerri, and G. Chambaud, "Piezoelectric Properties of AlN, ZnO, and Hg x Zn 1− x O Nanowires by First-Principles Calculations," *J. Phys. Chem. C*, vol. 113, no. 17, pp. 6883–6886, Apr. 2009.

[215] T. D. Nguyen, J. M. Nagarah, Y. Qi, S. S. Nonnenmann, A. V Morozov, S. Li, C. B. Arnold, and M. C. McAlpine, "Wafer-scale nanopatterning and translation into high-performance piezoelectric nanowires.," *Nano Lett.*, vol. 10, no. 11, pp. 4595–9, Nov. 2010.

[216] T. Furukawa and N. Seo, "Electrostriction as the Origin of Piezoelectricity in Ferroelectric Polymers," *Jpn. J. Appl. Phys.*, vol. 29, no. Part 1, No. 4, pp. 675–680, Apr. 1990.

[217] S. Xu, G. Poirier, and N. Yao, "PMN-PT nanowires with a very high piezoelectric constant.," *Nano Lett.*, vol. 12, no. 5, pp. 2238–42, May 2012.

[218] Y. Qi, J. Kim, T. D. Nguyen, B. Lisko, P. K. Purohit, and M. C. McAlpine, "Enhanced piezoelectricity and stretchability in energy harvesting devices fabricated from buckled PZT ribbons.," *Nano Lett.*, vol. 11, no. 3, pp. 1331–6, Mar. 2011.

[219] H.-P. Chen, Y.-C. Wu, P. A. Mante, S.-J. Tu, J.-K. Sheu, and C.-K. Sun, "Femtosecond excitation of radial breathing mode in 2-D arrayed GaN nanorods," *Opt. Express*, vol. 20, no. 15, p. 16611, Jul. 2012.

[220] J. B. Wright, S. Liu, G. T. Wang, Q. Li, D. D. Koleske, P. Lu, H. Xu, L. Lester, T. S. Luk, I. Brener, and G. S. Subramania, "Multi-Color Arrays of III-Nitride Photonic Crystal Nanowire Lasers on a Single Chip," in *CLEO: 2013*, 2013, p. CTh3G.4.

[221] B. Tian, J. Liu, T. Dvir, L. Jin, J. H. Tsui, Q. Qing, Z. Suo, R. Langer, D. S. Kohane, and C. M. Lieber, "Macroporous nanowire nanoelectronic scaffolds for synthetic tissues.," *Nat. Mater.*, vol. 11, no. 11, pp. 986–94, Nov. 2012.

[222] P. Shields, M. Hugues, J. Zúñiga-Pérez, M. Cooke, M. Dineen, W. Wang, F. Causa, and D. Allsopp, "Fabrication and properties of etched GaN nanorods," *Phys. status solidi*, vol. 9, no. 3–4, pp. 631–634, Mar. 2012.

[223] M. Leszczynski, B. Beaumont, E. Frayssinet, W. Knap, P. Prystawko, T. Suski, I. Grzegory, and S. Porowski, "GaN homoepitaxial layers grown by metalorganic chemical vapor deposition," *Appl. Phys. Lett.*, vol. 75, no. 9, p. 1276, 1999.

[224] L. J. Schowalter, J. B. Whitlock, K. E. Morgan, S. B. Schujman, K. R. Evans, and G. A. Slack, "Status of Bulk AlN Crystal Growth and Substrate Preparation: the Native Nitride Alternative," in *GaN, AlN, InN and Their Alloys : 2004 MRS Fall Meeting Symposium Proceedings*, M. M. Bernard Gil, Christian Wetzel, Masaaki Kuzuhara, Ed. Materials Research Society, 2005, p. 784.

[225] R. S. Wagner and W. C. Ellis, "VAPOR-LIQUID-SOLID MECHANISM OF SINGLE CRYSTAL GROWTH," *Appl. Phys. Lett.*, vol. 4, no. 5, p. 89, 1964.

[226] V. Dubrovskii, N. Sibirev, G. Cirlin, A. Bouravleuv, Y. Samsonenko, D. Dheeraj, H. Zhou, C. Sartel, J. Harmand, G. Patriarche, and F. Glas, "Role of nonlinear effects in nanowire growth and crystal phase," *Phys. Rev. B*, vol. 80, no. 20, p. 205305, Nov. 2009.

[227] C. Chèze, L. Geelhaar, O. Brandt, W. M. Weber, H. Riechert, S. Münch, R. Rothemund, S. Reitzenstein, A. Forchel, T. Kehagias, P. Komninou, G. P. Dimitrakopulos, and T. Karakostas, "Direct comparison of catalyst-free and catalyst-induced GaN nanowires," *Nano Res.*, vol. 3, no. 7, pp. 528–536, Jul. 2010.

[228] T. Kuykendall, P. Pauzauskie, S. Lee, Y. Zhang, J. Goldberger, and P. Yang, "Metalorganic Chemical Vapor Deposition Route to GaN Nanowires with Triangular Cross Sections," *Nano Lett.*, vol. 3, no. 8, pp. 1063–1066, Aug. 2003.

[229] S. D. Hersee, X. Sun, and X. Wang, "The controlled growth of GaN nanowires.," *Nano Lett.*, vol. 6, no. 8, pp. 1808–11, Aug. 2006.

[230] R. Koester, J. S. Hwang, C. Durand, D. L. S. Dang, and J. Eymery, "Self-assembled growth of catalyst-free GaN wires by metal-organic vapour phase epitaxy.," *Nanotechnology*, vol. 21, no. 1, p. 015602, Jan. 2010.

[231] Z. Guo, C. Andreazza-Vignolle, P. Andreazza, T. Sauvage, D. X. Zhao, Y. C. Liu, B. Yao, D. Z. Shen, and X. W. Fan, "Tuning the growth of ZnO nanowires," *Phys. B Condens. Matter*, vol. 406, no. 11, pp. 2200–2205, May 2011.

[232] S. Xu, C. Lao, B. Weintraub, and Z. L. Wang, "Density-controlled growth of aligned ZnO nanowire arrays by seedless chemical approach on smooth surfaces," *J. Mater. Res.*, vol. 23, no. 08, pp. 2072–2077, Jan. 2011.

[233] N. Wang, H. Lin, J. Li, L. Zhang, X. Li, J. Wu, and C. Lin, "Strong Orange Luminescence from a Novel Hexagonal ZnO Nanosheet Film Grown on Aluminum Substrate by a Simple Wet-Chemical Approach," *J. Am. Ceram. Soc.*, vol. 90, no. 2, pp. 635–637, Feb. 2007.

[234] R. Hinchet, J. Ferreira, J. Keraudy, G. Ardila, E. Pauliac-Vaujour, M. Mouis, and L. Montes, "Scaling rules of piezoelectric nanowires in view of sensor and energy harvester integration," in *2012 International Electron Devices Meeting*, 2012, pp. 6.2.1–6.2.4.

[235] O. Graton, "Modélisations multi-physiques de la génération piezoélectrique à l'aide de nanofils d'oxyde de zinc," Universite François Rabelais, 2012.

[236] L. D. Landau, L. P. Pitaevskii, and E. M. Lifshitz, *Electrodynamics of Continuous Media*, Second Edi. Butterworth-Heinemann, 1979, p. 460.

[237] L. D. Landau and E. M. Lifshitz, *Course Of Theoretical Physics Vol 7: Theory Of Elasticity*. Elsevier Science & Technology Books, 1986, p. 235.

[238] S. P. Timoshenko and J. M. Gere, *Theory of Elastic Stability*, 2 edition. Dover Publications Inc, 2009, p. 560.

[239] J. Courbon, *Résistance des matériaux*, 2sd ed. 1964, p. 783.

[240] B. de. Saint-Venant, *De la torsion des prismes*. Imprimerie impériale, 1855, p. 328.

[241] R. W. Soutas-Little, *Elasticity*. Dover Publications Inc, 1999, p. 431.

[242] R. Agrawal and H. D. Espinosa, "Multiscale Experiments: State of the Art and Remaining Challenges," *J. Eng. Mater. Technol.*, vol. 131, no. 4, p. 041208, 2009.

[243] M. A. Haque, H. D. Espinosa, and H. J. Lee, "MEMS for In Situ Testing—Handling, Actuation, Loading, and Displacement Measurements," *MRS Bull.*, vol. 35, no. 05, pp. 375–381, Jan. 2011.

[244] G. Binnig and C. F. Quate, "Atomic Force Microscope," *Phys. Rev. Lett.*, vol. 56, no. 9, pp. 930–933, Mar. 1986.

[245] J. Liu, P. Fei, J. Song, X. Wang, C. Lao, R. Tummala, and Z. L. Wang, "Carrier density and Schottky barrier on the performance of DC nanogenerator.," *Nano Lett.*, vol. 8, no. 1, pp. 328–32, Jan. 2008.

[246] M.-P. Lu, J. Song, M.-Y. Lu, M.-T. Chen, Y. Gao, L.-J. Chen, and Z. L. Wang, "Piezoelectric nanogenerator using p-type ZnO nanowire arrays.," *Nano Lett.*, vol. 9, no. 3, pp. 1223–7, Mar. 2009.

[247] Z. Wang, *Nanogenerators for self-powered devices and systems*. SMARTech digital repository, 2011, p. 139.

[248] Y. S. Zhou, R. Hinchet, Y. Yang, G. Ardila, R. Songmuang, F. Zhang, Y. Zhang, W. Han, K. Pradel, L. Montès, M. Mouis, and Z. L. Wang, "Nano-Newton transverse force sensor using a vertical GaN nanowire based on the piezotronic effect.," *Adv. Mater.*, vol. 25, no. 6, pp. 883–8, Feb. 2013.

[249] A. Potie, "Study of SiGe nanowires growth by chemical vapour deposition and characterization by atomic force microscopy," 2012.

[250] R. Hinchet, G. Bouteloup, G. Ardila, L. Montes, R. Parsa, K. Akarvardar, R. T. Howe, and P. Wong, "Electrical and Mechanical Characterization of Lateral NEMS Switches," in *DTIP*, 2011, no. May, pp. 348–352.

[251] S. G. Nilsson, X. Borrisé, and L. Montelius, “Size effect on Young’s modulus of thin chromium cantilevers,” *Appl. Phys. Lett.*, vol. 85, no. 16, p. 3555, 2004.

[252] X. Li, T. Ono, Y. Wang, and M. Esashi, “Ultrathin single-crystalline-silicon cantilever resonators: Fabrication technology and significant specimen size effect on Young’s modulus,” *Appl. Phys. Lett.*, vol. 83, no. 15, p. 3081, 2003.

[253] C.-Y. Nam, P. Jaroenapibal, D. Tham, D. E. Luzzi, S. Evoy, and J. E. Fischer, “Diameter-dependent electromechanical properties of GaN nanowires.,” *Nano Lett.*, vol. 6, no. 2, pp. 153–8, Feb. 2006.

[254] S. Cuenot, C. Frétigny, S. Demoustier-Champagne, and B. Nysten, “Surface tension effect on the mechanical properties of nanomaterials measured by atomic force microscopy,” *Phys. Rev. B*, vol. 69, no. 16, p. 165410, Apr. 2004.

[255] E. W. Wong, “Nanobeam Mechanics: Elasticity, Strength, and Toughness of Nanorods and Nanotubes,” *Science (80-.).*, vol. 277, no. 5334, pp. 1971–1975, Sep. 1997.

[256] B. Wu, A. Heidelberg, and J. J. Boland, “Mechanical properties of ultrahigh-strength gold nanowires.,” *Nat. Mater.*, vol. 4, no. 7, pp. 525–9, Jul. 2005.

[257] M. Porkic, *Piezoelectric transducers modeling and characterization*. MP Interconsulting, 2004, p. 266.

[258] W. P. Mason, R. N. Thurston, A. D. Pierce, and M. Levy, *Physical acoustics : principles and methods*, vol. 145, no. 3639. New York : Academic, 1964.

[259] B. . Derjaguin, V. . Muller, and Y. . Toporov, “Effect of contact deformations on the adhesion of particles,” *Prog. Surf. Sci.*, vol. 45, no. 1–4, pp. 131–143, Jan. 1994.

[260] L. Fourdrinier, “Fabrication et étude physique de dispositifs électroniques à nanotubes de carbone,” Grenoble Institute of Technology, 2009.

[261] D. A. Scrymgeour, T. L. Sounart, N. C. Simmons, and J. W. P. Hsu, “Polarity and piezoelectric response of solution grown zinc oxide nanocrystals on silver,” *J. Appl. Phys.*, vol. 101, no. 1, p. 014316, 2007.

[262] Asylum Research, “Piezo Force Microscopy using Dual AC Resonance-Tracking,” 13, 2010.

[263] Z. Wang, A. P. Suryavanshi, and M. Yu, “Ferroelectric and piezoelectric behaviors of individual single crystalline BaTiO[sub 3] nanowire under direct axial electric biasing,” *Appl. Phys. Lett.*, vol. 89, no. 8, p. 082903, 2006.

[264] T. Ke, H. Chen, H. Sheu, J. Yeh, H. Lin, C. Lee, and H. Chiu, “Sodium Niobate Nanowire and Its Piezoelectricity,” *J. Phys. Chem. C*, vol. 112, no. 24, pp. 8827–8831, Jun. 2008.

[265] J. Wang, C. Stampfer, C. Roman, W. H. Ma, N. Setter, and C. Hierold, “Piezoresponse force microscopy on doubly clamped KNbO[sub 3] nanowires,” *Appl. Phys. Lett.*, vol. 93, no. 22, p. 223101, 2008.

[266] C. Falconi, G. Mantini, A. D’Amico, and Z. L. Wang, “Studying piezoelectric nanowires and nanowalls for energy harvesting,” *Sensors Actuators B Chem.*, vol. 139, no. 2, pp. 511–519, Jun. 2009.

[267] D. Look, G. Farlow, P. Reunchan, S. Limpijumnong, S. Zhang, and K. Nordlund, “Evidence for Native-Defect Donors in n-Type ZnO,” *Phys. Rev. Lett.*, vol. 95, no. 22, p. 225502, Nov. 2005.

[268] F. Sacconi, A. Di Carlo, P. Lugli, and H. Morkoc, “Spontaneous and piezoelectric polarization effects on the output characteristics of AlGaN/GaN heterojunction modulation doped FETs,” *IEEE Trans. Electron Devices*, vol. 48, no. 3, pp. 450–457, Mar. 2001.

[269] J. G. Lu, Z. Z. Ye, Y. Z. Zhang, Q. L. Liang, S. Fujita, and Z. L. Wang, “Self-assembled ZnO quantum dots with tunable optical properties,” *Appl. Phys. Lett.*, vol. 89, no. 2, p. 023122, 2006.

[270] V. Hoel, N. Defrance, J. C. De Jaeger, H. Gerard, C. Gaquiere, H. Lahreche, R. Langer, A. Wilk, M. Lijadi, and S. Delage, “First microwave power performance of AlGaN/GaN HEMTs on SopSiC composite substrate,” *Electron. Lett.*, vol. 44, no. 3, p. 238, 2008.

[271] G. Romano, G. Mantini, A. Di Carlo, A. D’Amico, C. Falconi, and Z. L. Wang, “Piezoelectric potential in vertically aligned nanowires for high output nanogenerators.,” *Nanotechnology*, vol. 22, no. 46, p. 465401, Nov. 2011.

[272] O. Graton, G. Poulin-Vittranta, L.-P. T. H. Huea, and M. Lethiecqb, “Modelling tools for the simulation of microgenerators based on piezo-semiconducting nanowires,” *Acoust. 2012 …*, no. April, pp. 129–134, 2012.

[273] D. Hofmann, A. Hofstaetter, F. Leiter, H. Zhou, F. Henecker, B. Meyer, S. Orlinskii, J. Schmidt, and P. Baranov, “Hydrogen: A Relevant Shallow Donor in Zinc Oxide,” *Phys. Rev. Lett.*, vol. 88, no. 4, p. 045504, Jan. 2002.

[274] Y. Hu, L. Lin, Y. Zhang, and Z. L. Wang, “Replacing a battery by a nanogenerator with 20 V output.,” *Adv. Mater.*, vol. 24, no. 1, pp. 110–4, Jan. 2012.

[275] S. Xu, C. Xu, Y. Liu, Y. Hu, R. Yang, Q. Yang, J.-H. Ryou, H. J. Kim, Z. Lochner, S. Choi, R. Dupuis, and Z. L. Wang, “Ordered nanowire array blue/near-UV light emitting diodes.,” *Adv. Mater.*, vol. 22, no. 42, pp. 4749–53, Nov. 2010.

[276] Y. Zhang, Y. Liu, and Z. L. Wang, “Fundamental theory of piezotronics.,” *Adv. Mater.*, vol. 23, no. 27, pp. 3004–13, Jul. 2011.

[277] K. A. Schmitz, D. L. Holcomb-Wygle, D. J. Oberski, and C. B. Lindemann, “Measurement of the force produced by an intact bull sperm flagellum in isometric arrest and estimation of the dynein stall force.,” *Biophys. J.*, vol. 79, no. 1, pp. 468–78, Jul. 2000.

[278] M. J. Moritz, K. A. Schmitz, and C. B. Lindemann, “Measurement of the force and torque produced in the calcium response of reactivated rat sperm flagella.,” *Cell Motil. Cytoskeleton*, vol. 49, no. 1, pp. 33–40, May 2001.

[279] F. Beyeler, A. Neild, S. Oberti, D. J. Bell, Y. Sun, J. Dual, and B. J. Nelson, “Monolithically Fabricated Microgripper With Integrated Force Sensor for Manipulating Microobjects and Biological Cells Aligned in an Ultrasonic Field,” *J. Microelectromechanical Syst.*, vol. 16, no. 1, pp. 7–15, Feb. 2007.

[280] S. N. Fry, D. P. Potasek, D. J. Bell, and B. J. Nelson, “Characterizing fruit fly flight behavior using a microforce sensor with a new comb-drive configuration,” *J. Microelectromechanical Syst.*, vol. 14, no. 1, pp. 4–11, Feb. 2005.

[281] E. Florin, V. Moy, and H. Gaub, “Adhesion forces between individual ligand-receptor pairs,” *Science (80-.).*, vol. 264, no. 5157, pp. 415–417, Apr. 1994.

[282] G. U. Lee, D. A. Kidwell, and R. J. Colton, “Sensing Discrete Streptavidin-Biotin Interactions with Atomic Force Microscopy,” *Langmuir*, vol. 10, no. 2, pp. 354–357, Feb. 1994.

[283] M. Rief, “Reversible Unfolding of Individual Titin Immunoglobulin Domains by AFM,” *Science (80-.).*, vol. 276, no. 5315, pp. 1109–1112, May 1997.

[284] C. Bustamante, J. Marko, E. Siggia, and S. Smith, “Entropic elasticity of lambda-phage DNA,” *Science (80-.).*, vol. 265, no. 5178, pp. 1599–1600, Sep. 1994.

[285] G. Meyer and N. M. Amer, “Novel optical approach to atomic force microscopy,” *Appl. Phys. Lett.*, vol. 53, no. 12, p. 1045, 1988.

[286] S. Alexander, L. Hellemans, O. Marti, J. Schneir, V. Elings, P. K. Hansma, M. Longmire, and J. Gurley, “An atomic-resolution atomic-force microscope implemented using an optical lever,” *J. Appl. Phys.*, vol. 65, no. 1, p. 164, 1989.

[287] M. B. Viani, T. E. Schäffer, A. Chand, M. Rief, H. E. Gaub, and P. K. Hansma, “Small cantilevers for force spectroscopy of single molecules,” *J. Appl. Phys.*, vol. 86, no. 4, p. 2258, 1999.

[288] E. Sarajli, M. J. de Boer, H. V Jansen, N. Arnal, M. Puech, G. Krijnen, and M. Elwenspoek, “Advanced plasma processing combined with trench isolation technology for fabrication and fast prototyping of high aspect ratio MEMS in standard silicon wafers,” *J. Micromechanics Microengineering*, vol. 14, no. 9, pp. S70–S75, Sep. 2004.

[289] T. Toriyama, Y. Tanimoto, and S. Sugiyama, “Single crystal silicon nano-wire piezoresistors for mechanical sensors,” *J. Microelectromechanical Syst.*, vol. 11, no. 5, pp. 605–611, Oct. 2002.

[290] H. Onoe, M. Gel, K. Hoshino, K. Matsumoto, and I. Shimoyama, “Direct measurement of the binding force between microfabricated particles and a planar surface in aqueous solution by force-sensing piezoresistive cantilevers.,” *Langmuir*, vol. 21, no. 24, pp. 11251–61, Nov. 2005.

[291] D. R. Baselt, G. U. Lee, K. M. Hansen, L. A. Chrisey, and R. L. Colton, “A high-sensitivity micromachined biosensor,” *Proc. IEEE*, vol. 85, no. 4, pp. 672–680, Apr. 1997.

[292] M. Gel and I. Shimoyama, “Force sensing submicrometer thick cantilevers with ultra-thin piezoresistors by rapid thermal diffusion,” *J. Micromechanics Microengineering*, vol. 14, no. 3, pp. 423–428, Mar. 2004.

[293] M. J. Gordon, T. Baron, F. Dhalluin, P. Gentile, and P. Ferret, “Size effects in mechanical deformation and fracture of cantilevered silicon nanowires.,” *Nano Lett.*, vol. 9, no. 2, pp. 525–9, Feb. 2009.

[294] R. Songmuang, O. Landré, and B. Daudin, “From nucleation to growth of catalyst-free GaN nanowires on thin AlN buffer layer,” *Appl. Phys. Lett.*, vol. 91, no. 25, p. 251902, 2007.

[295] M. E. Levinshtein, S. L. Rumyantsev, and M. S. Shur, Eds., *Properties of Advanced Semiconductor Materials: Gan, Ain, Inn, Bn, Sic, Sige*, 1st ed. John Wiley & Sons Inc, 2001, p. 216.

[296] T. C. Duc, J. F. Creemer, and P. M. Sarro, “Lateral nano-Newton force-sensing piezoresistive cantilever for microparticle handling,” *J. Micromechanics Microengineering*, vol. 16, no. 6, pp. S102–S106, Jun. 2006.

[297] P. D. Mitcheson, E. M. Yeatman, G. K. Rao, A. S. Holmes, and T. C. Green, “Energy Harvesting From Human and Machine Motion for Wireless Electronic Devices,” *Proc. IEEE*, vol. 96, no. 9, pp. 1457–1486, Sep. 2008.

[298] T. Starner, “Human-powered wearable computing,” *IBM Syst. J.*, vol. 35, no. 3.4, pp. 618–629, 1996.

[299] S. Roundy, “On the Effectiveness of Vibration-based Energy Harvesting,” *J. Intell. Mater. Syst. Struct.*, vol. 16, no. 10, pp. 809–823, Oct. 2005.

[300] R. Hinchet, S. Lee, G. Ardila, L. Montès, M. Mouis, and Z. L. Wang, “Performance Optimization of Vertical Nanowire-based Piezoelectric Nanogenerators,” *Adv. Funct. Mater.*, vol. 24, no. 7, pp. 971–977, Feb. 2014.

[301] C. Jean-Mistral and S. Basrour, “Récupération de l’énergie des vibrations mécaniques pour générer de l'électricité,” *Tech. l’ingénieur*, p. RE135, 2010.

[302] S. R. Anton and H. A. Sodano, “A review of power harvesting using piezoelectric materials (2003–2006),” *Smart Mater. Struct.*, vol. 16, no. 3, pp. R1–R21, Jun. 2007.

[303] J. F. Christmann, E. Beigne, C. Condemine, and J. Willemin, “An innovative and efficient Energy Harvesting Platform architecture for autonomous microsystems,” in *Proceedings of the 8th IEEE International NEWCAS Conference 2010*, 2010, pp. 173–176.

[304] M. Dini, M. Filippi, A. Romani, V. Bottarel, G. Ricotti, and M. Tartagni, “A nano-power energy harvesting IC for arrays of piezoelectric transducers,” 2013, p. 87631O.

[305] E. Dallago, D. Miatton, G. Venchi, V. Bottarel, G. Frattini, G. Ricotti, and M. Schipani, “Electronic interface for Piezoelectric Energy Scavenging System,” in *2008 IEEE Custom Integrated Circuits Conference*, 2008, pp. 555–558.

[306] S. Boisseau, “Récupération d’énergie vibratoire à électrets,” UNIVERSITÉ DE GRENOBLE, 2011.

[307] G. Zhu, A. C. Wang, Y. Liu, Y. Zhou, and Z. L. Wang, “Functional electrical stimulation by nanogenerator with 58 V output voltage.,” *Nano Lett.*, vol. 12, no. 6, pp. 3086–90, Jun. 2012.

[308] C.-Y. Chen, G. Zhu, Y. Hu, J.-W. Yu, J. Song, K.-Y. Cheng, L.-H. Peng, L.-J. Chou, and Z. L. Wang, “Gallium nitride nanowire based nanogenerators and light-emitting diodes.,” *ACS Nano*, vol. 6, no. 6, pp. 5687–92, Jun. 2012.

[309] C.-T. Huang, J. Song, W.-F. Lee, Y. Ding, Z. Gao, Y. Hao, L.-J. Chen, and Z. L. Wang, “GaN nanowire arrays for high-output nanogenerators.,” *J. Am. Chem. Soc.*, vol. 132, no. 13, pp. 4766–71, Apr. 2010.

[310] L. Lin, C.-H. Lai, Y. Hu, Y. Zhang, X. Wang, C. Xu, R. L. Snyder, L.-J. Chen, and Z. L. Wang, “High output nanogenerator based on assembly of GaN nanowires.,” *Nanotechnology*, vol. 22, no. 47, p. 475401, Nov. 2011.

[311] L. Gu, N. Cui, L. Cheng, Q. Xu, S. Bai, M. Yuan, W. Wu, J. Liu, Y. Zhao, F. Ma, Y. Qin, and Z. L. Wang, "Flexible fiber nanogenerator with 209 V output voltage directly powers a light-emitting diode.," *Nano Lett.*, vol. 13, no. 1, pp. 91–4, Jan. 2013.

[312] Z.-H. Lin, Y. Yang, J. M. Wu, Y. Liu, F. Zhang, and Z. L. Wang, "BaTiO 3 Nanotubes-Based Flexible and Transparent Nanogenerators," *J. Phys. Chem. Lett.*, vol. 3, no. 23, pp. 3599–3604, Dec. 2012.

[313] J. H. Jung, M. Lee, J.-I. Hong, Y. Ding, C.-Y. Chen, L.-J. Chou, and Z. L. Wang, "Lead-free NaNbO3 nanowires for a high output piezoelectric nanogenerator.," *ACS Nano*, vol. 5, no. 12, pp. 10041–6, Dec. 2011.

[314] Y.-F. Lin, J. Song, Y. Ding, S.-Y. Lu, and Z. L. Wang, "Piezoelectric nanogenerator using CdS nanowires," *Appl. Phys. Lett.*, vol. 92, no. 2, p. 022105, 2008.

[315] Y.-F. Lin, J. Song, Y. Ding, S.-Y. Lu, and Z. L. Wang, "Alternating the Output of a CdS Nanowire Nanogenerator by a White-Light-Stimulated Optoelectronic Effect," *Adv. Mater.*, vol. 20, no. 16, pp. 3127–3130, Aug. 2008.

[316] C.-T. Huang, J. Song, C.-M. Tsai, W.-F. Lee, D.-H. Lien, Z. Gao, Y. Hao, L.-J. Chen, and Z. L. Wang, "Single-InN-nanowire nanogenerator with upto 1 V output voltage.," *Adv. Mater.*, vol. 22, no. 36, pp. 4008–13, Sep. 2010.

[317] O. Graton, G. Poulin-vittrant, A. S. Dahiya, N. Camara, and L. T. H. Hue, "Evaluation of the performance of a piezoelectric nanowire-based composite microgenerator," in *UFFC joint symposia*, 2013, p. 4.

[318] S. Lee, R. Hinchet, Y. Lee, Y. Yang, Z.-H. Lin, G. Ardila, L. Montès, M. Mouis, and Z. L. Wang, "Ultrathin Nanogenerators as Self-Powered/Active Skin Sensors for Tracking Eye Ball Motion," *Adv. Funct. Mater.*, p. n/a–n/a, Oct. 2013.

[319] W. C. Young and R. G. Budynas, *Roarks Formulas for Stress and Strain*, 7th ed. 2000, p. 832.

[320] G. Ardila, R. Hinchet, M. Mouis, and L. Montès, "Scaling prospects in mechanical energy harvesting with piezo nanowires," *Eur. Phys. J. Appl. Phys.*, vol. 63, no. 1, p. 14407, Jul. 2013.

[321] K. a Cook-Chennault, N. Thambi, and a M. Sastry, "Powering MEMS portable devices—a review of non-regenerative and regenerative power supply systems with special emphasis on piezoelectric energy harvesting systems," *Smart Mater. Struct.*, vol. 17, no. 4, p. 043001, Aug. 2008.

[322] P. X. Gao, J. Song, J. Liu, and Z. L. Wang, "Nanowire Piezoelectric Nanogenerators on Plastic Substrates as Flexible Power Sources for Nanodevices," *Adv. Mater.*, vol. 19, no. 1, pp. 67–72, Jan. 2007.

[323] A. R. Abramson, W. C. Kim, S. T. Huxtable, H. Yan, Y. Wu, A. Majumdar, C.-L. Tien, and P. Yang, "Fabrication and Characterization of a Nanowire/Polymer-Based Nanocomposite for a Prototype Thermoelectric Device," *J. Microelectromechanical Syst.*, vol. 13, no. 3, pp. 505–513, Jun. 2004.

[324] Y. Hu, Y. Zhang, C. Xu, L. Lin, R. L. Snyder, and Z. L. Wang, "Self-powered system with wireless data transmission.," *Nano Lett.*, vol. 11, no. 6, pp. 2572–7, Jun. 2011.

[325] R. Hinchet, S. Lee, G. Ardila, L. Montes, M. Mouis, and Z. L. Wang, “Design and Guideline Rules for the Performance Improvement of Vertically Integrated Nanogenerator,” *Proc. PowerMEMS*, no. 7, p. 4, 2013.

[326] S. Xu, Y. Yeh, G. Poirier, M. C. McAlpine, R. A. Register, and N. Yao, “Flexible piezoelectric PMN-PT nanowire-based nanocomposite and device.,” *Nano Lett.*, vol. 13, no. 6, pp. 2393–8, Jun. 2013.

[327] X. Wang, J. Song, J. Liu, and Z. L. Wang, “Direct-current nanogenerator driven by ultrasonic waves.,” *Science*, vol. 316, no. 5821, pp. 102–5, Apr. 2007.

[328] K. Y. Lee, B. Kumar, J.-S. Seo, K.-H. Kim, J. I. Sohn, S. N. Cha, D. Choi, Z. L. Wang, and S.-W. Kim, “p-Type polymer-hybridized high-performance piezoelectric nanogenerators.,” *Nano Lett.*, vol. 12, no. 4, pp. 1959–64, Apr. 2012.

[329] O. Graton, G. Poulin-Vittrant, A. S. Dahiya, N. Camara, L.-P. T. H. Hue, and M. Lethiecq, “Equivalent circuit model of a nanogenerator based on a piezoelectric nanowire-polymer composite,” *Phys. status solidi - Rapid Res. Lett.*, vol. 7, no. 10, pp. 915–918, Oct. 2013.

[330] T. S. van den Heever and W. J. Perold, “Comparing three different energy harvesting circuits for a ZnO nanowire based nanogenerator,” *Smart Mater. Struct.*, vol. 22, no. 10, p. 105029, Oct. 2013.

[331] S. Franssila, *Introduction to Microfabrication*, 2nd ed. 2010, p. 508.

[332] X. Wang, J. Liu, J. Song, and Z. L. Wang, “Integrated nanogenerators in biofluid.,” *Nano Lett.*, vol. 7, no. 8, pp. 2475–9, Aug. 2007.

[333] X. Xu, B. Bercu, F. Lime, and L. Montes, “Finite elements study of high mechanical stress in nanostructures for innovative NEMS sensors,” in *2009 4th IEEE International Conference on Nano/Micro Engineered and Molecular Systems*, 2009, pp. 676–681.

[334] B. Bercu, L. Montes, F. Rochette, M. Mouis, X. Xin, and P. Morfouli, “High mechanical stress applied to FD-SOI transistors using ultra-thin silicon membranes,” in *2009 International Semiconductor Conference*, 2009, pp. 93–96.

[335] R. Lefevre, “Conception, Développement et Optimisation d’une Micropompe MEMS à Membrane pour Dispositif Médical d’Injection,” Université de Grenoble, 2013.

[336] R. Tao, R. Hinchet, G. Ardila, and M. Mouis, “Evaluation of Vertical Integrated Nanogenerator Performances in Flexion,” *Proc. PowerMEMS*, p. 5, 2013.

[337] S. Lee, S.-H. Bae, L. Lin, Y. Yang, C. Park, S.-W. Kim, S. N. Cha, H. Kim, Y. J. Park, and Z. L. Wang, “Super-Flexible Nanogenerator for Energy Harvesting from Gentle Wind and as an Active Deformation Sensor,” *Adv. Funct. Mater.*, vol. 23, no. 19, pp. 2445–2449, May 2013.

[338] S. Lee, J.-I. Hong, C. Xu, M. Lee, D. Kim, L. Lin, W. Hwang, and Z. L. Wang, “Toward robust nanogenerators using aluminum substrate.,” *Adv. Mater.*, vol. 24, no. 32, pp. 4398–402, Aug. 2012.

[339] G. E. J. Poinern, N. Ali, and D. Fawcett, “Progress in Nano-Engineered Anodic Aluminum Oxide Membrane Development,” *Materials (Basel).*, vol. 4, no. 12, pp. 487–526, Feb. 2011.

[340] G. E. Thomson and G. C. Wood, “Anodic films on aluminum,” in *Treatise on Materials Science and Technology*, J. C. Scully, Ed. New York: Academic Press Inc, 1982, pp. 205–329.

[341] S. Lee, M. Park, H.-S. Park, Y. Kim, S. Cho, J. H. Cho, J. Park, and W. Hwang, “A polyethylene oxide-functionalized self-organized alumina nanochannel array for an immunoprotection biofilter.,” *Lab Chip*, vol. 11, no. 6, pp. 1049–53, Mar. 2011.

[342] E. Aserinsky and N. Kleitman, “Regularly Occurring Periods of Eye Motility, and Concomitant Phenomena, During Sleep,” *Science (80-.).*, vol. 118, no. 3062, pp. 273–274, Sep. 1953.

[343] P. Maquet, J. Péters, J. Aerts, G. Delfiore, C. Degueldre, A. Luxen, and G. Franck, “Functional neuroanatomy of human rapid-eye-movement sleep and dreaming.,” *Nature*, vol. 383, no. 6596, pp. 163–6, Sep. 1996.

[344] M. A. Carskadon and W. C. Dement, “Normal Human Sleep : An Overview,” in *Principles and Practice of Sleep Medicine*, 5th ed., Meir H. Kryger, T. Roth, and W. C. Dement, Eds. Saunders, 2010, pp. 16–26.

[345] S. K. L. Lal and A. Craig, “A critical review of the psychophysiology of driver fatigue,” *Biol. Psychol.*, vol. 55, no. 3, pp. 173–194, Feb. 2001.

[346] K.-I. Park, J. H. Son, G.-T. Hwang, C. K. Jeong, J. Ryu, M. Koo, I. Choi, S. H. Lee, M. Byun, Z. L. Wang, and K. J. Lee, “Highly-Efficient, Flexible Piezoelectric PZT Thin Film Nanogenerator on Plastic Substrates,” *Adv. Mater.*, p. n/a–n/a, Feb. 2014.

[347] T. Ogawa, “Piezoelectric Bimorph with Giant Electromechanical Coupling Factor of Bending Mode Nearly 70% Fabricated by Low Symmetry Mono-Domain Pb[(Zn 1/3 Nb 2/3) 0.91 Ti 0.09]O 3 Single Crystals,” *Ferroelectrics*, vol. 320, no. 1, pp. 115–123, Jul. 2005.

[348] Q. Yang, X. Guo, W. Wang, Y. Zhang, S. Xu, D. H. Lien, and Z. L. Wang, “Enhancing sensitivity of a single ZnO micro-/nanowire photodetector by piezo-phototronic effect.,” *ACS Nano*, vol. 4, no. 10, pp. 6285–91, Oct. 2010.

[349] T.-Y. Wei, P.-H. Yeh, S.-Y. Lu, and Z. L. Wang, “Gigantic enhancement in sensitivity using Schottky contacted nanowire nanosensor.,” *J. Am. Chem. Soc.*, vol. 131, no. 48, pp. 17690–5, Dec. 2009.

[350] C. Xu, X. Wang, and Z. L. Wang, “Nanowire structured hybrid cell for concurrently scavenging solar and mechanical energies.,” *J. Am. Chem. Soc.*, vol. 131, no. 16, pp. 5866–72, Apr. 2009.

[351] C. Xu and Z. L. Wang, “Compact hybrid cell based on a convoluted nanowire structure for harvesting solar and mechanical energy.,” *Adv. Mater.*, vol. 23, no. 7, pp. 873–7, Feb. 2011.

Publications

1. Contribution to book chapter

V E Borisenko, S V Gaponenko, V S Gurin, C H Kam et al., "Physics, Chemistry and Applications of Nanostructures", World Scientific Publishing Company, July 7 2013. ISBN-13: 978-9814460170

Serge Luryi, Jimmy Xu, Alexander Zaslavsky et al., "Future Trends in Microelectronics: Frontiers and Innovations", Wiley-IEEE Press, May 28 2013. ISBN-13: 978-1118442166

2. International journal

S. Lee, **R. Hinchet**, Y. Lee, Y. Yang, Z.-H. Lin, G. Ardila, L. Montes, M. Mouis, Z. L. Wang, "Ultrathin Nanogenerators as Self-powered/Active Skin Sensors for Tracking Eye Ball Motion", Advanced Functional Materials, October 14 2013. DOI: 10.1002/adfm.201301971

Hinchet R., Lee S., Ardila G., Montes L., Mouis M., Wang Z. L., "Performance Optimization of Vertical NW-Based Piezoelectric Nanogenerators", Advanced Functional Materials, October 8 2013. DOI: 10.1002/adfm.201302157

R. Hinchet, S. Lee, G. Ardila, L. Montes, M. Mouis and Z-L. Wang , "Design and Guideline Rules for the Performance Improvement of Vertically Integrated Nanogenerator", Journal of Energy and Power Engineering, September 2013. ISSN:1934-8975

Ardila G., **Hinchet R.**, Mouis M., Montes L., "Scaling prospects in mechanical energy harvesting with piezo NWs", The European Physical Journal Applied Physics, July 5 2013. 10.1051/epjap/2013120483

Y.S. Zhou*, **R. Hinchet*** (*equal contribution), Y. Yang, G. Ardila, R. Songmuang, F. Zhang, Y. Zhang, W. Han, K. Pradel, L. Montes, M. Mouis and Z.L. Wang, "Nano-newton transverse force sensor using a vertical GaN NW based on the piezotronic effect", Advanced Materials, November 19 2012. DOI: 10.1002/adma.201203263

3. International conferences

R. Tao, **R. Hinchet**, G. Ardila and M. Mouis, "Evaluation of Vertical Integrated Nanogenerator Performances in Flexion", PowerMEMS 2013, December 3-6 2013, London, UK (Oral presentation).

G. Ardila, **R. Hinchet**, L. Montes and M. Mouis , "Piezoelectric nanostructures for the mechanical energy harvesting", Nanomeeting, May 28-31 2013, Minsk, Belarus (Invited presentation).

L. Montes, **R. Hinchet**, G.A. Ardila, X. Xu, A. Potie, T. Baron, M. Mouis, "Semiconductor NW based devices for energy and sensor applications", SPIE Microtechnologies conference, 24-25 April 2013, Grenoble, France (Oral presentation).

Y. Zhou, **R. Hinchet**, Y. Yang, R. Songmuang, F. Zhang, Y. Zhang, W. Han, G. Ardila, L. Montes, M. Mouis, Z.L. Wang, "Nano-Newton Transverse Force Sensor Using a Vertical GaN NW Based on Piezotronic Effect", MRS, April 1-5 2013, San Francisco, USA (Oral presentation).

L. Montes, X. Xu, A. Potie, B. Bercu, **R. Hinchet**, F. Rochette, G. Ardila, P. Morfouli, M. Mouis, "PiezoNEMS for Sensing and Energy Harvesting", Strategical Conference of EU-Taiwan, March 11-12 2013, Taipei, Taiwan (Invited presentation).

L. Montes, R. Lefevre, A. Salette, D. Rabaud, L. Dargent, H. Marko, X. Xu, A. Potie, B. Bercu, **R. Hinchet**, F. Rochette, G. Ardila, P. Morfouli, M. Mouis, T. Baron, B. Salem, R. Songmuang, "PiezoNEMS: How to enhance piezoelectricity and piezoresistance in semiconductor NW for sensors and energy devices", IWNST 2013, February 27-1 2013, Berhampur, India (Invited presentation).

M. Mouis, **R. Hinchet**, G. Ardila, L. Montes, "Piezoelectric properties of GaN-based NWs for energy harvesting: modelling and characterization", Xiangshan 2012, December 5-7 2012, Beijing, China (Invited presentation).

R. Hinchet, J. Ferreira, J. Keraudy, G. Ardila, E. Pauliac-Vaujour, M. Mouis and L. Montes, "Scaling rules of piezoelectric NWs in view of sensor and energy harvester integration", IEDM 2012, December 10-12 2012, San Francisco, USA (Oral presentation).

R. Hinchet, S. Lee, G. Ardila, L. Montes, M. Mouis and Z.L. Wang, "Design and guideline rules for the performance improvement of vertically integrated NG", PowerMEMS 2012, December 2-5 2012, Atlanta, USA (Oral presentation).

G. Ardila, **R. Hinchet**, M. Mouis, L. Montes, "Mechanical energy harvesting devices based on nanostructures (NEMS)", ISCDG 2012, September 24-25 2012, Grenoble, France (Oral presentation). DOI: 10.1109/ISCDG.2012.6359985

L. Montes, X. Xu, A. Potie, B. Bercu, **R. Hinchet**, F. Rochette, G. Ardila, P. Morfouli, M. Mouis, T. Baron, B. Salem, R. Songmuang, "PiezoNEMS : semiconductor NWs and heterostructures for sensing and energy harvesting", ISCDG 2012, September 24-25 2012, Grenoble, France (Invited presentation). DOI: 10.1109/ISCDG.2012.6359987

R. Hinchet, X. Xu, J.W. Lee, B. Bercu, A. Potie, T. Baron, B. Salem, R. Songmuang, G. Ardila, M. Mouis and L. Montes, "A new AFM method to characterize the piezoelectric properties of nanostructures: Application for energy harvesting devices based on NWs", NEMS 2011, July 4-5 2011, Toulouse, France (Poster presentation)

R. Hinchet, L. Montes, G. Bouteloup, G. Ardila, R. Parsa, K. Akarvardar, R.T. Howe and H.-S. Philip Wong, "Electrical and mechanical characterization of lateral NEMS switches", DTIP 2011, May 11-13 2011, Aix-en-Provence, France (Oral presentation). ISBN: 978-1-61284-905-8

L. Montes, **R. Hinchet**, X. Xu, A.Potie, J.W. Lee, G. Ardila, T. Baron, M. Mouis, "NEMS Nanostructures with Enhanced Piezoresistive and Piezoelectric Properties. Application to Sensor Devices and Energy Harvesting", IEEE-NEMS 2011, February 20-23 2011, Kaohsiung, Taiwan (Oral presentation).

4. International workshops

S. Carapezzi, **R. Hinchet**, L. Montes, G. Priante, S. Rubini and A. Cavallini, "Adhesion Driven Self-Assembly of GaAs NW Arrays: Misalignment in theContext of NW-Based Nanoelectronic Devices", ICON 2013, September 23-26 2013, Annecy, France (Poster presentation).

G. Ardila, A. Kaminski-Cachopo, M. Pala, A. Cresti, L. Montes, **R. Hinchet**, J. Michallon, M. Daanoune, M. Mouis, "Towards self-powered systems: using nanostructures to harvest ambient energy", 2st Ukrainian-French Seminar, April 8-11 2013, Kiev, Ukraine (Oral presentation).

L. Montes, R. Lefevre, A. Salette, D. Rabaud,L. Dargent, H. Marko, X. Xu, A. Potie, B. Bercu, **R. Hinchet**, F. Rochette, G. Ardila, P. Morfouli, M. Mouis, C. Dehan, Q. Le Masne, "Semiconductor-On-Insulator materials, devices and circuits: physics, technology and diagnostics", 2st Ukrainian-French Seminar, April 8-11 2013, Kiev, Ukraine (Oral presentation).

L. Montes, **R. Hinchet**, X. Xu, A. Potie, B. Bercu, F. Rochette, G. Ardila, P. Morfouli, M. Mouis, T. Baron, B. Salem, R. Songmuang, "PiezoNEMS: new concepts for sensors and energy harvesting devices", Next generation of self-power smart sensors for environmental monitoring Workshop, March 19-20 2013, Nanyang Technological University, Singapore (Invited presentation).

G. Ardila, **R. Hinchet**, M. Mouis, L. Montes, "Mechanical energy harvesting with piezoelectric nanostructures: Great expectations for autonomous systems", 2012 Advanced Research Workshop, June 25-29 2012, Porquerolles, France (Poster presentation).

R. Hinchet, X. Xu , J.W. Lee, B. Bercu, A. Potie, T. Baron, B. Salem, R. Songmuang, G. Ardila, M. Mouis and L. Montes, "AFM characterization of piezoelectric NWs: Application to mechanical energy harvesting devices", MIGAS 2012, June 23-29 2012, Autrans, France (Poster presentation).

M. Mouis, L. Montes, X. Xu, J.W. Lee, F, Rochette, **R. Hinchet**, G. Ardila, "NWs in the Beyond CMOS and More than Moore perspectives : Electromechanical properties", SINANO-NANOSIL Workshop, September 17 2010, Seville, Spain (Invited presentation).

5. National conferences and workshops

R. Hinchet, "Mechanical sensors and energy harvesters based on piezoelectric NWs ", JNRDM 2013, June 10-12 2013, Grenoble, France (Poster presentation).

R. Hinchet, S. Lee, G. Ardila, L. Montes, M. Mouis and Z.L. Wang, "ZnO NWs as core of piezoelectric energy harvesters", Functional oxides for integration in micro and nano electronics, April 7-10 2013, Autrans, France (Poster presentation).

L. Montes, **R. Hinchet**, X. Xu, B. Bercu, G. Ardila, P. Morfouli, M. Mouis, S. Stein, D. Hauser, G. Savelli, R. Songmuang, B. Salem, T. Baron, "Integrated Micro & Nano Devices for Energy Harvesting & Control", Journees NanoMicroTechnologies aux services de l'energie, November 29-30 2012, Lyon, France (Poster presentation).

L. Montes, X. Xu, A. Potie, B. Bercu, **R. Hinchet**, F. Rochette, G. Ardila, P. Morfouli, M. Mouis, T. Baron, B. Salem, R. Songmuang, "Piezoresistivity and Pizeoresistance in Semiconductor NWs for sensors and energy devices", Semiconductor NWs Based Sensors GDR, November 13-14 2012, Rennes, France (Invited presentation).

R. Hinchet, X. Xu, J.W. Lee, B. Bercu, A. Potie, T. Baron, B. Salem, R. Songmuang, G. Ardila, M. Mouis and L. Montes, "A new AFM method to characterize the piezoelectric properties of nanostructures", 4th GDR NWs Meeting, October 7-21 2011, Porquerolles, France (Poster presentation).

R. Hinchet, X. Xu, J.W. Lee, B. Bercu, A. Potie, T. Baron, B. Salem, R. Songmuang, G. Ardila, L. Montes, M. Mouis, "Une nouvelle methode AFM pour caracteriser les proprietes piezoelectriques de

nanostructures : Application pour la recuperation d'energie a partir de nanofils", JNRSE, October 14-15 2010, Paris, France (Poster presentation).

.

Résumé en Français

Chapter V. Étude électromécanique de nano fils piézoélectriques semi-conducteurs. Application aux capteurs mécaniques et à la récupération d'énergie mécanique

Au cours des dernières années, les progrès en microélectronique ont entraîné une augmentation de la puissance de calcul en même temps qu'une diminution de la consommation en énergie des transistors. Le développement des technologies MEMS a créé de nouvelles fonctions apportant de nouvelles fonctionnalités dans les micros dispositifs et l'évolution des technologies de communication leur a permis d'être plus autonomes, ce qui signifie plus de temps d'exploitation, et organisées en réseaux. C'est ainsi qu'est apparu le concept de système intelligent. Il s'agit de l'intégration de micro ou nano dispositifs multifonctionnels ayant la capacité de détecter, contrôler, communiquer et actionner (ou répondre), qui pourrait être organisée en un internet des objets. Récemment ce concept a rencontré un grand succès dans de nombreux domaines : dans l'industrie pour la maintenance prédictive des machines, dans le secteur automobile avec des capteurs de pression des pneus par exemple et dans les infrastructures et l'environnement pour le contrôle de défaillances, fissures et variations de température. Mais aussi en matière de logement pour les capteurs de présence sans fil, l'électronique grand public dans les téléphones intelligents et les soins de santé en utilisant des capteurs de pression sanguine par exemple. Et enfin dans les applications militaires et spatiales avec des équipements de maintenance et de surveillance (surveillance des frontières …).

Actuellement les systèmes intelligents sont partout dans notre vie quotidienne, ayant pour conséquence l'intégration de plus en plus de fonctions et de capacités. Malgré tous les progrès réalisés dans la diminution de la consommation en énergie, les systèmes intelligents consomment de plus en plus d'énergie et un problème d'énergie des systèmes autonomes se profile. Par conséquent, il existe un besoin croissant de capteurs autonomes et de sources d'alimentation. Toutefois, les batteries prennent beaucoup d'espace et leur utilisation intense diminue leur durée de vie. Par exemple, les batteries des téléphones intelligents ne durent actuellement seulement qu'un jour environ. Leurs technologies n'évoluent pas beaucoup et offrent de faibles perspectives. En outre, il peut être difficile de les remplacer lors de l'examen d'énormes réseaux de capteurs autonomes dans des environnements difficiles. Ainsi, le développement de récupérateurs d'énergie et de capteurs autoalimentés est un moyen efficace de compléter les batteries en prolongeant la durée de fonctionnement des systèmes intelligents et en résolvant les problèmes d'énergie.

Parmi les énergies disponibles dans notre environnement quotidien, l'énergie mécanique est l'une des plus rependus et abondantes en termes de puissance. Parmi les technologies de récupération d'énergie mécanique, la piézoélectricité présente les avantages d'être compatible avec le secteur des circuits intégrés, elle génère des tensions élevées et à un haut couplage direct entre la physique mécanique et électrique par rapport aux technologies électromagnétiques et électrostatiques. Actuellement l'étude et l'application de nanofils (NFs) dans les nanotechnologies drainent beaucoup d'attention en raison de leurs capacités d'intégration et de leurs propriétés améliorées à l'échelle nanométrique. Pour ces mêmes raisons, parmi les matériaux piézoélectriques, les NFs piézoélectriques semi-conducteurs

pourraient avoir un avantage concurrentiel, car ils présentent de bonnes propriétés piézoélectriques et permettent de multiples façons d'intégration avec l'industrie des circuits imprimés.

Cette problématique est nouvelle et au laboratoire de l'IMEP-LAHC à Grenoble le travail sur les NFs piézoélectriques a commencé en 2010 par la caractérisation électromécanique AFM de NFs de GaN [1]. L'objectif principal de cette thèse est d'étudier le comportement électromécanique de NFs piézoélectriques semi-conducteurs de GaN et de ZnO pour les capteurs mécaniques de force et de déplacement et les applications de récupération d'énergie mécanique. Tout ce travail a été élaboré avec la collaboration de plusieurs laboratoires qui ont fourni des échantillons de NFs de GaN synthétisés (Institut Néel, Grenoble, France), de NFs de GaN gravés (CHREA, Nice, France) et de NFs de ZnO synthétisés (Chimie Paris, France). En outre, la croissance hydrothermale de NFs de ZnO et le prototypage de nano générateurs (NGs) ont été étudiés grâce à la collaboration étroite de Georgia Tech (Atlanta, USA). Dans cette thèse, les NFs de GaN et de ZnO ont été étudiés et évalués en tant que capteurs et intégré en tant que récupérateur d'énergie en utilisant des modèles théoriques et des dispositifs de preuve de concept. Pour répondre à ces objectifs, les recherches menées sont présentées dans ce manuscrit et se distinguent en 4 parties:

D'abord dans le premier chapitre, nous décrivons le contexte du problème énergétique des capteurs autonomes qui se profile et qui est lié au marché actuel de l'industrie IC qui intègre toujours plus de fonctionnalités dans les micros dispositifs ce qui réduis leurs autonomies. Ainsi les batteries ne suffisent plus à alimenter les capteurs autonomes pour une utilisation à long terme et pour nous attaquer à ce problème nous avons décidé de développer la récupération d'énergie et les capteurs autoalimentés. Parmi les sources d'énergie possibles, nous avons choisi de récupérer l'énergie mécanique grâce au phénomène piézoélectrique. Plus précisément nous nous sommes concentrés sur les NFs piézoélectrique semi-conducteur de ZnO et de GaN en raison de leurs bonnes propriétés et compatibilité avec l'industrie IC. Mais, avant d'étudier les NFs de ZnO et de GaN, nous présentons les bases théoriques de la piézoélectricité, les propriétés de ces matériaux, leurs applications et nous discutons également des propriétés piézoélectriques des NFs.

Ensuite dans le deuxième chapitre, nous étudions les différents procédés de fabrication des NFs de ZnO et de GaN. En particulier nous avons choisi de développer la croissance hydrothermale de NFs de ZnO à l'IMEP-LAHC pour leur caractérisation et utilisation. Mais avant d'utiliser un réseau de NFs il est important d'étudier le comportement théoriquement d'un NF de ZnO individuel. Ainsi nous avons réalisé une étude analytique et des simulations par la méthode des éléments finis (FEM) d'un NF de ZnO en flexion. Cette étude explique la distribution du potentiel piézoélectrique en fonction de la force et expose les règles d'échelle et de dimensionnement des NFs de ZnO. Ensuite, nous étudions la caractérisation mécanique par AFM de NFs de ZnO et de GaN. En effet la mesure du module de Young de NF de ZnO et de GaN individuels pourrait être un indice d'un quelconque effet d'échelle mécanique. En parallèle nous avons aussi effectué des caractérisations piézoélectriques par AFM de ces NFs pour comprendre leurs comportements sous des contraintes de flexion. Afin, les caractérisations PFM et électriques initiées sont présentés et les divers problèmes rencontrés sont discutés.

Une fois le comportement individuel des NFs compris, nous discutons dans le chapitre 3 des limites des modèles de NFs piézoélectriques utilisés et nous développons un modèle plus réaliste et plus proche des configurations expérimentales des réseaux de NFs en tenant comptent de leur distribution en tailles. Nous avons étudié le comportement de NFs de ZnO quand des forces élevées sont appliquées (mécanique non linéaire) et en fonction de la forme, du substrat, de l'environnement et du dopage. Par la suite, les simulations montrent qu'il est possible d'utiliser des NFs de ZnO pour des

capteurs de force et de déplacement en surveillant le potentiel généré et que leurs sensibilités et résolutions spatiales peuvent être réglées en sélectionnant les NFs utilisés. Expérimentalement l'utilisation de NFs de GaN pour réaliser des capteurs de force a été démontrée en mesurant le courant à travers un NF.

Mais la récupération d'énergie est également nécessaire pour répondre aux futurs problèmes d'énergie et nous étudions plus profondément dans le chapitre 4 la récupération d'énergie mécanique. Dans un premier temps nous établissons d'abord un état de l'art des ressources énergétiques mécaniques et des technologies de récupération d'énergie mécanique. Pour cela les NFs de ZnO et de GaN pourraient être de bons candidats. Pour bien comprendre la problématique, nous dressons un état de l'art des NG et de leurs architectures potentielles. Nous analysons leurs avantages et inconvénients et ainsi nous définissons une structure de NG de référence. Après une étude analytique globale de cette structure, pour d'avoir une compréhension plus profonde de son fonctionnement nous effectuons plusieurs simulations FEM afin de définir des voies d'optimisation et de permettre de concevoir un NG optimisé fonctionnant en compression ou en flexion. Enfin, nous fabriquons des prototypes de NG et développons leur caractérisation.

V.1. Contexte et bases théoriques

Ces dernières années, les progrès en microélectronique et le développement des technologies MEMS ont permis d'ajouter de nouvelles fonctionnalités dans les micros dispositifs et l'évolution des technologies de communication leur a permis d'être plus autonomes. Cette évolution a permis l'apparition de système dis intelligents qui consistent en l'intégration de micro ou nano dispositifs multifonctionnels ayant la capacité de capter, traiter et communiquer des informations et qui peuvent être organisée en réseaux (Figure 115).

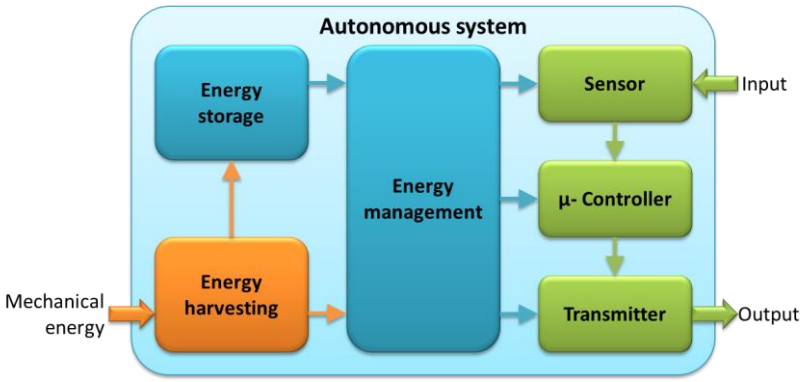

Figure 115 Schéma d'un système autonome utilisant une unité de récupération d'énergie.

Ces dispositifs ont récemment rencontré un grand succès. Actuellement ils sont tout autour de nous dans notre vie quotidienne. Cependant, malgré tous les progrès réalisés pour diminuer leur consommation en énergie, ils peuvent tout de même augmenter de manière conséquente la consommation en énergie des dispositifs les intégrant. Ainsi il se profile un problème énergétique touchant notamment les systèmes intégrant de plus en plus ces nouveaux micros dispositifs.

Pour remédier à ce problème, la conversion de l'énergie mécanique qui est présente tout autour de nous dans notre vie quotidienne, indépendamment des conditions de température ou de pression, est une des solutions envisageables. Ainsi le développement de capteurs mécaniques autoalimentés et de récupérateur d'énergie mécanique pourrait permettre d'augmenter l'autonomie des futurs systèmes autonomes intégrant une multitude de nouvelles fonctions. Parmi les technologies de conversion d'énergie mécanique, la piézoélectricité présente les avantages d'être compatible avec le secteur des

circuits intégrés, elle génère des tensions élevées et à un haut couplage direct entre la physique mécanique et électrique par rapport aux technologies électromagnétiques et électrostatiques.

La piézoélectricité a été découverte en 1880 par les frères Pierre et Jacques Curie. Elle consiste en la propriété de certains corps à se polariser électriquement sous l'application d'une contrainte mécanique et réciproquement à se déformer sous l'application d'un champ électrique. Le premier phénomène est appelé effet piézoélectrique direct et le second est nommé effet piézoélectrique inverse. Ce phénomène est dû au fait que dans un matériau piézoélectrique au repos les centres de gravité des charges négatives et positives du cristal coïncident et leurs effets se neutralisent (Figure 116a). Lorsqu'une contrainte mécanique est appliquée sur cette maille cristalline, elle se déforme et les barycentres des charges négatives et positives s'éloignent ce qui génère un dipôle dans le cristal (Figure 116b). Ainsi dans le matériau, les dipôles se neutralisent et il apparait une charge à sa surface (Figure 116c).

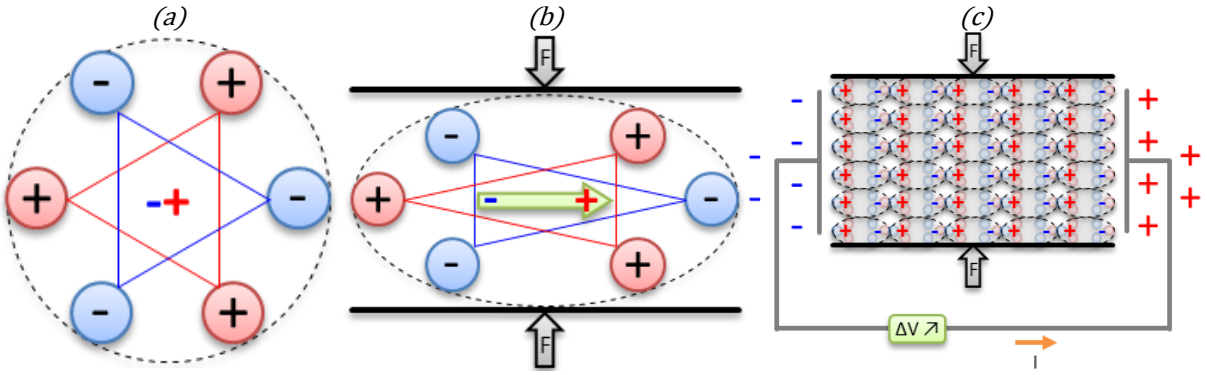

Figure 116 Modèle moléculaire simple expliquant l'effet piézo-électrique, (a) molécule intacte, (b) une molécule soumise à une force externe. (c) Schéma du phénomène piézo-électrique directe sur un matériau piézo-électrique en court-circuit et soumis à une force externe, un courant circule à travers le circuit pour neutraliser le potentiel piézoélectrique.

De manière analytique la piézoélectricité est décrite par l'utilisation d'une matrice de coefficients dit piézoélectriques et reliant les grandeurs mécaniques tels que la contrainte ou la déformation aux grandeurs électriques tels que le déplacement électrique ou le champ électrique. Ainsi les équations les plus couramment utilisées décrivant la piézoélectricité sont :

$$\begin{cases} \boldsymbol{T_p} = \boldsymbol{c_{pq}} \cdot \boldsymbol{S_q} - \boldsymbol{e^t_{kp}} \cdot \boldsymbol{E_k} \\ \boldsymbol{D_i} = \boldsymbol{e_{iq}} \cdot \boldsymbol{S_q} + \boldsymbol{\varepsilon^S_{ik}} \cdot \boldsymbol{E_k} \end{cases} \qquad \textit{Equation 102}$$

Ou T_p représente la contrainte mécanique, c_{pq} la matrice de souplesse du matériau, S_q la déformation, e^t_{kp} la transposé de la matrice de coefficients piézoélectriques e_{kp}, E_k le champ électrique, D_i le déplacement électrique et ε^S_{ik} la matrice de la permittivité a S constant ou nul.

Il existe de nombreux matériaux piézoélectriques qui peuvent être classés selon 4 types distincts : les cristaux (quartz, …), les polymères (PVDF, …), les céramiques (PZT, …) et les semi-conducteurs (ZnO, GaN, …). Dans notre étude nous nous sommes concentrés sur l'étude et l'utilisation du ZnO et du GaN (Figure 117). Ces matériaux ont l'avantage d'être compatibles avec les industries de la microélectronique et des MEMS, ils sont très étudiés et utilisés en optoélectronique et microélectronique et faciles à intégrer et enfin ils présentent de bons coefficients piézoélectriques. Les formes piézoélectriques du ZnO et du GaN ont une structure cristalline wurtzite qui est de type hexagonal.

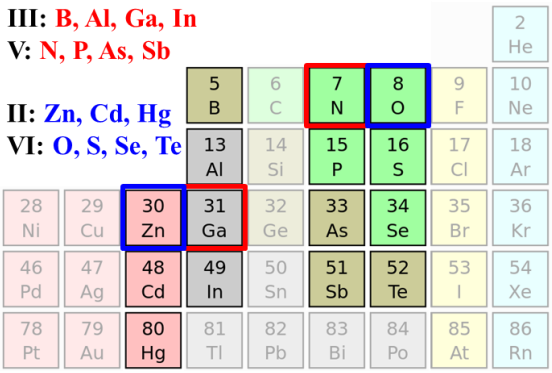

Figure 117 Tableau périodique de Mendeleïev. Matériaux piézoélectriques semi-conducteurs II-VI et III-V.

Les propriétés de ces matériaux sous leur forme wurtzite sont résumées dans la Table 21.

Table 21 Propriétés physique du ZnO et du GaN.

	ZnO	GaN
Phase	Wurtzite	Wurtzite
Densité ρ_v (g.cm^{-3})	5.606	6.150
Module de Young Y (GPa)	Y=111.2 [100], [158]	Y=210 [159]
Ratio de Poisson υ	υ=0.33 [160] to 0.356 [161]	υ=0.183 [162] to 0.198 [163]
Coefficients d'élasticité c_{ij} (GPa)	c_{11}=209 c_{12}=121 c_{13}=105 c_{33}=211 c_{44}=42.5 $c_{66}=\frac{c_{11}-c_{12}}{2}$ [164]	c_{11}=390 c_{12}=145 [165] c_{13}=106 c_{33}=398 [166] c_{44}=105 $c_{66}=\frac{c_{11}-c_{12}}{2}$ [167]
Polarisation intrinsèque P_i (C.m^{-2})	P_i=-0.047 to -0.057 [100], [115]	-0.029 [98]
Coefficient piézoélectrique e_{ij} (C.m^{-2})	e_{15}=-0.45 to -0.59 e_{31}=-0.51 to -0.61 e_{33}=1.22 [168] to 1.14 [153]	e_{15}=-0.30 to -0.30 e_{31}=-0.33 to -0.49 e_{33}=0.65 [168] to 0.73 [169]
Constante diélectrique ε	ε=8.656 [170]	ε=8.9[171]
Permittivité relative ε_r	ε_{11}=8.22 [168] to 8.49 [172] ε_{33}=7.40 [172] to 7.83 [164]	ε_{11}=9.5 [168] ε_{33}=10.4 [173]
Largeur de bande E_g (eV)	E_g=3.40 (direct) [167]	E_g=3.42 (direct) [167]

À l'état naturel, ces matériaux possèdent une polarisation intrinsèque qui est faible (Table 22).

Table 22 Polarisation intrinsèque dans un cristal wurtzite de ZnO et de GaN.

	GaN	ZnO
$\overrightarrow{P_{spont}}$ (V)	-0.029 [98]	-0.057 [100], [115]

Actuellement l'étude des nano fils (NFs) drainent beaucoup d'attention dans les nanotechnologies en raison de leurs capacités d'intégration et de leurs propriétés améliorées à l'échelle nanométrique. Pour ces mêmes raisons, parmi les matériaux piézoélectriques, les NFs piézoélectriques semi-conducteurs et en particulier les NFs de ZnO et de GaN sont de plus en plus étudiés, car ils présentent notamment de bonnes propriétés piézoélectriques et permettent de multiples façons d'intégration avec l'industrie des circuits imprimés.

Ainsi des études récentes [29], [40] montrent que les propriétés piézoélectriques des NFs de ZnO et de GaN augmentent (Table 23). Cependant cette augmentation reste sujet a de nombreux débat du a la forte variation des résultats théoriques, obtenus par simulation ab-initio, et expérimentaux principalement obtenue par caractérisation AFM.

Table 23 Coefficients piézoélectriques de matériaux nano structurés par rapport aux matériaux massifs.

d_{33} (pm/V)	Théorique (nano)	Expérimental (nano)	Expérimental (Bulk)
PVDF	-	-38 [42]	-25 [216]
PZT	-	101 [64]	650
ZnO	168.2 [29]	14-26.7 [36]	9.93 [36]
GaN	65.8 [29]	12.8 [30]	1.86 [29]
PMN-PT	-	381 [217]	2500 [217]

V.1.1. Conclusion

Dans le premier chapitre, nous avons présenté le contexte scientifique et international de la thèse, principalement en termes du problème énergétique des systèmes intelligents et capteurs autonomes. En effet, ces systèmes consomment plus d'énergie alors que l'amélioration de la capacité des batteries est très modérée et ne suffit pas à soutenir cette tendance. Une solution pour résoudre ce problème est de développer les capteurs autoalimentés et les récupérateurs d'énergie. Parmi les différentes sources d'énergie, la récupération d'énergie mécanique présente l'avantage important d'être très lié aux activités humaines avec de fortes densités d'énergie ce qui la rend très prometteuse pour des mises en œuvre industrielle. La technologie piézoélectrique et plus précisément les dispositifs à base de NFs piézoélectriques semblent être pertinents pour récupérer efficacement l'énergie mécanique. Le succès de ces dispositifs à base de NF repose surtout dans leur fort potentiel d'intégration dans les nano systèmes avec de grandes fonctionnalités. Par exemple, des capteurs de contrainte ayant une sensibilité accrue, fournie par l'effet piézoélectrique [37], ou des NG [38] pour alimenter des capteurs autonomes [39] ont déjà été démontrés. La plupart des applications basées sur des NFs utilisent des NFs semi-conducteurs [40] telles que des NFs de ZnO et de GaN, qui montrent une nette amélioration de leur performance piézoélectrique à l'échelle nanométrique par rapport à l'efficacité de matériaux massifs. Cependant, une compréhension plus profonde des performances piézoélectriques de tels NFs est nécessaire, car seuls quelques travaux ont été réalisés sur l'étude des propriétés électromécaniques de ces NFs individuels. Nous allons donc étudier en détail dans le chapitre II la piézoélectricité et plus profondément les propriétés des NFs de ZnO et de GaN à l'échelle nanométrique.

V.2. Étude piézoélectrique de nano fils de ZnO et de GaN

La compréhension du phénomène piézoélectrique et la connaissance de la physique des matériaux piézoélectriques permettent une large gamme d'applications. En outre, l'évolution de la physique des semi-conducteurs et des procédés de micro fabrication a conduit à la synthèse de micro et nano structures telles que les nano fils et leur application en microélectronique. Ainsi, nous pouvons imaginer de nouveaux dispositifs tels que des nano capteurs mécaniques ou récupérateurs d'énergie. Mais pour la recherche et le développement, le contrôle d'un processus de fabrication facile de NFs de ZnO est un point clé. Par conséquent, nous avons examiné les différentes méthodes pour synthétiser des NFs de ZnO et de GaN. Ensuite, nous avons choisi et appris la synthèse hydrothermale de NFs de ZnO et nous avons étudié son contrôle dans l'optique de futures intégrations. En effet, le contrôle de la taille et de la densité de NFs est important parce que cela influence leurs réponses piézoélectriques aux

stimulations. En outre, nous avons travaillé sur la qualité et l'intégration de tapis de NFs ayant peu de défauts afin de les utiliser correctement. Ensuite, nous avons besoin de comprendre le comportement des NFs piézoélectriques semi-conducteurs tels que les NFs de ZnO et de GaN. Dans ce contexte, la modélisation analytique et la simulation FEM sont deux outils importants pour décrire des NFs de ZnO et de GaN et ainsi les dimensionner et fonctionnaliser en vue d'applications futures. Ces approches sont complémentaires pour expliquer les problèmes piézoélectriques tels que l'inversion du potentiel à la base d'un NF de ZnO courbé. Par conséquent, nous avons étudié et développé ces deux aspects. Enfin, les NFs de ZnO et de GaN doivent être caractérisés pour étudier leurs paramètres et comportements réels afin de corriger les modèles si nécessaire dans le but de développer des applications fonctionnelles. Pour procéder, nous avons choisi des méthodes en champs proches et en particulier la caractérisation AFM pour étudier les propriétés mécaniques des NFs de ZnO et de GaN telles que leur module de Young. Ensuite des études piézoélectriques ont été développées pour mesurer le potentiel piézoélectrique généré par des NFs contrains et enquêter plus profondément leur effet piézoélectrique.

V.2.1. La fabrication des nano fils

Dans un premier temps nous nous sommes intéressés à la fabrication de NFs de ZnO et de GaN. Il existe en effet plusieurs techniques de fabrication qui peuvent être divisés en deux groupes : les processus dits « Top-Down » et les processus dits « Bottom-Up » (Table 24). Ces techniques sont généralement longues à développer et complexes à mettre en œuvre. C'est pourquoi nous avons établi plusieurs collaborations afin d'étudier différents types de NFs. Nous avons ainsi pu étudier en collaboration avec l'institut Néel des NFs de GaN fabriqué par MBE, avec le CHREA des NFs de GaN Top-Down et avec le CEA-LETI des NFs de ZnO fabriqué par MOCVD.

Table 24 Processus de fabrication des NFs piézoélectriques semi-conducteurs.

Bottom-up	Top-down
Chemical Synthesis	Micro machining
Electro Chemical Synthesis	Nano imprint
Pulse laser deposition (PLD)	Deep reactive-ion etching (DRIE)
Chemical vapor deposition (CVD)	
Metal organic chemical vapor deposition (MOCVD)	
Molecular beam epitaxy (MBE)	

Cependant, pour étudier intensivement des NFs de ZnO et développer et optimiser des dispositifs à base de ces NFs, nous avons appris, en collaboration avec l'université de Georgia Tech, la croissance de NFs de ZnO par CBD au sein du laboratoire de l'IMEP-LAHC. Cette technique a l'avantage d'être simple, rapide et très peu chère à mettre en œuvre tout en offrant la capacité de croitre des NFs de ZnO à très basse température (<100°C) sur divers substrats pouvant avoir une taille et une forme variée. Ainsi il m'a été possible de faire croitre des NFs de ZnO d'une longueur de 1 à 6 µm, d'un diamètre de 50 à 250 nm avec une densité allant de 5×10^{8} à 10^{10} cm^{-2} (Figure 118).

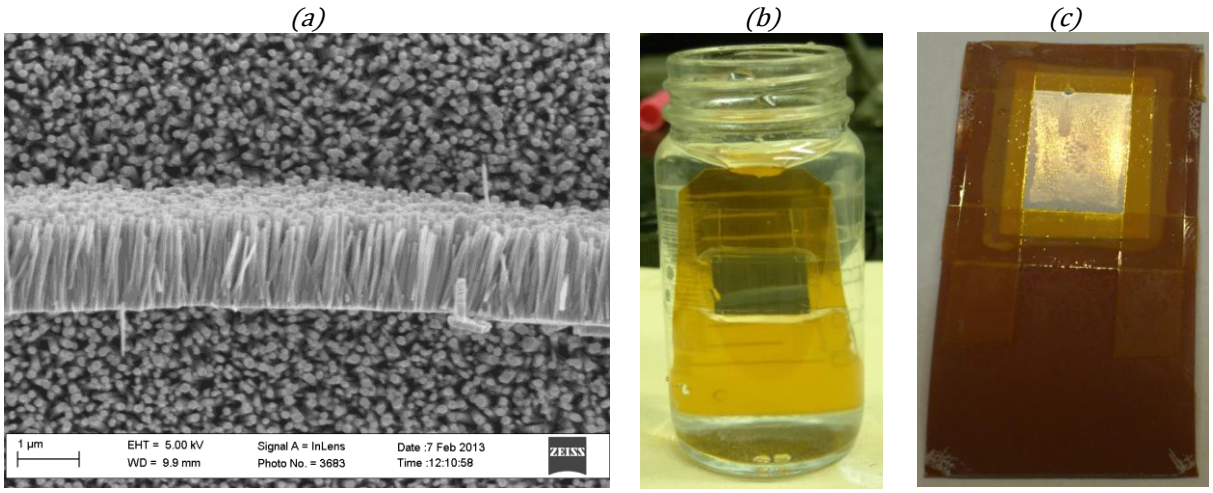

Figure 118 (a) Tapis de NFs de ZnO fabriqué en utilisant le processus de croissance hydrothermale. (b) échantillon incliné face vers le bas dans la solution de croissance. (c) Divers défauts de croissance sur l'échantillon.

V.2.2. Modélisation du comportement en flexion d'un nano fil de ZnO

Pour comprendre le comportement de NFs de ZnO soumis à une contrainte de flexion par exemple, nous avons d'abord développé un modèle analytique simple d'un tel NF en flexion. Ce modèle permet de comprendre simplement la distribution du potentiel généré dans un NF de ZnO de 600 nm de long et de 50 nm de large, attaché à sa base à un substrat solide mis à la masse et fléchi par l'application d'une force latérale de 80nN à l'extrémité libre du NF. Ainsi on constate que le coté en extensions du NF généré un potentiel positif de +0.3V alors que le coté en compression génère un potentiel de -0.3V.

Pour être plus précis, nous avons ensuite étudié ce comportement à l'aide de simulations par éléments finis (FEM). Ces simulations permettent de mieux voir la distribution du potentiel piézoélectrique généré dans le NF (Figure 119). En particulier on voit apparaitre une zone d'inversion du potentiel à la base du NF. Cette inversion s'explique par des phénomènes de cisaillements qui n'ont pas été pris en compte dans les calculs analytiques, car trop complexe.

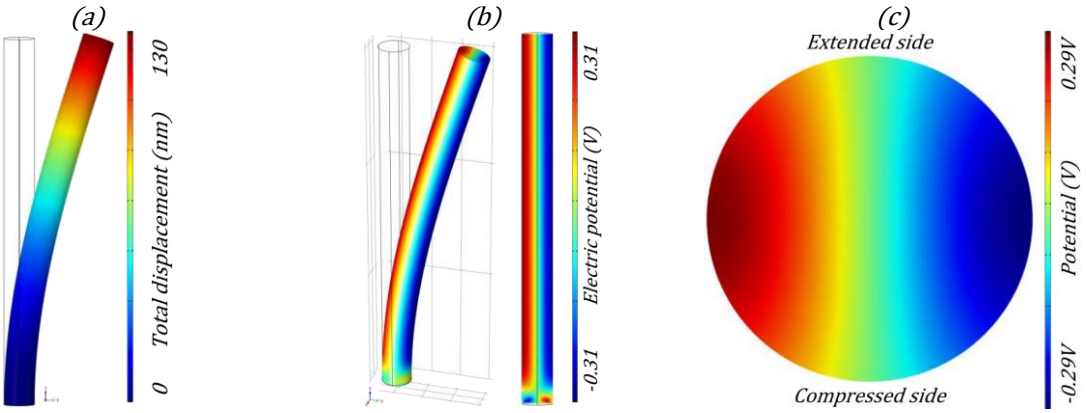

Figure 119 Simulation FEM d'un NF de ZnO (l=600nm et r=25nm) fléchi par une force latérale F=80nN appliqué à son extrémité libre. (a) Déplacement total, (b) distribution du potentiel piézoélectrique généré dans une coupe verticale et (c) horizontal au milieu du NF.

Ces résultats sont en accord avec les rares études présentes dans la littérature. La valeur et la distribution du potentiel généré par l'application d'une force latérale de 80nN à l'extrémité libre du NF sont très proches.

Une fois le fonctionnement des NFs de ZnO compris nous nous sommes intéressés à leurs lois de dimensionnement et leurs règles d'échelles. Ainsi nous avons constaté que la différence de potentiel piézoélectrique entre le côté en extension et le côté en compression est inversement proportionnelle au rayon des NFs (Figure 120).

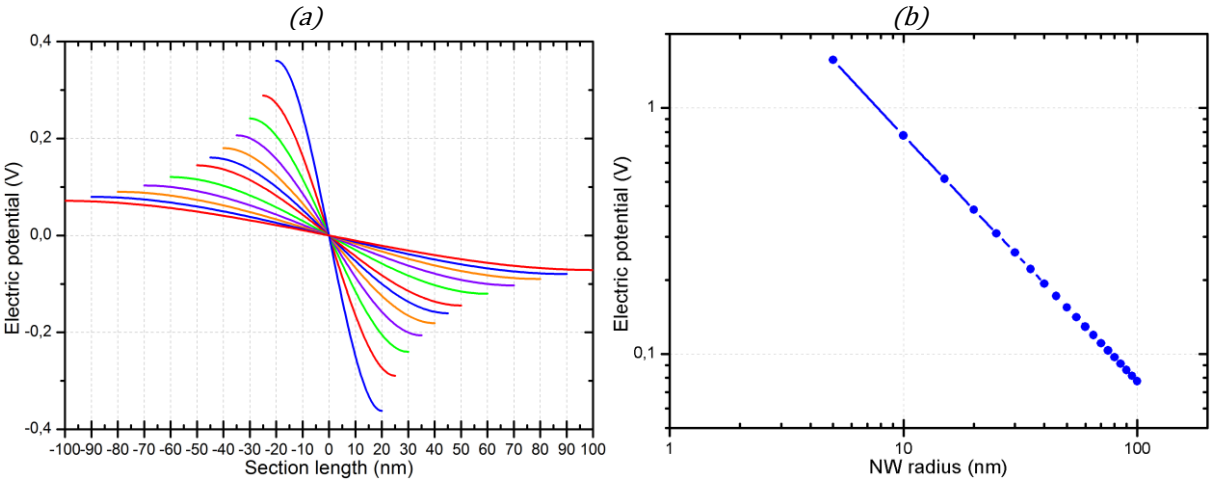

Figure 120 Simulation FEM de l'évolution du potentiel électrique généré par un NF piézoélectrique encastré simple (r=25nm, l=600nm), pliée par une force latérale F = 80nN appliquée à son extrémité libre, en fonction du rayon. (a) Profil du potentiel le long de l'axe y au milieu du NF à z = 300 nm et (b) potentiel positif maximum sur le côté en extension du NF.

Par contre la longueur des NFs n'a pas d'influence sur la différence de potentiel généré (Figure 121a). Enfin la différence de potentiel généré est proportionnelle à la force appliquée sur les NFs (Figure 121b). Ceci est important parce qu'il est alors possible d'imaginer un capteur de force ou un générateur de tension, ce qui est abordé dans les chapitres suivants.

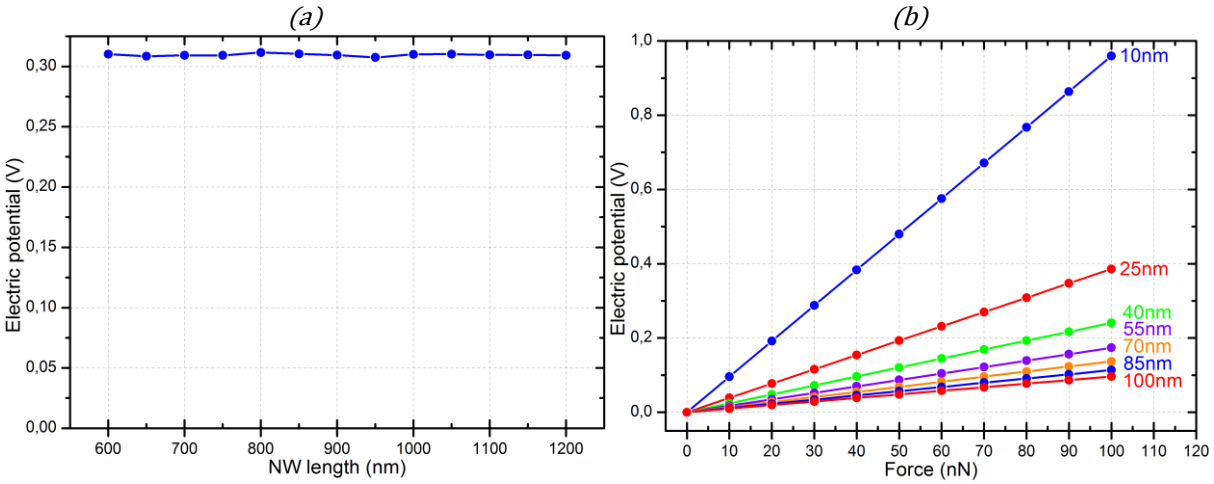

Figure 121 (a) Simulation FEM de l'évolution du potentiel généré par un NF piézoélectrique encastré simple (r=25nm, l=600nm), pliée par une force latérale F = 80nN appliquée à son extrémité libre. (a) Profil du potentiel positif maximal sur le côté en extension du NF en fonction de la longueur du NF et (b) en fonction du rayon du NF et plié par différentes forces latérales appliquées à son extrémité libre.

V.2.3. La caractérisation de nano fils piézoélectriques

Expérimentalement il existe peu d'études des propriétés piézoélectriques des NFs de ZnO et de GaN et les résultats varient fortement en fonction des procédés de croissances utilisées et de la qualité des NFs. Cependant la plupart des études ont été réalisées par microscope à force atomique (AFM). C'est notamment le cas des études réalisées par le Pr. Wang à l'université de Georgia Tech qui a utilisé un

AFM muni d'une pointe recouverte de platine pour scanner verticalement des échantillons de NFs. Lorsque la pointe AFM touche un NF, elle le fléchit ce qui génère une distribution de potentiel dans celui-ci. La pointe AFM étant recouverte de platine, il se forme une jonction Schottky à l'interface Pointe AFM / NF qui laisse passer un pic de courant lorsqu'elle touche le côté en compression du NF.

De cette manière, il est possible d'observer les réponses en tension et courant des NFs piézoélectriques. Cependant cette méthode est peu précise, car lors du balayage vertical de la pointe AFM sur les NFs il est difficile de maitriser la force appliquée sur les NFs et sa position. C'est pourquoi au sein de l'IMEP-LAHC nous avons mis au point une technique de caractérisation AFM de NFs latéraux afin de mieux contrôler la force appliquée sur les NFs et sa position [1].

À l'aide de cette technique, nous avons dans un premier temps réalisé des caractérisations mécaniques du module de Young de différents NFs de GaN (Figure 122a). Pour cela nous appliquons une force le long d'un NF qui va alors se fléchir (Figure 122b). Pendant ce temps, nous mesurons cette flexion en suivant la déflexion de la pointe AFM en fonction de sa course (Figure 122c). Enfin, en utilisant le modèle de déformation d'une poutre encastrée-libre en mécanique classique [319] et en connaissant la position de la pointe AFM, nous extrayons la valeur du module de Young du NF (Figure 122d). Les résultats montrent que les valeurs des modules de Young sont comprises entre la valeur du GaN massif [159] et celle des NFs de GaN [200], [253]. Mais nous n'avons constaté aucun effet nano notable.

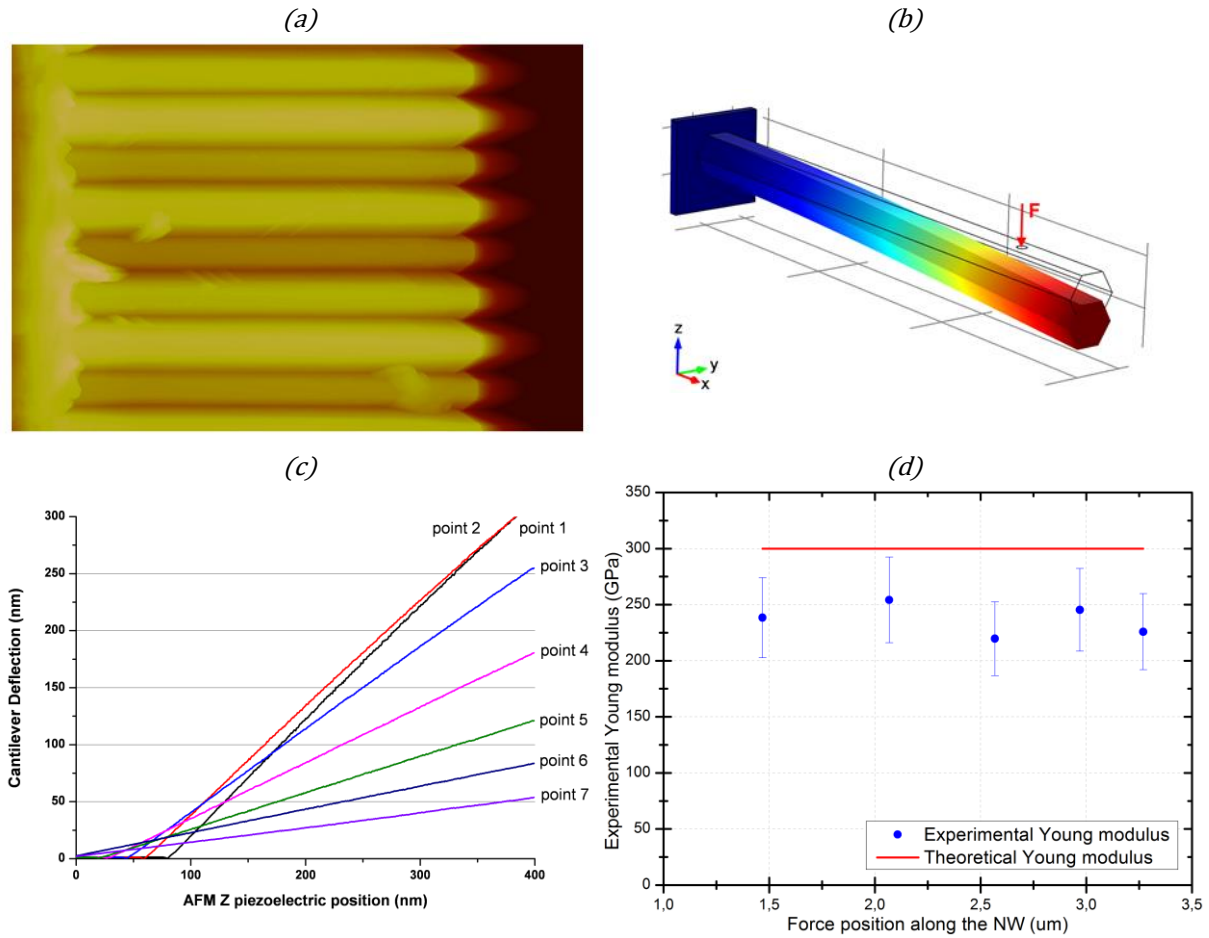

Figure 122 (a) Illustration d'un NF hexagonal plié par une pointe AFM appliquant une force F (b) image MEB d'un NF de GaN "top-down". (c) courbes AFM d'approche - retrait. (d) Extraction du module de Young à partir des courbes AFM d'approche-retrait. Valeur théorique: 300 GPa [200], [253].

Ensuite nous avons réalisé des caractérisations piézoélectriques de NFs de GaN (Figure 123a) et de ZnO. Pour cela nous avons utilisé le même dispositif AFM expérimental auquel nous avons ajouté une

pointe AFM recouverte de platine (pour la rendre conductrice) ainsi qu'un circuit de mesure doté d'un amplificateur de tension et d'un oscilloscope (Figure 123b). De cette manière il nous est possible de mesurer le potentiel piézoélectrique généré par les NFs de ZnO et de GaN fléchi par la pointe AFM. Les résultats expérimentaux (Figure 123c & d) montrent que le potentiel généré est proportionnel à la force appliquée. Par contre la variabilité des résultats est grande d'un échantillon à l'autre et varie notamment en fonction du dopage et du type de fils. Une caractérisation plus approfondie et précise est donc nécessaire pour comprendre tous les phénomènes mis en jeux dans ces NFs.

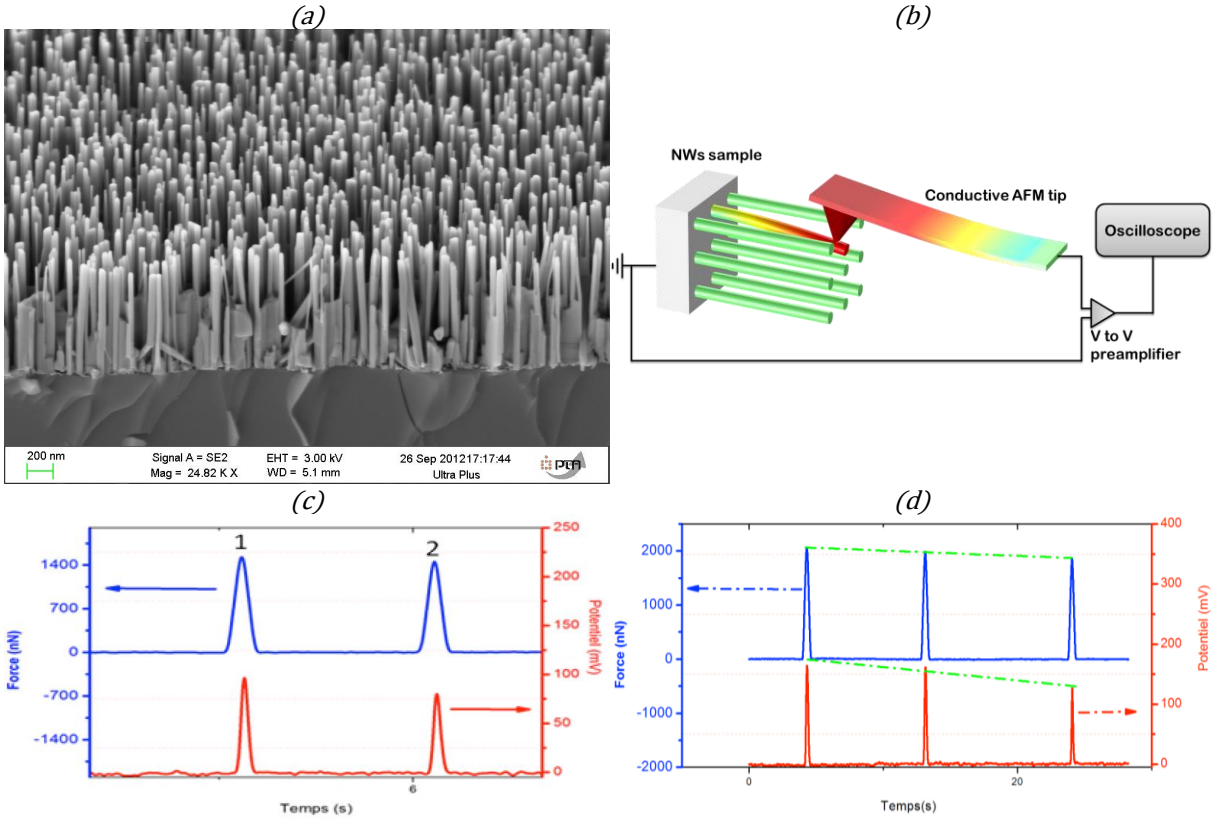

Figure 123 (a) Image MEB d'un échantillon de NFs de GaN non dopé réalisé par MBE sur un substrat de Si dopé de type p. (b) Schéma du dispositif AFM de caractérisation. (c) et (d) Magnitude du potentiel électrique mesuré par un AFM munie d'une pointe recouverte de Pt, en fonction de la force appliquée (estimé qualitativement). La force a été appliquée proche de l'extrémité de chaque NFs.

Afin de mieux caractériser les propriétés piézoélectriques des NFs de ZnO et de GaN nous avons étudié la réalisation de caractérisation piézoélectrique par AFM (appelé PFM). Cependant nous nous sommes heurtés à plusieurs problèmes qui sont détaillés dans ce manuscrit.

V.2.4. Conclusion

En résumé, dans ce chapitre, nous avons introduit des procédés de fabrication les plus couramment utilisés pour croitre des NFs de ZnO et de GaN. L'approche par gravure permet un meilleur contrôle de la régularité des NFs en termes de taille, de forme et de position, mais avec la technologie actuelle, il est très difficile de fabriquer NFs avec des diamètres inférieurs à quelques dizaines de nm. D'autre part, les processus de croissance sont des procédés classiques en vue d'obtenir des NFs de ZnO et de GaN, ce qui permet la fabrication de NFs ayant un rapport d'aspect élevé et un diamètre de l'ordre de quelques dizaines de nanomètres. Mais ces méthodes conduisent à une plus grande dispersion des tailles (y compris la hauteur), tandis que la position et l'organisation des NFs sont mal contrôlées et souvent aléatoires. Nous avons présenté le procédé MBE qui est une méthode de croissance utilisée

pour faire croitre des NFs de GaN de haute qualité étudiée dans cette thèse. Nous avons également étudié plus profondément la croissance hydrothermale de NFs de ZnO qui permet la croissance de NFs de ZnO à basse température (<100°C) sur de grands substrats divers. Les NFs de ZnO hydrothermale présentent plus de défauts cristallographiques qu'en utilisant les autres méthodes, mais ce procédé est plus extensible et facile à utiliser tout en étant compatible avec l'industrie des circuits imprimés. Bien qu'il soit difficile de faire croitre de grands et réguliers réseaux de NFS de ZnO avec le moins possible de défauts de croissance, de poussières et de contaminations chimiques (ou structurelles), nous sommes parvenus à développer des réseaux de NFs de ZnO avec des profils différents (plat, en coin , en zigzag) sur différents substrats (tranche de silicium, aluminium, film Kapton et verre) et de différentes tailles (de $1cm^2$ a des tranches de 2 pouces).

Pour comprendre plus profondément le comportement électromécanique des NFs de ZnO et de GaN et évaluer leur potentiel, nous avons développé des modèles analytiques et de simulation FEM d'un NF de ZnO courbé par une force latérale appliquée au sommet du NF. Grâce au modèle analytique, nous avons compris le mécanisme de la physique piézoélectrique survenant chez un NF individuel en flexion. En complément, les simulations FEM ont donné une estimation précise de la distribution du potentiel piézoélectrique dans le NF. La confrontation des modèles analytique et de simulation FEM a montré de petites différences dues à la simplification des équations piézoélectriques au premier ordre dans l'étude analytique et a de petits effets de bord et de maillage dans la simulation FEM. Nous avons constaté qu'il existe une inversion du potentiel à la base de la NF où le potentiel électrique est fort, et qui est due à la contrainte de cisaillement générée par la force de flexion. Une étude paramétrique approfondie a été réalisée pour définir les règles d'échelle et de dimensionnement qui sont importantes pour la prédiction et l'optimisation des performances de dispositifs. Nous avons montré que le potentiel généré augmente linéairement avec la force appliquée tandis qu'elle augmente fortement quand le rayon diminue et reste constante en fonction de la longueur du NF. Ainsi, ces règles d'échelle permettent la conception optimale de dispositifs à base de NFs de ZnO en vue d'applications spécifiques telles que des capteurs de peau artificielle.

Enfin, pour les utiliser plus tard et intégrer des NFs piézoélectriques dans des capteurs et récupérateurs d'énergie fonctionnels, nous avons caractérisé expérimentalement les propriétés électromécaniques de NFs de ZnO et de GaN individuels. Nous avons choisi d'utiliser une configuration AFM latérale originale développée à l'IMEP- LAHC pour effectuer la caractérisation mécanique et piézoélectrique de NFs de ZnO fabriqués par croissance et de NFs de GaN gravé. Cette configuration unique permet un contrôle plus facile et plus efficace de la force appliquée sur les NFs piézoélectriques. Nos enquêtes montrent qu'il n'y a pas d'effet de taille sur les propriétés mécaniques de ces NFs. Ainsi, il n'y a pas d'impact significatif de la réduction d'échelle à l'ordre du nanomètre sur les propriétés mécaniques des NFs. Nous avons ensuite étudié les caractéristiques piézoélectriques en courbant individuellement des NFs et en mesurant en même temps le potentiel généré à l'aide d'une pointe AFM conductrice. L'ensemble des résultats confirme que le potentiel généré varie linéairement en fonction de la force appliquée. En outre, les NFs de GaN non dopés semblent générer plus de potentiel électrique que ceux dopés. Fait intéressant, les tensions les plus élevées ont été observées sur des NFs de GaN individuels ayant plusieurs hétérojonctions d'AIN. Pour donner un meilleur aperçu des propriétés piézoélectriques des NFs individuels, différents modes électriques de caractérisations (tels que le PFM) ont été initiés et pourraient donner des résultats complémentaires importants à l'avenir.

V.3. Capteur de force à base de nano fils piézoélectriques

La meilleure compréhension des propriétés des NFs piézoélectrique ouvre de nouvelles perspectives d'application du phénomène piézoélectrique. Surtout, le contrôle de l'effet piézotronique à l'échelle nano permet le développement de capteurs mécaniques améliorés et performants. Mais pour pouvoir utiliser correctement et intégrer des NFs piézoélectriques semi-conducteurs, nous devons étudier divers effets parasites. Le comportement piézoélectrique de NFs piézoélectrique semi-conducteur change sous l'action de contraintes non linéaires générées par l'utilisation de forces élevées. L'environnement environnant des NFs modifie la distribution du potentiel électrique généré. Enfin, la croissance des NFs peut générer des défauts, du dopage et des fluctuations de la taille des NFs. Les porteurs libres générés par les défauts et le dopage dans les NFs piézoélectriques semi-conducteurs masquent l'effet piézoélectrique et diminue considérablement le potentiel piézoélectrique généré tandis que les variations de taille des NFs peuvent modifier le potentiel. Néanmoins, il est possible de surmonter ces problèmes et même de les utiliser pour personnaliser des dispositifs piézoélectriques et piézotroniques. Nous avons modélisé des capteurs mécaniques sur la base de la mesure du potentiel électrique générée par une force, un déplacement ou une pression grâce à l'effet piézoélectrique direct. Ainsi les capteurs mécaniques à base de NFs piézoélectriques semi-conducteurs peuvent atteindre une très forte sensibilité en termes de force, déplacement et pression en choisissant une taille des NFs et une résolution spatiale faible. Mais il est également possible de construire un capteur de force sur la base de la mesure de la variation du courant à travers une jonction de Schottky, la variation de la hauteur de barrière Schottky étant induite par l'effet piézotronique. Un tel dispositif a été caractérisé en utilisant un AFM et a montré une très bonne sensibilité à des nano forces.

V.3.1. Comportement réaliste des nano fils piézoélectriques semi-conducteurs

Dans le but d'intégrer des NFs piézoélectriques semi-conducteurs dans des systèmes autonomes il faut d'abord étudier leur comportement en prenant en compte les divers effets et phénomènes parasites susceptibles d'influencer le comportement de tels NFs. Dans cette démarche nous avons étudié l'effet de plusieurs paramètres comme la prise en compte des effets de déformations mécaniques non linéaires, de la géométrie du NF, de l'influence du substrat et du dopage des NFs.

Tout d'abord, lors de l'étude comportementale des NFs par simulation FEM, la prise en compte des déformations mécaniques non linéaire montre que pour l'application de fortes forces latérales à l'extrémité libre du NF, la valeur du potentiel généré dans le NF augmente à l'extrémité libre en extension et diminue proche de la base du NF en compression (Figure 123).

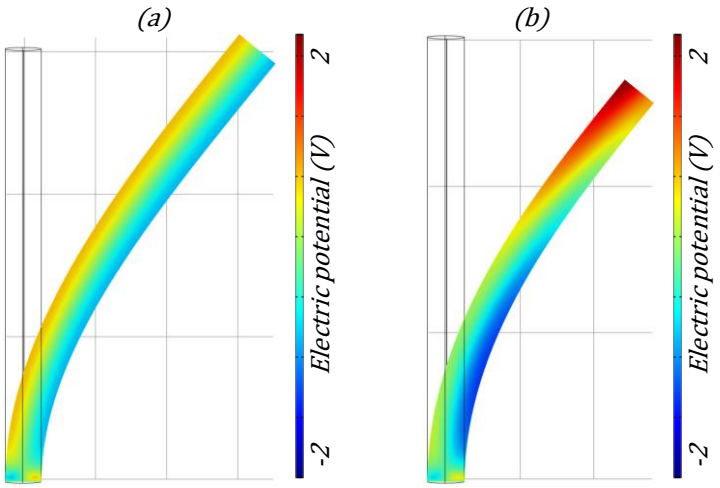

Figure 124 Distribution du potentiel électrique dans un NF de ZnO (l=600nm et r=25nm) plié par une force F=200nN. (a) simulation FEM prenant en compte les déformations mécaniques linéaires et (b) non-linéaires.

La Figure 125a montre l'évolution du potentiel généré le long des côtés en extension et en compression du NF en régime de déformation linéaire et non linéaire. Comme le montre la Figure 125b, ce changement de la distribution du potentiel dans le NF de 600 nm de long et 50 nm de diamètre en régime non linéaire est notable pour des forces latérales supérieures à 10 nN ce qui est très faible. Cet effet peut devenir important et ne doit pas être négligé aux fortes forces.

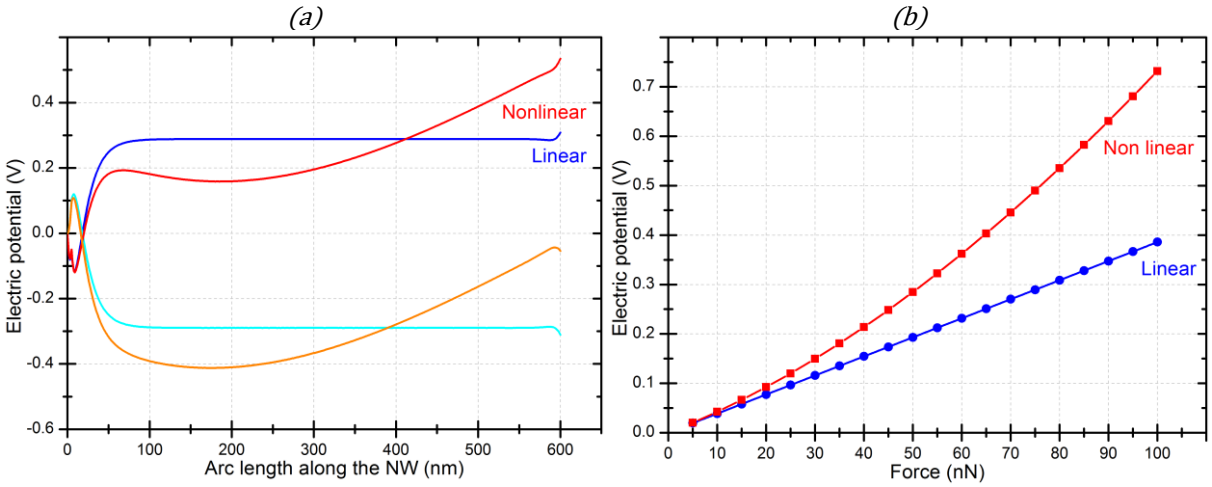

Figure 125 Simulation FEM de l'évolution du (a) potentiel électrique le long de la paroi latérale en extension et en compression du NF en fonction de l'axe Z et (b) le maximum du potentiel positif sur la paroi en extension d'un NF encastré simple (l=600nm et r=25nm), en fonction de la force latérale de flexion appliquée à son extrémité libre et en considérant des déformations mécaniques linéaires et non linéaires.

Nous avons aussi étudié l'effet de la géométrie du NF sur la distribution du potentiel piézoélectrique généré en considérant un NF de section cylindrique ou hexagonal. Les simulations FEM montrent que l'influence de ce paramètre est très faible et peut être négligée dans la plupart des cas.

Ensuite nous nous sommes aussi intéressés à l'influence du substrat sur le potentiel généré. Lors de cette étude par simulation FEM nous avons constaté que l'influence du substrat est très importante sur les valeurs et la distribution du potentiel piézoélectrique généré à la base du NF. En effet si le substrat est conducteur et relié à la masse électrique alors l'inversion du potentiel à la base du NF est faible et se restreint à deux petits lobes. Par contre si le NF est sur un substrat isolant alors ces lobes d'inversion grossissent fortement, la zone d'inversion remonte un peu plus haut dans le NF et elle se répand dans le substrat (Figure 126a & b). Ainsi le potentiel généré à la base du NF est multiplié par 5. Si l'on ajoute à cela une couche de germination de 50 nm de ZnO par exemple (Figure 126c & d),

alors l'effet du substrat est moindre et dans les deux cas les lobes d'inversion s'amplifient et se rependent dans la couche de germination faisant office de substrat plus ou moins isolant et permettant l'expression plus ou moins forte des lobes d'inversions, ce qui a été observé dans la littérature [194].

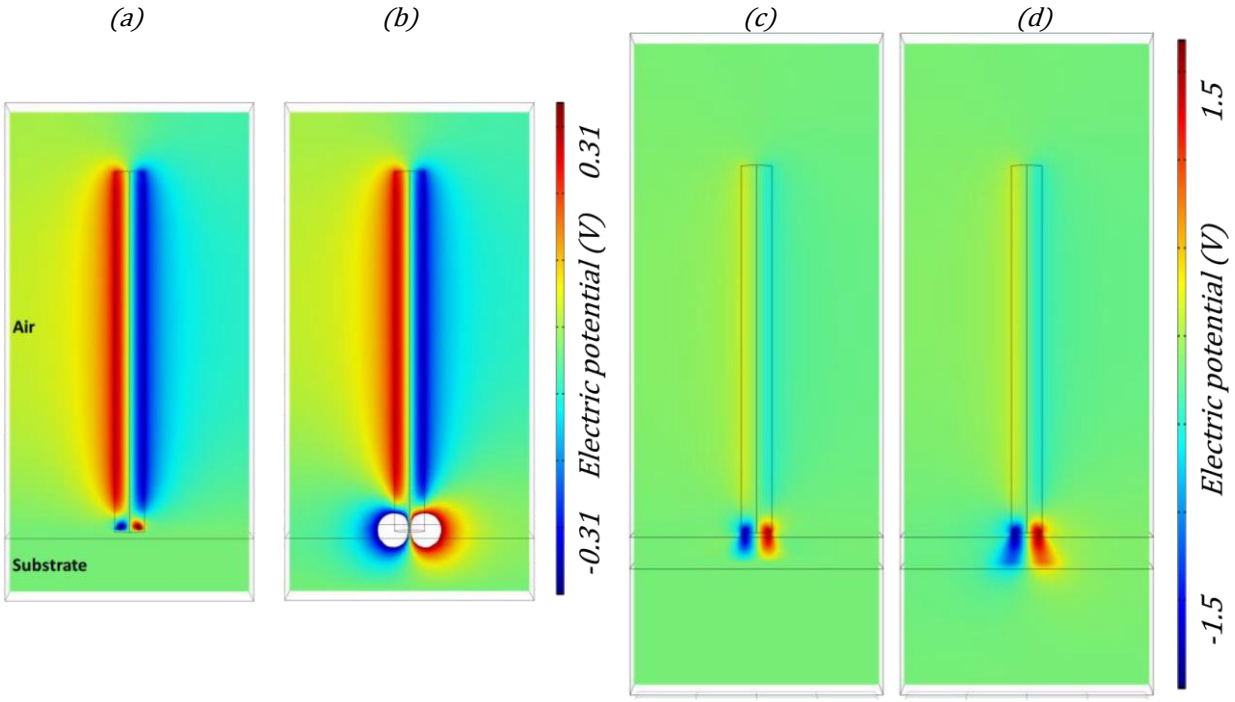

Figure 126 Distribution du potentiel piézoélectrique généré par un NF de ZnO en flexion (F=40nN), entouré d'air et attaché (a) sur un substrat en Si conducteur et mit à la masse, (b) sur un substrat de Si isolant.(c) Distribution du potentiel piézoélectrique généré par un NF de ZnO en flexion (F=80nN), entouré d'air, attaché sur une couche de germination de ZnO (w=50nm), sur un substrat de Si conducteur et mit à la masse et (d) sur un substrat de Si isolant.

Enfin nous avons étudié l'effet du dopage des NFs sur le potentiel généré. Comme le montre la littérature [194], [195], la présence de dopants ou de charges dans les NFs piézoélectriques semi-conducteurs diminue grandement le potentiel piézoélectrique mesuré. Ceci est dû à l'effet de masquage du potentiel piézoélectrique généré par les charges. Ainsi le potentiel mesuré diminue fortement en fonction du dopage du NF, atteignant une différence de potentiel quasi nul pour des dopages supérieurs à 10^{17} cm^{-3}.

V.3.2. Capteur de forces à base de mesure de tension

Comme établi dans le chapitre précédent, le potentiel généré par un NF de ZnO ou de GaN est proportionnel à la force appliquée. C'est aussi le cas si l'on applique une pression ou un déplacement sur le NF, mais les règles de variation en fonction du rayon du NF changent un petit peu (Figure 127a). Cependant, en mesurant le potentiel généré il doit être possible d'en déterminer la force, la pression ou le déplacement appliqué et donc de réaliser un capteur de force, de pression ou de déplacement. Pour réaliser un tel capteur, il est difficile technologiquement de connecter l'extrémité libre d'un NF, extrémité qui génère la différence de potentiel maximal en régime non linéaire et permettrait d'atteindre une sensibilité maximale. Par contre il serait plus facile de contacter la base du NF ou juste au-dessus de celle-ci ce qui nous permettrait de mesurer le potentiel généré par le NF tout en gardant un comportement linéaire pour de fortes contraintes (Figure 127b).

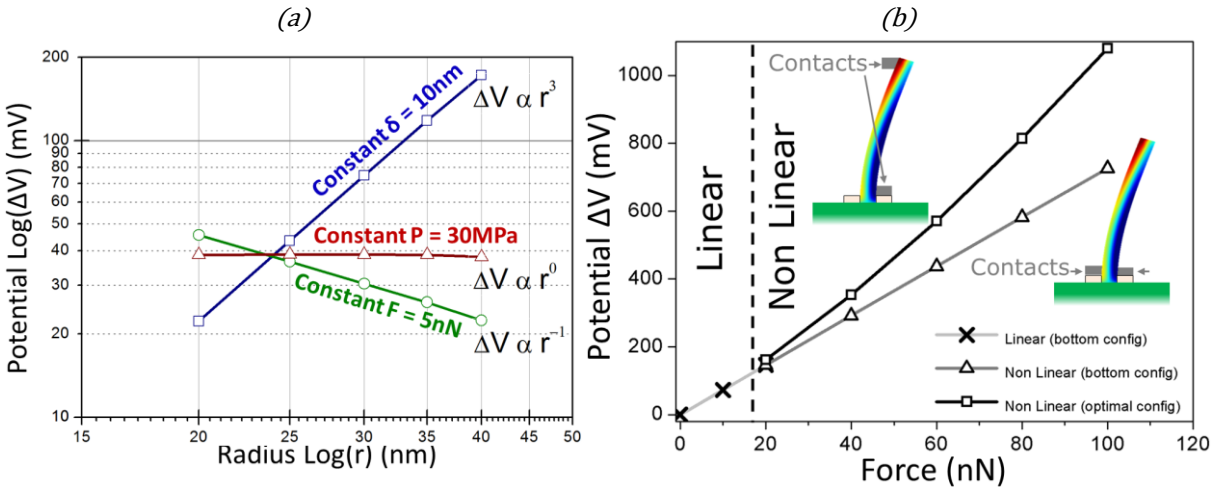

Figure 127 (a) Lois de variation de ΔV(r) pour une longueur de NF donné (l=600nm). Différents cas de sollicitation menant à des déformations similaires: F constant (5nN), δ constant (10nm) et P constant (30MPa). (b) ΔV(F) considérant des déformations mécaniques linéaires et non-linéaires. Dans la configuration de contacts a la base du NF, the potentiel augmente en suivant une loi linéaire ($a=7.3\times10^6$ V/N), alors que dans la configuration de contact haut-bas, $\Delta V=bF+cF^2$ avec $b=7.5\pm0.1\times10^6$V/N et $c=3\times10^{13}$V/N² [234].

En pratique, lors de la réalisation de NFs il y a une certaine variabilité du rayon des NFs. Or comme le potentiel généré est proportionnel au rayon des NFs, cette variabilité peut avoir un impact sur les dispositifs qui utilisent ces NFs. Pour mieux comprendre cet impact sur un capteur de force par exemple, nous avons tout d'abord expérimentalement trouvé que la distribution du rayon des NFs est de type gaussien (Figure 128a). La conséquence de cette distribution est que les NFs vont générer différents potentiels pour une même force. Une certaine proportion de NFs va donc générer un certain potentiel (Figure 128a). Ceci peut être un inconvénient, mais aussi un avantage, car si l'on choisit soigneusement quels NFs on connecte pour réaliser un capteur de force, alors il est possible de choisir la sensibilité du capteur en fonction du rayon des NFs connecté (Figure 128b). Celle-ci pouvant atteindre 11mV/nN en utilisant les NF de 16nm de rayon. Par contre la résolution spatiale du capteur sera aussi impactée par l'abondance des NFs de ce rayon dans l'échantillon.

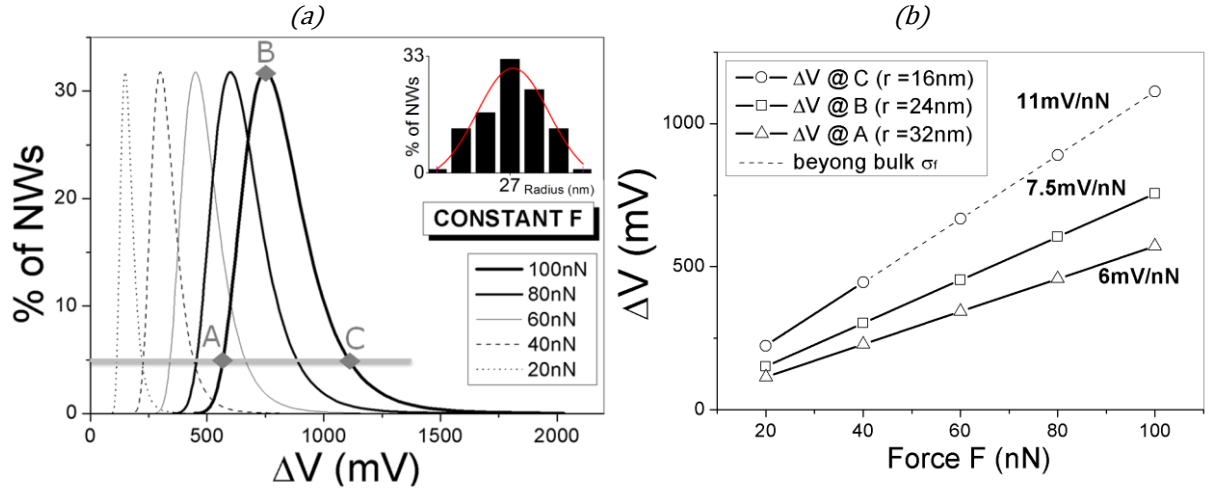

Figure 128 (a) Distribution normalisé du potentiel pour différentes valeurs de F appliqué sur une matrice de NFs avec une dispersion de leur rayon donné en insert. Le maximum B correspond à une proportion de 31% des NFs de r=24nm. Pour 5% des NFs, r=16 (C) ou 32nm (A). (b) Sensibilités en mV/nN pour divers r de NFs. La résolution latérale chute par un facteur 2,6 entre (C) et (B). Le cas 11mV/nN (r=16nm) peut être contestables car au-delà des limites de rupture admises (σ_f) pour les NFs ZnO pour F>30nN.

V.3.3. Capteur de force à base de mesure de courant

Expérimentalement nous avons montré à l'aide d'un AFM que le potentiel généré par un NF de ZnO ou de GaN fléchi était proportionnel à la force appliquée. Cependant nous avons noté la présence d'une jonction Schottky à l'interface entre le NF et la pointe AFM recouverte de platine. Pour mieux comprendre son rôle, nous avons effectué une caractérisation AFM plus poussée de cette jonction en réalisant des mesures I-V de cette jonction en fonction de la force appliquée sur le NF. Pour cela nous avons utilisé le même dispositif de mesure AFM connecté à un analyseur de paramètres (Figure 129a). Après avoir imagé les NFs (Figure 129b) nous appliquons une force à leur extrémité. Puis, une fois la force appliquée nous restons sur le NF et nous polarisons le NF afin d'effectuer des mesures I-V (Figure 129c).

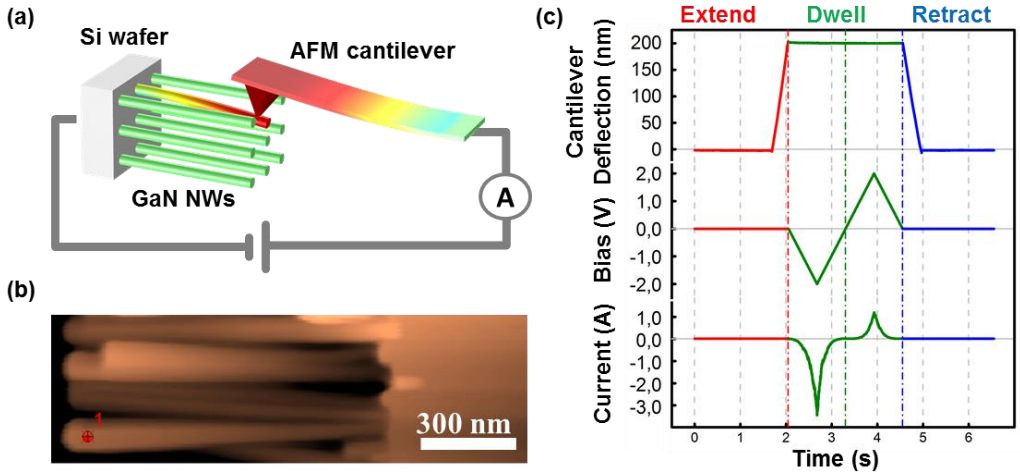

Figure 129 (a) Schéma du dispositif AFM expérimental. (b) Image AFM d'un NF de GaN incline a 90°. La marque rouge sur l'un des NFs indique la position de la pointe AFM pendant les mesures électriques. (c) Illustration du processus d'expérimentation: de haut en bas, la déflexion de la pointe AFM qui est proportionnelle a la force appliquée sur le NF de GaN; la polarisation appliquée entre la pointe AFM et l'échantillon; et le courant détecté correspondant [248].

Les résultats des mesures I-V faites sur des NFs de GaN en flexion (Figure 130a) montrent que lorsque le NF est polarisé en direct le courant augmente très faiblement avec la force appliquée sur le NF. Par contre lorsque le NF est polarisé en inverse alors le courant à travers le NF augmente de manière exponentielle avec la force appliquée. Ce résultat est dû au fait que lorsque l'on applique une force sur le NF on crée une distribution de potentiel piézoélectrique qui localement au niveau de la jonction Schottky va diminuer la barrière de potentiel (Figure 130b). Or cette jonction régule le courant à travers le NF lorsque celui-ci est polarisé en inverse, en abaissant sa barrière de potentiel le courant va fortement augmenter. Par contre lorsque le NF est polarisé en direct, cette jonction Schottky a un effet minoritaire dans l'équation du courant qui n'est donc que faiblement influencé par la force appliqué sur le NF. Ceci explique que lorsque le NF est polarisé en inverse il existe une relation entre le courant passant dans le NF et la force appliquée, et qu'il est ainsi possible de réaliser un capteur de force en mesurant ce courant. Un tel capteur de force aurai une sensibilité de 1,2 ln(I)/nN et un temps de réponse inférieur à 5ms.

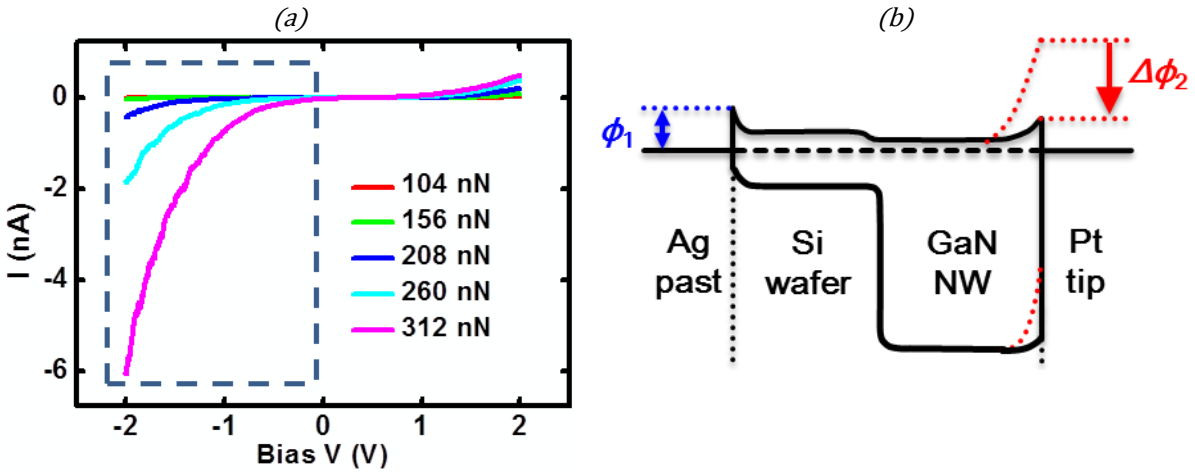

Figure 130 (a) Mesures expérimentales de la caractéristique I-V d'un NF de GaN en fonction de la force qui lui est appliquée à l'aide d'une AFM recouvert de Pt sur son extrémité libre. (b) Diagramme de band énergétique de l'échantillon de NFs de GaN caractérisé par AFM. Illustration des barrières Schottky Ag-Si (ϕ_1) et Pt-GaN (ϕ_2) lorsqu'un potentiel piézoélectrique est induit dans le NF par l'application d'une force extérieure [248].

V.3.4. Conclusion

Dans ce chapitre, nous avons étudié et discuté des principales questions liées aux NFs piézoélectriques semi-conducteurs qui n'ont pas été prises en compte auparavant. Nous avons montré que le comportement non linéaire d'un NF piézoélectrique ne doit pas être négligé lors de la prise en compte de cas impliquant des forces élevées, car cela génère une distribution de potentiel piézoélectrique non linéaire dans le NF. Le substrat et la couche de germination jouent également un rôle important dans la distribution de potentiel à l'intérieur de NFs piézoélectrique. Par exemple, nous avons montré que le potentiel piézoélectrique est multiplié par un facteur 2,5 à la base NF et qu'il se propage à travers le substrat. Un tel phénomène pourrait contribuer à simplifier les connexions de dispositifs et d'augmenter leurs sensibilités. Il est important de tenir compte de tous ces aspects, car ils peuvent influencer fortement sur la distribution piézoélectrique et ainsi influencer la conception de dispositifs à base de NF. Enfin les propriétés semi-conductrices des NFs de ZnO et de GaN ne doivent pas être ignorées, car elles peuvent diminuer fortement le potentiel électrique généré dans un NF dopé et donc diminuer les performances des appareils.

La technologie des NFs piézoélectriques offre une approche idéale pour les réseaux de capteurs nano mécaniques intégrées. Le cœur de cette technologie, les NFs piézoélectriques semi-conducteurs, est compatible avec l'industrie de la microélectronique, peut être densément intégrée et le signal du capteur est autoalimenté par l'effet piézoélectrique qui génère un potentiel électrique proportionnel à la force appliquée. La géométrie des NFs piézoélectriques peut être adaptée pour répondre de manière appropriée à la compression et à la flexion ce qui peut potentiellement créer un capteur 3D de force ou de déplacement.

Nous avons étudié les capacités théoriques des capteurs tension-force à base de réseaux de NFs de GaN. Les principaux facteurs de mérite ont été discutés dans différentes conditions de travail (F, δ, P,) correspondant à une grande variété d'applications de détection. Nous avons conclu à plusieurs tendances importantes concernant la conception des dispositifs et le choix des matériaux. Selon l'application visée, la réponse des réseaux de NFs peut être optimisée en sélectionnant la taille des NFs appropriés. Nous avons montré qu'une sensibilité élevée, jusqu'à 10^7V/N, peut être accessible et permettre la détection de nN, nm ou MPa, ce qui est une nette amélioration vis-à-vis des dispositifs piezorésistifs comparables ayant une sensibilité d'environ 3×10^2V/N [296].

Expérimentalement, nous avons démontré les capacités de détection de force transversale par des NFs de GaN alignés verticalement en utilisant l'effet piézotronique sur le passage du courant à travers une jonction métal-NF de GaN. En utilisant un AFM nous avons vérifié que, en modulant la hauteur de la barrière Schottky grâce au phénomène piézoélectrique, la force transversale externe pouvait être reliée linéairement au logarithme népérien de la circulation du courant. La sensibilité à la force transversale a été mesurée comme étant de 1,24±0,13 ln(A)/nN avec un temps de réponse inférieur à 5ms, ce qui sont des valeurs très impressionnantes. Ce capteur de nano force démontre le potentiel des matériaux piézoélectriques semi-conducteurs comme principal élément constitutif pour les micros et nano réseaux de capteurs.

V.4. Récupérateurs d'énergie mécanique à base de nano fils piézoélectriques

Une des nouvelles perspectives de la piézoélectricité à l'échelle nano concerne le domaine de la récupération d'énergie mécanique. Aujourd'hui la récupération d'énergies propres et renouvelables de l'environnement constitue une réponse efficace à l'alimentation de systèmes autonomes qui ont besoin de centaines de µW à quelques mW. En particulier l'énergie mécanique est parmi les sources les plus abondantes et fiables d'énergie dans notre vie quotidienne et qui nous accompagne quelles que soient les conditions climatiques ou de température. Nous avons distingué trois méthodes pour récupérer l'énergie mécanique à l'aide du phénomène piézoélectrique. Tout d'abord, nous pouvons utiliser des nanostructures piézoélectriques vibrantes. Mais les fréquences de résonance mécanique de ces dispositifs sont élevées (quelques MHz) et elles sont donc difficiles à adapter à la récupération d'énergie mécanique à partir de sources humaines, à l'exception probablement d'ultrasons. Deuxièmement, le dispositif de récupération d'énergie peut fonctionner sous des cycles de compression. Nous avons étudié une structure simple composée de NFs piézoélectriques semi-conducteurs immergés dans un polymère isolant souple et intégré entre des électrodes inférieure et supérieure. Pour évaluer les performances de cette structure simple, nous avons développé un modèle analytique et nous avons effectué des simulations FEM pour l'optimiser. Nous avons fabriqué des prototypes en utilisant la croissance hydrothermale de NFs de ZnO et nous les avons caractérisés. En troisième lieu, il est intéressant de récupérer l'énergie de mouvements en utilisant des structures en flexion. Notre structure simple utilisant des NFs alignés verticalement permet également de récupérer des mouvements de flexion du substrat. La récupération des compressions et des mouvements de flexion avec une structure simple est un avantage fort et a motivé l'étude de notre structure en utilisant des modèles de flexion. Enfin, nous avons étudié expérimentalement ce type de dispositif.

V.4.1. Introduction à la récupération d'énergie mécanique

L'énergie mécanique est présente tout autour de nous quotidiennement sous forme de chocs, déformations, contraintes ou vibrations. Ces formes d'énergie mécanique sont notamment présentes dans les mouvements naturels tels que les vagues et le vent, dans les mouvements du corps humain comme la marche et la course, mais aussi la respiration et les flux sanguins, dans les activités industrielles avec les mouvements et les vibrations des machines, mais aussi plus généralement dans tous les flux d'air et de liquides et enfin dans tous les transports. L'énergie contenue dans ces sources est relativement faible et s'étend jusqu'au Watts. Cependant seule une partie de cette énergie est récupérable et on estime que ces sources d'énergie pourraient fournir des puissances allant de la dizaine de µW à la dizaine de mW. Cette énergie pourrait avoir de multiples applications dans divers domaines comme dans l'industrie pour la maintenance prédictive des machines et structures, dans le

secteur automobile pour l'auto-alimentation de divers capteurs (de pression, de collision, …) et dans les infrastructures et l'environnement pour le contrôle de défaillances, fissures et de toutes variations d'un paramètre. Mais aussi en matière de logement pour les applications de domotique (capteur de présence, …), dans électronique grand public dans les téléphones intelligents par exemple et dans les soins de santé pour la surveillance des patients (capteurs de pression sanguine, …). Et enfin dans les applications militaires et spatiales avec des équipements de maintenance et de surveillance (surveillance des frontières, …).

Pour récupérer et convertir cette énergie mécanique en énergie électrique il existe plusieurs technologies dont les plus utilisées sont les technologies électromagnétiques, électrostatiques et piézoélectriques. Nous avons choisi la technologie piézoélectrique, car elle possède plusieurs avantages dont le fait d'être compatible avec l'industrie des MEMS, de générer de fortes tensions et d'avoir un fort couplage électromécanique. Par contre ce couplage est dépendant des matériaux utilisés. Cette technologie, qui permet d'atteindre de hautes densités d'énergie, fait encore l'objet de nombreuses études notamment à l'échelle nanométrique où l'utilisation de NFs piézoélectriques semi-conducteurs pourrait améliorer son efficacité.

La conversion de l'énergie mécanique en énergie électrique en utilisant l'effet piézoélectrique peut se décomposer en trois étapes (Figure 131) :

- Premièrement, une étape de transfert de l'énergie mécanique extérieur (fourni par la source d'énergie) vers les structures piézoélectriques de conversion de l'énergie (situées dans le dispositif de récupération d'énergie).
- Ensuite une étape de conversion de l'énergie mécanique en énergie électrique grâce au phénomène de piézoélectrique
- Enfin une étape de transfert de l'énergie électrique généré dans les structures de conversion piézoélectrique vers le circuit électrique de sortie du récupérateur d'énergie.

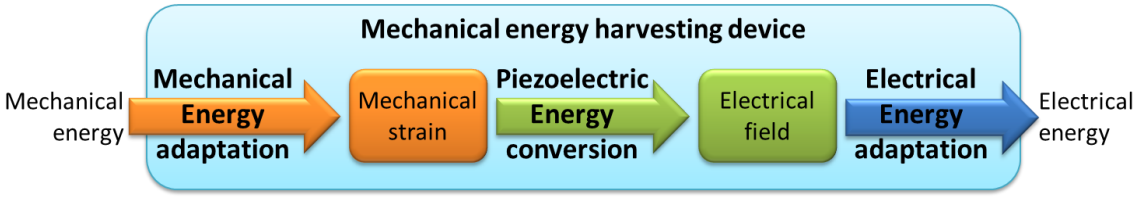

Figure 131 Diagramme des différentes étapes de conversion de l'énergie mécaniques en énergie électrique par un dispositif piézoélectrique de récupération d'énergie mécanique (1 adaptation de l'énergie mécanique, 2 conversion d'énergie piézoélectrique et 3 adaptation de l'énergie électrique).

Généralement une quatrième étape est nécessaire et consiste en la mise en forme du signal électrique pour l'adapter aux besoins électriques. Cependant cette étape complexe fait l'objet d'intenses recherches dans d'autres laboratoires [303]–[305] et par conséquent n'est pas traitée dans cette étude.

Pour réaliser un dispositif de récupération d'énergie efficace, il faut maximiser l'efficacité de ces trois étapes. Mais pour efficacement transférer l'énergie mécanique dans le dispositif de récupération d'énergie, il faut préalablement savoir quel type d'énergie mécanique nous souhaitons convertir. En effet, il existe plusieurs formes d'énergie mécanique qui peuvent se classer en deux catégories : les chocs, déformations et contraintes mécaniques d'un côté et les vibrations et variations d'accélération de l'autre (Figure 132).

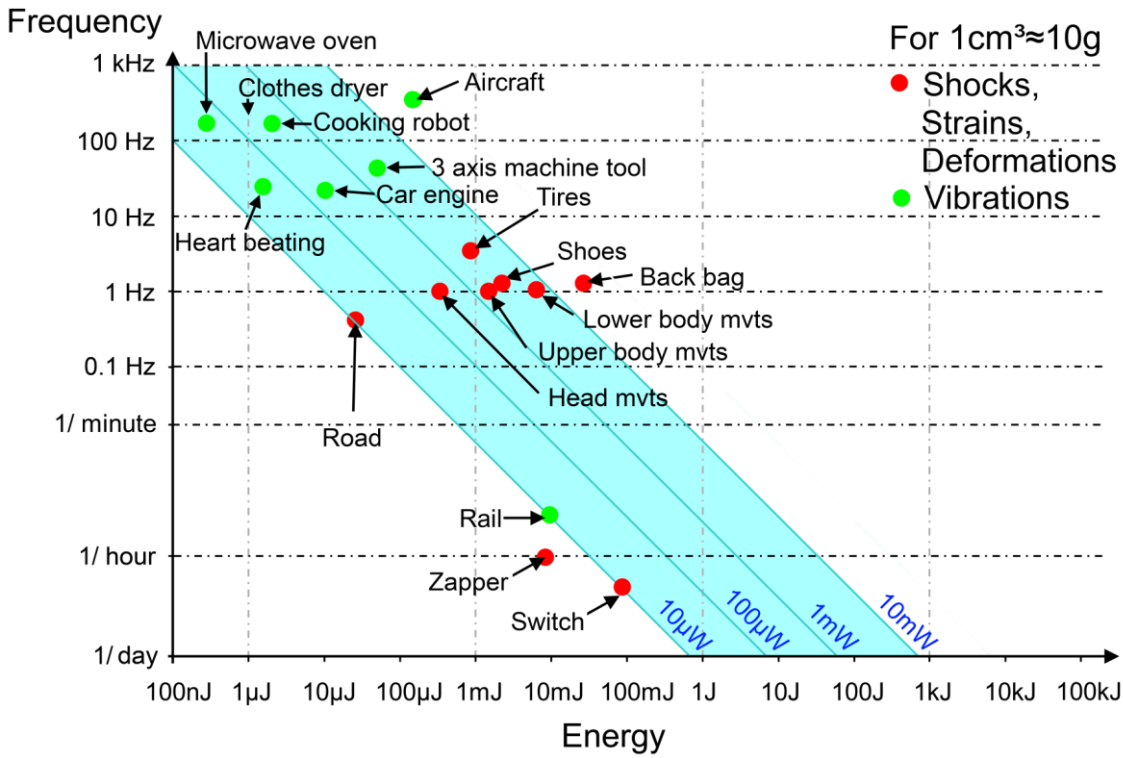

Figure 132 Type et quantité d'énergie mécanique disponible dans les activités humaines (adapté de [306]*).*

Ces catégories correspondent à des sources d'énergie mécanique ayant un comportement différent, l'une vibratoire et l'autre quasi statique, et qui influencent fortement la structure des dispositifs de récupération d'énergie.

L'état de l'art illustre ceci parfaitement. Le professeur Z. L. Wang de l'université de Georgia Tech a commencé à travailler sur les récupérateurs d'énergie mécanique à base de NFs piézoélectriques, dis nano générateurs (NG), dès 2006. C'est un précurseur qui a conçu de nombreux NG ayant des structures différentes et adaptées pour récupérer différents stimulus mécaniques. On distingue notamment des NG optimisés pour récupérer les vibrations, les contraintes de compression ou encore les déformations et flexions.

La fréquence de résonnance d'un NF de ZnO de 600nm de long et 50nm de diamètre est très élevée, de l'ordre de la centaine de MHz. Or les fréquences de vibration des sources d'énergie mécaniques les plus accessibles et abondantes s'étendent jusqu'au kHz, donc il parait difficile de récupérer efficacement cette énergie en utilisant les fréquences de résonnance de tels NFs. Par conséquent, pour la suite de notre étude nous avons choisi d'étudier la récupération de l'énergie mécanique à l'aide de NFs piézoélectriques semi-conducteurs en mode non résonnant.

V.4.2. Récupération d'énergie en mode non résonant : compressions axiales

Dans un premier temps nous avons étudié la conception, l'optimisation et la réalisation de NGs fonctionnant en compression axial par rapport aux NFs. La structure que nous avons conçue en collaboration avec les Professeur Wang de Georgia Tech s'inspire de ses précédents NGs et VING (Vertically Integrated Nano Generator). Notre structure se compose (Figure 133a) :

- D'une électrode inférieure
- D'un tapis de NFs aligné verticalement et immergé dans un isolant

- D'une couche isolante sur les NFs
- D'une électrode supérieure

La couche isolante enrobant les NF servant à augmenter la robustesse du NG tout en diminuant les fuites de courant et les courts circuits. Le fonctionnement de ce dispositif est simple et peut se décomposer en trois étapes (Figure 133b) :

- Une première étape de transfert de l'énergie mécanique extérieur aux NFs. La force de compression appliquée sur le NG va contraindre le NG et générer une contrainte mécanique verticale dans chaque NFs situé au cœur du dispositif.
- Puis une étape de conversion de l'énergie mécanique en énergie électrique. La contrainte mécanique dans les NFs va générer une différence de potentiel dans le NFs grâce à l'effet piézoélectrique.
- Enfin une étape de transfert de l'énergie électrique généré au circuit électrique externe. Le champ électrique créé dans les NFs va attirer les charges libres situées dans le circuit extérieur. Ces porteurs libres vont venir charger la capacité formée par les deux électrodes du NG et vont ainsi créer un courant de déplacement dans le circuit externe.

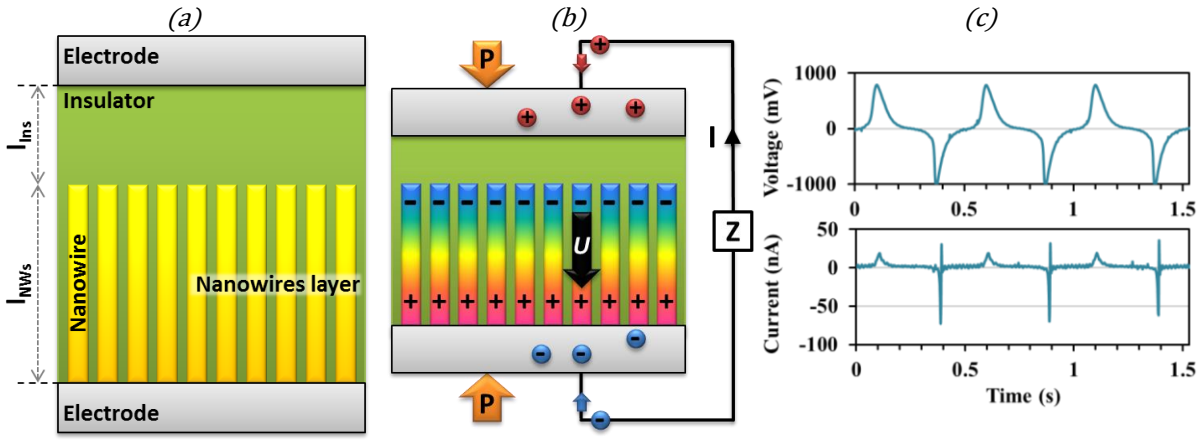

Figure 133 (a) Structure du VING avant et (b) principe de fonctionnement après compression verticale. (c) Résultats expérimentaux de caractérisation d'un prototype de VING soumis à des forces de compression [300].

Expérimentalement la caractérisation de prototypes de NG montre qu'en effet l'application d'une force de compression sur le NG va générer un pulse de tension et de courant dans le circuit externe (Figure 133c). Pour mieux comprendre ce fonctionnement et optimiser l'efficacité des NG nous avons réalisé un modèle analytique simplifié entre chaque étape supposée stationnaire. Ce modèle montre que le rendement de ce NG peut être optimisé en utilisant une épaisseur d'isolant la plus fine possible ainsi qu'un module de Young et une permittivité de la couche de NFs la plus faible possible. Cependant ce modèle simpliste, qui permet de mieux comprendre le fonctionnement du NG, ne permet pas de connaitre facilement et exactement les paramètres optimaux de ce NG.

Pour mieux comprendre le fonctionnement de ce NG, l'influence de chaque paramètre et optimiser ses performances, nous avons réalisé des simulations FEM de ce NG. Pour cela nous avons simulé une seule cellule élémentaire du NG. La cellule de référence se compose (Figure 134a) d'un NF de ZnO encapsulé dans du PMMA. Lors de la compression de cette cellule, les premiers résultats ont mis en lumière deux problèmes : une déviation du champ de contraintes autour du NF ce qui dissipe l'énergie mécanique autour du NF et diminue le transfert d'énergie mécanique. Mais aussi des pertes diélectriques entre le haut du NF et l'électrode supérieure, ce qui diminue l'efficacité du transfert d'énergie électrique du NF a l'électrode. Pour remédier à cela, nous proposons d'utiliser une couche isolante au-dessus des NFs constitués d'un matériau dur à haute permittivité ce qui doit linéariser le

champ de contrainte dans la structure et diminuer les pertes diélectriques dans l'isolant. Ensuite nous avons étudié l'effet de la densité de NFs sur les performances du NG. Pour cela nous avons introduit un paramètre qui est le ratio du diamètre des NFs par la largeur de la cellule de NG (Figure 134a). Les simulations montrent que l'énergie générée est maximale en utilisant une densité moyenne de NFs correspondant à un ratio de 0,5 (Figure 134b). Par contre l'efficacité du NG est maximale en utilisant une forte densité de NF correspondant à un ratio de 0,9 (Figure 134c). Si l'on compare ces résultats aux performances d'une couche mince de ZnO ayant la même épaisseur alors, en utilisant une densité moyenne de NF, il est possible de générer jusqu'à 5,6 fois plus d'énergie qu'une couche mince tout en gardant la même efficacité. Ceci traduit le fait que la couche de NFs est plus sensible qu'une couche mince a efficacité égale. Enfin nous avons aussi étudié l'effet des dimensions des NFs. L'énergie générée était dans ce cas maximal en utilisant des NFs longs et fins.

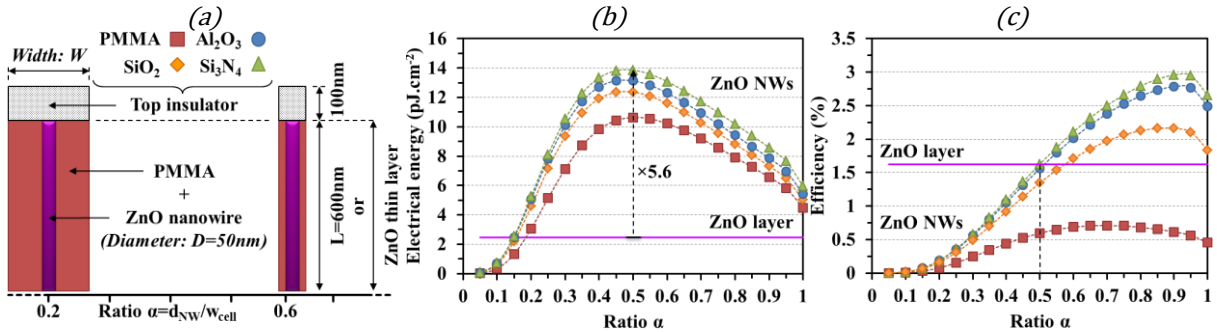

Figure 134 (a) Schéma de différentes structures de NGs utilisant divers matériaux (PMMA, SiO_2, Al_2O_3, et Si_3N_4) et densités de NFs, (b) énergie électrique et (c) efficacités d'une cellule de base NG. La comparaison avec une couche mince de ZnO (w=600nm) a été faite en utilisant les mêmes paramètres de simulations FEM.

Dans le cadre de notre collaboration avec le professeur Wang de l'université de Georgia Tech, nous avons réalisé de nombreux prototypes de NGs (Figure 135). Au cours de leur fabrication, nous avons mis en lumière plusieurs difficultés, dont des problèmes de déposition de particules et de poussières ainsi que des défauts de croissances des NFs. Pour augmenter le rendement de fabrication nous avons donc travaillé a l'amélioration des étapes de fabrication des NGs ce qui nous a amené à croitre des NFs de ZnO plus vite avec moins de défauts et de particules tout en fabricant de plus grand NGs.

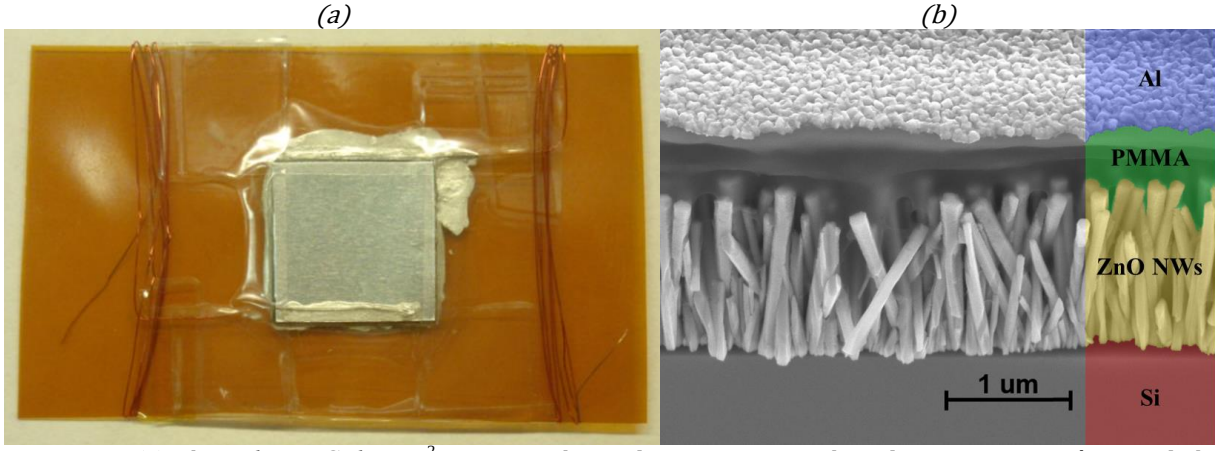

Figure 135 (a) Photo d'un NG de 1cm^2 avec une plaque de protection en Al au-dessus et connectée avec de la laque d'argent. (b) Image MEB d'une vue en coupe d'un prototype de VING utilisant des NFs de ZnO.

Enfin, afin de caractériser précisément les performances de ces NGs et connaitre leur rendement, nous avons mis au point un banc de test adapté à la caractérisation de ces NG en compression. Ce banc de test nous permettant de contrôler et mesurer la force appliquée et son profil et ainsi de mieux connaitre le comportement réel de ces NGs.

V.4.3. Récupération d'énergie en mode non résonant : flexions

Outre la compression axiale, il existe une autre façon de solliciter mécaniquement les NFs d'un NG. Il s'agit des déformations non axiales. Pour cela il suffit de disposer le NG sur un corps d'épreuve et de lui faire endurer des déformations. C'est un moyen couramment utilisé pour récupérer de l'énergie mécanique. Ceci peut se faire par l'intermédiaire de poutres, de plaques ou de membranes qui sont notamment étudiées et développées sur technologie silicium au laboratoire de l'IMEP-LAHC. Or d'après la littérature notre structure de NG peut aussi fonctionner de cette manière en flexion. Pour étudier ce cas et les performances de notre NG dans ces conditions nous avons simulé le comportement d'un NG sur une plaque encastré double et soumis à une pression hydrostatique de 1,8kPa (Figure 136a). Les simulations montrent que si le NG est assez éloigné de l'axe neutre de la plaque, alors la flexion de la plaque va engendrer une compression latérale du NG. Pour étudier et comprendre le fonctionnement du NG en compression latérale nous avons réalisé des simulations FEM d'une cellule de NG comprimé latéralement (Figure 136b & c). Cette cellule se compose d'une couche isolante inférieure en Si3N4, d'une couche de germination en ZnO, d'un NF de ZnO entouré de PMMA et d'une couche isolante supérieure.

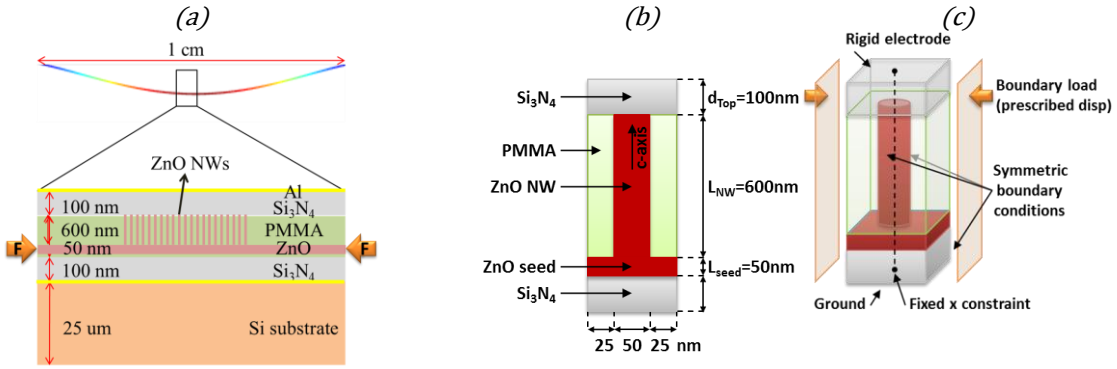

Figure 136 (a) Schéma de la section d'une membrane avec un VING, courbé par une pression hydrostatique P=1.8kPa et avec un agrandissement de la structure. (b) Structure d'une cellule de base de NG compressé latéralement et (c) conditions aux limites utilisées pour les simulations FEM. (adapté de [336]*).*

Comme pour le cas du NG en compression, les résultats de simulation mettent en évidences deux problèmes. Une déviation du champ de contraintes dans l'isolant entourant les NFs et des pertes diélectriques dans la couche isolante supérieure. Pour remédier à ces problèmes, les simulations montrent qu'il est préférable cette fois d'utiliser un matériau isolant a module de Young et permittivité moyenne, et non élevée comme dans le cas précédent. Ceci étant notamment dû au fait que l'utilisation d'un matériau isolant trop dur entre les NFs diminuerait leur compression latérale. Cependant cette étude est préliminaire et toujours en cours afin d'optimiser les performances de notre NG pour récupérer l'énergie mécanique des déformations et mouvements de flexion.

En parallèle de cette étude, nous avons aussi fabriqué des prototypes de NG fonctionnant en flexion. Pour cela nous avons utilisé comme substrat des feuilles d'aluminium sur lesquelles nous avons fabriqué des NGs (Figure 137). Au cours de leur fabrication encore constaté des problèmes de dépôt de particules et de poussières et des défauts de croissance des NFs. Mais aussi des problèmes de délamination des couches déposées lorsque la flexion imposée au NG était trop forte.

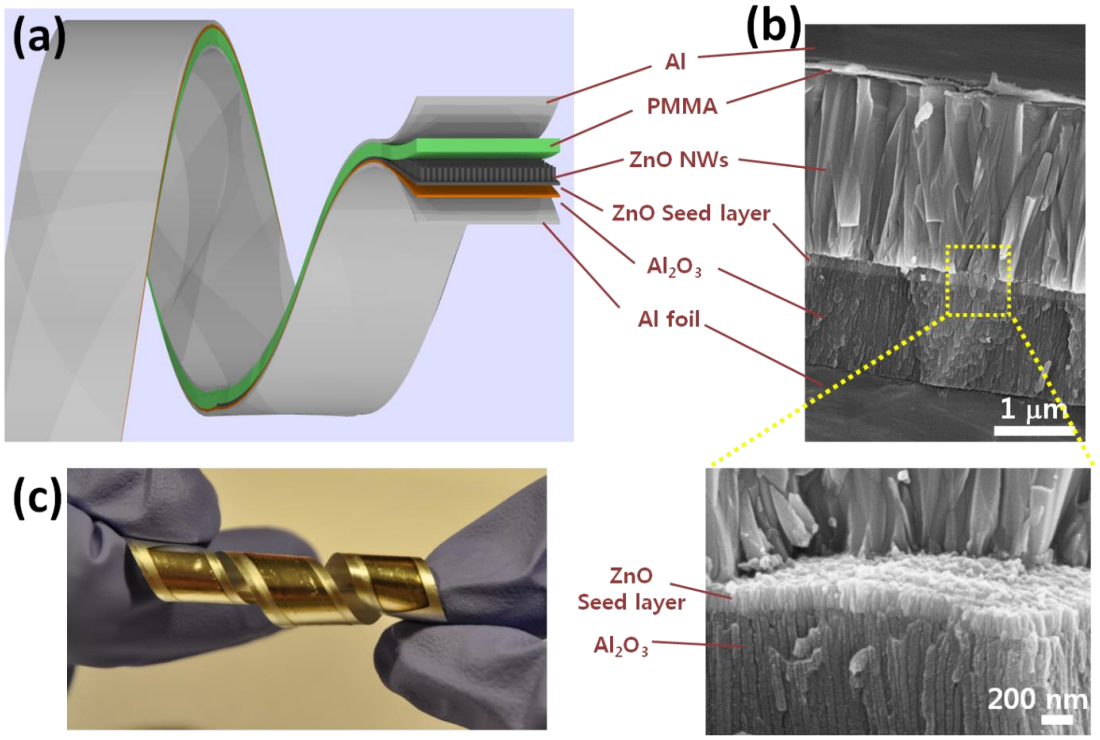

Figure 137 (a) Schéma d'un NG super flexible utilisant une couche isolante d'Al_2O_3 anodisée (AAO). La couche d'AAO a été formée sur une feuille d'Al ultra fine avant la croissance des NFs de ZnO pour obtenir une forte sensibilité et durabilité du NG ainsi qu'un bon rendement de fabrication en raison des liens covalents partagés par les atomes d'oxygène et de l'augmentation de la surface de contact, du aux nano pores, entre la couche d'AAO et la couche de germination. (b) Images MEB de la section d'un NG. (c) Image optique d'un NG super flexible tordu [318].

Nous avons caractérisé ces NGs en les fléchissant. Les résultats (Figure 138) montrent que ces prototypes pouvaient générer une tension allant jusqu'à 0.12V et un courant de 0.6μA. Cependant nous avons noté que les performances des NGs diminuaient fortement lorsque l'épaisseur de la couche isolante inférieure diminuait. Une caractérisation plus pousse de ces prototypes a montré que cette diminution des performances était dû à la mauvaise résistance de la couche isolante qui, lorsqu'elle est trop fine, laisse passer des porteurs libres qui vont masquer le potentiel piézoélectrique. L'utilisation d'une couche plus isolante ou plus épaisse est donc à privilégier.

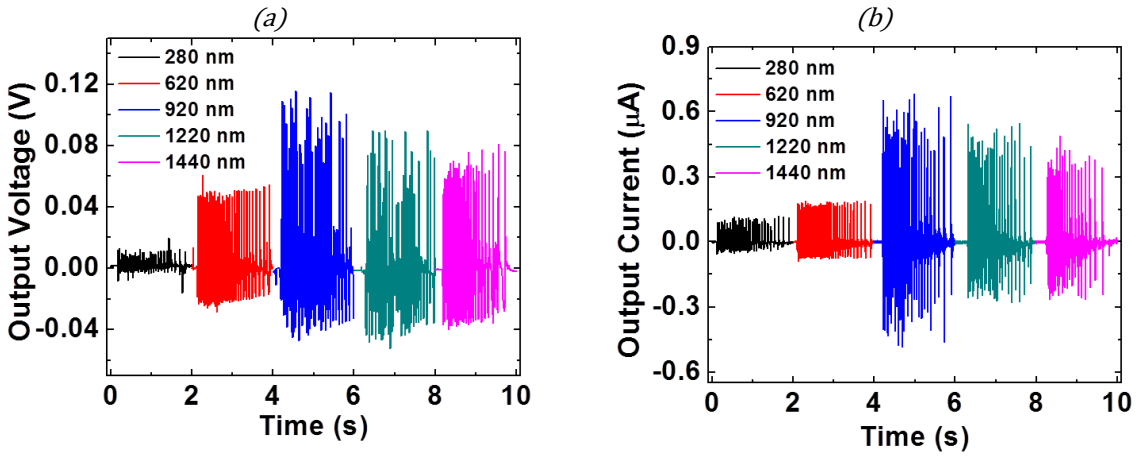

Figure 138 (a) Résultats expérimentaux de la tension de sortie et (b) du courant de sortie d'un prototype de NG en fonction de l'épaisseur de la couche isolante d'AAO et sous les mêmes conditions expérimentales [318].

V.4.4. Conclusion

En conclusion, notre étude de la récupération d'énergie démontre clairement que les NFs piézoélectriques, tels que les NFs de ZnO et de GaN, sont bien adaptés à la récupération d'énergie mécanique que s'ils sont correctement intégrés. Notre étude dynamique de NFs de ZnO typiques (de quelques centaines de nanomètres de longueur et quelques dizaines à une centaine de nanomètres de diamètre) montre que la fréquence de résonance mécanique est assez élevée, de l'ordre du MHz. Prenant en compte le phénomène piézoélectrique dans les NFs, la fréquence de résonance diminue légèrement, mais reste trop élevée pour récupérer des vibrations mécaniques quotidiennes provenant de l'activité humaine et qui se trouve dans la gamme des basses fréquences. De plus cette conclusion tient toujours même en regroupant les NFs et en mettant dessus une masse sismique lourde pour diminuer la fréquence de résonance de l'ensemble du système. C'est pourquoi nous avons concentré notre étude sur une approche plus appropriée en considérant des déformations en temps réel ou quasi statique. En effet ces déformations peuvent être rencontrées dans les applications basse fréquence ou lorsque des stimulations mécaniques aléatoires sont disponibles sur le corps humain par exemple.

Nous avons développé des modèles analytiques et des simulations FEM de NG pour examiner les optimisations électromécaniques possibles de ces dispositifs en utilisant divers matériaux isolants et géométries. Après une analyse approfondie, nous avons proposé une structure de NG innovante et efficace [300]. Une fois optimisé, la couche de NFs piézoélectrique du NG est très comparable à une couche de matériau composite piézoélectrique, ayant un potentiel piézoélectrique générée optimum pour des NFs longs et minces. La comparaison entre le NG optimisé à base de NFs de ZnO et un NG à base d'une couche mince de ZnO, dans les mêmes conditions, prouve la viabilité et l'intérêt d'utiliser des NFs pour les applications de conversion d'énergie comme la récupération d'énergie mécanique. Si l'on considère seulement la nanostructure électromécanique, l'énergie électrique récupérer par un NG peut être multipliée par un facteur de 6 tout en conservant la même efficacité qu'une couche mince piézoélectrique et en augmentant la sensibilité à la force. Alors que nous avons limité notre étude au ZnO, ces modèles peuvent être étendues à d'autres matériaux piézoélectriques en forme de NFs, nano poutres et nano fibres telles que le GaN [308], [309], BaTiO3 [33], [312] et PZT [218], [311] entre autres. Comme pour les NFs piézoélectriques semi-conducteurs, le masquage par les dopants ionisés limite fortement les performances pour les forts dopages, même dans l'hypothèse de pleine désertion des charges. Cette dégradation pourrait être compensée en partie par l'augmentation des coefficients piézoélectriques qui est attendue à l'échelle nanométrique [40]. Même s'ils sont difficiles à faire croitre, les NFs piézoélectriques non dopés semblent la meilleure option. Pour contrer les effets du masquage, la qualité des NFs pourrait être améliorée en utilisant un plasma ou un recuit [274]. Une alternative serait de déserter les NFs en utilisant un matériau de matrice chargée positivement tel que le P_3HT [328].

Nous avons ensuite étudié la fabrication de prototypes de VING utilisant la croissance hydrothermale de NFs de ZnO que nous avons développé et qui nous a permis de réaliser des dispositifs de grande surface (jusqu'à $12cm^2$). La fabrication est très difficile en raison de problèmes de court-circuit. Pendant le processus de fabrication des NG nous avons mis en évidence quatre obstacles qui doivent être résolus pour obtenir de bon NG: la rugosité du substrat, la présence de poussière et de particules, les défauts de croissance et les manipulations délicates. L'utilisation d'un seul processus de masquage peut aider à augmenter le rendement de NGs fonctionnels, mais ce n'était pas assez. Par conséquent, nous conseillons d'utiliser une couche inférieure d'isolation en plus de celle du dessus afin de mieux contrôler les fuites de courant entre les électrodes et les NFs. Pour obtenir des NG encore plus

performants, il est nécessaire de construire la structure optimisée qui comprend une couche composite de PMMA-NFs et un isolant supérieur mince et dure.

De plus, nous avons montré que la structure VING peut être optimisée pour récupérer l'énergie de flexions. Nous avons étudié divers matériaux et nous avons défini des lignes directrices d'optimisation en utilisant différents matériaux de matrice isolants. Par rapport au PMMA précédemment défini comme étant le meilleur matériau de matrice pour les NG fonctionnant en compression, le matériau de matrice Al_2O_3 est mieux adapté pour le NG fonctionnant en flexion, ce qui améliore le potentiel généré par deux et l'énergie électrique récupérée par six fois ce qui est essentiel pour la récupération d'énergie. D'autre part SiO_2 doit être préférée afin de maximiser le rendement de conversion d'énergie. Cependant le mauvais rendement global de cette configuration en flexion peut être expliqué par le fait que la contrainte est normale à l'axe des NFs. Par conséquent, en raison du coefficient de Poisson du matériau de matrice et les coefficients piézoélectriques plus faibles en mode transverse (d_{13}), l'énergie mécanique transformée est plus faible. Néanmoins, bien que les VING n'ont pas une efficacité optimale en flexion, ils montrent des performances raisonnables. La structure la plus adaptée dans ce cas reste le LING qui consiste en plusieurs dispositifs VING empilés et inclinés à 90°. Comme la fabrication de LING est difficile, nous avons d'abord étudié la fabrication de prototypes de VING fonctionnant en flexion. De même que pour les prototypes précédents, la fabrication n'est pas simple surtout en raison des problèmes de court-circuit. L'ajout d'une couche isolante inférieur permet la fabrication fiable de longs rubans de NG. Pendant le processus de fabrication de ces dispositifs, nous avons souligné le rôle important de la couche isolante inférieur et la forte influence de ses propriétés électriques. Avoir une couche isolante aussi mince que possible tout en gardant son rôle d'isolant est un point clé pour réaliser des NG efficaces. Dans ce cas, nous avons comparé l'AAO et l'Al_2O_3 évaporé comme couches isolantes. L'AAO a montré une résistivité électrique plus faible et donc de plus grands courants de fuite par rapport à l'Al_2O_3 évaporée. Cependant, l'AAO résiste mieux à la flexion des NG. Enfin, des prototypes fonctionnels ont été caractérisés et un exemple d'application originale a été démontré : un capteur de déplacement autoalimenté pour le mouvement des pupilles.

V.5. Conclusion et perspectives: Vers les capteurs autoalimentés

Les systèmes intelligents sont le résultat combiné des progrès de la microélectronique conduisant à une augmentation de la puissance de calcul, une diminution de la consommation des transistors, l'ajout de nouvelles fonctionnalités (More than Moore), amélioration des moyens de communication et en particulier aux intégrations et applications dans notre vie quotidienne. L'évolution du domaine des systèmes intelligents est prometteuse et les attentes sont élevées dans de multiples domaines d'applications concernant les activités humaines et la surveillance de l'environnement. Mais, victime de leurs succès, l'intégration de plus en plus de fonctions dans les systèmes intelligents les conduisent face à un problème énergétique où l'autonomie de ces systèmes intelligents devient de plus en plus souvent le principal problème. Il existe donc un besoin croissant en capteurs autonomes et sources d'énergie. Développer la récupération d'énergie et les capteurs autoalimentés est une façon de répondre à ce problème d'énergie. Parmi les technologies étudiées, la piézoélectricité présente plusieurs avantages. Elle est compatible avec l'industrie IC / MEMS, génère des tensions élevées (jusqu'à 100 V [346]) et à un haut couplage direct entre les physiques mécaniques et électriques (jusqu'à 80 % [347]). Parmi les matériaux piézoélectriques, les NFs piézoélectriques semi-conducteurs pourraient être l'un de ses points forts, car ils présentent de bonnes propriétés piézoélectriques et permettent de multiples façons d'intégration avec l'industrie des circuits imprimés. Ces propriétés piézoélectriques améliorées,

qui pourraient être dues à des effets mécaniques (module de Young amélioré, flexibilité) ou électriques, doivent être étudiées pour obtenir le meilleur des NFs piézoélectriques.

L'objectif principal de cette thèse est d'étudier le comportement électromécanique des NFs piézoélectriques semi-conducteurs de GaN et de ZnO pour les applications de capteurs mécaniques et de récupérateur d'énergie mécanique. Cela implique de multiples physiques : la mécanique et l'électronique, mais aussi la physique piézoélectrique et des semi-conducteurs. Il s'agit d'un problème multiéchelle utilisant des nanostructures pour des applications macroscopiques telles que des NG et réseaux de capteur de force de 1 cm^2. Ce sujet est relativement nouveau, pour cette raison nous avons dû développer les connaissances et les outils nécessaires pour l'étude de NFs individuels, mais aussi d'ensembles de NFs à différents niveaux théoriques : conceptuel, analytique et de simulation ; et pratiques : fabrication, caractérisation et d'intégration dans des dispositifs.

Pour mieux comprendre comment les NFs piézoélectriques pourraient aider à répondre à cette question énergétique et de choisir la meilleure approche, nous avons étudié la piézoélectricité, les matériaux utilisés et leurs propriétés. Avec les dernières avancées en synthèse et caractérisation optoélectronique de NFs de ZnO et de GaN, ceux-ci sont devenus très intéressants. Ce sont des matériaux piézoélectriques ayant de bonnes propriétés, par rapport aux meilleurs matériaux ferroélectriques, qui augmentent à l'échelle nanométrique par plus d'un facteur deux [29]. Ils ont l'avantage d'être compatibles avec l'industrie des circuits imprimés, relativement facile à synthétiser par des approches par gravure ou croissance sous forme de NFs semi-conducteurs ce qui les rend plus faciles à intégrer dans les technologies d'aujourd'hui.

Par conséquent, nous avons développé la croissance hydrothermale de NFs de ZnO. Son contrôle nous a permis de faire croitre des NFs de ZnO sur différents substrats (dure ou flexibles) avec des NFs de diamètres allant de 50 à 250nm, de longueurs de 1 à 7µm et des densités de 10^8 à $10^{10} cm^{-2}$. Il s'agit d'une étape essentielle pour la recherche et le développement de la technologie basée sur les NFs. Ensuite, l'autre point clé est de modéliser et de comprendre le comportement des NFs piézoélectriques. Nous avons donc réalisé une étude analytique et des simulations FEM de NFs de ZnO en flexion. Nous avons trouvé une distribution de potentiel piézoélectrique comparable à la littérature, de ±0,3V sous une force latérale F=80nN. Nous avons noté et expliqué l'inversion de potentiel à la base du nanofil et abordé les règles d'échelle et de dimensionnement de ces NFs où le potentiel piézoélectrique augment linéairement avec la force et lorsque le diamètre diminue. Enfin, afin d'étudier les propriétés des NFs de ZnO et de GaN, nous avons développé et réalisé des caractérisations AFM mécaniques et piézoélectriques des NFs. La caractérisation du module de Young de NFs de taille supérieure à 100nm n'a pas mis en évidence d'effet nano mécanique spécifique. La caractérisation piézoélectrique a montré qu'un potentiel électrique allant jusqu'à 300mV est généré lorsque des NFs de GaN sont déformés par des forces de l'ordre du µN. Ce potentiel est proportionnel à la force appliquée, peut saturer et dépend des propriétés des NFs : coefficient piézoélectrique, module de Young et permittivité. Un développement des techniques de caractérisation est encore nécessaire afin de mesurer quantitativement les coefficients piézoélectriques des petits NFs considérés dans ce travail et de comprendre le rôle des porteurs libres, du dopage et la structuration des NFs sur le potentiel généré.

Avec cette compréhension de base du phénomène piézoélectrique dans les NFs de ZnO et de GaN, il est possible de concevoir des applications. Cependant, nous avons pris en compte les phénomènes qui peuvent perturber ou modifier l'effet piézoélectrique. Nous avons modélisé des géométries de NFs cylindrique et hexagonale qui ont un effet négligeable sur l'amplitude du potentiel généré. Les NFs cylindriques sous-estiment de 6% le potentiel généré par des NFs de structure wurtzite. De même, le comportement non linéaire de NFs soumis à de grandes forces affecte fortement l'amplitude et la

distribution du potentiel piézoélectrique qui alors augmente. L'environnement, et notamment le substrat, a une grande influence sur la répartition et l'amplitude du potentiel piézoélectrique qui peut être jusqu'à 7 fois plus fort à la base du NF. Enfin, l'augmentation du dopage des NF peut masquer entièrement le potentiel piézoélectrique et le réduire à zéro [300]. Ces effets sont importants et doivent être pris en compte lors de la conception de dispositifs utilisant des NFs de ZnO ou de GaN. Dans le cas d'un capteur de force ou de déplacement basé sur la réponse en potentiel de NFs piézoélectriques, nous avons montré que la conception, la sensibilité et la résolution d'un tel capteur sont fortement influencées par ces phénomènes parasites, mais qu'ils peuvent être transformés en avantages. Par exemple la variabilité du diamètre des NFs peut permettre le réglage de la sensibilité des capteurs jusqu'à $10mV.nN^{-1}$ ou l'augmentation de la résolution spatiale. Expérimentalement, il est possible de mesurer le courant traversant une jonction Schottky NF-métal pour produire un tel capteur. Ainsi, par AFM, nous avons démontré la faisabilité d'un tel capteur pouvant atteindre une sensibilité de 1,24 $ln(A).nN^{-1}$. Nous avons mis en évidence l'effet piézotronique consistant en l'influence du potentiel piézoélectrique local sur la structure de bande dans les semi-conducteurs et de leurs interfaces. Cet effet est très intéressant et pourrait conduire à l'amélioration de technologies telles que des capteurs UV très sensibles [348], [349] ou notre capteur de force qui est 3×10^4 fois plus sensible que les dispositifs comparables [296].

Acclamée au cours des dernières années, une autre application concerne la récupération d'énergie mécanique à base de NFs piézoélectriques. Grâce à une étude détaillée de cette technologie, nous avons mis en évidence la pertinence de cette approche pour les systèmes intelligents et capteurs autonomes. Ensuite, nous avons étudié et adapté le concept de la récupération d'énergie mécanique à l'utilisation de NFs piézoélectriques. Ceci permet, en plus des avantages de la piézoélectricité, un paramétrage fin des structures et des propriétés physiques pouvant conduire à de nouvelles améliorations. Au début, nous avons étudié la récupération d'énergie dynamique, mais nous avons réalisé que les fréquences de résonance des NFs sont trop élevées (quelques MHz) et qu'il était très difficile de les diminuer à des valeurs adaptées aux vibrations présentes dans notre environnement quotidien (typiquement des fréquences inférieures à 200 Hz). Ainsi, la récupération d'énergie quasi statique est une autre approche du problème. Nous avons distingué deux cas : la sollicitation axiale des NFs lorsque l'appareil est sous compression axiale et la sollicitation transversale un lorsque l'appareil est sous une force de flexion. Ces deux cas sont les meilleurs et les pires cas de contraindre les NFs et ils permettent d'évaluer les performances du NG de notre conception. Dans le premier cas, en utilisant une approche analytique simple nous avons pu comprendre comment le NG fonctionne et mettre en évidence des lignes directrices d'optimisations possibles. Puis, à travers des simulations FEM nous avons clairement compris tous les avantages et les inconvénients de ce problème. Nous avons montré en utilisant ce modèle que la structure optimisée est constituée de NFs piézoélectriques minces et longs avec une densité suffisante. Ainsi des NG à base de NFs de ZnO pourraient être plus sensibles et générer jusqu'à six fois plus d'énergie qu'une couche mince de ZnO avec la même épaisseur et sous la même force, à la manière d'un matériau composite. En plus cela pourrait conduire à une plus grande sensibilité des NG par rapport aux micros récupérateurs d'énergie mécanique standard, utilisant le PZT par exemple, permettant la récupération d'énergie électrique à partir de forces ou de contraintes plus petites. Par conséquent en optimisant la structure des NG à base de NFs de ZnO, à 1Hz sous 1MPa il devrait être possible de récupérer jusqu'à $500nW.cm^{-3}$ et jusqu'à $1.2\mu W.cm^{-3}$ en tenant compte d'un doublement des coefficients piézoélectriques à l'échelle nanométrique. En sollicitation transversale (flexion), l'efficacité du dispositif est plus faible qu'en compression, mais reste supérieure par rapport à un dispositif utilisant une couche mince de ZnO avec la même quantité de ZnO que de NFs. Au cours de ces études, nous avons conçu une structure optimisée de NG et nous avons réalisé

des prototypes pour la compression et la flexion. Pour caractériser ces prototypes, nous avons développé un banc d'essai spécifique et les premiers résultats sont encourageants. Les améliorations sont fascinantes et une telle optimisation électromécanique des NG peut être étendue à d'autres matériaux piézoélectriques tels que l'AIN et le $BaTiO_3$ par exemple. Ainsi les matériaux nano composites piézoélectriques pourraient conduire à de grandes améliorations dans le domaine de la récupération d'énergie piézoélectrique.

Tout au long de cette thèse, j'ai essayé de construire et d'orienter le projet avec une approche réaliste et pratique pour répondre aux principales questions : est-ce que les NFs piézoélectriques peuvent être utiles pour les capteurs autoalimentés et récupérateurs d'énergie mécanique ? J'ai démontré qu'ils peuvent apporter de grandes améliorations dans ces domaines en termes d'intégration, de structuration et de sensibilité. Cette approche est nécessaire pour convaincre de l'intérêt et de la pertinence de ces recherches. C'est pourquoi cette étude est à la fois globale et aussi détaillée que possible sur ce vaste sujet. D'autres études sont encore nécessaires pour continuer à améliorer ces technologies. Des simulations plus précises tenant compte de la physique des semi-conducteurs des NFs de ZnO et de GaN sont nécessaires pour optimiser encore plus les NG et les capteurs de force. La synthèse de NFs faiblement dopés et la fabrication de NG optimisé doivent être développées pour accroître leurs performances et d'atteindre leur plein potentiel. De plus, plusieurs questions doivent être abordées : quel est l'effet du comportement non linéaire piézoélectrique sur les performances des NG ? Le potentiel piézoélectrique généré sature-t-il pour des forces élevées ? Mais aussi quel est l'impact des charges et des pièges dans le matériau de matrice et de quelle façon peut-on transformer les propriétés semi-conductrices des NFs de ZnO et de GaN en avantages ? Tout ceci en améliorant la fiabilité, l'endurance et le vieillissement des NG. De plus, pour alimenter de futurs systèmes autonomes, des récupérateurs d'énergie multi sources pourraient récupérer encore plus d'énergie. C'est pourquoi l'intégration de NG avec d'autres récupérateurs d'énergie devrait être étudiée [350], [351]. Ces améliorations pourraient surmonter les faibles perspectives d'évolution des batteries et ainsi former un duo plus efficace qui avec des systèmes de gestion d'énergie adaptée pourrait rallonger les durées de fonctionnement des futurs capteurs autonomes. Ainsi les NFs piézoélectriques semi-conducteurs, et en particulier les NFs de ZnO et de GaN, pourraient devenir une technologie clé pour les récupérateurs d'énergie future et les capteurs autoalimentés. Tout cela est fascinant et peut conduire à de grandes améliorations dans les futurs capteurs autonomes.